

---

# Multi-year Campaign of the Gamma-Ray Binary LS I +61° 303 and Search for VHE Emission from Gamma-Ray Binary Candidates with the MAGIC Telescopes

---

PhD Thesis

*Author*

Alicia López Oramas

*Supervisor*

Dr. Oscar Blanch Bigas

*Tutor*

Dr. Enrique Fernández Sánchez

Barcelona, 18<sup>th</sup> September 2014

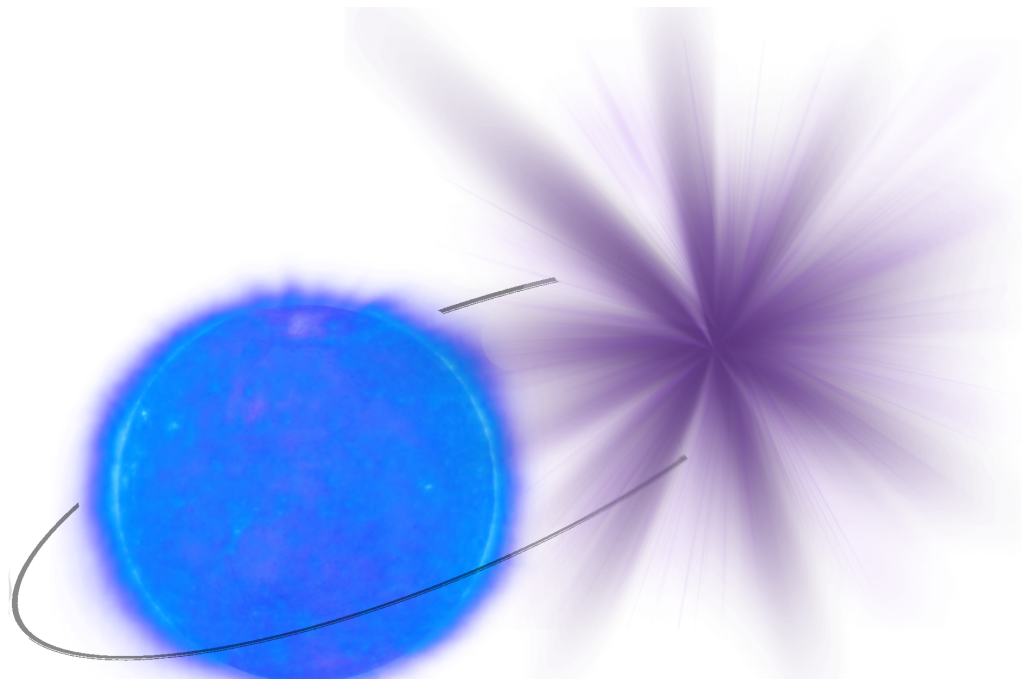
Institut de Física d'Altes Energies  
Universitat Autònoma de Barcelona - Departament de Física  
08193 Bellaterra (Barcelona)



---

# Multi-year Campaign of the Gamma-Ray Binary LS I $+61^{\circ}$ 303 and Search for VHE Emission from Gamma-Ray Binary Candidates with the MAGIC Telescopes

---



PhD Thesis

Alicia López Oramas



*L'essentiel est invisible pour les yeux*

*Le Petit Prince*



## **Declaration of Autorship**

I, Alicia López Oramas, hereby declare that I am the sole author of this thesis titled *Multi-year Campaign of the Gamma-Ray Binary LS I +61° 303 and Search for VHE Emission from Gamma-Ray Binary Candidates with the MAGIC Telescopes*. The data presented in this thesis is property of the MAGIC Collaboration, if not otherwise stated.

I authorize Universitat Autònoma de Barcelona to lend this thesis to other institutions or individuals for the purpose of scholarly research.

Alicia López Oramas  
Bellaterra, 18<sup>th</sup> of September of 2014



# Acknowledgements / Agradecimientos

It is difficult to summarize in few pages all the people that has crossed my life in this four years of PhD. After this time, I have lived many happy moments that will stay with me my whole life and that I have shared with many friends, family and co-workers. But also, on the hardest epochs, I have always felt supported. I feel grateful in hundred different ways. I will try not to forget anyone...

First of all, I want to thank Oscar Blanch Bigas, my supervisor. You have taken very good care of me among these years and I feel very grateful for your support and patience (and we both know you have a lot! ;)). It has been wonderful to live this experience guided by you. De tot cor, moltes gràcies.

On second place, I also want to thank Enrique Fernandez, my tutor, for supporting me along these years of thesis.

I can not forget all the members of the MAGIC/CTA IFAE group. It has been an honor to work with you. Thanks for your advices and your critics. I have learnt a lot from of you. I want to especially thank Julian, who has always patiently been available for solving all the analysis doubts. For sure this thesis would not have been possible without your help! A warm thanks also goes to Abelardo, Stefan K. and Daniel M. for always helping resolving my doubts. Also thanks to JohnE, who helped me with some of my English skills!

I can not forget the engineering team, especially Joan and Oscar A., who have suffered with me many times testing PMTs and components of the LIDAR. It has been very nice to work with you.

This research has been possible by the support of the former Ministerio de Ciencia e Innovación, actually Ministerio de Economía y Competitividad, which has supported this thesis through the concession of the FPI grant with reference BES-2010-037561, part of the project FPA2009-07474.

In the hearth of UAB lies what I consider my second working group. LLuís, Markus and Michele you have been great co-workers and friends. I have always felt part of your little family. You all are splendid physicists and people. Thanks.

I want to warmly thank Ramón García López, who introduced me in the world of astroparticle physics. You have been a wonderful teacher and guide during my University years. If I am here today, it is because of you. Siempre te estaré muy agradecida.

During this thesis, I have performed two stays abroad at Pisa and Paris. It has been wonderful to spend a month with you in Pisa Riccardo; I will always remember the gelati and that amazing lunch in Livorno. Thanks for your spontaneity and sense of humor. Sylvain, thanks for taking care of me in Paris without even knowing me and for giving the opportunity of working with you. I am looking forward for my new french experience!

CTA and MAGIC collaborations. There is many amazing people that I have crossed in meetings, shifts, workshops... It has been a unique experience to be part of these two collaborations. I do not only have learnt but also enjoyed a lot, especially at MAGIC meetings. I want to thank of all you for all those moments. However, there are few

of you I want to individually thank: Paolo (mira mira!), sei stato il migliore guida di tutta la Toscana (e Elisa anche) e sempre così felice... sei grande! También están mis niñas locas Pepa e Irenhinha, que a pesar de que ya nos conocíamos de la uni, gracias a MAGIC y CTA ahora las tengo que soportar más... son las mejores! Y tenemos un viaje pendiente eh! ;) (o dos, o tres, o los que quieran... noveleras!). I also want to thank Javi and Martin (La Palma Postdocs) for always taking such a good care of all of us in La Isla Bonita :) I also spent great time with Max (best shift ever!) and Valeria (gracias por endulzarnos la vida) on shift. Special thanks go to Pere, who has suffered with me in the world of upper limits and to Christian F., Tobias J., Daniela H. and Roberta Z. for x-check analysis of LS I.

Quiero agradecer enormemente a mis antiguos compañeros de despacho, quienes me acogieron calurosamente en el IFAE y que incluso me dieron la bienvenida con un chupito de Arehucas en mi primer día (no se puede recibir a una canaria de mejor manera!). Jelena, gracias por tus buenos consejos y por tu predisposición a ayudar antes cualquier duda de análisis (y por la rakija, por supuesto). Roberta, eres una persona divertidísima que contagias alegría donde vas, eres todo un ejemplo a seguir. Gianluca, con quien nunca se regresa a casa de fiesta antes del amanecer... sabes que el IFAE no es lo mismo sin ti. Ignasi, los buenos momentos vividos contigo son innumerables! Las escaladas, el vèlib pa' arriba, el vèlib pa' abajo, los planes locos... eres una cajita de sorpresas. Me encanta haber vivido tantas experiencias contigo y espero seguir repitiéndolas allá donde estemos. Diego, a pesar de haber compartido despacho durante menos de un año, te convertiste rápidamente en un amigo incondicional, que igual se apunta a un paseo o se mete a las 00 h en el mar en la Nit de Sant Joan para que yo no me bañe sola :)

Aprovecho también para agradecer a gente que ha pasado por el IFAE (o institutos colindantes) a lo largo de mis años de doctorado. A los italianos que me acogieron tan bien cuando llegué a Barcelona: Gianluca (di L.) gracias por hacerme reír en tantas ocasiones. Lorenzo, una de las personas con el corazón más grande que conozco. Y Andrea y Michela que me dieron la oportunidad de vivir la verdadera experiencia plugiana. Una mención especial va para *Calos*, a quien siempre llevo en mi corazón.

Ahora toca al grupo más de moda en las gasolineras de España (LP ya a la venta!): Alisia y loh Godoh. Dani (también conocido como el niño o Daniéh) siempre has sido un *ifaer* más. Eres un niño estupendo y una de las personas más dulces que conozco. Adiv, con quien he compartido tantos paseos fotográficos y time-lapses tormentosos. Creo que ya sé tanto de México como mi amiga Silvia! Rubén, el señor López, siempre te recordaré como mi gran compañero de meetings y por las discusiones sobre phe. Y por último Jeza, la niña más mona que ha pasado por el IFAE, con un corazón tan grande que no te cabe en el pecho. Me alegra que la vida nos haya hecho coincidir en esta experiencia porque me habría perdido a una magnífica persona :-\* .

A los nuevos compañeros de despacho, Alba, Dani y Quim les deseo muchos ánimos. Aprendan a disfrutar de esta etapa maravillosa y única que es el doctorado.

Por supuesto no me puedo olvidar de la gente del IEEC, siempre juntos y revueltos. Mis locas!! Elsa, la pirañita más linda y más maja de Madrid. Fuiste la primera en incluirme en vuestro grupito e incluso lograste convencer a Nataly de que me aceptaran jijiji ;) Me hubiera encantado haber coincidido más tiempo contigo en Barcelona porque eres una chica que merece la pena tener al lado. Daniela, tienes una personalidad tan linda y animada que siempre estás radiante. Contagias buen humor y felicidad allá donde vas. Nataly, has sido un gran apoyo y me has sacado muchísimas carcajadas. Desde que pueda me voy al Médano contigo a montar el chiringuito ;) Jonny, los ángeles se te están dispersando... así cómo vamos a completar nuestras misiones?! Gracias por

los paseos en coche y sobre todo por los helados de cheesecake! Mmmm. Y por último Jacobo, el fotón de Badal, el chico más eléctrico que conozco. Eres un gran personaje al que me alegra de tener en mi vida. Cuando pienso en ti, inevitablemente sonríó.

En *Parigmonamoug* conocí a mis Bombones favoritos. A todas ellas les agradezco tres de los meses más maravillosos de mi vida, en los que acumulé momentos que permanecerán en mi memoria para siempre: la llama, la línea rosita clara, las demis, Chatelet... A ustedes sólo les puedo decir una cosa: Ola k ase? Divinis o k ase? ;)

Gracias a mi compañeros de piso, Fabio y Ale, por hacer de Valldonzella un piso vivo en el que recuperar fuerzas tras los largos días de escritura. Gracias también a mi maridito catalán, el tallarín más animado del planeta, Iñaki, por estar siempre ahí y pasarme en la moto por todo Barna.

Esta etapa no podría haberse completado sin el apoyo de mis maridines. María, por fin vimos cumplido nuestro sueño de adolescencia! Me alegra muchísimo de haber compartido momentos como ese junto a ti. Jairo, estemos donde estemos y aunque nos separen miles de kilómetros, siempre serás mi sombrerero. *Estás loco, majareta; pero... ¿sabes qué?, las mejores personas lo están.* Y, evidentemente, a quien debo un gracias en mayúsculas es a mi Amelia, con quien siento que, a pesar de la distancia, cada día estamos más unidas. Hemos compartido alegrías y mis penas, todos los días a todas horas. Sabes que me has ayudado enormemente en esta etapa de mi vida y que gracias a ti he crecido mucho. Que las cosas que no nos pasan a nosotras no le ocurren a nadie más! Y ahí seguiremos compartiendo comilonas, flores de Chasna y bañitos en el Socorro (entre tantas otras cosas).

Cipe, sei stato la più grande sorpresa di quest' anno. Il tuo sorriso, la tua gioia e gli canzoni stupidini mi hanno dato la forza per scrivere la tesi. Ma non solo io ti ringrazio... anche io mio occhio sinistro ti ringrazia ;) Sei immensamente Cipe =)

Bea, no sé cómo agradecerte todo lo que has hecho por mí y todo lo que me has dado. Se quedan cortas las palabras cuando te digo que eres mi medio pomelito y que has sido mi familia en Barcelona. Contigo la ciudad cobró vida y una nueva etapa se abrió paso... la de moderna de poble! ;). Eres lo más grande que he tenido aquí y te llevaré en mi corazón siempre, porque una novelera así como tú no se encuentra todos los días. No te librarás tan fácilmente de mí, que lo sepas y es que... amiguita sólo hay una!!! Así que cuidadito con las escaleras que me tienes que durar! Borjis, gracias "por prestármela" tantos días... cuídamela bien eh! Arriba esos Patz! (poo pi pararara poooo piriririi parapararapoooo).

Por último, pero no por ello menos importante, quiero agradecer a mi familia. Gracias abuela por cuidar de mi y por los sabios consejos sobre las horas de estudio y sus posibles efectos sobre los cortes de digestión. Abuelo, gracias por criarme y motivarme a estudiar. Eres uno de los hombres más sabios que he conocido. Gracias Juan Manuel, porque sé que siempre has estado muy orgulloso de tu sobrina. Tere, sabes que no sólo eres mi tía preferida, sino que eres una segunda madre para mí. Si no fuera por tus potajitos y tus consejos culinarios no sé cómo habría sobrevivido. Finalmente, mi más sincero agradecimiento a mis padres, Carlos e Isabel, que han sido un modelo a seguir para mí desde siempre. Papá, gracias por incentivar mi amor por la astrofísica, te estaré eternamente agradecida. Desde que viste mi curiosidad por las estrellas hiciste todo lo posible por enseñarme las maravillas de este campo. Mamá, gracias por incentivar mis ganas de viajar, de aprender, de estudiar. Gracias por enseñarme a ser una mujer independiente capaz de valerse por sí misma y por siempre alentarme a salir fuera de las islas. Y gracias por ver más allá de la "Alicia astrofísica". Gracias a los dos por todo esto y por mucho más, realmente no soy capaz de expresar con palabras todo lo que siento. Les quiero.



# Contents

<b>Acknowledgments</b>	i
<b>Summary</b>	1
<b>Resumen</b>	3
<b>1 Very High Energy <math>\gamma</math>-ray Astronomy</b>	7
1.1 Cosmic Rays . . . . .	7
1.2 $\gamma$ -Ray Astronomy . . . . .	9
1.2.1 $\gamma$ -ray Production . . . . .	9
1.2.2 $\gamma$ -ray Sources . . . . .	10
1.2.3 HE $\gamma$ -ray Detection: Satellite-based Instruments . . . . .	12
1.2.4 VHE $\gamma$ -ray Detection: The IACT Technique . . . . .	13
<b>2 Atmospheric Characterization for CTA</b>	19
2.1 The Need of Atmospheric Monitoring . . . . .	19
2.2 The LIDAR Technique . . . . .	20
2.3 The IFAE/UAB Raman LIDAR . . . . .	23
2.3.1 Configuration . . . . .	23
2.3.2 The Primary Mirror . . . . .	25
2.3.3 The Pulsed Laser . . . . .	26
2.3.4 The Light Guide . . . . .	27
2.3.5 The Optical Detector . . . . .	29
2.3.6 The Readout Electronics . . . . .	29
2.4 Tests . . . . .	30
2.4.1 The Primary Mirror . . . . .	30
2.4.2 The Pulsed Laser . . . . .	33
2.4.3 The Light Guide . . . . .	35
2.4.4 The Optical Detector . . . . .	38
2.4.5 Conclusions from the Tests . . . . .	41
<b>3 The MAGIC Telescopes</b>	45
3.1 Telescopes Description . . . . .	45
3.1.1 Camera . . . . .	46
3.1.2 Reflecting Surface . . . . .	48
3.1.3 Structure . . . . .	49
3.1.4 Drive System . . . . .	49
3.1.5 Readout Electronics and Trigger . . . . .	50
3.1.6 Calibration . . . . .	51

3.1.7	Data Acquisition . . . . .	52
3.1.8	Telescope Operation . . . . .	55
3.1.9	Monte-Carlo . . . . .	56
3.2	Data Analysis . . . . .	56
3.2.1	Low-level Analysis . . . . .	58
3.2.2	Intermediate-level Analysis . . . . .	61
3.2.3	High-level Analysis . . . . .	62
3.3	Moonlight Observations . . . . .	65
3.3.1	Cycle VI dedicated analysis . . . . .	66
<b>4</b>	<b>Compact Binary Systems</b>	<b>71</b>
4.1	Introduction to Binary Systems . . . . .	71
4.2	X-Ray Binaries . . . . .	72
4.2.1	High Mass X-Ray Binaries . . . . .	73
4.2.2	Low Mass X-Ray Binaries . . . . .	74
4.2.3	X-ray Binaries as possible $\gamma$ -Ray Emitters . . . . .	76
4.3	$\gamma$ -Ray Binaries . . . . .	76
4.3.1	Why Only Five $\gamma$ -ray Binaries? . . . . .	78
4.3.2	Scenarios . . . . .	80
<b>5</b>	<b>Multi-year Observations of the <math>\gamma</math>-Ray Binary LS I +61°303</b>	<b>83</b>
5.1	Unveiling the System . . . . .	83
5.1.1	Multiwavelength Context . . . . .	84
5.2	Accretion Model vs Pulsar Wind Scenario . . . . .	91
5.2.1	Microquasars: Accretion Scenario . . . . .	92
5.2.2	Pulsar-wind Scenario . . . . .	94
5.3	Multi-year Observations of LS I +61°303 . . . . .	97
5.3.1	Cycle VI Campaign . . . . .	98
5.3.2	Cycle VII Campaign . . . . .	104
5.3.3	Cycle VIII Campaign . . . . .	107
5.3.4	Cycle IX Campaign . . . . .	111
5.4	Super-orbital variability . . . . .	114
5.4.1	Periodicity Analysis . . . . .	121
5.5	Spectral Variability Studies . . . . .	128
5.6	Optical H $\alpha$ -TeV Correlation . . . . .	131
5.7	Discussion . . . . .	139
<b>6</b>	<b>Observations of the <math>\gamma</math>-Ray Binary Candidate MWC 656</b>	<b>143</b>
6.1	Historial Introduction . . . . .	143
6.2	MAGIC Observations . . . . .	145
6.3	Data Analysis . . . . .	146
6.4	Results . . . . .	147
6.5	Discussion . . . . .	150
<b>7</b>	<b>Search for <math>\gamma</math>-ray Emission from the Microquasar SS-433</b>	<b>155</b>
7.1	The Microquasar SS 433 . . . . .	155
7.1.1	$\gamma$ -ray Emission and Absorption Processes . . . . .	157
7.2	MAGIC Observations of SS 433 . . . . .	159
7.3	Results . . . . .	160
7.4	Discussion . . . . .	161

<b>8 Conclusions &amp; Perspectives</b>	<b>167</b>
<b>Acronyms</b>	<b>167</b>
<b>Conclusions &amp; Perspectives</b>	<b>167</b>
<b>Bibliography</b>	<b>171</b>
<b>List Of Figures</b>	<b>185</b>
<b>List Of Tables</b>	<b>189</b>
<b>Acronyms</b>	<b>189</b>
<b>A Acronyms</b>	<b>191</b>



# Summary

Light is the primary source of information used by humans to study the Universe, and photons are its messengers. The electromagnetic spectrum of the light spans from low energies (radio) up to very high energy photons ( $\gamma$  rays). The optical wavelengths have been used by astronomers since ancient times to study the Cosmos. However, as time passed, new and improved techniques led to the discovery of astronomy in other wavelengths: infrared, ultraviolet, millimeter and radio.

The later decades of the XX century saw an advance in the study of the most energetic part of the electromagnetic spectrum: X rays and  $\gamma$  rays. Since these photons are absorbed by the Earth's atmosphere, there is a need to either perform observations with satellites in outer space, which has only been possible since the space age started. In the case of  $\gamma$  rays, they can also be detected indirectly from Earth. Furthermore, relativistically charged particles arriving at Earth from outer space, denominated cosmic rays, were first detected. But where do these highly-energetic particles come from? The question is not straightforward to answer, since charged particles are deflected by magnetic fields in the Universe as they travel from their source of origin. However, since  $\gamma$  rays are generated by the collisions and / or interaction between particles or particles and photons, they can be used as an indirect tool to reveal the origin of the sources that host relativistic particles. Since  $\gamma$  rays are photons, they are not deflected by magnetic fields and can directly be tracked to the astronomical source were they were generated.

In the 70's, the Imaging Air Cherenkov Technique was first developed, being Whipple the first telescope of this kind. These telescopes, also called Cherenkov telescopes, detect the extensive air showers produced when a primary incoming particle interacts with atmospheric nuclei. As the charged particles produced in the cascade travel faster than light in dielectric mediums (the atmosphere), a UV flash of Cherenkov light is emitted. This light is collected, in this case, by large reflectors and focused onto a sensitive pixelized camera. Both  $\gamma$  rays and charged cosmic rays produce air showers, although they develop differently and are thus distinguishable with appropriate hardware and software.  $\gamma$  rays from energies above 25 GeV are detected using this technique. The current generation of IACTS, like HESS, MAGIC and VERITAS have led to the discovery of new sources emitting in the very high-energy  $\gamma$ -ray regime: supernova remnants, active galactic nuclei and binary systems, among others.

This thesis is focused on the study of compact binary systems that emit  $\gamma$ -ray emission, the so-called  $\gamma$ -ray binaries, with the MAGIC telescopes. The bulk of the non-thermal emission of these sources peaks in the  $\gamma$ -ray domain. Only five systems are the members of this reduced group. All of them host massive stars and a compact object, remnant of a supernova explosion. Only the compact object of one of these binaries is known, a neutron star. Although none of them display pulsations (associated with neutron stars) or double-jet structures (associated with microquasars), most of the theories and observations suggest a neutron star as the compact object. The most accepted scenario to explain the VHE emission of this source class is the *pulsar wind scenario*. The wind of the massive star and the wind of the neutron star interact,

accelerating particles up to relativistic energies with the consequent emission of  $\gamma$ -ray photons.

The outline of the thesis is the following:

- Chapter 1 is an introduction to very high energy  $\gamma$ - ray astronomy. First, a brief history of cosmic rays and their relation with  $\gamma$  rays is introduced. Direct methods for the detection of  $\gamma$  rays in outer space are described, as well as indirect detection on Earth with ground-based observatories. Since this thesis uses data from a ground-based observatory, the MAGIC telescopes, the Imaging Air Cherenkov Technique and its physics principles are introduced.
- In Chapter 2, the restrictions of IACTs in terms of the systematic uncertainties due to atmospheric conditions and the need for correcting them are discussed. A LIDAR is introduced in this chapter as a solution for the next generation of IACTs, the Cherenkov Telescope Array (CTA), to reduce systematic errors and enlarge the duty cycle. The LIDAR which is being developed and characterized at IFAE is described, as well as the performance of this system.
- Chapter 3 shows a description of the MAGIC telescopes. The hardware and software components, with a special contribution to the data acquisition system by the author of this thesis, are described. The standard data analysis chain is also collected in this chapter as well as the special treatment of the data under moderate - strong moonlight conditions.
- Chapter 4 is an introduction to compact binary systems. It describes the large variety of these sources in this Universe, finally focussing in X-ray binaries and  $\gamma$ - ray binaries. The possible scenarios to account for the  $\gamma$ - ray emission of these sources are also introduced.
- Chapter 5 is the complete and detailed description of the  $\gamma$ -ray binary LS I +61°303. The results of a multi-year campaign are shown in this Chapter. Studies on the yearly flux variability and the possible existence of a super-orbital modulation in the flux are investigated. Furthermore, searches for spectral variability (found in another energies) are performed. Finally, a correlation study of the TeV flux with the mass-loss rate of the Be star through simultaneous observations with an optical telescope is performed.
- In Chapter 6, a search for TeV emission of the  $\gamma$ -ray binary candidate MWC 656 is performed. This system is especially interesting for being the first Be star to be proven to host a black hole.
- Chapter 7 details the search for VHE  $\gamma$ -ray emission of the binary system SS 433, which is a microquasar embedded in a nebula. It is the only super-critical accretor in the Galaxy and displays hadronic jets emission.
- Finally, concluding remarks from the presented studies and future perspectives are discussed in Chapter 8.

# Resumen

La luz es la principal fuente de información utilizada por el hombre para estudiar el Universo y, los fotones, son los mensajeros que portan dicha información. El espectro electromagnético se extiende desde muy bajas energías, desde las frecuencias de radio, hasta muy altas energías, los rayos  $\gamma$ . Desde la antigüedad, los astrónomos han estudiado el Cosmos en el rango visible u óptico. Con el paso de los años y el descubrimiento de nuevas técnicas, el rango de observaciones se expandió a otras longitudes de onda: infrarrojo, ultravioleta, milimétricas y radio.

Las últimas décadas del siglo XX supusieron un avance en el estudio de la parte más energética del espectro electromagnético, correspondiente a los rayos X y los rayos  $\gamma$ . Dado que estas radiaciones son absorbidas por la atmósfera terrestre, sólo cabe dos posibilidades para su estudio: a través de satélites espaciales, hecho que ha sido posible a partir del comienzo de la carrera espacial. La radiación gamma también puede detectarse a través de medidas indirectas desde la Tierra. Además, a principios de siglo, se descubrió la existencia de partículas relativistas con carga eléctrica que provenían del espacio, los denominados rayos cósmicos. Pero, ¿de dónde proceden estas partículas tan energéticas? Esta pregunta no es sencilla de responder, debido a que las partículas con carga son desviadas por los campos magnéticos presentes en el Universo y son desviadas de su trayectoria original. Por tanto, no es fácil saber cuál es la fuente que los ha emitido. Sin embargo, dado que los rayos  $\gamma$  son generados en colisiones o interacciones entre partículas o partículas y fotones, suponen una manera indirecta de estudiar qué tipo de fuentes astrofísicas albergan partículas relativistas. Dado que los rayos  $\gamma$  son fotones, no se ven afectados por los campos magnéticos y se puede conocer cuál es el objeto que los ha generado.

En los años 70, se desarrolló por primera vez la técnica por imagen Cherenkov en el aire (IACT en inglés). Este tipo de telescopios, también llamados telescopios Cherenkov, detectan las cascadas de partículas que producen en la atmósfera terrestre los rayos  $\gamma$  o los rayos cósmicos al interactuar con los elementos atmosféricos. Dado que las partículas viajan más rápido que la luz en un medio dieléctrico (como la atmósfera), unos rápidos flashes de luz ultravioleta denominados luz Cherenkov son emitidos. Esta luz es recibida por el telescopio y es focalizada en una cámara ultrasensible. Aunque tanto los rayos cósmicos como los rayos  $\gamma$  producen cascadas, éstas son diferentes y se pueden discernir la una de la otra mediante la electrónica y la programación adecuada. Los rayos  $\gamma$  con energías mayores de 25 GeV son detectados con esta técnica. La nueva generación de telescopios Cherenkov, como HESS, MAGIC y VERITAS ha llevado al descubrimiento de nuevas fuentes que emiten en el régimen de los rayos  $\gamma$  de alta energía, tales como remanentes de supernova, núcleos activos de galaxias o sistemas binarios, entre otros.

Esta tesis se centra en el estudio de sistemas binarios compactos que emiten rayos  $\gamma$ , las denominadas binarias de rayos  $\gamma$ , con los telescopios MAGIC. La mayoría de la emisión no térmica de estas binarias se realiza en el régimen de la radiación  $\gamma$ , de ahí su nombre. Sólo cinco sistemas son los componentes de este reducido grupo. Todos ellos tienen estrellas masivas, pero sólo se conoce la naturaleza del objeto compacto

de una de ellas, que se trata de una estrella de neutrones. Aunque ninguno de ellos muestra pulsaciones (propio de estrellas de neutrones) ni estructuras que se asemejen a jets (típico de agujeros negros), la mayoría de las teorías apuestan a que el objeto compacto de estos objetos es una estrella de neutrones. El escenario más aceptado para explicar la emisión  $\gamma$  de muy alta energía es aquel en el que el viento estelar interactúa con el viento de la estrella de neutrones, acelerando las partículas presentes en el sistema hasta velocidades relativistas, con la consecuente emisión de rayos  $\gamma$ .

El esquema de la tesis es el siguiente:

- El Capítulo 1 es una introducción a la astronomía de rayos  $\gamma$  de muy alta energía. En primer lugar se presenta un pequeño resumen de la historia de los rayos cósmicos y su relación con los rayos  $\gamma$ . A continuación, se describen los métodos directos para la detección de rayos  $\gamma$  desde el espacio, así como la utilización de métodos indirectos desde observatorios en tierra. Debido a que esta tesis utiliza datos de un telescopio terrestre, MAGIC, también se introduce la técnica IACT y sus fundamentos físicos.
- En el Capítulo 2, se discuten cuáles son las restricciones de los telescopios Cherenkov debido a las incertidumbres sistemáticas provocadas por el desconocimiento de las condiciones atmosféricas y la necesidad de corregirlas. Como posible solución, se propone la utilización de sistemas LIDAR y se describe el instrumento de este tipo que está siendo desarrollado y caracterizado en el IFAE.
- Los telescopios MAGIC, desde los componentes electrónicos y mecánicos hasta ciertos programas que trabajan en él, están descritos en el Capítulo 3. Se hace especial hincapié en el sistema de adquisición de datos, en el que la autora de la tesis ha contribuido desarrollando una pequeña parte del software. La cadena de análisis estándar de MAGIC también se describe en este Capítulo. Por último, se dedica un apartado especial a las observaciones tomadas bajo condiciones de luna moderada o fuerte.
- El Capítulo 4 es una introducción a los distintos tipos de sistemas binarios que se conocen en el Universo, prestando especial atención a los sistemas binarios en rayos X y en rayos  $\gamma$ . Los posibles escenarios para explicar la emisión gamma de estos últimos se discuten aquí también.
- El Capítulo 5 es una completa y detallada descripción de la binaria de rayos  $\gamma$  LS I + 61°303 y se muestran los resultados de una campaña multi-anual. Se investiga la variabilidad anual en la emisión a muy altas energías de esta fuente, así como la posible existencia de una modulación super-orbital en su flujo. Además, se realiza un estudio sobre variabilidad espectral (hecho que ocurre en otras energías). Finalmente, se estudia la posible correlación entre el flujo en rayos  $\gamma$  de muy alta energía y la pérdida de masa de la estrella, a través de observaciones simultáneas de MAGIC y el telescopio óptico LIVERPOOL.
- En el Capítulo 6, se describen las observaciones realizadas sobre la candidata a binaria de rayos  $\gamma$  MWC 656, que se trata de un sistema es muy interesante debido a que se trata de la primera estrella masiva tipo Be en albergar un agujero negro, probado experimentalmente.
- En el Capítulo 7 se muestra la búsqueda de emisión  $\gamma$  del sistema binario SS 433, un microquasar que se encuentra sumergido en una nebulosa. Es el único acretora en régimen super-crítico que se conoce en la Vía Láctea, y además muestra jets hadrónicos que interaccionan con la nebulosa.

- Finalmente, las conclusiones de los estudios realizados y algunas perspectivas de futuro se recogen en el Capítulo 8.



# 1

## Very High Energy $\gamma$ -ray Astronomy

THE electromagnetic spectrum spans over twenty orders of magnitude in energy, from radio up to TeV  $\gamma$  rays. Since X-rays and  $\gamma$  rays are absorbed in the Earth's atmosphere, it was not until the last decades of the XX century that X-ray and  $\gamma$ -ray astronomy were born, thanks to the construction of space satellites and the development of new indirect techniques for the ground detection of  $\gamma$  rays. The past four decades, from the 1980's to the 2000's, have been the golden age of  $\gamma$ -ray astronomy:  $\gamma$ -ray satellites were launched to space and, since the first Cherenkov telescope was operative back in the 80's, now the third generation of Imaging Air Cherenkov Telescopes is born, and the next generation is under prototyping with the Cherenkov Telescope Array. This Chapter is an introduction to  $\gamma$ -ray astronomy, describing the mechanisms and sources of production of  $\gamma$  rays in the Universe. It also relates  $\gamma$  rays with cosmic rays. Finally, the technique for the detection of extensive air showers is described.

### 1.1 Cosmic Rays

---

In the beginnings of the XX century, physicists discovered an intriguing fact: electroscopes were naturally discharged without any specific reason. They attributed this discharging to the interaction with an ionizing radiation whose origin was unknown. In 1912, Austrian physicist Viktor F. Hess discovered an ionizing radiation that was originated in outer space thanks to the balloon flight experiments that he performed. In 1926, Millikan denominated this radiation *cosmic rays* (CRs) [150].

Hess did not detect the original CRs generated in outer space, but secondary particles produced after the interaction of CRs with the Earth's atmosphere. In 1938, Pierre Auger showed that CRs can generate extensive air showers (EAS) when interacting with the atmosphere, distributing their initial energy in the production of millions of lower energetic particles that arrive to the ground almost simultaneously [41]. The discovery of the EAS led to the discovery of new particles such as the positron, the muon or the pion, through the use of cloud chambers.

CRs are mainly composed by charged particles: 87% are protons, 11% are  $\alpha$  particles ( $He^{++}$ ), 2% are electrons and positrons and 1% are ionized nuclei of heavier elements (C, N, O, Fe). The remaining  $\sim 0.1\%$  are neutrons, neutrinos and  $\gamma$  rays. The chemical abundance of protons and nuclei (98%) is similar to that in the Solar System.

The energy spectrum of CRs spans over 13 decades in energy, from  $10^9$  to  $10^{21}$  eV (see Figure 1.1). The spectrum can be approximated to a simple power law  $F \sim E^{-\Gamma}$  described by non-thermal processes, which are those independent on the temperature of the source and are not caused by the transition of electrons in their orbits. Two

important features are identified in the spectrum: the *knee*, located at  $\sim 5$  PeV (1 PeV =  $10^{15}$  eV) and the *ankle*, situated at  $\sim 3$  EeV (1 EeV =  $10^{18}$  eV). At low energies, the CR flux is modulated by the Solar wind. Below the knee and above the ankle, the spectrum is described by a power-law with index  $\Gamma = 2.7$ . Between this two features, the spectrum softens to  $\Gamma = 3.0$ . At energies of  $\sim 10^{20}$  eV, lies the *Greisen-Zatsepin-Kuzmin limit* (GZK limit) [99, 210], the value for which the CRs would interact with the cosmic microwave background and lose energy through pion production.

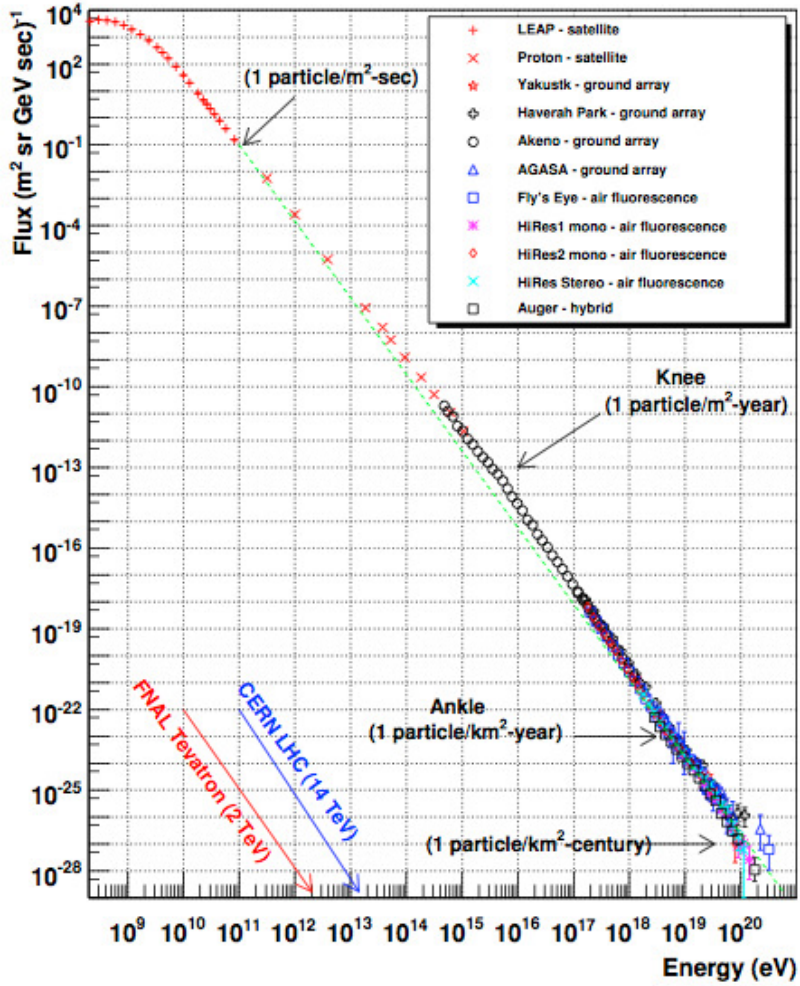


Figure 1.1: Cosmic ray spectrum measured by different experiments. The *knee* and the *ankle* spectral breaks are marked. The red and blue arrows mark the energies reached by the largest human-built experiments.

The CRs reaching the Earth with energies up to the knee are thought to have a galactic origin, while above the ankle the nature of CRs is extragalactic. However, the origin of CRs between this two features is still under debate [108, 109]. Galactic CRs have largely been thought to be accelerated in supernova remnants (SNRs) (see [17] for a review). Recently, *direct* evidence of pion-decay signatures in SNRs has been reported [10]. The origin for ultra-high energetic CRs (UHECRs) above the ankle is still unknown. The proposed sources for acceleration are active galactic nuclei (AGNs) and gamma ray burst (GRBs), both sources of extragalactic origin. The detection and measurement of these particles is difficult due to their low fluxes: one particle per square kilometer per century. Alternative models propose UHECRs to be produced in the decay of super-heavy objects as dark matter particles. Measurements of the arrival

direction, primary mass composition and flux will be the key ingredients to solve this puzzle.

Direct detection of CRs with balloons and space experiments is feasible only up to energies of  $10^{14}$  eV. Above this energy, the flux is too low to be detectable by space detectors, hence they are observed by ground-based detectors thanks to air-shower development. Some of these ground observatories are AUGER, HEGRA or KASCADE [196, 65, 120]

## 1.2 $\gamma$ -Ray Astronomy

---

Charged cosmic rays are deflected in their propagation through the interstellar and intergalactic medium by the Lorenz force that is created when a charged particle is moving in a magnetic field. Therefore, they can not be tracked back to the astronomical source of origin. A supplementary approach to solve the CR mystery is through the study of  $\gamma$  rays, which are the most energetic photons of the electromagnetic spectrum. As it will be explained below,  $\gamma$  rays are produced by charged particles via different mechanisms. As they are neutrally charged, they can be tracked until the source of origin, providing information on the population of particles in astronomical sources.  $\gamma$  rays are worth studying because they provide information of:

- The sources of origin where they are produced.
- The mechanisms of particle acceleration and production.
- The characteristics of the interstellar / intergalactic medium that they have crossed until reaching the Earth.

$\gamma$  rays can be divided into soft ( $E > 100$  MeV), high energy ( $HE > 1$  GeV) and very high energy ( $VHE > 100$  GeV). HE  $\gamma$  rays are detected by satellite detectors, while VHE  $\gamma$  rays are detectable through indirect observations by ground-based telescopes (see Subsection 1.2.4 for more details). The work resumed in this thesis is focused on the latter.

### 1.2.1 $\gamma$ -ray Production

---

$\gamma$  rays are produced due to non-thermal processes, which are not described by black-body radiation. Two possible scenarios for the production of  $\gamma$  rays are feasible: a leptonic scenario where the primary particles producing  $\gamma$ -ray emission are electrons (or positrons) and a hadronic scenario, where protons (and ions) play a major role in the production. The most important mechanisms of production of  $\gamma$  rays in astrophysical environments are:

#### Leptonic Scenarios

- *Bremsstrahlung*: radiation emitted by the deceleration of an electron when it is deflected in the electrostatic field produced by a nucleus or ion. In a non-relativistic regime, the  $\gamma$  rays emitted will have the same spectrum as the electron acceleration spectrum, a power-law. In a relativistic regime, the spectrum flattens to a power law with index  $\Gamma - 1$ . The process becomes inefficient for a certain threshold energy,  $\sim 350$  MeV in the case of hydrogen. It requires an ambient with matter.

- *Inverse Compton (IC)*: a relativistic electron scatters up a low-energy photon, transferring part of its energy and producing a  $\gamma$  ray. It requires an ambient with a radiation field and an environment transparent to  $\gamma$  rays to permit them escape from the production region. Depending on the energy of the incident electron  $E_e$  and the energy of the target photon  $E_\gamma$ , two different regimes are distinguishable: if  $E_e E_\gamma \ll m_e^2 c^4$ , the populations lie below the *Thomson* limit and the power-law has a spectral index  $(\Gamma + 1)/2$ . The average energy of the produced photons is  $\frac{4}{3} < E_\gamma > \gamma_e^2$ , with  $\gamma_e$  the Lorentz factor. If  $E_e E_\gamma \gg m_e^2 c^4$ , the *Klein-Nishima* regime is set and the spectrum is steeper,  $(\Gamma + 1)$ . In this case, the energy of the photons is  $\frac{1}{2} < E_e >$ .

Typical photon fields are those from stars, cosmic microwave background or synchrotron radiation (Synchrotron-Self-Compton emission, SSC).

- *Synchrotron Radiation*: electromagnetic radiation produced by relativistic electrons moving in a magnetic field. In general, the energy of the generated photons is less than that of the parent electrons, but at some astrophysical environments  $\gamma$ -ray emission can be produced. Strong magnetic fields are required. Furthermore, synchrotron radiation may be a source of seed photons for the IC scattering.

## Hadronic Scenarios

- *Pion ( $\pi^0$ ) Decay*: in the case of a population of protons (and / or ions), their interaction through inelastic scattering with ambient gas can produce mesons ( $\pi$ ). The neutral meson  $\pi^0$ , which is produced with a probability of  $\sim 30\%$  and has a short lifetime ( $\sim 10^{-17}$ s), decays as:  $\pi^0 \rightarrow \gamma + \gamma$ , producing  $\gamma$ -ray emission. In this scenario, the charged pions  $\pi^\pm$  decay producing large amount of HE neutrinos. The neutrinos, if detected, can also be used as trackers for CRs and suppose a clear signature of a hadronic scenario.

### 1.2.2 $\gamma$ -ray Sources

$\gamma$  rays are produced in sources where violent events occur, accelerating particles up to relativistic energies. The astronomical sites of VHE  $\gamma$ -ray production in the Universe are:

## Galactic Sources

- *Compact Binary Systems*: Systems composed of a massive O – B type star and a compact object, either a neutron star (NS) or a black hole (BH). Although both the microquasar and pulsar wind scenarios are accepted, most theories point that the compact object is most likely a NS [72] and that the VHE emission is due to the interaction between the wind of the star and the wind of the pulsar. Only five  $\gamma$ -ray binaries have been detected. These systems are the main subject of study of this thesis.
- *Galactic Center (GC)*: The center of the Milky Way host a supermassive black hole, *Sgr A\**, which has been established as a steady source of VHE emission up to 10 TeV. However, it is a crowded area and it is difficult to point the exact location of the VHE source.
- *Supernova Remnants (SNRs)*: When a massive star ends its life, the internal pressure is not capable to sustain the gravitational pressure and it collapses in an

explosion called supernova. An external shell is ejected forming a gas nebula and a compact object (BH or NS, depending on the mass of the initial star) is created. The energy released in a SNR is enough to accelerate particles and non-thermal processes occur. It has been theorized that SNRs are the accelerators of galactic CRs. The interaction with the interstellar medium is critical for the acceleration of particles up to TeV energies. Several SNRs have been detected in the HE and VHE regime, as Cas A [18], W 51 [31] or W44 (only in HE) [4]. The emission of some of these sources has been proven to be well described by hadronic models, supporting the theory of the origin of galactic CRs.

- *Pulsars*: A pulsar is a rapidly rotating neutron star with a strong magnetic field. The rotation period vary from few milliseconds up to few seconds. Jets are present in these systems. The magnetic axis might not be aligned with the rotation axis, provoking that the jet sweeps. If the beam points towards the Earth, a periodic pulsed signal is detected. Several pulsars have been detected in the 100 MeV – 10 GeV range. At VHE, the Crab Nebula pulsar has been detected from 25 GeV [34] up to 400 GeV [26].
- *Pulsar Wind Nebulae (PWN)*: When a pulsar display a prominent nebular emission, it is denominated as pulsar wind nebulae. PWN are classified differently from SNRs because the models describing them are different, since in PWN the bulk of radiation is given to the nebula by the pulsar. The VHE emission is most likely leptonic. The rotational energy of the pulsar is converted into a relativistic *wind* of particles, which terminates in a shock when it collides with the surrounding nebula. The most famous PWN is the Crab Nebula, which is the most steady and strong VHE emitter in the sky and which is used as standard candle for the GeV – TeV regime. Both the nebula and the pulsar have been detected in the VHE regime.

## Extragalactic Sources

- *Active Galactic Nuclei (AGNs)*: AGNs are galaxies with a supermassive black hole in their center. This supermassive BH accretes mass from the surroundings creating a highly relativistic accretion disk, surrounded by fast-moving clouds. Two collimated relativistic jets might be created perpendicularly to the galaxy plane. If the viewing angle is small, the jet emission is amplified. These sources are denominated *blazars* or *BL-Lacs* and constitute the bulk of AGNs detected at VHE. The VHE radiation is supposed to be produced by energetic electrons interacting with soft photons inside the jet by IC scattering or by protons that generate hadronic cascades. About 10% of AGNs are radio-loud. A radio-loud object with low optical flux is classified as *radio galaxy*. A radio-quiet object with low optical flux it is called *Seyfert galaxy*. The first AGN to be detected at TeV energies is was Mrk 421 [174].
- *Gamma-ray Bursts (GRBs)*: GRBs are the most energetic short phenomena in the Universe. It is a very short and intense emission of  $\gamma$  rays. They are isotropically distributed in the sky. There are basically two kinds: short-duration, lasting from few milliseconds to  $\sim$ 2 seconds and long-duration, lasting from  $\sim$ 2 to few hundreds of seconds. Their origin it is still not clear. In the case of short-duration GRBs, they might be the result of binary mergers, like two NS. Long-duration GRBs, might be related to supernova or hypernova explosions. Although several GRBs have been detected at HE, none has been detected in the VHE regime. MAGIC

has been especially designed to *catch* this kind of sources. For that purpose, a light structure has been constructed so the telescopes can point anywhere in the sky in less than 40 seconds (details on the structure is resumed in Subsection 3.1.3).

### 1.2.3 HE $\gamma$ -ray Detection: Satellite-based Instruments

The Earth's atmosphere is not transparent to energetic photons: X rays and  $\gamma$  rays are absorbed and can not be directly detected from ground. Hence, direct detection of  $\gamma$ -ray emission is only possible with space-based experiments. The main drawback is the size of the detector, that can not be very large due to limitations of the payload mass that can be sent to space. Therefore, these experiments are characterized by having small effective areas. However, the advantage of these detectors is that they perform very good background rejection and have an accurate spatial resolution and energy reconstruction, achieved thanks to the direct detection technique. An anti-coincidence system is necessary in order to reject the CR background. The rejection is performed by a veto in the trigger.

The general detection principle is based on pair production: the primary  $\gamma$  ray is converted to an electron-positron ( $e^- - e^+$ ) pair by means of a converter material. The paths of these particles are revealed in the tracker, allowing the reconstruction of the direction of the initial  $\gamma$  ray. Finally, the particles reach the calorimeter, where their energy is estimated. See Figure 1.2 for an example describing the *Fermi*-LAT detector.

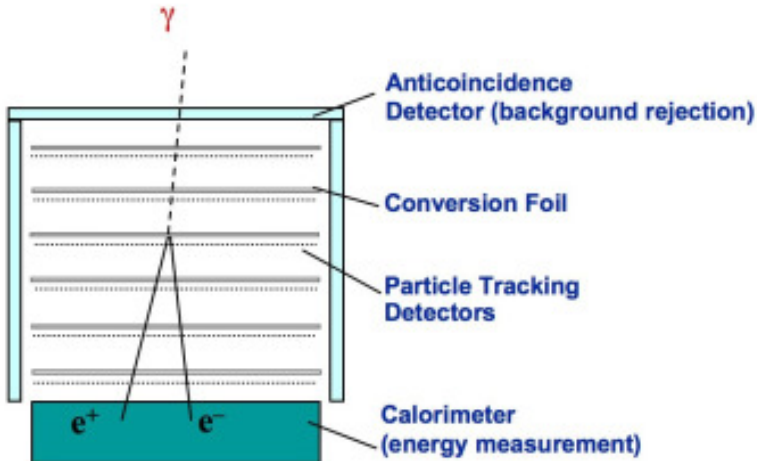


Figure 1.2: *Fermi*-LAT detector. The different components are labelled. [Credit: Fermi Collaboration].

Some relevant  $\gamma$ -ray space-based missions are described below:

- The former (1991 – 2000) EGRET (Energetic Gamma Ray Experiment Telescope) detector was on-board Compton Gamma Ray Observatory satellite [197]. It detected  $\gamma$  rays from 30 MeV to 30 GeV and created a map of the  $\gamma$ -ray sky. It was the predecessor of *Fermi* -LAT [40].
- LAT (Large Area Telescope) is a instrument onboard of *Fermi* satellite, formerly GLAST, which was launched in 2008 and that orbits the Earth in a low Earth orbit. It detects  $\gamma$  rays from 20 MeV to 300 GeV. *Fermi*-LAT performs observations in *survey mode*: it points north and south in alternative orbits, covering all parts of the sky for about 30 minutes every 3 hours. The effective area of

this telescope is  $8000\text{ cm}^2$  at energies above 1 GeV, and the FoV is  $2.4\text{ sr}$  at 1 GeV. It has an energy and angular resolution with no precedents, from 18% to below 6% and  $3.5^\circ$  to less than  $0.15^\circ$  respectively, depending on the energy. A second instrument, the Gamma-ray Burst Monitor (GBM) is onboard *Fermi*. It is sensitive to X-rays and low-energy  $\gamma$  rays from 8 keV to 30 MeV. Its aim is the detection of bursts.

- *AGILE* (Astro - Rivelatore Gamma a Immagini Leggero) is a X-ray and  $\gamma$ -ray satellite [191]. It was launched on 2007 and relies in a low-Earth orbit, It is sensitive to X rays in the  $18 - 60\text{ keV}$  and to  $\gamma$  rays in the  $350\text{ keV} - 1\text{ GeV}$ . Opposite to *Fermi*, it works on pointing mode.

Currently, *AGILE* and *Fermi*-LAT are the only space satellites covering the energy range from few MeV to few hundreds of GeV. Afterwards, other instruments like Gamma-400 [88] or DAMPE<sup>1</sup> will takeover, covering the energy range from 100 MeV to 3000 GeV [88].

#### 1.2.4 VHE $\gamma$ -ray Detection: The IACT Technique

Indirect detection can be performed on Earth by the observation of electromagnetic air showers, produced when the primary  $\gamma$  ray interacts with the particles in the atmosphere, developing a cascade of secondary particles and photons. Imaging Atmospheric Cherenkov Telescopes (IACTs) perform observations of these electromagnetic showers by studying the image of the shower created in the camera. HESS (High Energy Stereoscopic System) [200], MAGIC (Major Atmospheric Gamma-ray Imaging) [32] and VERITAS (Very Energetic Radiation Imaging Telescope Array System) [113] are the three current ground-based observatories dedicated to the study of VHE  $\gamma$  rays. The  $\gamma$  rays detected with this technique have energies from  $\sim 25\text{ GeV}$  up to  $100\text{ TeV}$ . The detection of VHE  $\gamma$  rays requires large effective areas because the flux decreases exponentially towards higher energies.

##### Extensive Air Showers

When a VHE primary CR or  $\gamma$  ray arrives on the top atmosphere at  $20 - 25\text{ km}$  height a.s.l, it interacts with the nuclei of the particles there present and initiates an *extensive air shower* (EAS). Depending on the nature of the primary, two types of cascades are possible (see Figure 1.3):

- *Electromagnetic shower*: a VHE primary  $\gamma$  ray interacts with the Coulomb field of the atmospheric nuclei and produces an electron-positron pair, via pair production. These particles, via Bremsstrahlung, emit part of their kinetic energy in form of high energetic  $\gamma$ -ray photons. If the energy of these photons is larger than  $1.022\text{ MeV}$ , they will produce another  $e^- - e^+$  pair and the process will be repeated iteratively. The development of the cascade is described by the *Heitler model* [85], that predicts that the number of particles is a function of  $2^n$ , where  $n$  is the number of generations. When the secondary particles start to be absorbed by the atmosphere, the cascade stops its development. It dies when the energy loss of the secondary particles due to ionization is larger than their loss by Bremsstrahlung.

---

<sup>1</sup><http://dpnc.unige.ch/dampe/>

- *Hadronic shower:* in the case of a proton or nuclei being the primary particle interacting with the atmosphere, hadronic interactions as pion and meson production will be dominant. The shower development will be broader and more irregular than in the electromagnetic shower case. A larger amount and variety of secondary particles is produced with respect to the electromagnetic cascade. These secondary particles initiate other showers, if they are energetic enough. Most of the secondary particles created in this cascade are pions. As the neutral pion decays into two photons, roughly one third of the primary hadron energy develops electromagnetic cascades.
- $e^-$  *showers:* the primary particle is an electron. The development of the shower is similar to an electromagnetic cascade, since only positrons, electrons and photons are produced. It constitutes a background source difficult to disentangle from a real  $\gamma$ -ray generated shower.

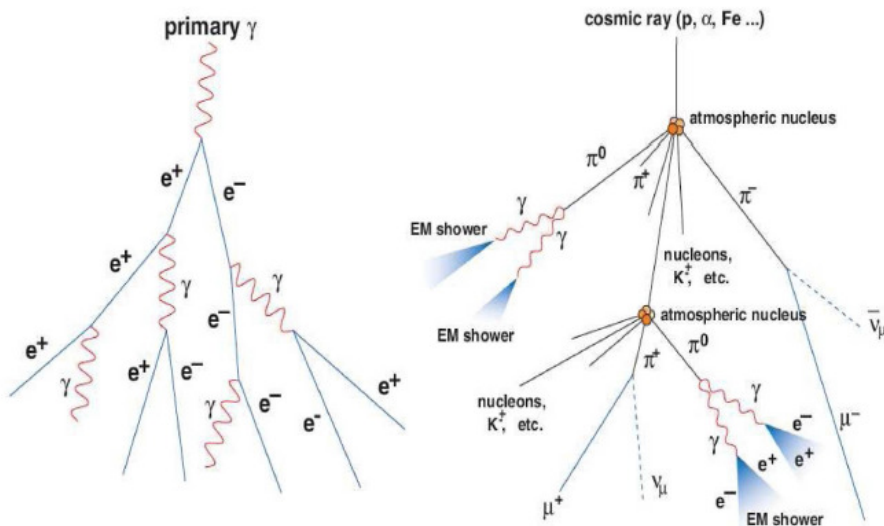


Figure 1.3: *Left:* Electromagnetic air shower generated by a primary  $\gamma$  ray and purely composed of electron-positron pairs and photons. *Right:* Hadronic cascade originated by a hadronic particle (proton or nucleus) producing a large variety of secondary particles: pions, muons, neutrinos, photons, kaons...

Both in electromagnetic and hadronic showers, particles are moving in a transparent dielectric medium (the atmosphere) faster than the speed of light, producing the so-called *Cherenkov light* [59]. The Cherenkov emission appears as dim fast ( $\sim 3 - 4$  ns) flashes of UV light with a spectrum that peaks at  $\sim 350$  nm at  $\sim 2000$  m a.s.l. The critical energy for the production of Cherenkov light is about 83 MeV, which corresponds to the energy at which the ionization losses are equal to the Bremsstrahlung or pair-production losses. This radiation is originated by the re-orientation of electric dipoles which have been previously polarized by the charge passage: when a charged particle moves in a dielectric medium, it disrupts the electromagnetic field and the electrons are displaced from the equilibrium and become polarized. When they return to the original equilibrium situation, a photon will be emitted. In the case of a particle traveling faster than light, the wavefronts emitted along the charged particle's trajectory sum coherently. The emitting angle of the Cherenkov radiation is  $\cos\theta = 1/\beta n \Rightarrow \theta \sim 1^\circ$  (with  $\beta = 1/n$ , being  $n$  the refractive index of the air). The light pool of the Cherenkov emission at 2000 m a.s.l is about 120 m radius for  $\sim 100$  GeV electromagnetic showers.

If an IACT (also denominated Cherenkov telescope) lies inside the light pool, it will collect the photons of the shower and focuses them in the camera. In the case of hadronic showers, the larger transversal momentum provokes a wider spread of the shower and a broader light pool. This distinction is used in the data analysis to distinguish between  $\gamma$ -ray generated showers and hadronic-originated cascades. This differentiation is important, since IACTs have high amount of hadronic background. For each  $\gamma$ -ray,  $\sim 1000$  hadronic particles generating hadronic cascades are present.

However, Cherenkov photons suffer absorption processes in their propagation through the atmosphere. The attenuation is caused, mainly by Rayleigh and Mie scattering with the interaction of the photons with the molecules and aerosols. Correction techniques for this absorption processes are under development. A possible solution the use of device denominated LIDAR. Studies on the development and characterization of an instrument of this kind is resumed on the Chapter 2 of this thesis.

## The IACT Technique

The most efficient technique to detect  $\gamma$  rays above  $\sim 100$  GeV is by the use of Cherenkov telescopes with the IACT technique. In order to detect the low  $\gamma$ -ray fluxes, large collection areas are needed to collect as much photons as possible. As the Cherenkov flashes are very fast, a highly sensitive pixelized camera composed of photomultiplier tubes (PMTs) is used. A fast trigger system and readout electronics are necessary in order to achieve an optimal signal-to-noise ratio between the Cherenkov light and the night sky background and minimize the background light integration time. Lowering the energy threshold is challenging, since the amount of Cherenkov photons is less in the case of low energy showers. The energy threshold can be described as:

$$E_{th} = \frac{\sqrt{\phi \Omega \tau}}{\epsilon A} \quad (1.1)$$

where  $\phi$  is the background flux,  $\Omega$  is the solid angle of the mirror,  $\tau$  is the integration time of the Cherenkov signal,  $\epsilon$  is the efficiency and  $A$  is the surface of the mirror. This equation support the listed requirements for an IACT. For lowering the threshold, as it is the case of MAGIC which aims to detect showers at  $\sim 50$  GeV, large collection areas are needed. Details on the hardware components and software of the MAGIC telescopes is resumed in Chapter 3.

Cherenkov telescopes detect the secondary photons produced in the air shower, hence the focus is not set to infinite but roughly to the height of the shower maximum. The Cherenkov light is reflected in the mirrors and focused in the pixelized camera. Depending on the angle between the telescope axis and the incoming photon direction, the photons of the different part of the shower will reach different regions in the camera. In a  $\gamma$ -ray initiated cascade where the emission comes from the pointing direction, the photons emitted in the higher atmosphere are reflected to the center of the camera, while the tails are extended into the edges of the camera. Hence, the electromagnetic shower is concentrated in a narrow distribution pointing to the direction of the primary incoming  $\gamma$  ray. Electromagnetic showers initiated by a primary  $\gamma$  ray image in the camera as a compact ellipse (which is the projected shower axis onto the camera plane) pointing to the source location, and its parameters are used to extract information of the primary photon that initiated the shower. Hadronic cascades show a more irregular and broader shape due to the iterative hadronic interactions. Secondary electromagnetic showers due to  $\pi^0$  decay are also detected in the camera plane and they widen the hadronic shower image.[16]. Examples of the different shapes of the recorded showers

is shown on Figure 1.4. An schematics of this detection technique is represented in Figure 1.5.

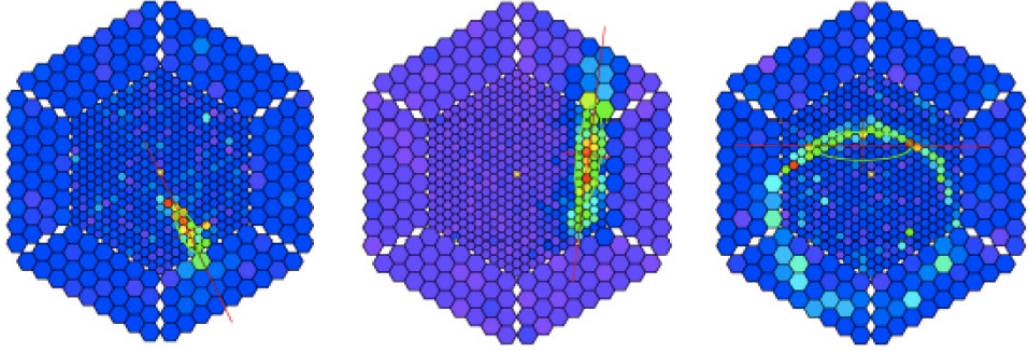


Figure 1.4: Camera images produced by different EAS. *Left*:  $\gamma$ -ray initiated shower. The compact ellipse points to the source direction. *Center*: Hadronic shower, broader than the electromagnetic shower ellipse and with an arbitrary direction. *Right*: Ring-shaped image associated to an isolated muon.

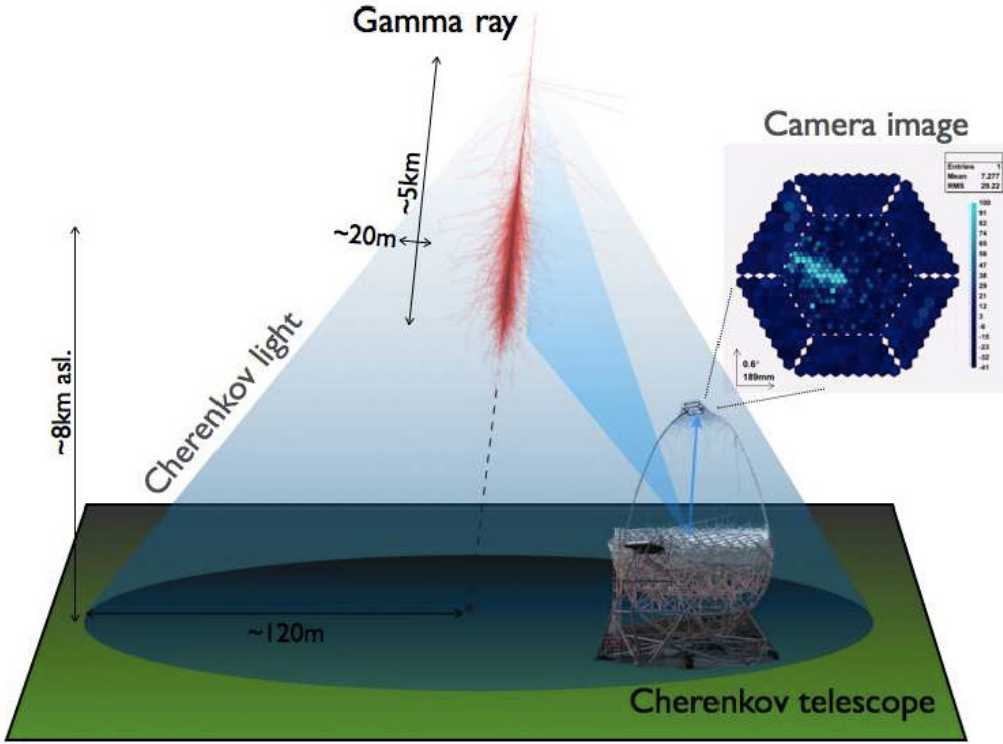


Figure 1.5: Principle of the IACT technique. The  $\gamma$ -ray shower axis is aligned with the axis of the Cherenkov telescope. The telescope lies inside the light pool created by the Cherenkov flash. The light is focused into the pixelized camera, where the shower is represented as an ellipse pointing in the source direction. The numbers corresponds to a shower of an energy of  $\sim 1$  TeV. [Credit: N. Sidro].

The first telescope to use the IACT technique was Whipple, a 10 m diameter telescope placed on Mt. Hopkins, Arizona, operative since 1968 [119]. It detected  $\gamma$  rays between 300 GeV and 10 TeV. It detected the first VHE  $\gamma$ -ray signal, coming from the Crab Nebula in 1989 [203]. Afterwards, the HEGRA experiment [65] introduced for the first time the concept of stereoscopic observations, with the use of an array of

IACTs (among other instruments). On the 2000s, the new generation of Cherenkov telescopes started with the construction of HESS, MAGIC and VERITAS, improving the sensitivity with respect to former experiments and lowering the energy threshold. The next generation of  $\gamma$ -ray observatory will be CTA (Cherenkov Telescope Array) [11], an observatory that will improve the sensitivity of current IACTs in at least four orders of magnitude in energy, with improved angular and energy resolution.

### *The Hillas Parameters*

The imaging technique relies in the parametrization of the images formed in the camera to extract the information contained in the shower. The IACT technique is based in some fundamental parameters denominated *Hillas parameters* [112]. These parameters are related to the image shape and are computed considering different order momenta of the spatial distribution in the camera plane. The  $\gamma$ -ray initiated showers can be described as a compact ellipse. The momenta are defined with respect the center of gravity (CoG) of the shower image. The definition of the parameters is performed after the image cleaning (see Section 3.2 for details of the data processing and analysis). The parameters can be divided in those depending on a reference point and those independent of the source position. The most relevant parameters are displayed on Figure 1.6. The basic parameters (including Hillas and some other useful parameters for the shower characterization) used in the MAGIC analysis are listed below:

#### Source-position independent parameters:

- **Size:** total charge, in terms of the number of phe, collected in a image. It is directly related to the number of Cherenkov photons in a EAS and hence and it is proportional to the energy of the incoming primary  $\gamma$  ray or particle.
- **Length:** Second moment of the light distribution along the major axis of the ellipse, or major semi-axis of the ellipse. It is related to the longitudinal development of the shower.
- **Width:** Second moment of the light distribution along the minor axis of the ellipse, or minor semi-axis of the ellipse. It is related to the transversal development of the shower. It is a useful parameter to suppress the contribution of hadronic showers, since these are spreader.
- **Conc:** is the fraction of the total charge contained in the two brightest pixels. As  $\gamma$ -ray induced showers are more compact than hadronic showers, they exhibit a higher concentration.
- **Leakage:** Fraction of the total charge contained in the outermost ring of pixels of the camera. It is useful to define images that are truncated in order to be excluded.

#### Source-position dependent parameters:

- **Dist:** Distance from the CoG of the ellipse and the source position in the camera. It is correlated with the impact parameter, which is the distance of the shower from the telescope axis.
- **M3Long:** Third moment of the distribution of charge along the major axis of the ellipse. It is useful to resolve the degeneracy between head and tail of the

image, since it determines the side of the ellipse with larger charge. It is positive when the head of the image points to the source position

- **Alpha ( $\alpha$ ):** Angle between the major axis of the ellipse and the line joining the CoG of the imaged and the source position. It depends on the direction of the incident shower. It shall be small in the case of  $\gamma$ -ray initiated showers. This angle is define in Figure 1.6.
- **Theta ( $\theta$ ):** Angular distance between the source position and the estimated source position for an event. It is conceptually equivalent to  $\alpha$ . The source position is estimated through the *disp method* (see Section 3.2). Normally,  $\theta^2$  is used in the analysis, since the distribution is approximately flat for background events and it is exponential for  $\gamma$ -ray signals. (See Figure 1.7)

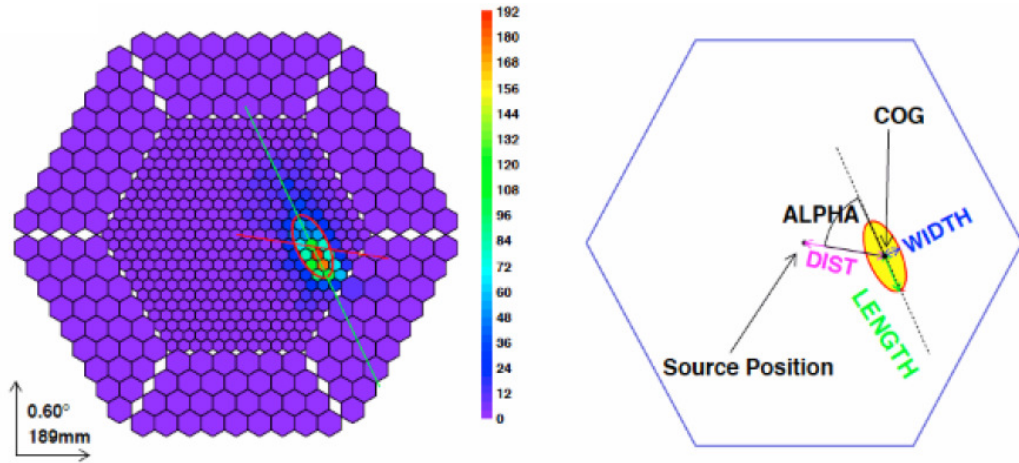


Figure 1.6: *Left:* Electromagnetic shower in the camera plane. *Right:* Hillas parameters of the specified shower. The center of gravity and the source position are also indicated.

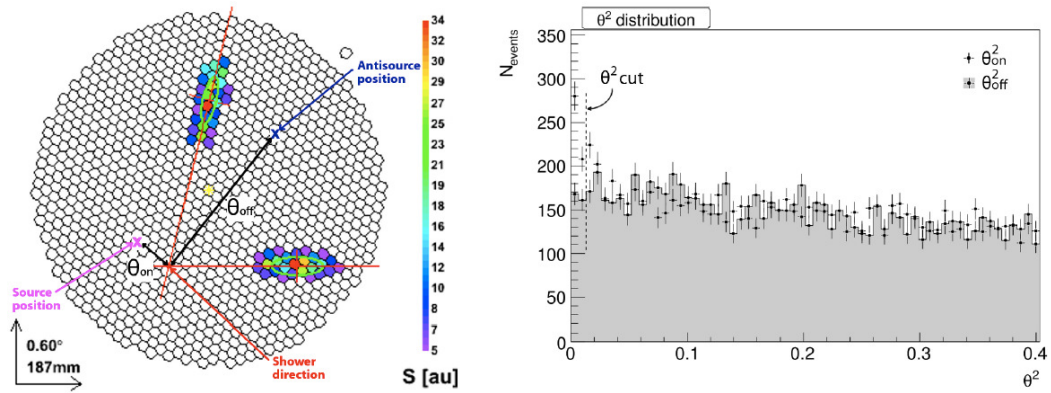


Figure 1.7: *Left:* Definition of the theta parameter for the source and anti-source (see Section 3.1.8 for more details). *Right:* Typical  $\theta^2$  plot distribution. The vertical line marks the cut of the signal region. [Credit: G. Giavitto]

By setting this parameters, our shower is firstly identified to start with the data analysis chain.

# 2

## Atmospheric Characterization for CTA

THE Cherenkov Telescope Array (CTA) is the next generation of IACT observatory . It will reach a sensitivity and an energy resolution with no precedent in very high energy  $\gamma$ -ray astronomy. In order to achieve this goal, the systematic uncertainties derived from the atmospheric conditions shall be reduced to a minimum. For that purpose, a Raman LIDAR is being developed at IFAE/UAB, a device which can reduce the systematic uncertainties in the reconstruction of the gamma-ray energies from 20% down to 5%. This Chapter describes the components of the LIDAR which is being built at IFAE and the different tests performed to characterize the system.

### 2.1 The Need of Atmospheric Monitoring

---

When a  $\gamma$  ray enters and interacts with the Earth's atmosphere, it will initiate an electromagnetic air-shower. The particles travel faster than the photons in the atmosphere, hence Cherenkov light will be produced. The emission of this light peaks at 350 nm and appears in the form of short dim flashes produced at a height of  $\sim 10 - 20$  km. Imaging Air Cherenkov Technique (IACT) uses ground-based telescopes to collect this Cherenkov light.

The atmosphere acts as a calorimeter in Cherenkov astronomy, hence the knowledge of the atmospheric parameters is crucial [69]. It is important to calculate the total extinction that the Cherenkov radiation suffers from the point where the Cherenkov photons are produced at 10 – 20 km height until the Cherenkov light reaches the detector, in order to properly estimate the total flux and energy scale.

The performance of Cherenkov telescopes is limited by the systematic uncertainties associated with the inferred energy of the primary gamma-ray photon. The main contribution to the systematic uncertainties in IACTs is the uncertainty in the (height- and wavelength-dependent) atmospheric transmission for a given moment in time. For current IACTs, systematic uncertainties in the determination of the energy scale at a given time is quoted at  $\sim 20\%$ . MAGIC studies have concluded that atmospheric conditions contribute nearly 10 % toward the uncertainty of their energy scale [32]. On the other hand, H.E.S.S. collaboration suggests that there are two main contributors:  $\sim 10\%$  is estimated for the uncertainty associated with the assumed atmospheric profile, and approximately  $\sim 15\%$  is estimated for run-by-run atmospheric variations [15] (MAGIC also derives 12 % additional uncertainty on the flux due to run-by-run variations, but do not state explicitly that this could be due to atmospheric variations). These estimates are lower-limits on the uncertainties, as these calculations were

performed upon data recorded under clean atmospheric conditions.

The amount of Cherenkov light produced is highly dependent upon atmospheric conditions. Thus atmospheric quality affects the measured Cherenkov yield in three different ways:

1. Air shower development: the vertical profile of the atmospheric density determines the refractive index of air and hence influences the number and angular distribution of the Cherenkov photons and the amount produced in the air-shower.
2. Photon scattering: Cherenkov light produced in air-showers is subject to Rayleigh and Mie scattering. In case any photon is scattered away from the field of view (FoV) of the telescope, the image will be dimmer and blurrier. Depending on the particle size, scattering of light may be strongly peaked in forward direction. Photons scattered in forward direction are not lost, but remain in the field-of-view of the telescope and blur and/or create halos around the main image. Multiple scattering of light will enhance this effect.
3. Photon absorption: Cherenkov light is absorbed in its way down to the ground, mainly by the aerosols present in the atmosphere. This absorption results in a dimmer image.

The Cherenkov Telescope Array (CTA) [11] will be the next generation gamma-ray observatory. It intends to improve the current sensitivity of IACTs by an order of magnitude and enlarge the energy range for the detection of gamma rays, covering almost four decades in energy. Additionally, it aims at considerably improved energy and angular resolution. For that purpose, it is necessary to reduce the systematic uncertainties as much as possible.

A possible improvement could be achieved by the use of a LIDAR (which stands for *Light Detection And Ranging*), a device designed to monitor the atmosphere transmission probability, a key fact in a large observatory as CTA would be. On the one hand, the knowledge of the vertical distribution of aerosols would reduce systematics errors due to atmospheric quality changes. On the other hand, the knowledge at any moment of the atmosphere transmittivity would allow CTA to correct data taken with non optimal weather conditions. Currently, Cherenkov telescopes simply discard this date, which may account for more than 30% of the duty cycle. The economical effort and concept of CTA make this approach unreasonable and LIDARs may be the solution.

Because of all these necessities and requests, this thesis has contributed in the development and characterization of the Raman<sup>2</sup> LIDAR which is being built at IFAE for CTA observatory, with the aim of understanding the start-up and functioning of a Raman LIDAR and its limitations. The author has worked on a prototype, testing the different components of the system, to search for the optimum point of operation in order to find the best configuration for the final implementation in CTA.

## --- 2.2 The LIDAR Technique

Basically, there are two different types of LIDARs: elastic and inelastic (Raman). These systems have been used for long time to successfully characterize the atmosphere ([115], [38]), also within the astronomical context [214].

---

<sup>2</sup>see next Section 2.2 for an extended review.

The LIDAR technique is based in the analysis of the light backscattered by the molecules in the atmosphere when a monochromatic beam characterized with a frequency  $\nu$  is thrown over them. A fraction of the backscattered light will be elastically dispersed at the same frequency, which is called *Rayleigh Scattering*. This elastically backscattered light does not provide information about the elements in the atmosphere. Nevertheless, a small fraction is scattered in an inelastic way, the so-called *Raman Scattering*, which is rotor-vibrational and non-elastic. In the latter, the backscattered radiation would suffer a shift in its wavelength, characteristic of the stationary states of each molecule, what allows to identify the chemical composition of the sample. These shifts are independent of the incoming radiation and are characteristic of the physical state and the chemical nature of the component. As Cherenkov astronomy uses the atmosphere as a calorimeter, atmospheric quality has to be taken into account. The study of Rayleigh and Raman Scattering provides a tool to characterize the atmosphere.

Main components of a LIDAR are a laser, a reflecting surface and a detector element. It can be interpreted at the optical analogous of a radar, by studying the atmosphere through the sending of short light pulses with a laser. The laser and the collecting surface will point at the same direction so the light emitted by the first one and reflected by the elements in the atmosphere will be collected by the second one. The light is then guided to the detector. There, the interesting wavelengths are selected by means of filters, beam splitters and dichroic mirrors. Each wavelength is sent to a different photodetector, which is used to record the amount of light which is reaching the LIDAR as a function of time. Time can be easily converted to height by computing the light path. That would be the experimental input to finally get the optical depth  $\tau$ .

As the laser is a known source, we could study how the radiation that reach us is scattered by the molecules in the atmosphere and how the optical depth varies with the altitude. We could also determine the vertical distribution of aerosols and clouds, elements which absorb part of the light coming from Cherenkov fluorescences. That would permit us to convert the amount of Cherenkov light measured by the telescope to that really produced in the atmosphere.

The amount of light backscattered from the molecules depends on the attenuation suffered by the laser radiation since it was emitted until it reached the focal plane and it also depends on the backscatter cross section from the point of scattering. This last one is dependent on the composition and shape of aerosols, so its variable depending on the components present in the atmosphere. The backscattered signal is described by the LIDAR equation [160]:

$$P(r, \lambda) = P_0 \frac{ct_0}{2} \beta(r, \lambda) \frac{A}{r^2} e^{-2\tau(r, \lambda)} \quad (2.1)$$

where  $P(r, \lambda)$  is the radiation scattered by the molecules,  $P_0$  is the initial radiation emitted by the laser,  $c$  is the speed of light,  $t_0$  is the time of the transmitted pulse,  $\beta(r, \lambda)$  is backscatter coefficient, where  $r$  is the distance to the molecule and  $\lambda$  is the wavelength.  $\tau(r, \lambda)$  represents the optical depth, which could be written in terms of the extinction,  $\alpha$ :

$$\tau(r, \lambda) = \int_{r_0}^r \alpha(r, \lambda) dr \quad (2.2)$$

The backscattered power return of a LIDAR depends on two unknown physical quantities, the total optical extinction ( $\tau(r, \lambda)$ ) and the backscatter ( $\beta(r, \lambda)$ ) coefficients. As there is only one equation with two unknown factors, in the case of an elastic LIDAR, these parameters need to be inferred from a single measurement (See Equation 2.1)

and assumptions need to be made, or boundary conditions introduced. Furthermore, these unknowns could depend not only on the distance ( $r$ ) but also on the wavelength ( $\lambda$ ).

To overcome this fundamental problem, the introduction of additional elastic and/or Raman (inelastic-scattering) channels are required, allowing for simultaneous and independent measurement of the extinction and backscatter coefficients with no need for a priori assumptions [38]. Raman spectroscopy provides information of the chemical and structural composition of the elements in the terrestrial atmosphere. Raman Scattering is associated to a variation in the vibrational and rotational states of molecules and, so, it depends on energy changes. This effect takes place when the light collides with a molecule and interacts with its electron cloud. When the photon interacts with the molecule, this last one is transiently elevated from its ground state to a virtual vibrational or rotational energy state, see Figure 2.1. This state is rapidly abandoned to fall into a permitted level different from the initial one and, during this process, it emits a photon whose frequency,  $\nu_R$ , is shifted from the initial monochromatic beam frequency,  $\nu$ . This shift in the emitted photon frequency depends on the difference in energy between these two levels and could be positive or negative, depending if the energy transfer is done from the molecule to the photon or vice-versa: if the final state is more energetic, then the emitted photon will be shifted to a lower frequency so the total energy of the system remains balanced, process known as *Stokes shift*; if it goes to a more energetic state it is called *Anti-Stokes shift*. The importance of using the Raman LIDAR technique is not only the knowledge of the elements in the atmosphere but also to break the degeneration present in Equation 2.1 to obtain the vertical distribution of these aerosols.

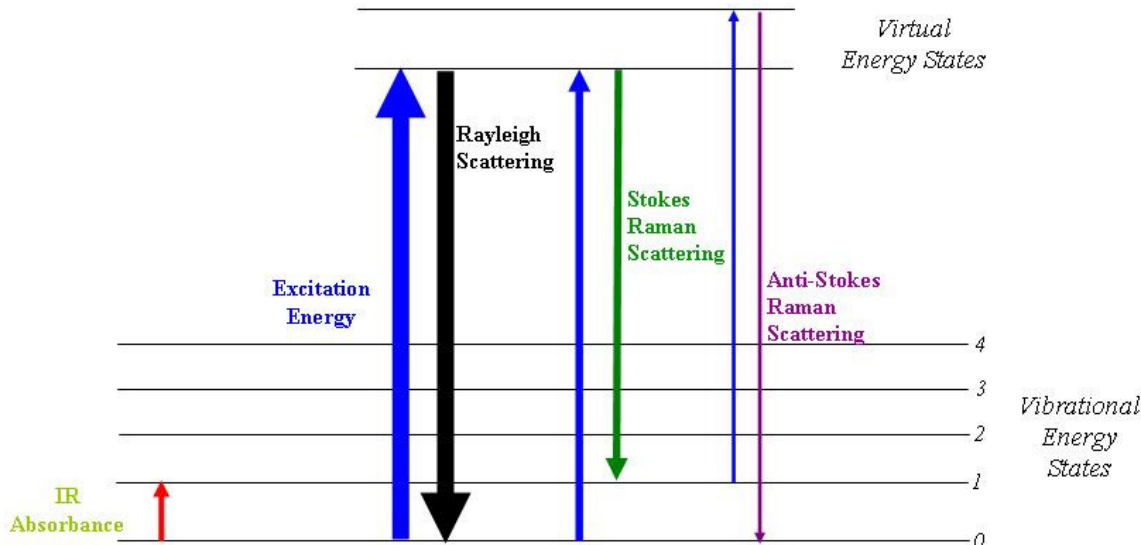


Figure 2.1: Energy diagram for the Rayleigh and Raman Scattering. Stokes and Anti-Stokes possibilities are represented. Image credit: <http://cambridgeforecast.files.wordpress.com>

Elastic LIDARs could have up to a 20% systematic error when determining extinction. With a Raman LIDAR, we dispose the tools to break the degeneration between  $\beta(r,\lambda)$  and  $\tau(r,\lambda)$ . The wavelength dependence would permit to correct systematic biases on the energy scale and flux. This will help not only to reach the desired energy re-solution but also to increase the duty cycle, because the observatory will be able to produce scientific data under non-optimal weather conditions. The use of an instru-

ment of this kind would be a great step in Cherenkov astronomy because it permits the reduction of the systematic uncertainties and increase the duty cycle. However, a problem of using Raman LIDAR is that the backscatter cross section is approximately 2 – 3 orders of magnitude smaller than the Rayleigh one. The study of both Rayleigh and Raman backscattered light will improve the knowledge of the height- and wavelength-resolved atmospheric extinction to from the current  $\sim 20\%$  down to  $\sim 5\%$ .

## 2.3 The IFAE/UAB Raman LIDAR

---

The Raman lines are characterized by a small cross section, about 2 – 3 order of magnitude smaller than the elastic one. Hence, a large reflecting area is needed to collect a substantial amount of light for the needed range. The solution adopted by IFAE/UAB was to adapt an old CLUE (Cherenkov Light Ultraviolet Experiment) unit [33] and convert it into a Raman LIDAR. CLUE was an array of cosmic ray detectors (eight in total) that searched for the Cherenkov light emitted by hadronic showers. It formed part of the larger HEGRA (High Energy Gamma Ray Astronomy) experiment, placed at the Canary Island of La Palma, and which was operative from 1987 to 2002 [111].

Each CLUE unit was composed of a 1.8 m diameter telescope housed inside a container that can be opened in two halves for operation. IFAE bought two of these units: one of them is placed at IFAE (Figure 2.2), being already converted to a Raman LIDAR to act as a prototype to optimize the design and to understand the best operation point. Once the design is proven to be correctly working, a clone will be built using the other container, which is located in El Roque de los Muchachos in La Palma with the aim to test its capabilities when operating together with a real Cherenkov telescope, MAGIC. The final goal would be to use them in CTA. Both the telescope and the container can be controlled remotely. Another CLUE unit is being used at Laboratoire Univers et Particules de Montpellier (LUPM) in France also with the purpose of developing a Raman LIDAR for CTA. Although the approach is slightly different, the basic configuration adopted is the same [132, 131].

The IFAE/UAB LIDAR consist, mainly, on a primary mirror, a pulsed laser, a liquid light guide, that collects the light from the focal plane, and an optical module. I have tested the different components of the device. This is important first to take decisions concerning the final design and second to characterize the system in order to be able to perform simulations to study its performance and response. The different parts of the instrument and the performed experiments to test them are described in Section 2.4. All the tests have been performed on the LIDAR that lies in the IFAE.

### 2.3.1 Configuration

---

The IFAE/UAB Raman LIDAR has been designed to be coaxially aligned, which means that the laser beam is coincident with the optical axis of the telescope. Although there is a small hole in the center of the main dish, we have not planned to place the laser there because it would interfere with the elements placed in the focal plane. Furthermore, the laser can not physically be placed in the back of the mirror, due to the shape of the holding structure of the dish. This implies dedicated optics and mechanics to guide the laser beam towards the optical axis of the telescope.

Although biaxial LIDARs are easier to operate in the sense that they are simpler and that the telescope axis and the laser axis do not need to be exactly coincident,

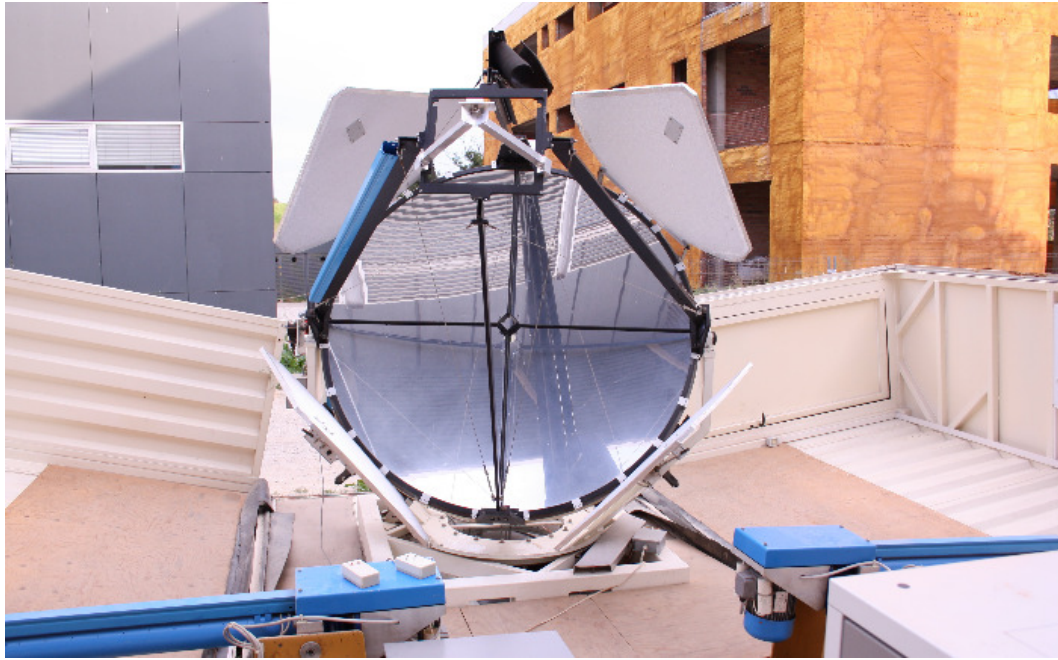


Figure 2.2: CLUE unit acquired by IFAE to develop a Raman LIDAR. The mirror is housed inside a container which can be opened in two halves. The mirror is protected by four petals, opened in this figure.

the overlap between the telescope FoV and the laser beam is smaller than in the case of a coaxial configuration. Figure 2.3 shows the overlapping factor for a coaxial and a biaxial configuration. The range for full overlap will be smaller in the case of a biaxial LIDAR and will occur at higher altitudes than in the case of a coaxial LIDAR.

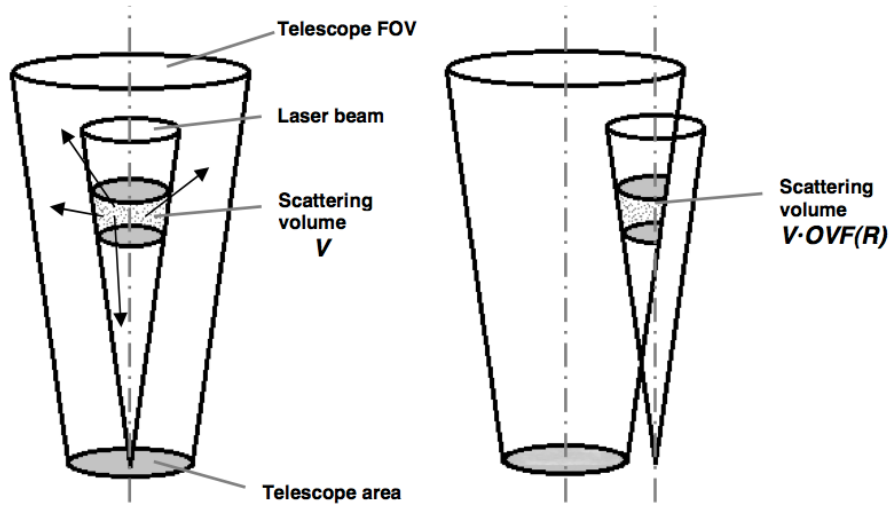


Figure 2.3: Overlap between the telescope FoV and the laser, for a coaxial (*left*) and a biaxial (*right*) configuration.

In general, the starting point for full overlap in a biaxial LIDAR occurs at tens – several hundreds of meters, while in a coaxial in can be severely reduced. For a bi-axial

LIDAR, the range of full overlap,  $R$  can be calculated as [122]:

$$R = \frac{2x + d}{\frac{R_{det}}{f} - 2\theta} \quad (2.3)$$

where  $x$  is the distance from the laser to the center of the telescope mirror,  $d$  the diameter of the mirror,  $R_{det}$  the radius of the detector in the focal plane,  $f$  the focal length of the telescope ( $R_{det}/f$  is also called the field-of-view of the detector) and  $\theta$  the opening angle of the laser beam in radians. This formula can be applied to CLUE to check what the starting range would have been in case of a biaxial configuration. In this specific case,  $f = d = 1.8 \text{ m}$ . The laser beam divergence is 0.5 mrad and it can be assumed that  $R_{det} \sim 4 \text{ cm}$ . Taking into account aberrations, the resulting values is 400 – 500 m. For a coaxial configuration, this number is reduced to  $\sim 150 \text{ m}$ , considering possible aberrations in the mirror.

A good overlap is needed to measure the optical depth starting from the lower height possible. It is important to start measuring from low altitudes to perform a proper atmospheric characterization, because it is at these low altitudes where the atmosphere is more hazy. The most important aerosol contribution lies below 500 m and also the light of the Cherenkov showers is considerably absorbed in this range. Because of these reasons, it has being decided to adopt this configuration for the IFAE/UAB LIDAR.

### 2.3.2 The Primary Mirror

The collecting area is a single-dish parabolic mirror. The diameter and the focal length are both 1.8 m, hence the focal-to-diameter ratio is  $f/D = 1$ . The aperture is  $26.6^\circ$ . The mirror is the original designed for CLUE. It is made of a 6 mm thick float glass with a particularly smooth surface. It was coated by Osservatorio Astrofisico of the University of Padova with a layer of aluminum of 50 nm thickness and has a hole in its center of 5.5 cm of diameter. It is placed on an altazimuthal mount.

The Point Spread Function (PSF) and the reflectivity were measured when it was built [33]. 80% of the light was enclosed in a diameter of  $\sim 6 \text{ mm}$ . It is worth noticing that the deviation from the nominal parabolic surface and the defects of the glass introduced differences on the slope of the parabolic mirror of less than 1.6 mrad, these effects enlarge the image in the focal plane by 5.8 mm at maximum. The reflectivity, at first, was 95%. However, after four years it was degraded to 50% and re-coated. However, this values could have changed due to aging, which causes that the quality of the mirror decreases and hence these parameters could have worsen. I have actively worked on the determination of these values, which is needed not only to study the performance of the system but also to design the optical pieces. The tests performed to characterize the mirror are explained on Subsection 2.4.1. The first concluding remark from these tests is that the optical quality of the mirror has not decreased along these years, being the PSF approximately the same as when the mirror was produced,  $\sim 6 \text{ mm}$  for 80% of the light containment. The second conclusion is that the focal reflectivity at 350 nm is  $\sim 64\%$  [130].

#### *Re-coating*

The reflectivity tests (see Subsection 2.4.1) have proven that is has decreased since the mirror was produced to a  $\sim 64\%$  at 350 nm. However, despite the low value, it does not suppose a problem for the LIDAR purpose. The LIDAR response can be

simulated through the *link budget* method. This a set of equations has been applied to our system [75]. The major effect of the low reflectivity in the LIDAR system is a reduction of the maximum distance at which the LIDAR can perform measurements [68]. However, the photon abundance on the far range is enough for a good signal to noise ratio, hence it is not a major problem. If there would be special interest in this range, it might be possible to re-aluminate the mirror. Nevertheless, a problem is encountered: there is the need of a large coating chamber, since the mirror has a diameter of 1.8 m. This implies the dismounting and shipping of the mirror. But the mirror is already quite old and fragile, at the hole in its center makes the dismounting more risky, since it may break. Hence, it has been decided not to re-aluminate it and, in case of need, it might be better solution the production of a new mirror, despite the higher cost.

### 2.3.3 The Pulsed Laser

Atmospheric measurements will be performed with a Brilliant Class IV Nd-YAG 1064 nm laser developed by *Quantel*. This laser has a compact lightweight housing and offers remarkable performance in terms of energy (short and long-term stabilities) and an outstanding beam quality. Its active temperature stabilizer, complete computer control and dust free housing make integration quite easy.

The laser also has second and third harmonic generators at 532 nm and 355 nm, respectively. They are assembled in compact modules, including the non-linear crystals and a removable set of dichroic mirrors. Phase matching for the second and third harmonics is obtained by simple mechanical adjustment (adjustment screw accessible from the top of the module). The emitted pulses would have energies of 360mJ/p, 100mJ/p and 100 mJ/p for each of the 1064 nm and the two mentioned harmonics, respectively. The introduction of additional wavelengths permit the Raman measurement of  $N_2$  at 387 nm and 607 nm (see Subsection 2.3.6 for more details). These are the wavelengths of our main interest because the peak emission of Cherenkov light is located at 355 nm. The laser will emit 5 ns pulses with a 20 Hz frequency. The beam divergence at 1064 nm is 0.5 mrad. The main characteristics are collected on Table 2.1.

Parameter	Value	Comments
Pulse repetition rate	20 Hz	
Power drift	3%	Over 8 h
Pointing Stability	< 75 $\mu$ rad	On 200 pulses at the focal plane of a 2 m focus lens
Jitter (1064 nm)	$\pm$ 0.5 ns	measured at half-width of 500 accumulated shots
Beam divergence (1064 nm)	0.5 mrad	Full angle, 85% of total energy
Beam diameter (1064nm)	6mm	At the output of the laser

Table 2.1: Main characteristics of the pulsed laser

It is possible to make frequency double and triple output: if taking away the dichroic mirror inside the main body, it is possible to obtain the three wavelengths from the same output; the configuration without the beam dump allows to separate the third harmonic from the other two; standard version permits only 355 nm wavelength to be emitted. A schematic view is shown in Figure 2.4. For the LIDAR purpose, we are mainly interested in second and third harmonic. There is now way of only displaying these two wavelengths without also shooting the first one. In our case, the configura-

tion without dichroic mirror, were the tree wavelengths are displayed from the same output is suitable. The tests performed on the LLG have proven the need to absorb the 1064 nm radiation. For more details, refer to [2.4.3](#).

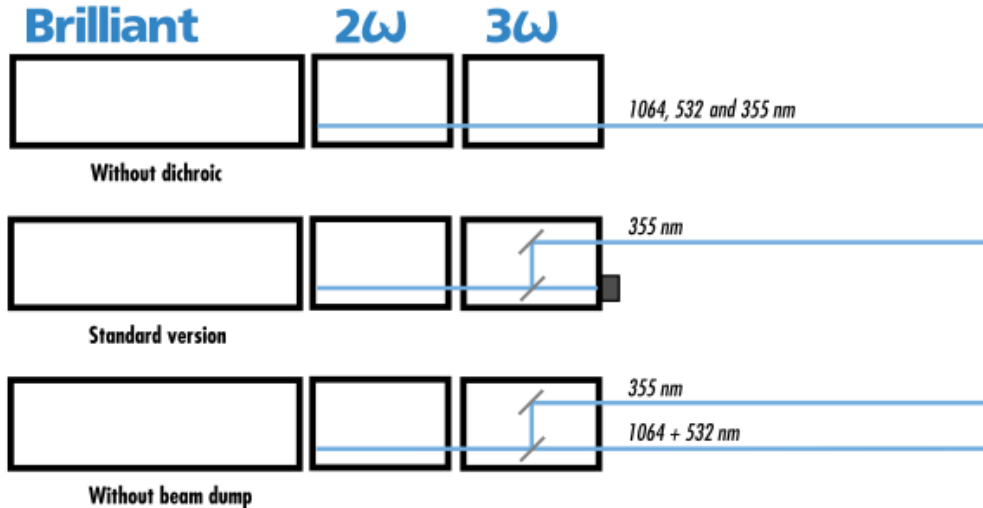


Figure 2.4: Harmonic configuration for the pulsed laser output.

### Mechanical arm and guiding mirrors

The laser relies on a mechanical arm placed on a side of the primary mirror. It guides the laser beam to the desired direction and position. Currently<sup>3</sup>, two flat highly resistant 1-inch mirrors have been placed, one in front of the laser (at a distance of about 1.5 m) and the other one next to the focal plane, in order to guide the laser light in such a way that it becomes coaxial with the optical axis of the primary mirror. These two mirrors are strongly and precisely fixed on the telescope structure, on the positions of maximum alignment, where the coaxial configuration and hence a good overlapping factor are achieved. The movements of the LIDAR will cause a certain misalignment of the system, because of gravity. Two stepping motors and an XY table can correct these deviations. First, a pre-alignment is performed which lasts about 10 min. Then, the laser return signal at large distances is maximized by moving the laser beam. With this setup, the coaxial configuration is achieved, see Figure [2.5](#).

#### 2.3.4 The Light Guide

The light backscattered in the atmosphere and reflected by the primary mirror is collected at the focal plane by a liquid light guide (LLG) and transported until the detector. Liquid light guides are fibers filled with a liquid which show a very high transmittivity, larger than conventional optical fibers. The transmission of a LLG is around 80% in the UV, while the maximum transmission for a bundle fiber is  $\sim 40\%$  in the same wavelength range. They also show high flexibility, which is important for the operation. Furthermore, the numerical aperture is large,  $72^\circ$ , which is necessary in our case due to the focal relation of the telescope,  $f/D = 1$ . LLGs do not transmit

<sup>3</sup>After some tests, the IFAE/UAB team has decided to change the mirrors for two larger ones with slightly different characteristics.

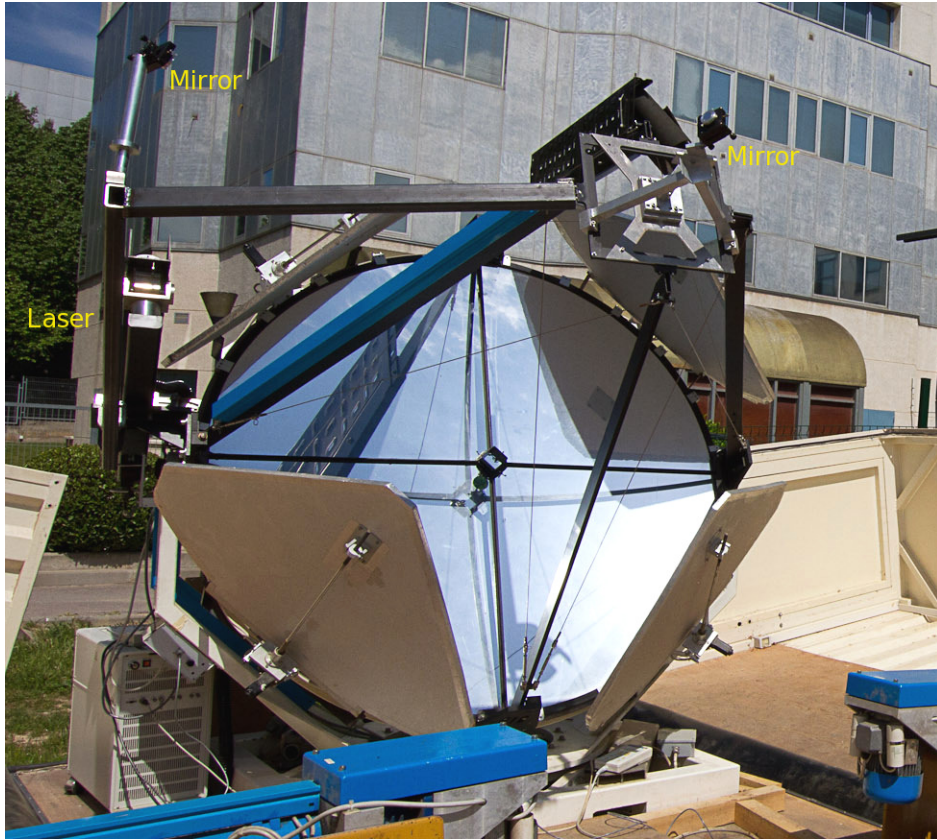


Figure 2.5: Coaxial configuration of the IFAE/UAB LIDAR. The laser is mounted on the mechanical arm situated in the side of the structure. Two small flat mirrors guide the laser beam and make it coaxial with the optical axis of the primary mirror..

images but light, although it does not suppose a problem since the LIDAR technique is not an imaging technique.

A 8 mm diameter (to collect all the incoming light) and 3.2 m long (from focal plane to detector) LLG type *LUMATEC Series 300* is used in the IFAE/UAB LIDAR. It is optimized to transmit light in between 320 nm and 650 nm. The liquid inside the LLG is stable over the years if it is not exposed to wavelength shorter than 320nm, which may destroy the transmission properties, or higher than 650nm, which may lead to the formation of bubbles. This implies that the 1064 nm wavelength of the pulsed laser can not be transmitted through the LLG in order not to degrade it. A filter should be then used in order to absorb it.

In terms of temperature, a normal operation is expected between -5°C and +35°C. Reaching lower temperature values for a few hours may cause bubbles inside the LLG which will disappear after few days of storage at room temperature. On the other hand, reaching temperatures up to +50°C is not a problem for a period of few days. This will not destroy the liquid itself but may cause an irreparable degradation of the sealing, due to the formation of bubbles.

Tests of the performance of the LLG has been assessed on the laboratory (see Sub-section 2.4.3). Main results from those tests are that the measured transmittivity is in agreement with the values claimed by the manufacturer, that the transmission does not depend on the shape adopted by the LLG and that it remains stable with temperature changes.

### 2.3.5 The Optical Detector

---

The optical detector is a device which will collect the light from the output of the LLG, split the beam into the different wavelengths of interest and focus each of them onto a photomultiplier (PMT). The design has been done in such a way that the dimension and the number of optical components was the smallest possible and the efficiency was maximum.

From the LIDAR equation 2.1, it is known that the return power of an elastic channel is related to the atmospheric extinction through the LIDAR ratio, which is the fraction between the extinction and the backscatter coefficient. For a single elastic channel, the uncertainty is 25%. By including a second channel, the color-ratio, which is the dependence of the extinction parameters with the wavelength can be reconstructed. This second elastic channels helps to determine the LIDAR calibration parameters and decreases the uncertainties in the atmospheric transmission calculation to a 15%. Introducing a Raman channel, the degeneration in the LIDAR equation is broken. The discrimination between particles and molecules in the atmosphere is easily performed because the returned light has only interacted with the molecules, in the case of a Raman line, and the LIDAR ratio can be determined to a precision of 5%. The degeneration in the LIDAR equation is broken. By including a second Raman channel, this uncertainty can be reduced to less than 5%.

The final design foresees 4 read-out channels: two for analyzing the elastic-backscatter light at 355 nm and 532 nm and two for studying the Raman Nitrogen back-scattered light, at 387 nm and 607 nm respectively. Figure 2.6 shows the final design [64]. This multiwavelength detector is composed of lenses, dichroic mirrors, interference filters and PMTs. The light which arises from the light guide at the detector entrance has a wide opening angle ( $70^\circ$  aperture angle) due to the  $f/D = 1$  relation of the primary mirror. Hence, collimation and focalization of the beam onto the PMT is not straightforward. Due to this reason, a couple of lenses are placed to collimate the beam. Then, dichroic mirrors will separate the light into the wavelengths of interest. Now that the channels are differentiated, each single beam will go through another pair of lenses which will help to collimate it into the PMT and through an interference filter to improve the wavelength selection. Finally, the single-wavelength light arrives at the PMT. For each channel, 80% of the energy is enclosed in the PMTs.

### 2.3.6 The Readout Electronics

---

The data acquisition system it is a commercial device developed by *Licel*. This transient recorder is specially designed for remote sensing applications, reaching the best dynamic range together with high temporal resolution at fast signal repetition rates. It combines analog detection of the PMT current and single-photon counting. The combination of a 12-bit A/D converter (at 40 MHz) with a 250MHz fast photon counting system increases the dynamic range of the acquired signal. A high speed data interface to the host computer allows readout of the acquired signal even between two laser shots. High speed and high gain amplification is necessary for photon counting, whereas linear amplification of the A/D converter is needed for the analog measurement. The photon counting acquisition system includes a fast three-stage preamplifier and a discriminator with 64 threshold levels, controlled by the host computer. A time resolution of 50 ns without dead time or overlap between two memory bins is reached by using a continuous counter together with a multichannel scaler

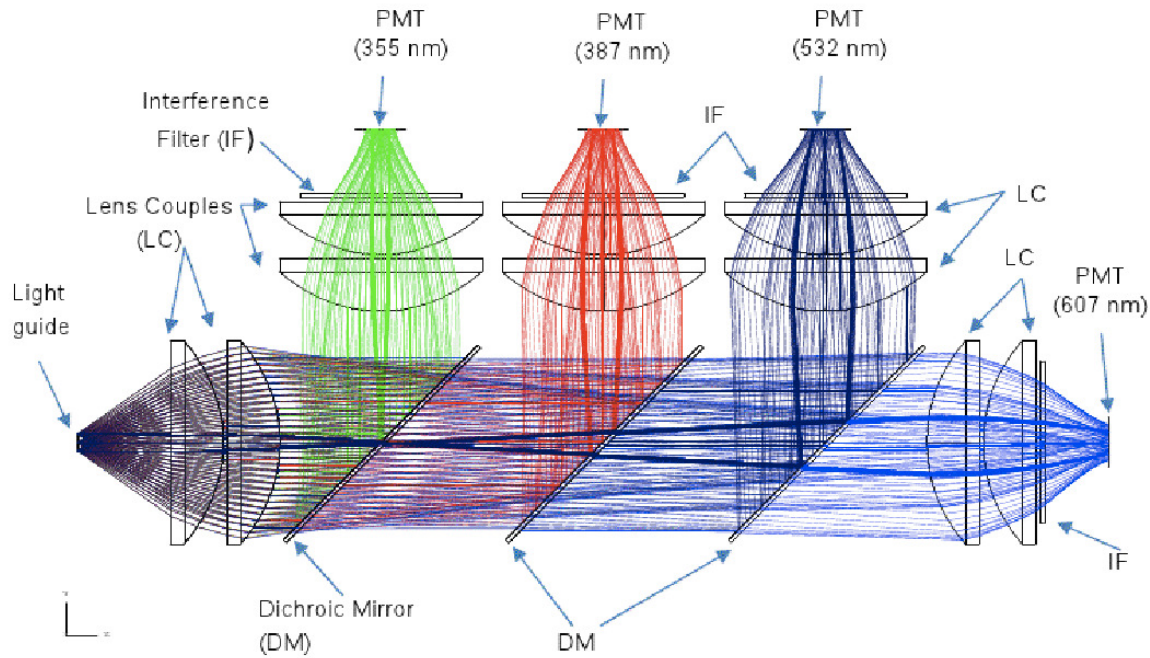


Figure 2.6: Four-channel detector design for the IFAE/UAB Raman LIDAR. The outgoing light from the LLG is well collimated onto each PMT. [Credit: V. da Depo]

## 2.4 Tests

Several tests to study the performance of the single components and to characterize the overall response of the system have been performed by the author of this thesis and are collected below.

### 2.4.1 The Primary Mirror

#### Point Spread Function

The Point Spread Function (PSF) describes the response of an imaging system to a point source. It can be interpreted as the irradiance distribution of a certain point. In functional terms it is the spatial domain version of the modulation transfer function.

Due to aberrations and diffraction in the optical system, a point-like source image will not necessarily be point-like. Its light will spread over a finite area. It is important to know the size of this spot, the PSF, to collect all the light inside the light guide and to characterize the mirror and be able to simulate the behavior of our instrument. Finally, it is worth studying how the aging has degraded (or not) the optical quality of the primary mirror.

Three different attempts have been performed in order to determine the PSF of the LIDAR:

- On the first attempt, I tried to determine the PSF through observing stars by directly point the LIDAR in their direction [130].  $\alpha$ -Lyr was observed at different zenith angles, between  $10^\circ$  and  $30^\circ$ . Polaris was also observed. The measurement of the size of the spot was performed by adjusting to a gaussian with the

tasks *imexam* and *psfmeasure* of IRAF<sup>4</sup>, (Image Reduction and Analysis Facility), which is a dedicated software for the reduction and analysis of astronomical data. The resulting value was that the light was enclosed in a circle of 5 mm of diameter<sup>5</sup>. Although the result is compatible with the value measured by CLUE, the background light was large and the image of the star was very dim. The method is suitable to determine the dimension of the spot, but the resolution is poor to determine the shape of the spot. The main problem of this technique was that the LIDAR is inside the university campus, where there is a large light contamination. Also, high buildings surrounds the device, hence the possibility to observe stars is reduced.

- The second experiment mounted to determine the PSF of the mirror, included a green laser pointer at double the focal distance, acting as a point-like source. The intensity of this light is much larger than in the previous case and it is easy to measure it. The images are taken with a CANON EOS 1000D which is mounted behind the focal plane. The images are digitized and an intensity is assigned to each pixel. Four different cuts are performed over the spot: horizontal, vertical and two diagonal, to obtain the intensity profile. Then, pixels are transformed into distance and numerical integrals are performed iteratively to obtain a relative measurement of the light. Figure 2.7 shows the resulting plot for the horizontal and vertical cuts. The 90% of the light is contained inside a circle of  $\sim 8$  mm of diameter and it is compatible with the original measurement. For a detailed description, refer to [185] (in catalan). Since the source was placed at two times the focal distance, it may not exactly reproduce a source at infinite. The method will reproduce a source in the infinite in the case of perfect optics. Nevertheless, the system has aberrations and, hence, the equivalence is not real.

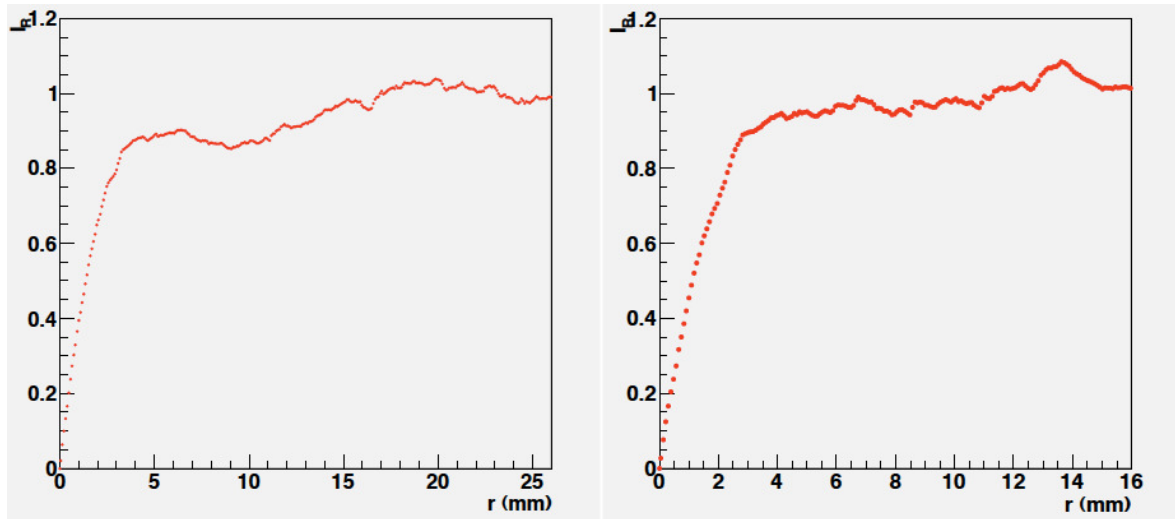


Figure 2.7: Gaussian profile of the horizontal cut. The x-axis is the number of pixels, while the y-axis is intensity [arbitrary units]. The data points are plotted in red, while the gaussian fit is represented on black..

- A third and final experiment was performed by using the same green laser pointer, which was pointed to a wall, creating an artificial star which was 65 m far from the

<sup>4</sup><http://iraf.noao.edu/>

<sup>5</sup>The resulting images and plots can not be shown as the computer that contained the data was stolen after finishing the analysis. The author asks for pardon.

telescope. Although the spot of the laser is relatively large (12 mm x 24 mm), the angular dimension of such a spot at 65 m is about 0.4 mrad ( $\text{arctg}(24/65000)$ ), which is similar to the aperture of the pulsed laser to be used in the Raman LIDAR (0.5 mrad). Hence, the dimensions of the PSF observed at the focal plane are equivalent to the PSF of the LIDAR laser at infinity. With a focal length of 1.8 m, the telescope has then a magnification of about 0.03. It may happen that the shape of the pictured spot may be slightly influenced by the irregular shape of the reflected spot on the wall, but it can be accepted as an approximation. The Canon camera was installed and fixed about 25 cm behind the focal plane of the CLUE telescope. The diffusive paper was attached in the focal plane. Then, the CLUE telescope was moved to point the artificial star. The image generated in the diffusive paper was remotely recorded with the camera and stored. The images have been analyzed using a ROOT macro, after conversion to FITS format. The images are treated as 2D histograms and then retrieved into an array of numbers. After extracting a background image (a picture without the artificial laser star), the program searches for the spot maximum by scanning the image and calculates the center of gravity of the spot. Finally, different containment radii (enclosing 50%, 80%, 90%, 95%, 99% and 99.9% of the light in a circular shape) are calculated and displayed. For the conversion from pixel size to millimeters, we used the marks on the metric paper and calculated their distance in pixels: one millimeter corresponds to approximately 27 pixels. The analysis of the different images lead us to conclude that 80% of the light is enclosed in a circle of about 6 mm diameter (see Figure 2.8), while 90% falls in a circular area of around 7 mm diameter. These results are compatible with those obtained in [33], [130] and [185].

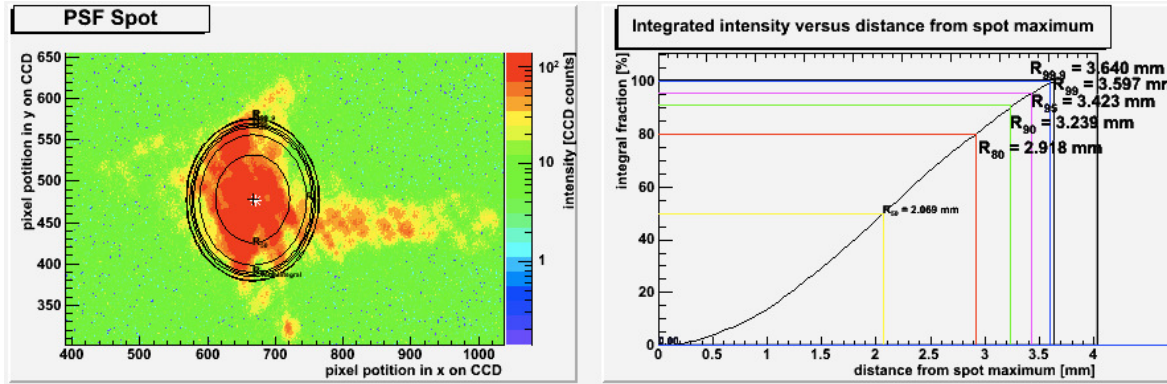


Figure 2.8: Gaussian profile of the horizontal cut. The x-axis is the number of pixels, while the y-axis is intensity [arbitrary units]. The data points are plotted in red, while the gaussian fit is represented on black.

The PSF of the primary mirror has been maintained since the mirror was built, being the 80% of the light enclosed in a  $\sim$ 6 mm circle, which means that the optical quality of the mirror has not decreased along the years. The light is perfectly contained into the liquid light guide, that has a diameter of 8 mm. For the LIDAR purpose, it is enough that the system works as a light collector, as no imaging is performed. Since high image quality is not needed, the measured spot size is enough for the LIDAR set-up and its shape it is not important. The requirement is that the spot should be smaller than 8 mm, which is fulfilled.

## Reflectivity

In order to characterize the system, both the superficial and focused reflectivity of the mirror have been measured [130]. Moreover, due to aging and a lack of care for the last years (the telescope has been stored since it stopped working for HEGRA experiment), the mirror have some slightly damaged areas and it is covered by a stacked layer of dust, so its capacity of reflect the light could have decreased. Because of that, measurements of the reflectivity in different positions of the mirror are needed to understand if it is suitable for the LIDAR purpose or if an aluminizing is needed.

The value of the superficial reflectivity at 350 nm, wavelength of the peak emission for Cherenkov light, is around 80% of the incoming radiation. The local reflectivity can be translated into focal just by multiplying by the factor  $f = 0.79$ . This lead to a reflectivity of  $\sim 64\%$  at 350 nm, where the peak of the Cherenkov light is. The description of the performed tests is collected in [130].

---

### 2.4.2 The Pulsed Laser

#### Laser Spot Size

The value of the spot size (given by the manufacturer) at 1064 nm is about 6 mm diameter. As we are mainly interested in the second (532 nm) and third (355 nm) harmonics, we wanted to measure the diameter of these two wavelengths. The beam divergence at 1064 nm is 0.5 mrad, it would be assumed the same value for all wavelengths.

The laser was placed over the arm. The laser was shot repeated times into a target that was positioned at a distance of 2.5 m. The images were captured with an Canon EOS Camera inside a laboratory. The images were analyzed following the same procedure and macro that was used in the third method to determine the PSF of the mirror described in Subsection 2.3.2.

For the 355 nm wavelength, about 80% of the light is enclosed in a circle of 2.6 mm of diameter, while 90% falls in a circular area of about 3 mm diameter. Most of the light (99.9%) is inside a spot of 4 mm, of diameter, for the different distances measured. The resulting values are plotted on Figure 2.9.

On the other hand, for the 532 nm harmonic, about 80% of the light is enclosed in a circle of 3.6 mm of diameter, while 90% is enclosed in an area of about 4 mm of diameter. The 99.9% of light is in a diameter of about 5 mm. Figure 2.10 shows the obtained results.

It is worth noticing that these spots are measured at short distances (laboratory level). Nevertheless, the beam has a gaussian shape. The divergence of the beam at larger distances can be calculated as

$$w(z) = w_0 \sqrt{1 + \frac{z^2}{z_R^2}} \quad (2.4)$$

were  $w_0$  is the radial size of the beam at is narrowest point (at the exit of the laser),  $z$  is the altitude and were:

$$z_R = \frac{\pi w_0^2}{\lambda} \quad (2.5)$$

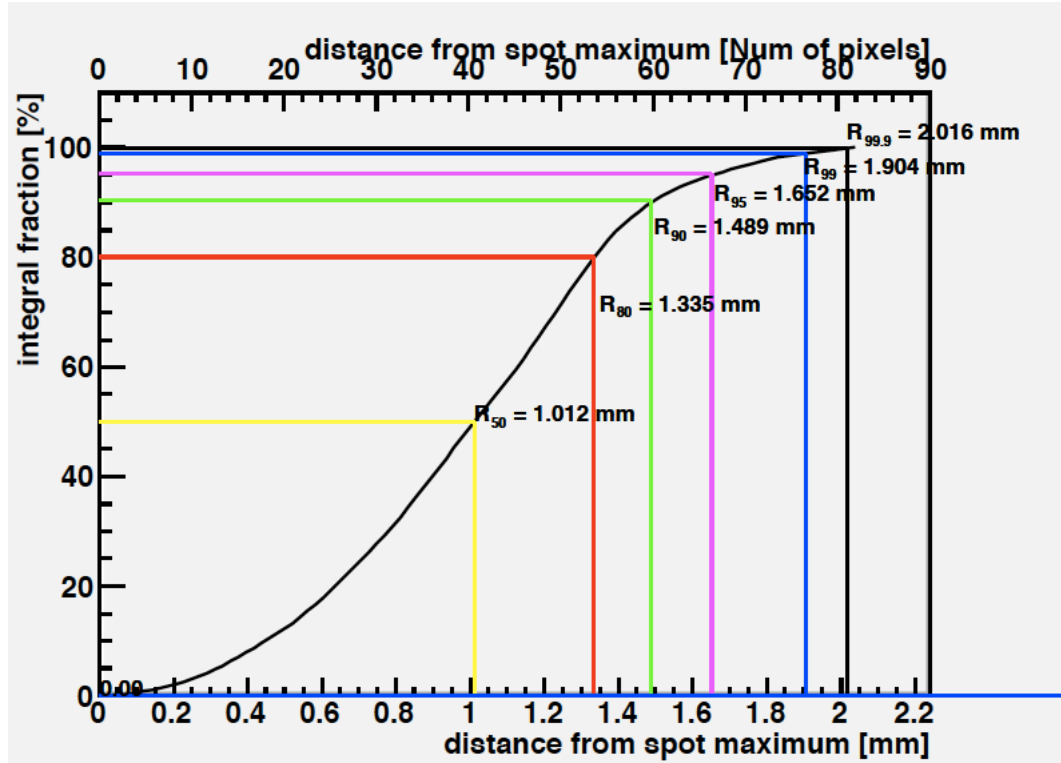


Figure 2.9: Curves of adjustment for different energy containers for the 355 nm wavelength.

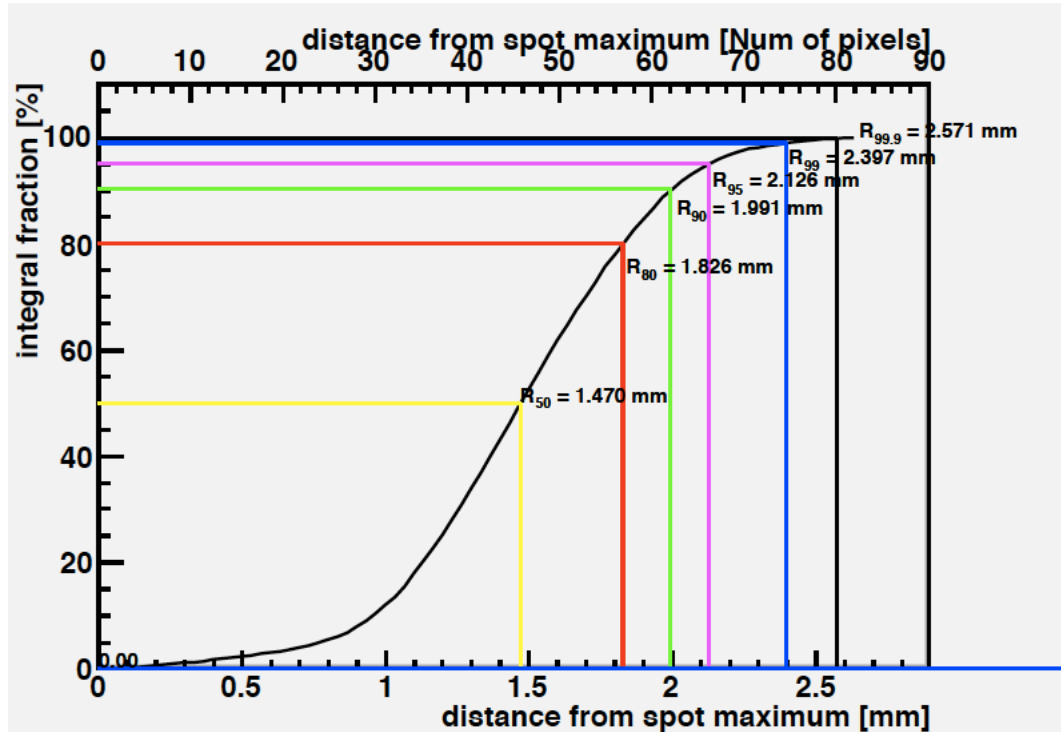


Figure 2.10: Curves of adjustment for different energy containers for the 532 nm wavelength

is the Rayleigh length (the distance along the propagation direction from the waist to the place where the area of the cross section is doubled).

### The mechanical arm

The requirement for the mechanical arm was that it should have a precision  $< 0.5$  mm at a distance of 2 m. A simple test was performed in order to confirm if it fulfilled the requisite. The arm was placed at a distance of 2.54 m (this distance was not chosen on purpose, it was just where the laser was placed for other tests) from a wall, where a millimetered paper was attached to a wall. First, the laser was shot forward and backwards in each of the two axis. One image per position was taken. Then, the maximum peak of the gaussian distribution is calculated making use of the *fv* program for each image. The maximum separation between the peaks of two images taken in the same position will give the precision of the movement. For the horizontal displacement, the maximum distance is  $\sim 0.25$  mm, while for the vertical is  $\sim 0.14$  mm. Systematics due to the determination of the position of the maximum of the emission could exist, but since the precision is better than expected, systematics will always be compatible with the requirement. Hence, the condition is fulfilled and can be used for the LIDAR purpose.

#### 2.4.3 The Light Guide

---

Different tests to fully characterize the LLG have been performed: the transmittivity and its dependence with temperature and bending, the output angle... For the measurements, a Deuterium source, a CM110 Monochromator and a light sensor Newport 818-UV have been used in a dark room under controlled conditions. Details on these measurements can also be found in [185].

##### Wavelength Transmission

The manufacturer claims a transmittivity of  $\sim 70 - 80\%$  every two meters in the UV. The first test performed was designed to check this transmission curve for the 3.2 m of LLG between 300 nm and 600 nm, on steps of 25 nm. The first step was to measure the output of the deuterium source and monochromator without the LLG. Later, the deuterium light behavior and the monochromator to select the wavelength were positioned at the entrance of the LLG. The ratio between these measurements denotes the transmittivity of the fiber. This procedure was repeated three times, to check consistency. The result is shown on Figure 2.11. The transmittivity is around 60 – 70% in the UV.

##### Temperature dependence

The LIDAR will be exposed to strong variations of the temperature, hence it is important to know if its components have a stable response under these conditions. For most of the components, the specifications in terms of temperature it is given, but that is not the case for LLG, which are a recent technology. I have tested the dependence of the transmission of the LLG with the wavelength for different temperatures. For the tests, the LLG was first set in contact with ice to study its behavior at low temperatures (next to 0°). Then, the trend at room and higher temperatures was measured. The resulting values are plotted on Figure 2.12. There is no dispersion for short wavelengths, although it becomes noticeable at wavelengths larger than 575 nm, with maximum changes of 0.9 nW. The behavior is stable for temperatures at low temperatures, below 23°, which is the optimal value for the operation of the fiber. For temperatures above 25°, the transmittivity is slightly worse.

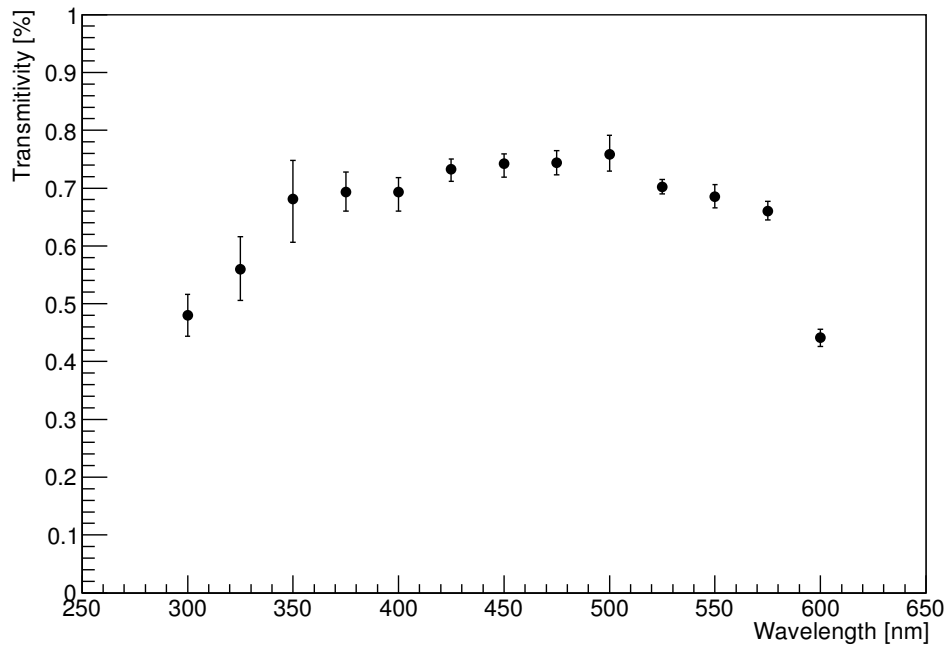


Figure 2.11: Transmittivity of the 3.2 m LLG in terms of the wavelength.

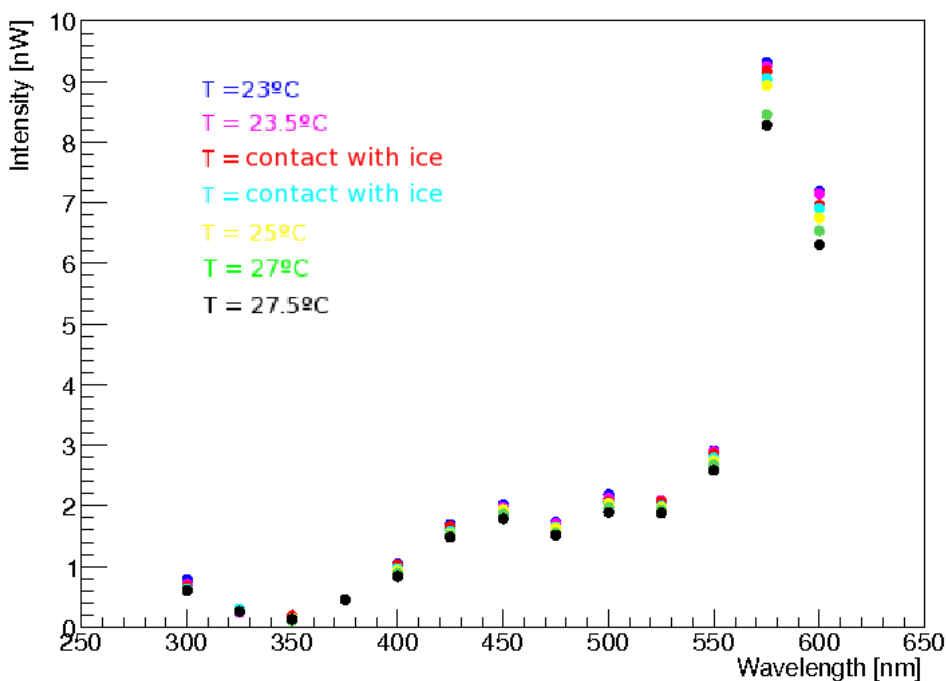


Figure 2.12: Intensity of the transmitted light in terms of the wavelength for different ambient temperatures.

### Transmission dependence with the entrance angle

The LLG is placed perpendicularly to the focal plane, so that the angle between the entering light beam and the head of the LLG is  $0^\circ$ . The mirror, which has  $f/D = 1$ , has a maximum opening angle of  $\theta_{max} = 26.57^\circ$ . It is then important that light coming from angles  $\theta > \theta_{max} \sim 27^\circ$  is not transmitted in the LLG to reduce the background. Since the opening angle is large, a LLG with a large numerical aperture (NA) was bought to try to collect the maximum light possible.

For these measurements, a class III green laser pointer has been used as light source. Its stability and response is known. The laser is attached to a rotating support which permits to change the angle. This device is set at the entrance of the LLG. The output radiation is measured for entrance angles ( $\theta_e$ ) between  $0^\circ$  and  $60^\circ$ , see Figure 2.13. The transmission is stable until  $\theta_e = 15^\circ$ , and then it starts decreasing. For angles larger than  $\theta_e = 30^\circ$ , the transmission falls one order of magnitude. In the LIDAR context, the maximum opening angle is  $\theta_{max} = 26.57^\circ$ , which is the range where the transmittivity is still high. All the photons below  $27^\circ$  will be collected by the LLG with a good transmittivity. Light coming from apertures larger than  $27^\circ$  is not transmitted, which is appropriate in our system to have a low background.

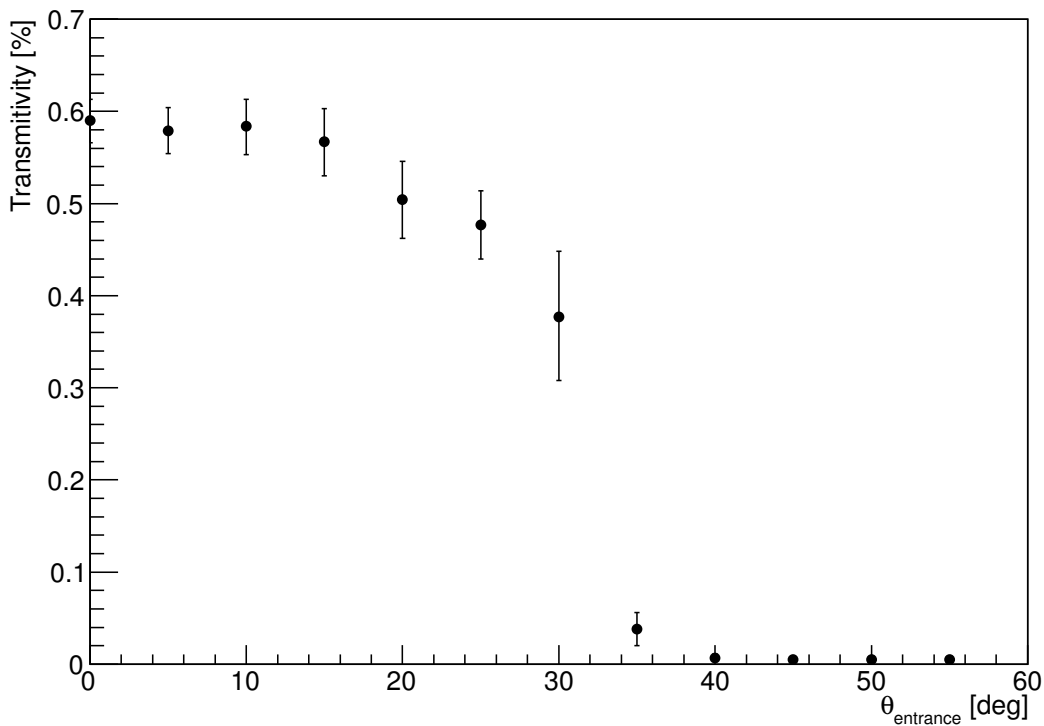


Figure 2.13: Dependence of the transmission with the incident angle.

### Relation between output and entering angle

The spot produced at the exit of the LLG may vary depending on the entrance angle. For that purpose, the same montage is used, but in the case a screen is placed at a distance  $d$  at the exit of the LLG to be able to measure the output radii  $r(\theta_e)$ .

The output angle:

$$\theta_{out} = \arctan \left( \frac{r(\theta_e)}{d} \right) \quad (2.6)$$

The resulting plot is shown on Figure 2.14. There is a positive linear dependence of the output angle with respect to the incident one. The output angle increases with increasing entering angle. This relation is important for the design of the optical detector.

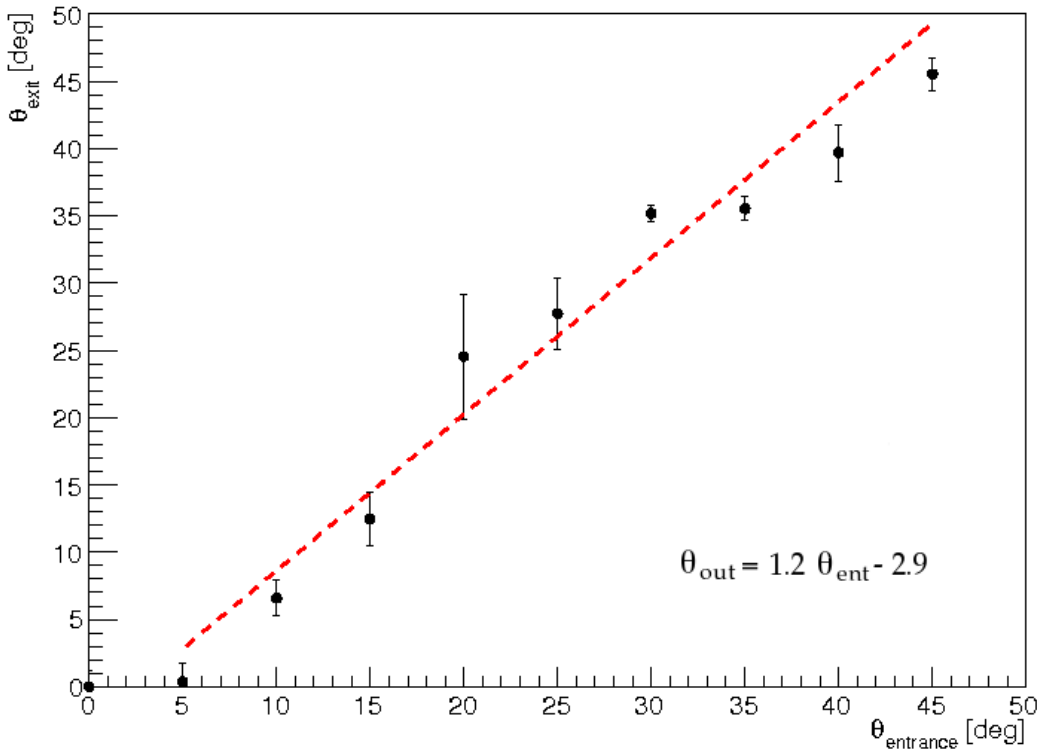


Figure 2.14: Dependence of the output angle with the incident angle. The dashed line is the fit to a first order polynomial.

### Shape dependence

The LIDAR will be under continuous movement during the observations, hence it is required that the transmission capabilities of the LLG do not change with its shape. To test if there exists a dependence, the transmittivity of the LLG turning over itself has been measured. The ratio between this new configuration and the already measured transmittivity for each wavelength is calculated. The result is shown on Figure 2.15. The ratio is constant for the complete wavelength range. Hence, there is no dependence of the transmission capacity of the LLG and its position or acquired shape.

#### 2.4.4 The Optical Detector

The final design for the optical detector is a four-channel design to study two elastic lines, at 355 nm and 532 nm, and two Raman channels, at 387 nm and 607 nm, that correspond to nitrogen ( $N_2$ ). The nitrogen has been chosen since it is the major atmospheric element. But before building this multiwavelength detector, it is important to

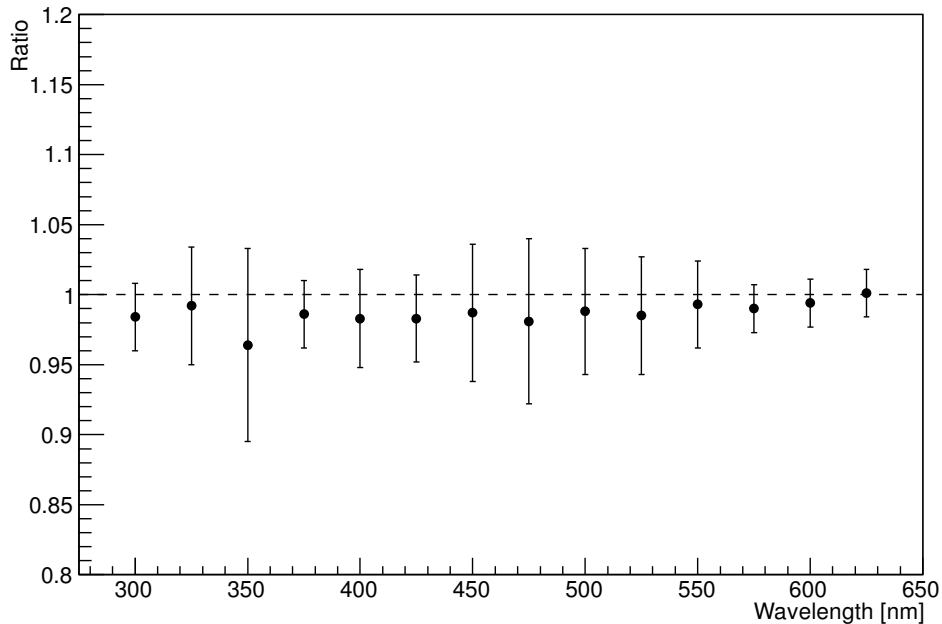


Figure 2.15: Dependence of transmittivity with the shape. The dashed line understand how a single channel works.

### The Monochromatic Wavelength Detector

A single channel detector has been built for the IFAE/UAB Raman LIDAR , called the *monochromatic detector*, in order to test the LIDAR response. It is meant only for testing purposes to commission the rest of the LIDAR with a simple optical detector, then a multiwavelength detector will be used. It is a simple instrument which hosts a photomultiplier, a filter (although currently there are two slots for optical elements ) and a diaphragm, see Fig. 2.16. Because the intensity of the Rayleigh scattered light is not a limitation, it will collect the light from a single elastic channel.

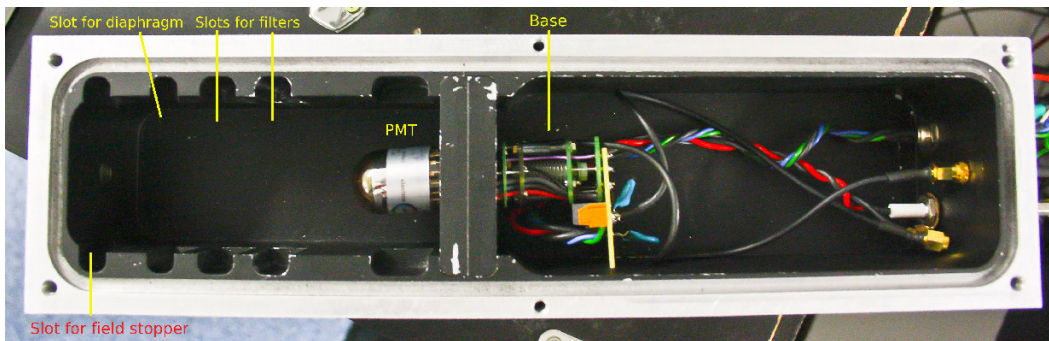


Figure 2.16: Monochromatic Wavelength Detector. The slots for the field stopper and filters are indicated. A PMT will collect a single elastic channel.

The readout chain, the optics and all elements will be tested with this device. It will help to understand the full performance of the LIDAR and will allow the optimization of the system. It will first be tested in the laboratory to understand the behavior in a controlled environment. Then, it will be mounted on the LIDAR and will be operated

to test the real response of the system during night operation.

The readout needs to have the capability of detecting continuum emission and measure single photon-counting. For that purpose, a proper PMT which can detect single phe has to be used.

### Pulsed Light Tests

A test bench has been mounted at IFAE to test different PMTs which are former pixels of the MAGIC-I telescope. We tested each PMT separately to search for the signature of the single photon-counting.

For the test, a pulsed 4 Hz signal created by a UV LED. The LED is fed by a 12 V source. This pulsed light is focused into the entrance of the monochromatic wavelength detector shown on Figure 2.16, which is a thigh box that contains the PMT and has slots for other possible elements (filters, field stopper). The PMT is fed by a source of high voltage (1600 V). The PMT is connected to pre-amplifier in order to enlarge the signal. The electronics of the PMT can also read DC current. The information is then read by an oscilloscope and a *Labview* program that reads the amplitude values measured by the oscilloscope and creates a histogram. If there is single phe detection, it would appear as a second broader bump in the graphic. After testing six different PMTs, the selected one has been PMT num 072, whose amplitude histogram is plotted on Figure 2.17). Two other spares, with lower single phe capability, labeled with numbers 1911 and 1896 are also available in case of need.

The stability of the response of the PMT over time was also measured for several hours. The shape is not time dependent, within statistical fluctuations.

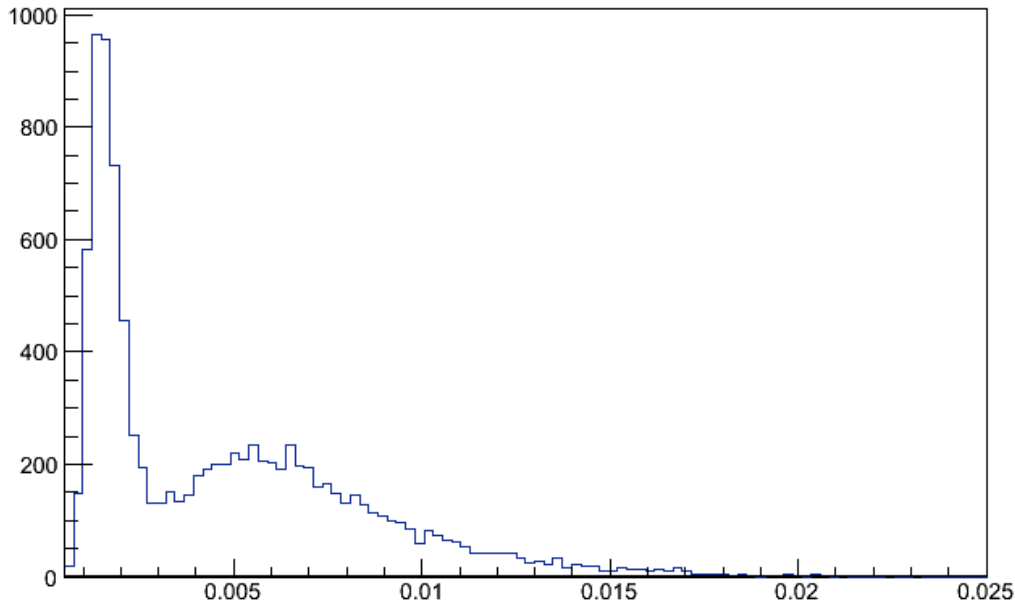


Figure 2.17: Amplitude histogram of the selected PMT for the monochromator purpose. The pedestal (first peak) and single phe peak (second broader peak) are visible.

### The Multiwavelength Detector

Preliminary tests to check the performance of some of the components of the optical

detector were performed. The main purpose is to understand how much the relative position and orientation of the optical components change the light throughput from the light source to the photon detector device. It is expected, after performing these tests, to know how sensitive the design is to the positioning and orientations of the optical elements, defining the required precision for the design.

Three DM will be used in this system: a DM that reflects the 355 nm line (DM355) and transmit the wavelengths above it, a DM that reflects light at 387 nm (DM387) and let the larger wavelengths pass and a DM that reflects the 532 nm line (DM532). The light source is a deuterium source. Also the CM 110 wavelength selector has been used. The detector is the pin-diode used in the LLG tests on Subsection 2.4.3.

The procedure was the following:

- The spectrum of the light source is measured before each observation.
- The first tests were a scan of each DM was performed. The reference angle was  $45^\circ$  with respect to the light source. The scan was performed increasing and decreasing the angle with respect to the light source, on steps of  $2^\circ$ .
- The second tests were equal to the first ones, but including the filter for the reflected wavelength is included in order to rule out harmonics.

It is expected that the DM transmits no signal at the wavelength indicated, and show a large transmittivity for larger wavelengths. The transmittivity at 355 nm (for DM355) and at 532 nm (for DM532) shall be almost zero, respectively, while for larger wavelengths it shall be around 95%. The transmittance for the DM reflecting the 355 nm wavelength is shown on Figure 2.18. The reference angle is  $45^\circ$ . In the tests performed only with the DM (left panel), the transmission at 355 nm is very low, as expected, since the DM shall not let pass that wavelength. The transmittivity at wavelengths larger than 355 nm varies from 50% up to 60%, which is much less than claimed by the manufacturer. When the 355 nm filter is placed at the output of the wavelength selector, the transmittivity increases to values similar to the specified, since harmonics were eliminated. A similar behavior is visible for the DM and mirror at 387 nm (Figure 2.19). For the 532 nm DM, the transmittance is also low at for the transmitted wavelengths (Figure 2.20). In this case there is no filter to test it with.

The main conclusions that have been reached are:

- The DMs have a coated face which, in principle, should face the light, however we have checked numerically that the transmission does not change if rotating the DM  $180^\circ$ .
- The DM tolerance angle is  $\pm 4^\circ$ . The dismissing of the light is 5%. Angles greater than the nominal 45% give better response than angles smaller than 45%.

#### 2.4.5 Conclusions from the Tests

---

The different elements of the LIDAR have been tested and characterized. Some conclusions from the tests can be listed:

- **Primary mirror:** The PSF of the mirror has been measured to be  $\sim 7\text{ mm}$  for the 95% light container, hence most of the light is collected by the LLG. 80% of the light is enclosed in a spot of  $\sim 6\text{ mm}$ , the same value that it had when it was produced, what indicates that the optical quality has not decreased with time. The superficial and focal reflectivity were measured: the

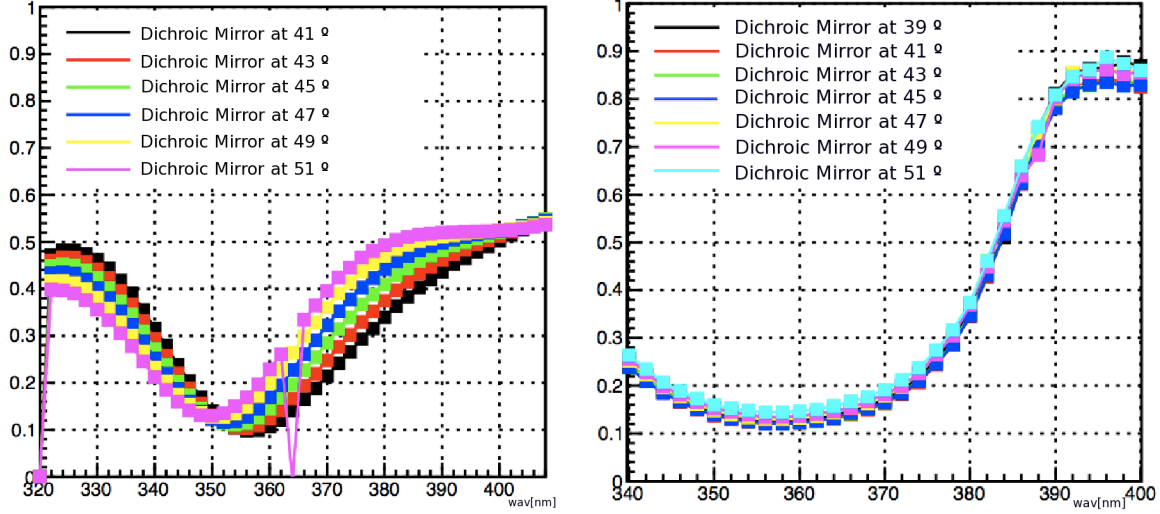


Figure 2.18: *Left:* Transmission of the DM at 355 nm. *Right:* Transmission of the DM at 355 nm, when the 355 nm filter is placed at the output of the wavelength selector.

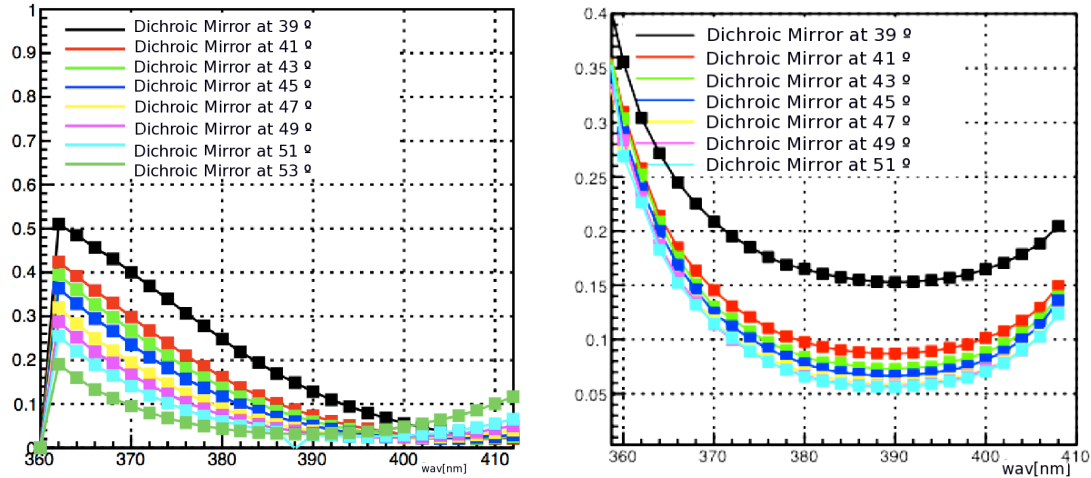


Figure 2.19: *Left:* Transmission of the DM at 387 nm. *Right:* Transmission of the DM at 387 nm, when the 387 nm filter is placed at the output of the wavelength selector.

superficial reflectivity for the peak emission of the Cherenkov light at 350 nm is 80%; in the case of focal reflectivity, this value decreases to  $\sim 64\%$  at the same wavelength. Although this last value is not too high, it would affect at most the maximum distance at which the LIDAR can perform measurements [68]. This does not suppose a problem and hence the primary mirror can be used for the LIDAR purpose.

- **Pulsed laser and mechanical arm:** The size of the spot for the second and third harmonic have been measured. 90% of the light is enclosed in a circle of 3 mm and 4 mm respectively. These measurements have been performed at the output of the laser, for short distances. At large distances it shall be considered the gaussian divergence of the beam. Furthermore, the precision of the mechanical arm has been tested, and it fulfills the requirement of  $< 0.5$  mm at 2 m distance.
- **LLG:** the 3.2 m LLG has been tested in the laboratory. Its transmission is 60

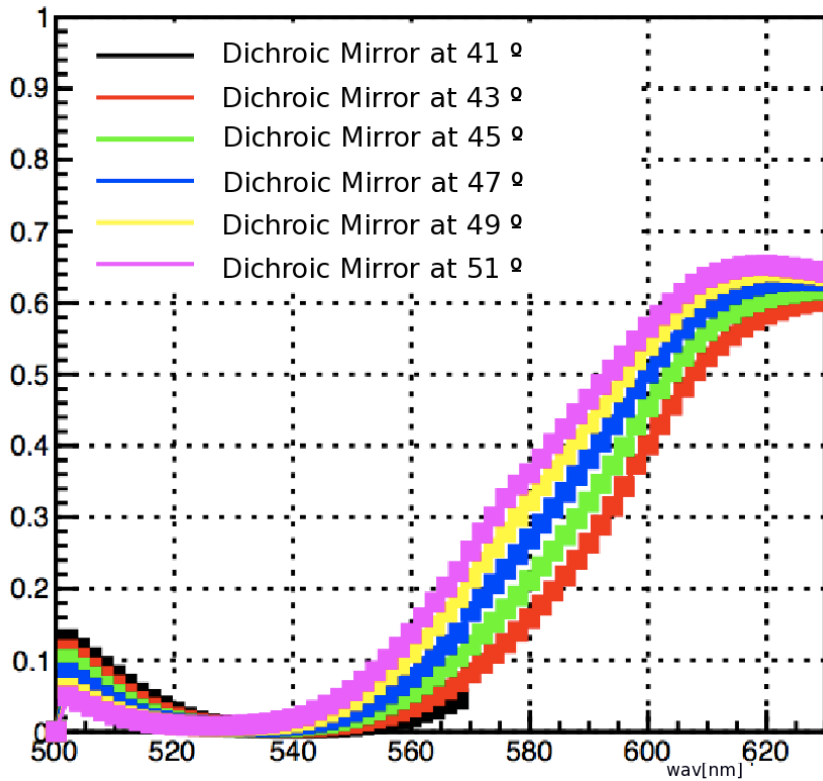


Figure 2.20: Transmission of the 532 nm DM.

- 70 % in the UV range, and it does not change with the shape of the LLG. The transmission is quite stable with changes in the temperature, being 23°. The optimal point for operation; for larger temperatures the transmittivity falls slightly. The transmission is constant for incident angles until 15° and decreases slightly until 30°. Above this value, the transmission falls an order of magnitude. Considering the opening angle of the mirror, 26.7°, this effect is appropriate for the system. Finally, the output angle has a linear dependence with the entrance angle.
- **Optical detector:** a single monochromatic detector was tested in the laboratory using a former MAGIC PMT. It shows a single-phe response, however it is not very prominent. The response of the PMT is stable over time. On the other hand, the DMs for the multiwavelength detector were tested. The tolerance angle is  $\pm 4^\circ$ . Larger angles than the nominal 45° give better response than shorter angles.



# 3

## The MAGIC Telescopes

*I*n this chapter, the description and performance of the MAGIC Telescopes are assessed. The most relevant hardware and software is described. The standard data analysis both for monoscopic and stereoscopic observations and a dedicated analysis under moderate moonlight conditions are also described. Finally, the contributions I made for the MAGIC upgrade which took place in 2011 are described.

### 3.1 Telescopes Description

---

The MAGIC *Florian Goebel* Telescopes are two IACTs (see Figure 3.1) located at the Observatorio del Roque de los Muchachos (ORM) on the Canary Island of La Palma<sup>6</sup> ( $28.75^{\circ}$  N and  $17.89^{\circ}$  W) at an altitude of 2230 m a.s.l. The first telescope, MAGIC-I (M1) is fully operative since 2003. The second telescope, MAGIC-II (M2), an improved clone of M1, started operations in 2009. The aim of this facility was to cover the uncharted energy range between 10 GeV and 100 GeV. Hence, the energy threshold ( $E_{th}$ ) had to be lowered from the previous generation of IACTs. As low-energy  $\gamma$  rays produce less Cherenkov light, the approach was to enlarge the mirror collection area and use photo-multipliers (PMTs) with enhanced quantum efficiency. This led to the construction of a 17m diameter dish with a collection area of  $236\text{ m}^2$ . Also, the high sampling speed of the readout electronics permitted the use of timing information in the data analysis, which enhances sensitivity. The inclusion of a second telescope supposed an improvement on the overall sensitivity, which increased by a factor 1.5 – 2, depending on the energy range [32]. Furthermore, the energy resolution and energy reconstruction also improved with the stereoscopic system.

The structure of the telescopes is made of steel, aluminum and carbon fiber tubes and it is mounted in an altazimuthal configuration over a circular rail of 19 m diameter. The readout electronics is not attached to the cameras but placed at the control house (namely "counting house", CH) where the signal is sent through optical fibers. The CH is a building, situated next to the telescopes, where all the electronics devices are stored and where the signal from the cameras is processed.

---

<sup>6</sup>Among the Canary Islands inhabitants, La Palma is known as *La Isla Bonita* (the beautiful island).

Having the electronics readout in the CH reduces the weight of the camera and, hence, diminishes the weight of the structure. Hence, with such a *light* structure (of about 60 Tons), the telescopes can be oriented to any point in the sky in less than 40 s. The drive system has a fast repositioning mode that allows to rotate the telescope 180° in less than 20 s. This design was followed to be able to move rapidly and try to "catch" gamma-ray burst (GRBs), which are flashes of  $\gamma$  rays which can last few tens of seconds. This fast mode is only used in the case of a *GRB alarm*.



Figure 3.1: *Left:* MAGIC-I telescope, after the upgrade, with Orion and Herschel and Swedish Solar telescopes in the background. *Right:* MAGIC-II telescope observing under moderate moon, with GTC in the background.

M1 started operations on 2003, and it was working as a stand-alone telescope until 2009, when M2 joined standard observations. Then stereoscopic observations, triggering both telescopes in coincidence, became possible. However, the telescopes were not exactly similar: M1 had an octagonal 577 pixel camera with pixels of different sizes, while M2 had a circular-shaped 1039 pixel camera. The first readout of M1 (denominated Siegen) was a 300 MHz system, which was later updated to a multiplexing system based on Flash Analog-to-Digital Converters, MUX-FADCs [93] while M2 was based on a chip Domino Ring Sampler v2, DRS2 [171]. On 2011, the telescopes underwent a major upgrade to make the systems more similar and uniform. The readout was updated to DRS version 4, DRS4 [189]. On 2012, the M1 camera and the M1 trigger were exchanged to be more equal to those in M2. Finally, software and hardware of several subsystems (mainly M1) were upgraded. With these implementations, both the overall performance, sensitivity (it boosted slightly, although it was not the goal) and stability were improved. The sensitivity of the upgraded MAGIC stereoscopic system is  $0.71\% \pm 0.02\%$  of the Crab Nebula flux in 50 h of observation for energies above 250 GeV [188]. See Figure 3.2 to see the evolution of the integral sensitivity of the telescope along the years.

### 3.1.1 Camera

The cameras of IACTs shall be very sensitive and be composed of fast-response detectors, in order to detect the fast Cherenkov flashes and collect as much Cherenkov light from the air showers as possible. Each PMT acts as a pixel

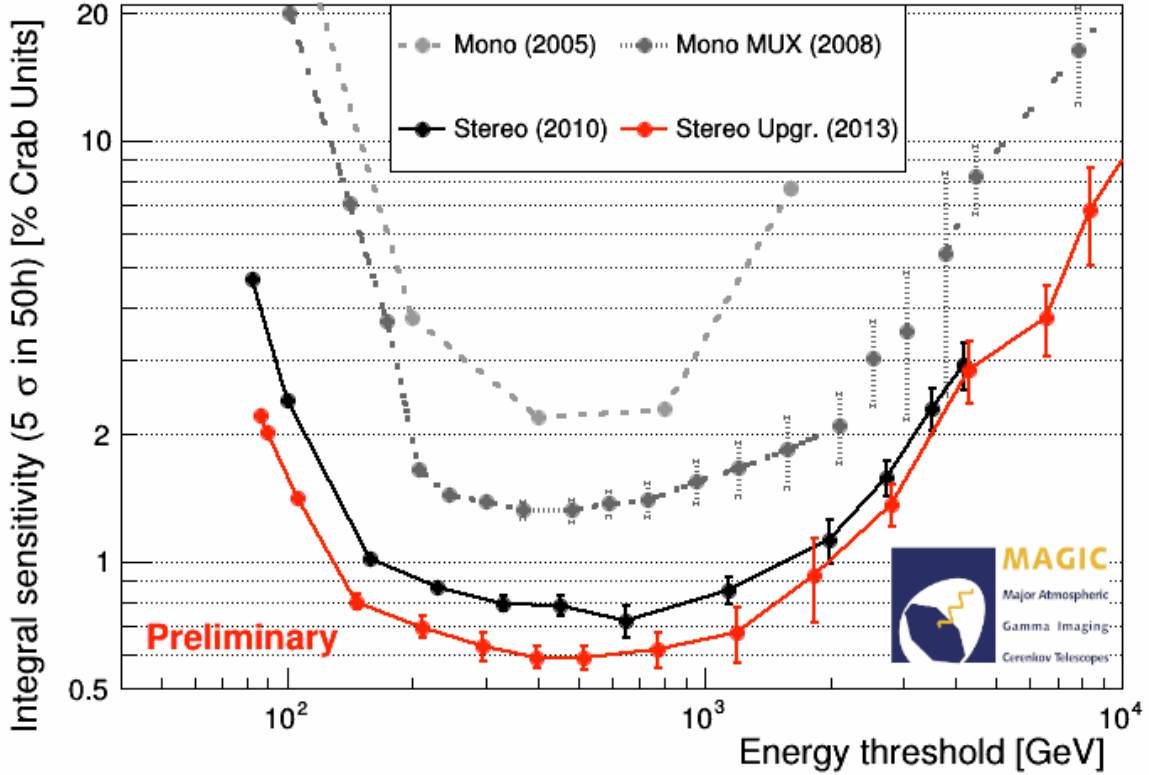


Figure 3.2: Evolution of the integral sensitivity of MAGIC for the different configurations adopted by the system. *Dashed light-grey*: MAGIC-I initial sensitivity for Siegen readout. *Dashed dark-grey*: MAGIC-I sensitivity for a multiplex readout. *Black line*: MAGIC pre-upgrade stereo sensitivity. *Red line*: MAGIC post-upgrade stereo sensitivity. [Credit: J. Sitarek & D. Tescaro] [194].

and provides a fast response of the order of few ns. The voltage of each individual PMT can be adjusted manually up to 1500 V. Using a *small* pixel size is needed for a better sampling of the shower. It also helps in reducing the integrated background from the night sky background, what allows the lowering of the trigger threshold. The FoV of each camera is 3.5°.

The cameras are placed at the focal plane of the telescopes held by a metallic arch supported by thin steel cables. A pexiglass window and metallic lids protect the PMTs from external agents and daylight. Winston cones (light concentrators) are placed between the PMTs and the pexiglass to match the shape of the PMTs, to cut albedo and to enhance photon-conversion efficiency. The water/air cooling and heating is also placed in the cameras, to stabilize the temperature. The structure is water-tight.

Until 2012, M1 was hosting the first camera built for the experiment. It was made of 397 inner pixels of 1 inch diameter (0.1° of FoV), surrounded by 180 larger pixels of 1.5 inch diameter (0.2° of FoV), all of them arranged in an hexagonal shape. The idea of placing smaller PMTs in the camera center is caused due to the fact that low energy showers (below 100 GeV) are rather small and lie close to the camera center and it is also due to coma effect, which is larger at the edges of the camera, hence larger PMTs are needed there. The entrance window of each PMT was coated in order to increase the quantum efficiency (QE) up to ∼30%. The low gain (<  $2 \times 10^4$ ) permitted moonlight observations. The camera weighted

$\sim 650$  kg. The top panel of Figure 3.3 shows the old camera.

M2 camera and the new camera of M1 have 1039 pixels of the same size ( $0.1^\circ$  of FoV). The QE is  $\sim 35\%$ . The gain of these PMTs is slightly larger,  $\sim 3 \times 10^4$ . Both cameras weight  $\sim 750$  kg. A picture is visible on Figure 3.3.

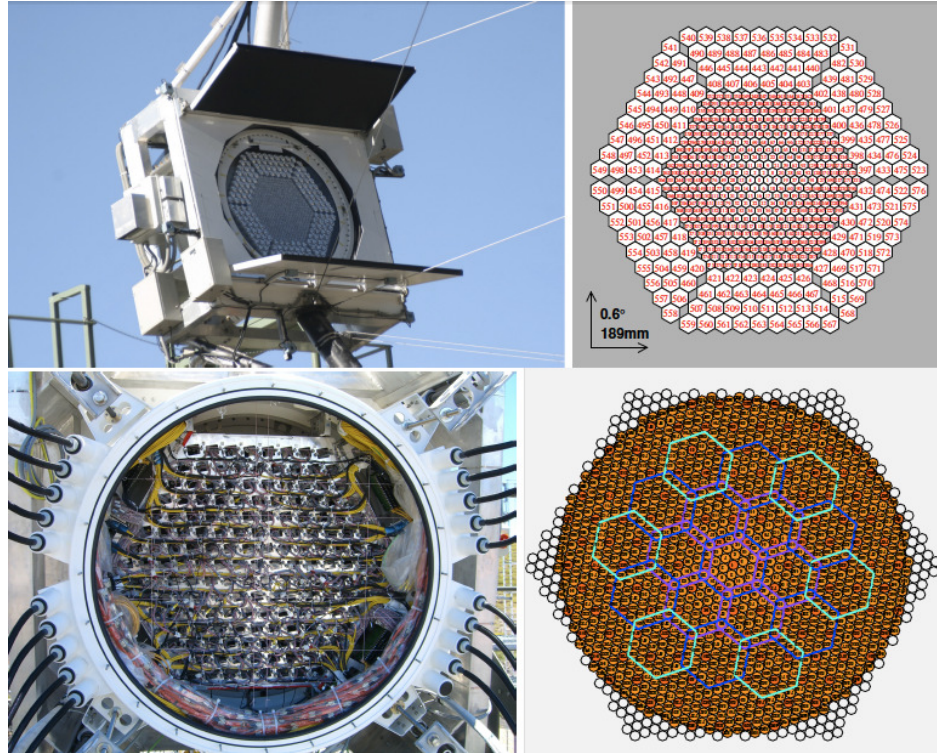


Figure 3.3: Cameras of the MAGIC telescopes. *Top*: Old M1 camera. On the left, front part of the camera. On the right, the camera layout. *Bottom*: M2 camera. On the left, back part of the camera. On the right: layout. [Credit: D. Tescaro]

### 3.1.2 Reflecting Surface

The dish holding the reflective surface has an octagonal parabolic shape and it is filled with spheric mirrors of different radius of curvature (from  $\sim 34$  m to  $\sim 37$  m), depending on the position on the paraboloid. M1 is composed by 956 aluminum mirrors of about  $0.5 \times 0.5$  m $^2$  grouped in panels of four facets, while M2 is composed by 143 aluminum mirrors of  $\sim 1$  m $^2$  in the center of the dish and 104 glass mirrors of  $\sim 1$  m $^2$  in the outer region. A detail on the reflective surface for both telescopes is shown on Figure 3.4. The external face of each mirror has been coated with a 100 nm thick layer of quartz, to protect them from corrosion and external agents (keep in mind that the telescopes do not have a dome to protect them). As the focal length is the same as the diameter, 17 m, leading to a focal-to-diameter ratio of  $f/D = 1$ .

The parabolic shape is an isochronous surface which guarantees the preservation of the temporal structure of atmospheric shower. By conserving the relative arrival times of the photons, the signal to noise ratio improves, reducing the contamination of the night sky background (NSB). By using the information of the arrival times in the data analysis, better image cleaning, angular resolution and energy estimation can be performed. As it can be seen in Figure 3.4, the M1

mirror dish has a *chess* structure, which is caused by a design problem. However, the delay on the arrival times of the photons is less than a ns and it is corrected. The point spread function (PSF), defined as the 39% containment radius of the spot of a point-like source on the focal plane of the mirror, of each single mirror is  $\sim 10$  mm, being contained inside a single PMT. However, the parabolic reflector suffers aberrations like spherical aberration, astigmatism or coma. The *active mirror control* (AMC) corrects the position for each facet by the use of *look-up tables* (LUTs). It corrects the misalignment of the individual mirrors at any position angle, since the deformation of the dish depends mainly on the zenith angle . Thanks to the AMC, the whole PSF can reach a value of  $\sim 12$  mm.

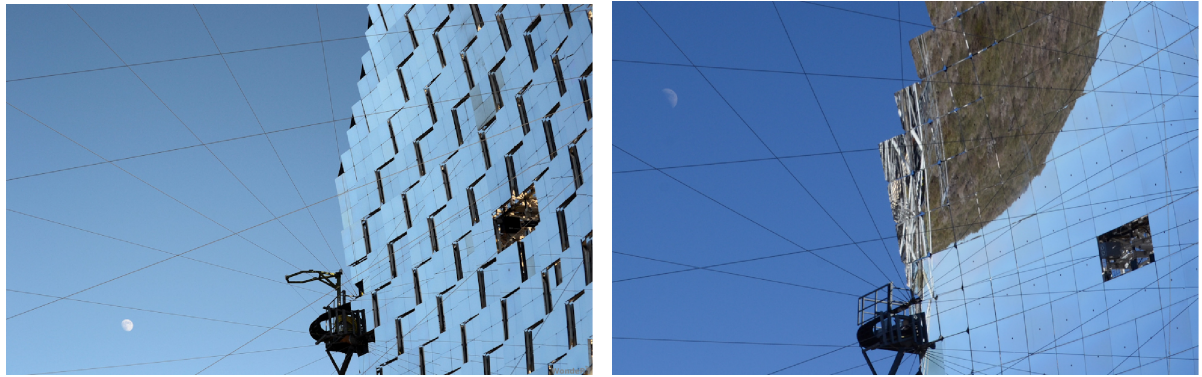


Figure 3.4: *Left:* Detail of MAGIC-I mirrors. *Right:* Detail of MAGIC-II reflective surface.

### 3.1.3 Structure

A main goal in the design of MAGIC was to achieve a fast pointing system. For that purpose, the telescope structure had to be light enough to be able to point the system anywhere in the sky in less than 40 s. A structure composed of carbon fibre-epoxy tubes joined by aluminum knots combines light weight and strong rigidity. The tubes and knots are modular. The total weight of the frame is 60 Tons, number that increases to 72 Tons considering all components [50]. The camera is sustained by an arch which continues over the back part of the mirror dish becoming a rail for the altitude drive and a support for the counterweights.

### 3.1.4 Drive System

Three motors take care of the movement of the telescopes, two in azimuth and one in elevation. The cables for the signal transmission until the CH impose a mechanical constraint over the movement, which is limited from  $-90^\circ$  to  $318^\circ$  in azimuth and from  $-10^\circ$  to  $160^\circ$  in zenith, what means that the telescope can be pointed backwards. The angular position is controlled by two shaft encoders, what provides a pointing accuracy of  $0.02^\circ$ . The calibration and precision of the tracking of the shaft encoders is performed by comparing its pointing coordinates with a sensitive CCD starguider camera mounted in the center of the dish. It compares the position of the telescope camera, using as a reference some LEDs placed in its frame, with that of the background stars.



Figure 3.5: Back of the structure of MAGIC-I telescope. White carbon fibre tubes compose the main frame. The counterweights are placed in the curved back part of the arch.

### 3.1.5 Readout Electronics and Trigger

As the  $\gamma$ -ray signal is very short, a fast readout electronics is needed. When the Cherenkov photon hits the entrance of the Winston cone, it is transmitted to the PMT cathode and transformed into an analog signal, which is amplified by a pre-amplifier. This signal is sent into a transmitter board where the electronic signal is transformed into a light pulse through a VCSEL (Vertical Cavity Surface Emitting Laser). The output is coupled to an optical fiber. The fiber conveys the signal from the camera to the CH.

Once in the CH, the signal enters into the receivers boards where is converted back to electrical and splitted into two branches: a trigger digital branch with a discriminator and an analog readout branch. In the old MAGIC-I readout chain, the signals were first splitted into the two branches and then converted, while in MAGIC-II and in the upgraded MAGIC-I readout the splitting of the signal occurs after the conversion. The digital signal is sent to the trigger system. After performing the triggering and readout of the analog signal, the sampled data is set to the data acquisition computer where the values are organized in events and stored as raw data files.

The telescope trigger is a multiple level decisional system which determines the acquisition of an event in time coincidence with an atmospheric shower. To discriminate an event, two properties are taken into account: the light of the air shower is a short flash which is more intense than the night sky background and it involves several compact neighbor pixels at the same time.

The *Level zero trigger* (L0T) is housed in the receivers: if the signal of a pixel is above a certain discriminator threshold, the receivers will generate a digital trigger which is sent to the corresponding digital channel. The width and the

delay can also be controlled. The L0T is regulated by the Individual Pixel Rate Control (IPRC), a control software designed to check for each single pixel if the signal is greater than the discriminator threshold (DT) and adjust the current in each pixel individually. If the individual pixel rate is between 300 kHz and 1.1 MHz, no action is taken. If it is larger, a very fast digital signal is generated with a standard duration of 1 ns (typical duration of a  $\gamma$ -ray induced Cherenkov flash). The aim of the IPRC is to target a L1T rate of 10 – 20 kHz, keeping the L3 accidental rate below 100 Hz. The rate of L0T spans from 1 MHz to about 10 MHz.

The *Level one trigger* (L1T) determines if there is temporal and spatial coincidence of the signals selected in the L0T. For the topology, it accepts only those signals where a certain number of neighbor pixels are illuminated within a compact configuration. The typical L1T rate is  $\sim$ 10 – 15 kHz.

In the case of stereo observations, a *Level three trigger* (L3T) coincidence trigger rejects the events which have been triggered only by one of the telescopes. In order to minimize the coincidence gate, reduce the number of accidental triggers and reduce the overall rate to a value manageable by the data acquisition system (DAQ), a delay (which depends on the pointing direction) has been added to the trigger [166]. The typical rate of L3T during data taking is 300 Hz (depending on the zenith angle).

An additional trigger system, the *sumtrigger* operates in parallel. It operates on the analog sum of groups of neighboring pixels, permitting to lowering the threshold of the observations down to  $\sim$ 25 GeV. A new updated version has been installed in 2013 and it is currently under test ([105], [89]).

After passing the trigger conditions, in the case of the old MAGIC-I telescope (before the upgrade), a custom made multiplexed system (MUX) [22] with *FADCs* (Fast Analog to Digital Converters) used for the digitization. The pulses were sampled at 2 GSsample/s. In the case of MAGIC-II and the upgraded MAGIC-I telescopes, the digitization and acquisition is based on an analog sampler called *Domino Ring Sampler* (DRS). At first, MAGIC-II used the version DRS2, while the upgraded system uses the DRS4, which present major updates. The sampling speed is the same.

### 3.1.6 Calibration

---

The calibration of the signal from each camera pixel is performed to translate the information recorded into light flux. It calculates the relation between the number of FADC counts from the readout system and the number of photo-electrons (phe) collected by the corresponding camera pixel. Each telescope is equipped with a light source placed at the center of the reflector. The light source is controlled by the *trigger calibration unit* (TCU), placed in the electronics room inside the CH. The light pulse periodically illuminates the camera at 355 nm. From the response of the system, a conversion factor can be estimated and applied. The calibration has several purposes: online-calibration to correct the uneven response of each channel, adjustment of the high voltage of the PMTs (performed during commissioning) and finally sending pedestal and pulse injection triggers to the readout and the camera.

### 3.1.7 Data Acquisition

---

The Data AcQuisition (DAQ) reads the data from the readout hardware, it performs the event building merging data from the different channels and checks its integrity, it also calibrates and analyzes the data samples and finally it stores the raw files in a hard disk. The author of this thesis has worked on the development and helped on the maintenance of the DAQ program since the 2011 upgrade, hence on this section I will mainly focus on readout based on DRS chips.

Due to the short duration of the Cherenkov pulses, a fast readout is needed. The pixels of each camera are sampled at a frequency of 2 GSsample/s. The readout of the MAGIC telescopes is composed by different parts: the receivers, which receive the analog pulses and eventually generates the input trigger signal, the digitization electronics, which digitizes of the Cherenkov pulses, and finally the DAQ program, which stores the final data on disk.

The layout of the new receivers boards, MONSTER (MAGIC Optical NanoSecond Trigger and Event Receiver) is divided in three parts: analog, trigger and control. The analog part converts the optical signal back to electrical and drives the pulses to the digitization electronics, the trigger part generates the first level (L0) trigger signal on the basis of a single pixel discriminator threshold, and the control part handles the board setting and the VME communication.

Connected to each receiver there is a multipurpose board used as interface denominated PULSAR (PULSer And Recorder). The mezzanines with the DRS chips are connected here. Before the upgrade, a PULSAR motherboard was equipped with four DRS2 mezzanines, each one capable to digitize 20 readout channels. The new DRS4 mezzanine handles 24 channels, for a total of 96 channels per PULSAR.

The output of the receivers goes through a HOLA<sup>7</sup> (High-speed Optical Link for Atlas) board. The HOLA is connected through a S-Link (used to connect front-end to read-out at any point of the data flow) optical link to a FILAR<sup>8</sup> card (Four Input Links for Atlas Readout). Each FILAR can manage data from up to four HOLA cards. Hence, the FILAR is the receiving end of the S-Link optical links that send the data from the digitization boards to the data acquisition PC. For the 1039-pixel cameras with the new 96-channels, 12 links are required for each telescope readout. An explicative scheme is shown on Figure 3.6.

### DAQ Program

The data acquisition software is a multi-thread C++ program based on the MAGIC-I DAQ and adapted to the new hardware features. Each of the tasks is performed in parallel thanks to its multithread structure. Two identical copies run on two dedicated servers, one per each telescope. The current DAQ program is called *Domino4Readout*, which is based on the previous version, *DominoReadout* [192].

Figure 3.7 shows a simplified scheme of the DAQ program. The initial parameters are stored in configuration files. The commands can be given either from the central control or can be introduced through console commands by the user. The

<sup>7</sup><http://hs1.web.cern.ch/hs1/s-link/devices/hola/Welcome.html>

<sup>8</sup><http://hs1.web.cern.ch/hs1/s-link/devices/filar/welcome.html>

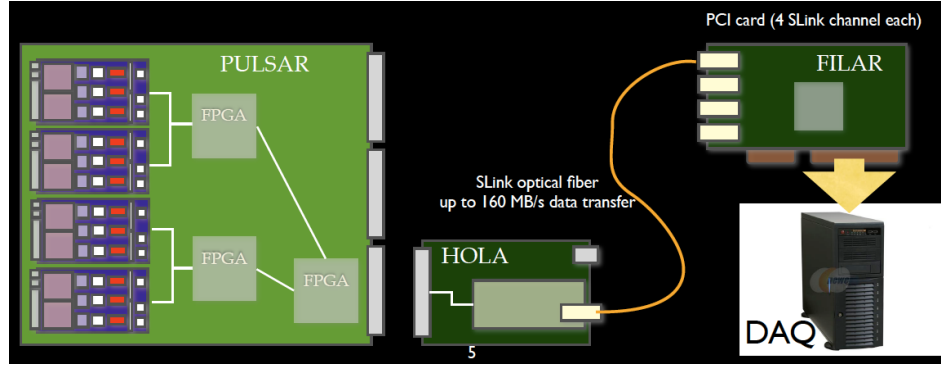


Figure 3.6: DAQ readout: Each pulsar is connected on the front part with a HOLA card. Each of these cards sends the information through a S-Link to a FILAR. A FILAR can be connected to four HOLAs. Finally the information is stored in the DAQ computer. [Credit: D.Tescaro].

program threads are controlled internally, being enabled or disabled depending on the external commands. The events are temporally stored in a memory ring buffer, thus the data can be accessible in parallel. The main threads are:

- *Reading thread*: it collects the data sample from the front-end electronics, interfacing through the FILAR board. It continuously checks if there is new data available in the share memory and, if so, it proceeds to the event building. Once the event has been completed, it is copied in a free segment of the ring buffer. In order to avoid data corruption, integrity checks are performed at this stage.
- *(Linearize)/Analysis thread*: this thread has two different purposes: perform the online pedestal subtraction and take care of the online data analysis. On the old DRS2 chip, it also *linearized* the domino chip, which is no-longer needed on DRS4. In order to calibrate the baseline of the DRS4 capacitors, a routine called *pedestal subtraction run* is used. The online time lapse correction (which is a major change from DRS2 and where the author of the thesis has participated) requires the knowledge of the time passed between two subsequent hardware readouts on cell by cell basis<sup>9</sup>. This requirement prevents the parallelization of the time-lapse correction because the time stamp of the last cell readout can not be stored on event by event basis (that would double the data size). We solve the problem using a single running-array containing the last cell readout time only, and processing the events sequentially. The parallelization is moved inside the single event i.e. four auxiliary threads, dedicated exclusively to this task, apply the correction on different chunks of the same event in parallel. A sustainable acquisition rate of 800 Hz is achieved [193]. This thread also analyzes the events, send the result to the central control, and store the relevant data-check parameters.
- *Writing thread*: it removes from the ring buffer the events which have already been analyzed and stores them in a raid disk.

### MAGIC Online Analysis (MOLA)

<sup>9</sup>The DRS chip can be viewed as an analog memory of 1024 capacitors (cells) that temporarily store the signal before its digitization.

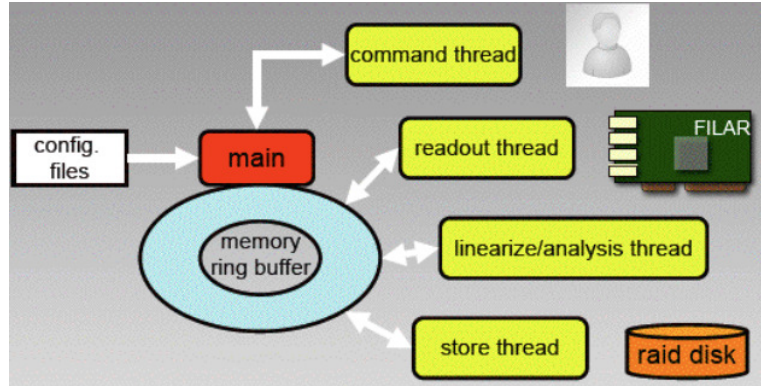


Figure 3.7: Scheme of the DAQ program. Three main threads interact with the ring buffer of the events: the readout, the analysis and the store thread. [Credit: D.Tescaro].

Since the 2011 upgrade, a multithread C++ program called MOLA (MAGIC Online Analysis) performs a real-time analysis and provides an on-the-fly esteem of the  $\gamma$ -ray fluxes of the source which is being observed by MAGIC. It runs simultaneously with the DAQ and it receives the event information computed by the DAQ software in real time [193].

In order to provide MOLA with the required information, a fourth thread, called the *Online Analysis Thread* has been developed by the author of this thesis and incorporated to the DAQ program [193]. A simple scheme is shown on Figure 3.8. Both M1 and M2 compute independently the arrival times and signal of the individual pixels. The Online Analysis thread copies the charge and arrival time information of each event calculated by the Analysis threads and creates a data string including additional key information. This information is outsourced via TCP/IP by means of ASCII *event reports* to MOLA, which is an independent program which runs in an independent computer.

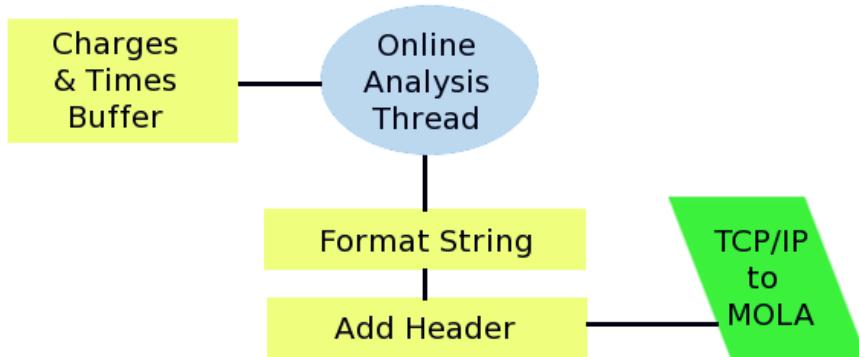


Figure 3.8: The Online Analysis threads reads the signal and arrival times of each pixel of the camera and creates a string with additional information which is send via TCP/IP to MOLA.

The report header contains relevant information like: telescope number (M1 or M2) and readout state, the date of the observation, the source name and coordinates, the data run number, the local DAQ event number, the stereo trigger event number, the event time stamp and trigger pattern. The report body contains the integrated charge (signal of each pixel) and the arrival time (with respect to the

time window). The data samples are compressed in hexadecimal format to reduce the report size. These reports are received by MOLA and stored in two independent ring buffers, one per data stream (one per telescope), optimizing the data flow with parallel streams. The advantages of this procedure are:

- Fast and real-time data processing and analysis.
- No need of storage of additional data, since once the strings are sent and used they are thrashed.
- No need to re-extract information from the raw data.

Once the reports are received, the two reading threads of MOLA interpret the information, perform the pixel calibration and image cleaning and finally calculates the Hillas parameters. A third thread, the analyzing thread, is appointed to match the events from the two received streams, to match the events by means of the unique trigger number and to perform the stereo event reconstruction. A MOLA display shows the  $\theta^2$  plots, skymaps and lighcurves for low ( $\text{Size}_{M1} = \text{Size}_{M2} > 125$  phe) and high ( $\text{Size}_{M1} = \text{Size}_{M2} > 40$  phe) energy cuts (among other information) which serves as a reference for the observers. Although the cuts used in the analysis are the most similar to the standard ones used in the complete analysis chain, it is worth remembering that MOLA is a fast analysis tool and, i.e, the background estimation is not the optimal. Hence the sensitivity is worse than in the real analysis case. The sensitivity of MOLA has been estimated to be 1.4% the Crab Nebula flux in 50 h [193].

### 3.1.8 Telescope Operation

---

MAGIC-I was operating as a stand-alone telescope until 2009, when the system was upgraded to a two-telescope stereoscopic observatory. The stereo observation mode improved the shower reconstruction and the background rejection. This has consequences on the sensitivity, angular resolution and energy reconstruction, which are also improved. Furthermore, the energy threshold of the experiment is lowered. Hence, the default operation mode in MAGIC is stereoscopic. The configuration of the L1T is set to  $\sim 10 - 15$  KHz with 3NN multiplicity. At low zenith angles, the L3T stereo trigger has a rate of  $\sim 300$  Hz. Interleaved calibration and pedestal events at 25 Hz are taken during the observations.

MAGIC has been designed to operate under moderate moonlight conditions (up to  $\sim 75\%$  full in phase). Hence, observations are cancelled two days before full moon and are resumed two days later, approximately. The moon-condition permits the inclusion of about additional 600 h of the total scheduled  $\sim 1600$  h of dark time. About  $\sim 40\%$  of this scheduled time is lost due to bad weather or technical issues. During the 2011 and 2012 upgrade, the telescope was inoperative for about 8 months.

The sources to be observed are proposed by members of the MAGIC Collaboration in a yearly call, and are accepted/rejected by the Time Allocation Committee (TAC). The observations are performed by shift crews of four people (a shift leader, a deputy shift leader and two operators), who stay in the observatory for three (in the case of the leaders) and four weeks (for operators). The shift leader is the responsible of a proper operation of the telescope. The shift-leader also takes decisions in case of failure of the instrument (although for some specific reasons the shift leader can contact experts) and who takes care of the accomplishment of

the safety rules. The deputy shift-leader is the second-in-charge, and replaces the shift leader in his absence. However, the ultimate responsibility always falls upon the shift leader. The operators are not supposed to have any experience of the operation of the telescopes, and are there to learn. The telescopes are operated via the central control (CC) program, called *SuperArehucas*<sup>10</sup> (SA). SA is the central program which receives and sends commands from/to all the subsystems of the telescopes, taking care of the correct coordination and operation among systems. For details, see [209]. A resume of the observations and the incidents encountered during operations is written in a logbook, called runbook, to keep track of the status of the system.

### Observation Modes

Although some of the observations performed in MAGIC track the source in the center of the camera, the so-called ON mode, the majority of the observations take place with the source  $0.4^\circ$  off-axis with respect to the source position. This special observation mode is called *wobble* or *false-source tracking* [82]. All of the data analyzed in this thesis was taken on this mode.

On the wobble mode, the position of the source is swapped  $90^\circ$  every 20 minutes of observation, following the pattern shown on Figure 3.9. This procedure permits to record ON and OFF data at the same time, because when the source is at one position, the opposite one (called anti-source) and eventually also the two positions at  $90^\circ$  and  $270^\circ$  respect to the source, can be used as OFF data. The advantages of using the wobble mode are both the saving observation time and that the OFF used for the background estimation is recorded in the same conditions.

#### 3.1.9 Monte-Carlo

The response of MAGIC is calibrated through MC simulations [137]. It includes the simulation of atmospheric showers of different energies and incoming directions; the absorption and scattering that the photons suffer on their travel and their reflection on the mirrors. Finally, the camera response, the trigger and data acquisition are simulated. The MC samples have to resemble real data, hence a continuous production is necessary, to keep the simulations updated with the PSF variability, the decrease of the reflectivity of the mirrors, etc. Mainly, the MC is update when the system undergoes an upgrade.

## 3.2 Data Analysis

The final goal of the data analysis is to extract the information of the incoming photons and measure the  $\gamma$ -ray flux. The principal aims are:

- Locate the position and shape (in the case of an extended source) of the  $\gamma$ -ray emission in the sky, through a *skymap*.

<sup>10</sup>SuperArehucas is an improved version of the former CC, called Arehucas. The general belief among the Collaboration is that Arehucas received its name after a famous rum of the Canary Islands, produced in the city of Arucas (Gran Canaria), formerly named Arehucas. However, the developer of the software claims is it just a tribute to this ancient *guanche* settlement.

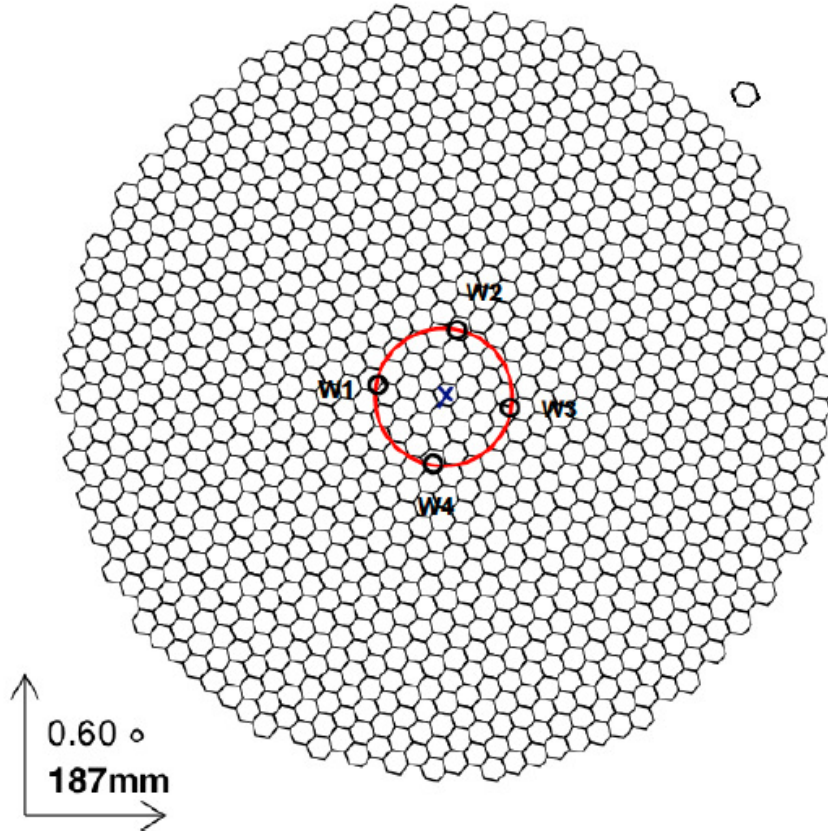


Figure 3.9: Wobble observation pattern, with the different wobble positions W1, W2, W3 and W4. When the source is on W1, the anti-source is W3.

- Extract the *spectral energy distribution* (SED) of the TeV emission.
- Study the temporal dependence of the source, by creating a *lightcurve*.

The standard code for the MAGIC data analysis is called MARS, which stands for *MAGIC Analysis and Reconstruction Software* [156], which is written in C++ language and that operates in a ROOT<sup>11</sup> framework, which is a program and library developed at CERN.

On this Section both the analysis for mono and stereo configurations will be introduced, as the data analyzed in this thesis has been taken under both configurations. In general, the main steps to follow are:

- Signal extraction: reconstruction and calibration of the size and arrival times of the Cherenkov pulses contained in the raw data.
- Event reconstruction: by performing the image cleaning and parametrization.
- Signal and background discrimination and energy estimation: by training of an algorithm to perform  $\gamma$ /hadron separation with the use of a sub-sample of Monte-Carlo (MC)  $\gamma$ -ray events and background (hadrons) events from a sub-sample of data.
- Signal evaluation: finally, the significance of the putative  $\gamma$ -ray detection, the lightcurve, the skymap and the energy spectrum are derived.

<sup>11</sup>[root.cern.ch](http://root.cern.ch)

### 3.2.1 Low-level Analysis

---

The steps defined in this section are the most low-level treatment of the raw data to extract basic information. These procedures are not normally performed by the users, who normally start the analysis at an advanced stage of the data processing. An analyzer will only need to perform these steps in case that special requirements are needed.

#### Signal extraction and calibration

This step consist in extracting, from the raw data files, the arrival time and intensity of the signal and transform it to physical units (calibration). Depending on the readout system, the number of samples per pixel varies from 50 for the MUX to 80 for DRS2. This procedure is performed by the *Callisto* executable on the MARS package in the case of mono observations. Later, in order to more easily calibrate DRS data, a new program named *Sorcerer* (which is a faster and less CPU demanding version of Callisto) was developed. This newer package is the default option for DRS4 stereo data. On first place, the pedestal level should be subtracted and then corrections for non-linearities in both the amplitude and timing of individual pixels shall be performed. These corrections depend on the last capacitor read in the domino ring. Dedicated pedestal and linearity (this only in the case of DRS2) runs are needed to calibrate. During data-taking, calibration runs, pedestal runs and interleaved events are taken to correct for these non-uniformities. The reconstructed signal should be directly proportional to the number of phe. This linearity is important in order to reconstruct the shower energy and, thus, the energy spectra. Then, the pulse, is extracted from the pedestal subtracted samples by different algorithms depending on the readout. The arrival time is defined as the position of the rising edge of the pulse at 50% of the peak value.

After performing a cross-calibration over the pixels, an absolute calibration to convert the signal amplitude from FADC to phe is performed. Due to the low gain of the MAGIC PMTs, there is no single-photoelectron resolution, hence the conversion is performed by applying the *F-Factor* method [154] over the calibration data events. The main assumption is that the number of phe generated during a calibration run follows a Poisson distribution with mean  $N$  and a mean square  $\sqrt{N}$ . The mean measured charge, after pedestal subtraction is  $\langle Q \rangle$  and  $\sigma$  its intrinsic standard deviation. The F-Factor can be defined as:

$$F = \frac{\sigma\sqrt{N}}{\langle Q \rangle} \quad (3.1)$$

and it takes into account the broadening of the distribution due to the multiplication process inside the dynodes. The *conversion factor*,  $C$ , from FADC counts to phe is defined as:

$$C = \frac{N}{\langle Q \rangle} = \frac{F^2 \langle Q \rangle}{\sigma^2} \quad (3.2)$$

Because of the variability in the response of the VCSELs (due to temperature changes, for example), the conversion factor might vary during data taking, hence

they are updated thanks to interleaved calibration events [90].

### Event reconstruction

At this stage, the data contains the extracted signal and the arrival times for each pixel of the camera. The next step is to determine which pixels should be considered part of the recorded shower image, by including pixels with the shower information and reject those that correspond to NSB fluctuations. Pixels that do not contain a shower signal must be removed in order to allow a proper determination of the shower parameters associated with the event. The procedure to follow for that purpose is to extract the shower information for each individual telescope image, by performing an *image cleaning* and perform the parametrization of the shower image. This procedure is performed by the *Star* executable, which convert the images from raw calibrated files to *star* files.

#### *Image cleaning*

The image cleaning algorithm uses two loops with two different signal threshold values, defined in terms of phe. On the first loop, the *core* pixels, defined as clusters of at least two contiguous pixels above the considered threshold) are selected. On the second loop, a second threshold will select the *boundary* pixels, which are the neighbor pixels with a signal above the secondary lower threshold [35]. A scheme is shown on Figure 3.10.

Also, a timing coincidence window between the mean arrival time and the individual pixel arrival time is used to reject NSB signals, by defining the *time gradient* (which measures the magnitude of the time profile of the event) and the *time RMS* (which measures the time spread).

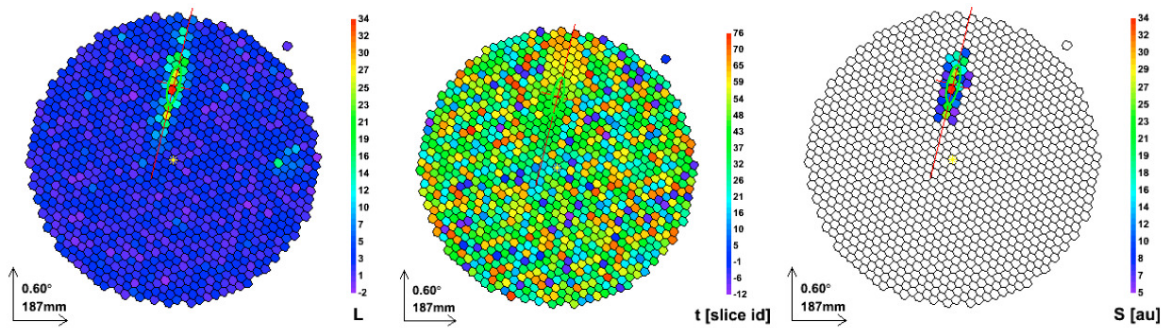


Figure 3.10: Image cleaning procedure. *Left:* Reconstructed shower charges[phe]. *Center:* Arrival times [FADC counts]. *Right:* Cleaned image.

The default threshold values for the MUX-FADC readout where 10 phe for the core pixels and 5 phe for the boundary pixels. The default values for the epoch of DRS2 data is 6-3 (core-boundary) for M1 and 9-4.5 for M2. For the new M1 camera, the default cleaning is 6-3.5.

Another image cleaning method called the *sum-cleaning* has been found to be more efficient at energies < 100 GeV [209]. The core pixels are selected if the clipped sum of and xNN group ( $x = 2, 3, 4$ ) is above a certain threshold and if its arrival time is inside a certain time window.

Relaxing the cleaning levels by lowering the charge thresholds results in a lowering of the thresholds of the  $\gamma$ -ray shower. However, it increases the probability of including in the clean image a pixel due to noise, worsening the image parameters and causing the loss of signal. This effect is more important at low  $\gamma$ -ray energies.

### *Image parametrization*

The next step, is the calculation of the image parameters defined on Subsection 1.2.4. By defining these parameters, the single pixel information is dropped and only the image parameters values are kept, reducing the size of the data files. For that purpose, the Hillas parameters [112] and some other useful parameters described in Subsection 1.2.4 are used.

**The *disp* method:** The *disp* parameter [82] is defined as the distance from the image CoG the source location along the major axis, calculated from the ratio between the Width and Length parameters:

$$DISP = a + b \frac{Width}{Length} \quad (3.3)$$

to estimate *dips*, a multi-dimensional classification algorithm such as the Random Forest (see next Subsection 3.2.3) is used. The disp method is valid both in mono and stereoscopic observation modes, see Figure 3.11. For monoscopic configuration, the shower impact reconstructions has two possible degenerate solutions. In the case of stereo shower reconstructions, it has proven to be an improvement from the simple *crossing* method [32] and the degeneration is removed. The pairs of solutions (one per telescope) with the smallest squared angular separation is chosen. Applying this method, the angular resolution gets to  $0.07^\circ$  at 300 GeV, improving at higher energies. The disp and the time gradient parameters are correlated for point-like sources. This correlations is not found in the case of hadronic images [35].

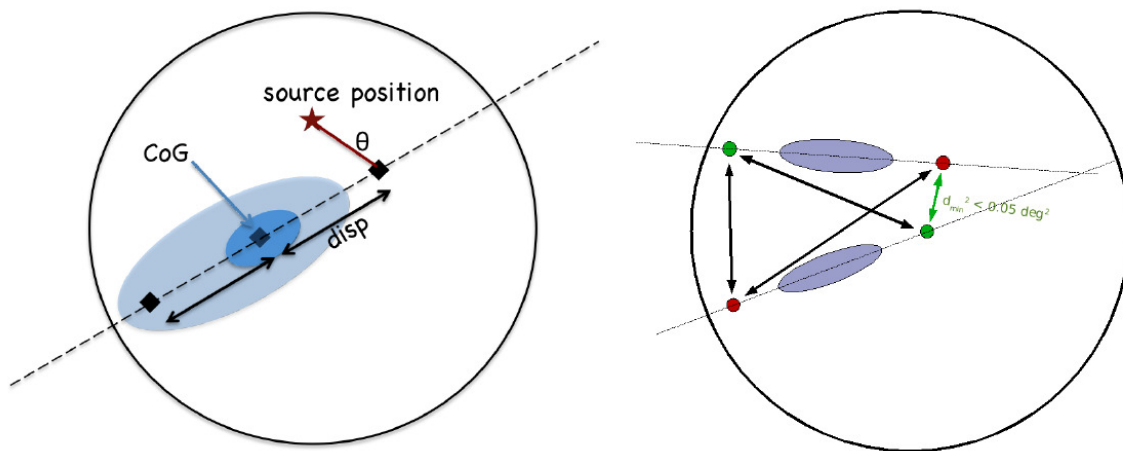


Figure 3.11: Disp parameter *Left*: monoscopic observations [Credit: R. Zanin]. *Right*: Stereoscopic shower reconstruction [Credit: S. Klepser].

### 3.2.2 Intermediate-level Analysis

---

Normally, the user starts the analysis of the MAGIC data from *star* files, which contain low-size, Hillas-parametrized information.

At this stage, and before advancing in the data processing, good-quality data has to be selected. Telescopes do not operate usually under perfect weather conditions, hence the atmosphere acquires an important role in the quality of the recorded data. Observations performed under clouds or calima (Saharan sand transported to the Canary Islands, mainly on summer, which remains in the atmosphere for several days per year) have to be manually rejected. Corrections are possible by using, for example, the LIDAR technique introduced on Chapter 2. However, and despite that MAGIC has an elastic LIDAR (which is in regular operation since 2013), this correction has not been introduced in the MAGIC analysis chain.

The trigger rate (for mono observations) or the L3T rate (for stereo observations) are good indicators of the data quality, since it is supposed to remain constant during the observation. A drop in the rate indicates a worsening of the weather conditions (i.e., a passing cloud), while an increase is usually associated to an increase in the accidental rate due to higher background light level (due to stars, moonlight). However, there is a zenithal dependence (ZA), described as  $\text{Rate} \sim \sqrt{\cos(ZA)}^{0.35}$ . A cut on this rate is normally enough to discard problematic data, considering that good quality data is  $\pm 15 - 20\%$  of the average rate.

Once the bad quality data has been removed from our samples, the final processing takes place. In the case of stereo analysis, first the *Star* files are merged into a single file where the parameters of both telescopes are stored, by using the *Superstar* executable. The individual image parameters are saved in a stereo file and the stereoscopic reconstruction of the shower parameters is performed.

## Signal/background discrimination and energy estimation

The recorded data does not only have  $\gamma$ -ray origins, but also contains hadronic showers, muons and fluctuations of the NSB. The proportion of  $\gamma$ -ray events is  $\sim 0.001\%$ , depending on the signal and the settings. Hence, a proper rejection of the background by performing an discrimination between photons and hadrons is needed.

The background rejection procedure is called  $\gamma/\text{hadron separation}$ , which is performed via an algorithm called Random Forest [45]. This classification method consist in the creation of a large number of decision trees, where the initial data sample is splitted according to a specific cut in a random variable. This is an iterating process which divides the data into subsequent subsamples, increasing the number of branches. The training is performed with samples of known nature, of  $\gamma$ -ray origin from MC simulations and hadronic origin (*hadronness*) from a real data sample. The method stops when a leaf of the tree is reached and labeled with a 0 or 1. A hadronness equal to the mean over 100 trees is associated to each event. 0 corresponds to a  $\gamma$ -event, 1 indicates a hadronic nature. This method is applied both in mono and stereoscopic observations, although the executables which perform the discrimination are different: *Osteria* in the case of mono observations and *Coach* for stereo, which is a simplified version of *Osteria*. The training is performed in these two executables.

The RF algorithm and the Hillas parameter are also used to estimate the energy of the  $\gamma$ -ray candidate events in the case of monoscopic data. The procedure is similar, but in this occasion the optimal cut in each node of the trees is chosen to minimize the variance of the true energies of the events, instead of their purity. The reached energy resolution is  $\sim 25\%$  between 100 GeV and 1 TeV. It improves slightly at higher energies but it worsens for lower energies. The energy estimation for low and high energies is significantly biased. For lower and higher energies the bias provokes an overestimation of the value. In the case of stereoscopic data, *look-up tables* (LUTs) are used. The estimated energy  $E_{est}$  of each event is the weighted average over both telescopes of the mean  $E_{true}$  value of the LUT bin to which the event corresponds. The energy resolution is 15% between 200 GeV and 1 TeV.

Finally, through the use of the *Melibea* executable, the *Superstar* files are processed with the output of *Osteria* or *Coach*, and the energy and hadronness are assigned. The output files are fully analyzed event files with assigned hadronness and energy.

### 3.2.3 High-level Analysis

---

The ultimate step is to evaluate, once the *Melibea* files have been produced, the signal significance and perform a spectral evaluation.

#### Evaluation of the $\gamma$ -ray excess

The signal is selected geometrically from the  $\alpha$  or  $\theta^2$  distributions (see Subsection 1.2.4 for more details), in the case of mono or stereoscopic observations respectively. The signal is determined by an upper cut in  $\alpha$  or  $\theta^2$  because  $\gamma$  rays from the observed source will be reconstructed with small  $\alpha$  or  $\theta^2$ , whereas the background will produce a featureless almost-flat distribution (see Subsection 1.2.4 for further details). The number of  $\gamma$  rays is defined as the number of excess events remaining after the subtraction of the  $\alpha$  or  $\theta^2$  distribution cuts of the ON ( $N_{on}$ ) and OFF ( $N_{off}$ ) samples,  $N_{ex} = N_{on} - N_{off}$ . The OFF is one or more false-source positions, as wobble data is being used. The significance of the signal,  $\sigma$ , is defined by the formula defined by Li&Ma [125]:

$$\sigma = \sqrt{2 \left[ N_{on} \ln \left( \frac{1 + F_{norm}}{F_{norm}} \right) \left[ \frac{N_{on}}{N_{on} + N_{off}} \right] + N_{off} \ln(1 + F_{norm}) \left[ \frac{N_{on}}{N_{on} + N_{off}} \right] \right]} \quad (3.4)$$

where  $F_{norm}$  is the on/off normalization parameter.

The cuts in  $\alpha$  and  $\theta^2$  are usually optimized with a Crab Nebula sample and MC. The optimization searches the best values of hadronness and Size for the data sample. This procedure is used in the case of a source discovery or under special conditions, as strong moon. *Standard* cuts for low energy (hadronness < 0.28, Size > 60), high energy (hadronness < 0.1, Size > 400) and full range (hadronness < 0.16, Size > 300) have been established.

The executable which performs the  $\theta^2$  plot in the case of stereo analysis for discovery of new sources is called *Odie*. In the case of mono, there is no dedicated executable.

### Sky map

A skymap of the region, which is another significance plot, is obtained to study the position and spatial distribution of the  $\gamma$ -ray excess. It is calculated by transforming the reconstructed arrival directions of all events into sky coordinates. The optimized cuts used in the  $\alpha$  or  $\theta^2$  analysis can be applied. An example is shown on Figure 3.12.

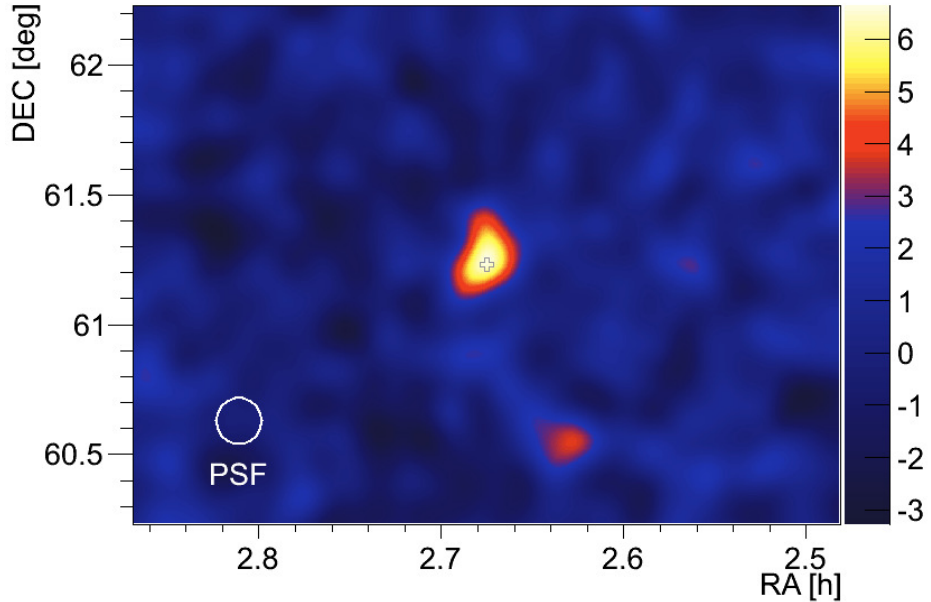


Figure 3.12: Skymap of LS I +61°303.

### Spectrum

The differential  $\gamma$ -ray energy spectrum of a source is defined by:

$$\frac{dF}{dE} = \frac{dN_\gamma(E)}{dt_{eff} dA_{eff}(E) dE} \quad (3.5)$$

where  $N_\gamma$  is the number of detected  $\gamma$  rays, computed as the number of excess  $N_{ex} = N_{on} - N_{off}$ .  $A_{eff}$  is the effective collection area (see Figure 3.13), which is calculated from MC-simulated  $\gamma$ -ray events and represents the area in which air showers can be observed by the telescope folded with the efficiency of the cuts applied in the analysis. The  $A_{eff}$  marks the threshold of the analysis, which is given by  $dt_{eff}$  is the effective observation time, which is the difference between the observed time and the dead time.

Loose background cuts are applied in order to calculate the spectrum. This improves the matching between data and MC, which is important for the effective area collection. Hence, the cuts applied in this case are different from the cuts used in the determination of the significance of the signal, which are more tighter.

The executables which perform the spectral energy distribution calculation are *Fluxlc* for mono and *Flute* for stereo. An example of differential energy spectrum is shown on Figure 3.14, obtained with *Fluxlc*. These executables also calculate

the lightcurve, which is the integrated flux in terms of time.

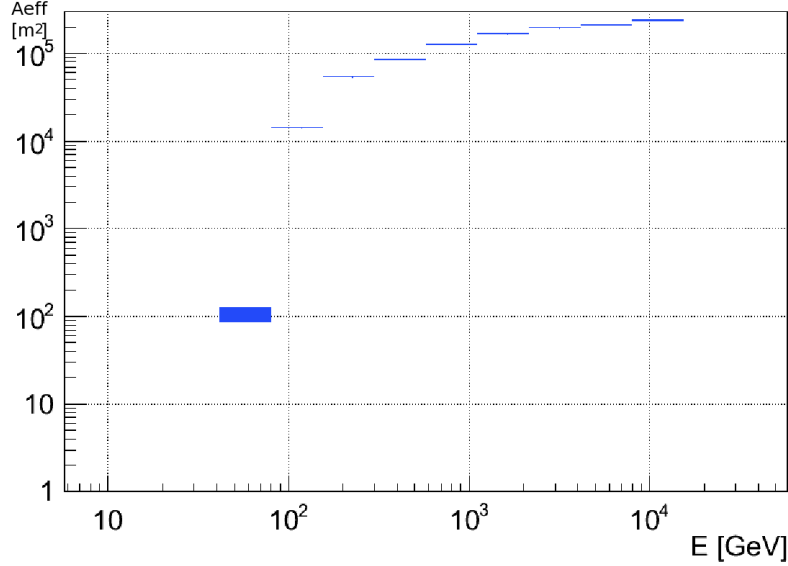


Figure 3.13: Effective area as a function of the reconstructed energy, obtained with *Flute*.

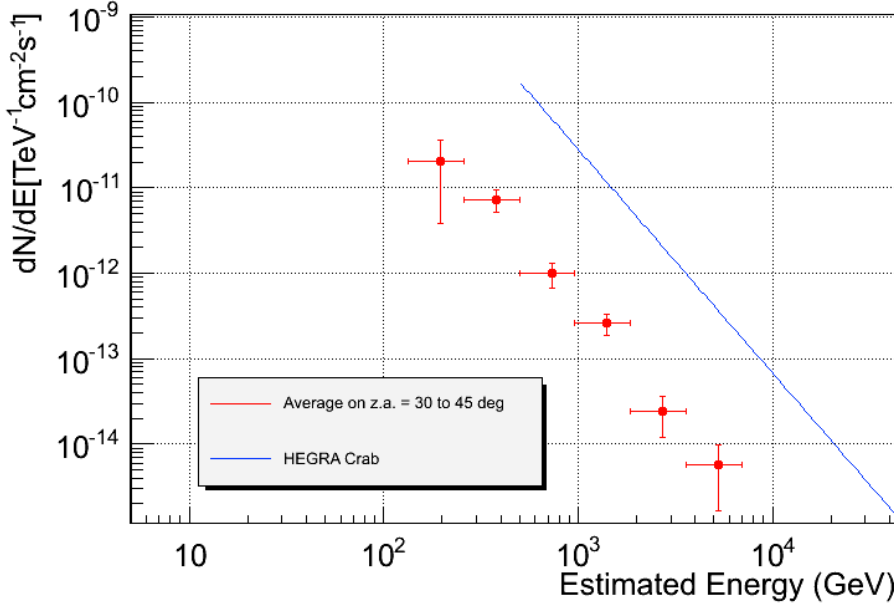


Figure 3.14: Differential Energy Spectrum of LS I +61°303 obtained with *Fluxlc*.

### Unfolding

The aim of the *Unfolding* [20] is to recover the original SED from the measured spectrum by using a resolution function which is determined from MC simulations. It transforms the distribution of an observable, in this case the estimated energy ( $E_{est}$ ), into the true distribution of a physical quantity, in this case the true energy ( $E_{true}$ ). The image parameters and the  $E_{est}$  are affected by the resolution of the

telescopes, biases and threshold effects. Mathematically, it can be written as:

$$Y(y) = \int M(x, y)S(x)dx + n(x) dx \quad (3.6)$$

where  $Y$  and  $S$  are the measured and true distribution, respectively,  $y$  is the estimated energy,  $x$  is the true energy,  $M$  is the migration matrix and  $n$  is noise. The aim of the Unfolding is to invert the migration matrix and retrieve from the estimated energy the true energy of the emitted  $\gamma$  rays. However, Unfolding is numerically very complex and the data has correlated errors, hence the method can be ambiguous if not applied rigorously. The Unfolding is performed by the CombUnfold.C ROOT macro, which is implemented in MARS. The unfolding methods are Forward, Bertero, Schmelling and Tikhonov. The Forward unfolding method performs a forward folding with few parameters assuming a power-law. This method is not sensitive to distinct features. This method is only applied as a useful check of the unfolding results as it is robust and no regularization strength has to be adjusted. These algorithms shall yield to similar results. An example is shown on Figure 3.15

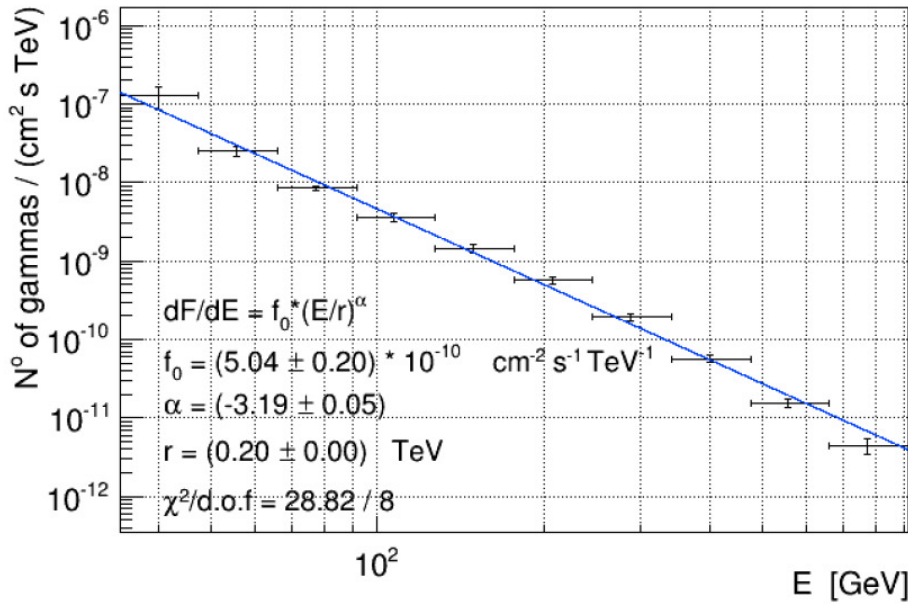


Figure 3.15: Unfolded spectra of RGB 0521+212, obtained with the Tikhonov algorithm. [Credit: G. Gumiero] [101].

### 3.3 Moonlight Observations

MAGIC has been designed to operate under moderate moonlight (up to moon phase  $\sim 75\%$ ), extending the duty cycle by  $\sim 60\%$ . Under twilight and moonlight conditions, the level of NSB is increased. This causes an increase in the fluctuations of the signal for each pixel, spoiling the precision in the estimation on the Hillas parameters for the shower reconstruction and lowering the acceptance [32]. Also, secondary islands may appear. The shower image might also be slightly distorted. The probability of accidental triggers is enlarged and also the anode

direct current (DC). The DC is in first order proportional to the phe rate and, hence, to the photon rate [134]. Since the increase of the NSB is visible as a rising of the photon rate, it can be measured through the DC [51]. The trigger discriminator threshold (DT) is set to ensure that the total rate is kept below the maximum allowed value and to reduce accidental rates. The differences in the events rates are due to the increase of the DT in order to keep a low number of accidental rates caused by the moonlight.

### 3.3.1 Cycle VI dedicated analysis

In the case of *Cycle VI*, all the observations were performed under twilight and moderate-to-strong moonlight conditions, what affected the quality of the data recorded. Also, the performance of the telescopes is modified with respect dark conditions due to the increase of the DC and DT. To avoid the incorporation of quality data affected by strong moonlight in the analysis, a study of dependence of the rate in terms of the DC and the DT is performed in this thesis, in order to correct for anomalous behaviors and reject the data that does not fit minimum quality requirements. These tests are performed over a Crab Nebula sample and, once checked that the results (integrated flux) are the expected, the same procedure is applied to LS I +61°303.

#### Data pre-selection

First, the correlation between DC and DT has been studied. In MAGIC it has been studied that there is a linear correlation between DT and  $\sqrt{DC}$ , since it is expected that the DT scales with the RMS which depends on the anode current as  $\sqrt{DC}$ . However, this correlation should be taken as an approximation, and shall not be followed as an universal rule. As a first quality check, this correlation has been checked and then the data points which are not following the general behavior have been eliminated (see Figure 3.16). With this procedure, the data that is not following the general trend has been removed from the analysis. The behavior of this data can be explained, for example, as a incorrect settings of the IPRC.

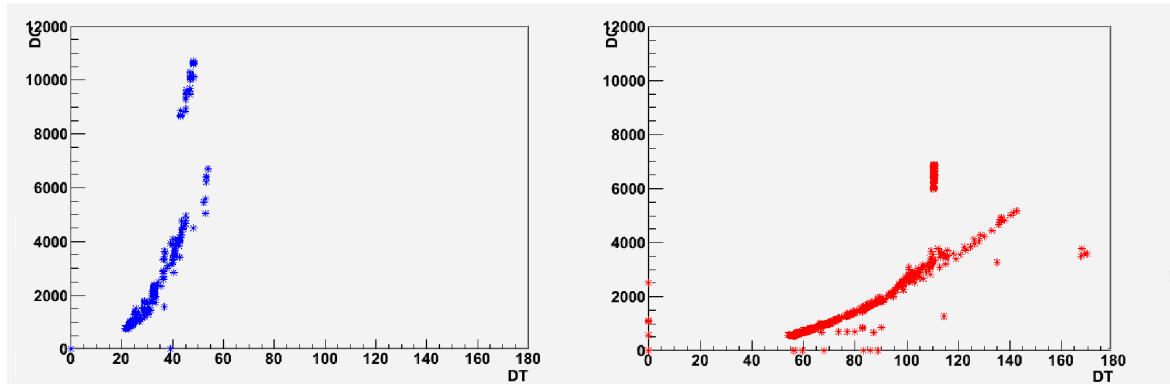


Figure 3.16: Dependence of the anode direct current, DC [mA], and the discriminator threshold, DT [arbitrary units] for MAGIC-I (left) and MAGIC-II (right) telescopes.

Once the first pre-selection check is done, we study the dependence of the rate with

the DT (See Figure 3.17), as they are used to stabilize the rates and diminish the accidentals probability. The rate decrease with increasing DT. The data which fulfills this behavior is corrected by fitting to a first order polynomial and performing a normalization of the rate in terms of it. The same condition can be applied to the DC, as DT and DC are correlated.

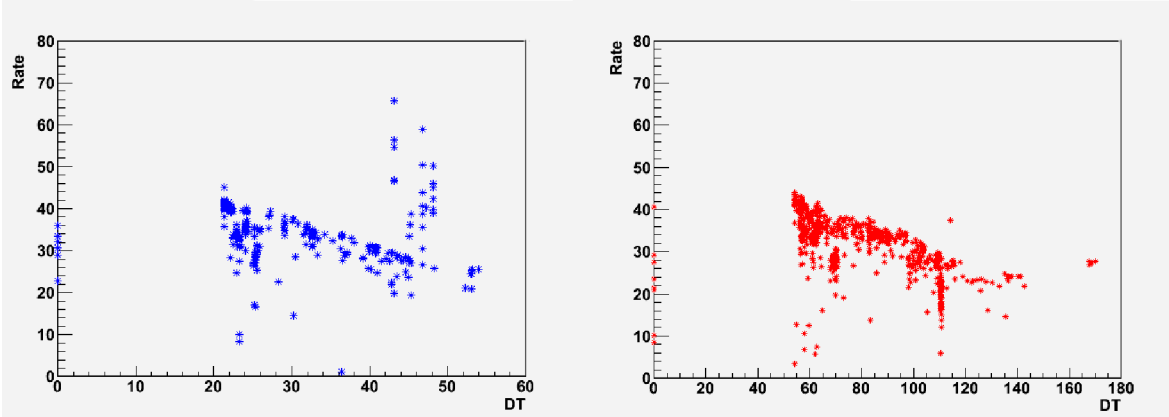


Figure 3.17: Rate [Hz] against DT [a.u. for MAGIC-I (left) and MAGIC-II (right) telescopes]. The  $\gamma$ -ray rate shall be linearly correlated with the DT, hence the data which does not fit this condition is rejected.

Finally, it can be checked how the pre-selection method has eliminated a considerable amount of data which does not follow the expected behavior in terms of the zenith angle (Figure 3.18). Most of this data points would not have survived the standard quality checks in terms of the zenith angle dependence. However, performing a close visual inspection, some other points lying inside the goodness of the selection have also been removed. In the inverse procedure would have been inverse, the selection would not have been so accurate, since some data would not had been removed.

### Data Selection

Once the pre-selection of data is over, the standard data quality selection is performed. The standard procedure has been followed, from here on, to analyze data of *Cycle VI* (see Section 5.3.1 for an extended review). The total remaining effective time for LS I +61°303 is 26.06 hours (out of 40 h). In this case, where there is strong moonlight conditions, it is normal to have low rates ( $\sim 35$  Hz, compared to  $\sim 100$  Hz). By 2010-2011, it was normal to have slightly higher rates in MAGIC-II telescope (Figure 3.19).

The moonlight condition increases the threshold of the telescopes. It has been proven that the increase of the DT (and usually due to the DC) produces also an increase of the energy threshold of the telescope [134]. The final check it is to study if there is any dependence on the integral flux with the DC. In principle, it is expected to detect a reduction in the  $\gamma$ -ray flux for increasing values of the DC. I have calculated what the flux dependence for a certain energy is in terms of the DC for the Crab Nebula sample treated before, as seen in Figure 3.20. The values of the integral flux remain constant, for each energy, until a certain value of DC. Then, the flux diminishes. Hence, if data with high values of DC want to be included in the analysis, the analysis threshold has to be increased. In general, for the LS I +61°303 analysis, we will compute the lightcurve above 300 GeV, in

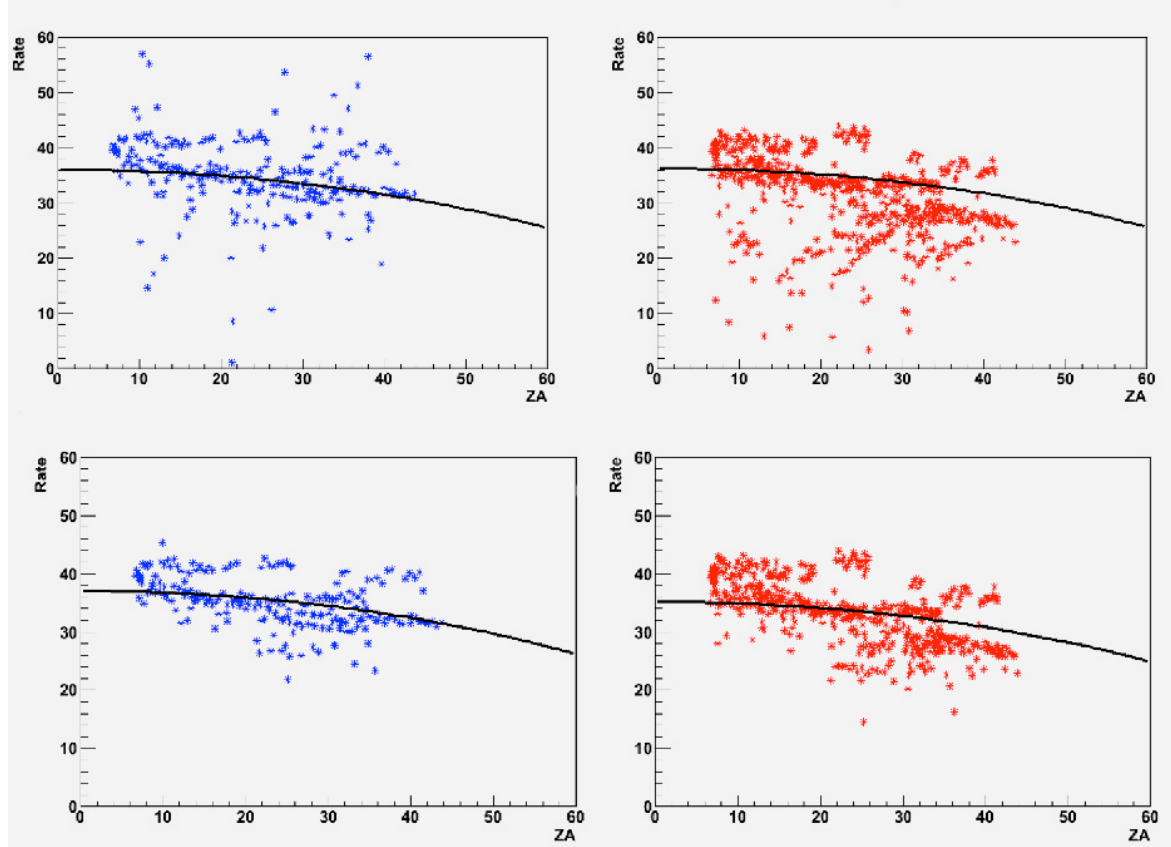


Figure 3.18: Plot of the rate, previously corrected by the DT, in terms of the zenith angle. In blue, MAGIC-I data points. In red, MAGIC-II. *Top:* the whole data set before the pre-selection is done. *Bottom:* the data which survived the pre-selection cuts.

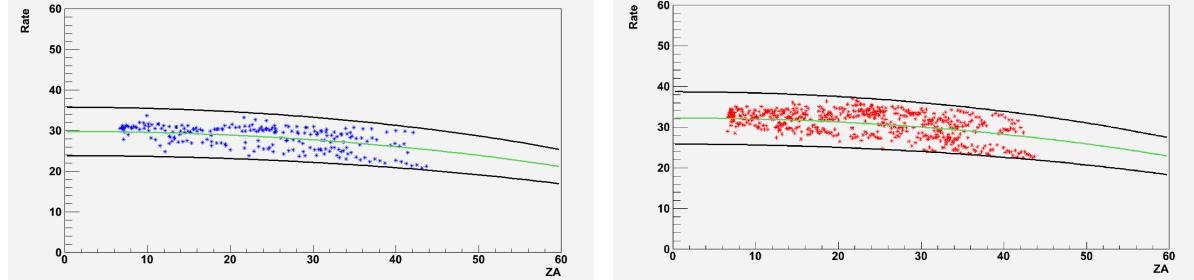


Figure 3.19: Plot of the rate [Hz], previously corrected by the DT, in terms of the zenith angle [deg] for the contemporaneous Crab Nebula data on *Cycle VI*. The plotted data survived both the pre-selection and selection quality cuts. *Left:* MAGIC-I rate. *Right:* MAGIC-II rate, slightly higher than MAGIC-I rate.

order to be consistent with previous analysis and be able to compare the results. Hence, in this specific case, that means we can include in the final analysis to compute the spectrum and the lightcurve, only the data with  $DC < 3000$  mA. Following this procedure, about 5 h of data were discarded. This data could be recovered by using dedicated MC with higher NSB and applying stronger cuts in the image cleaning. However, for the purpose of this study, the impact of including these few hours would not have worthed it.

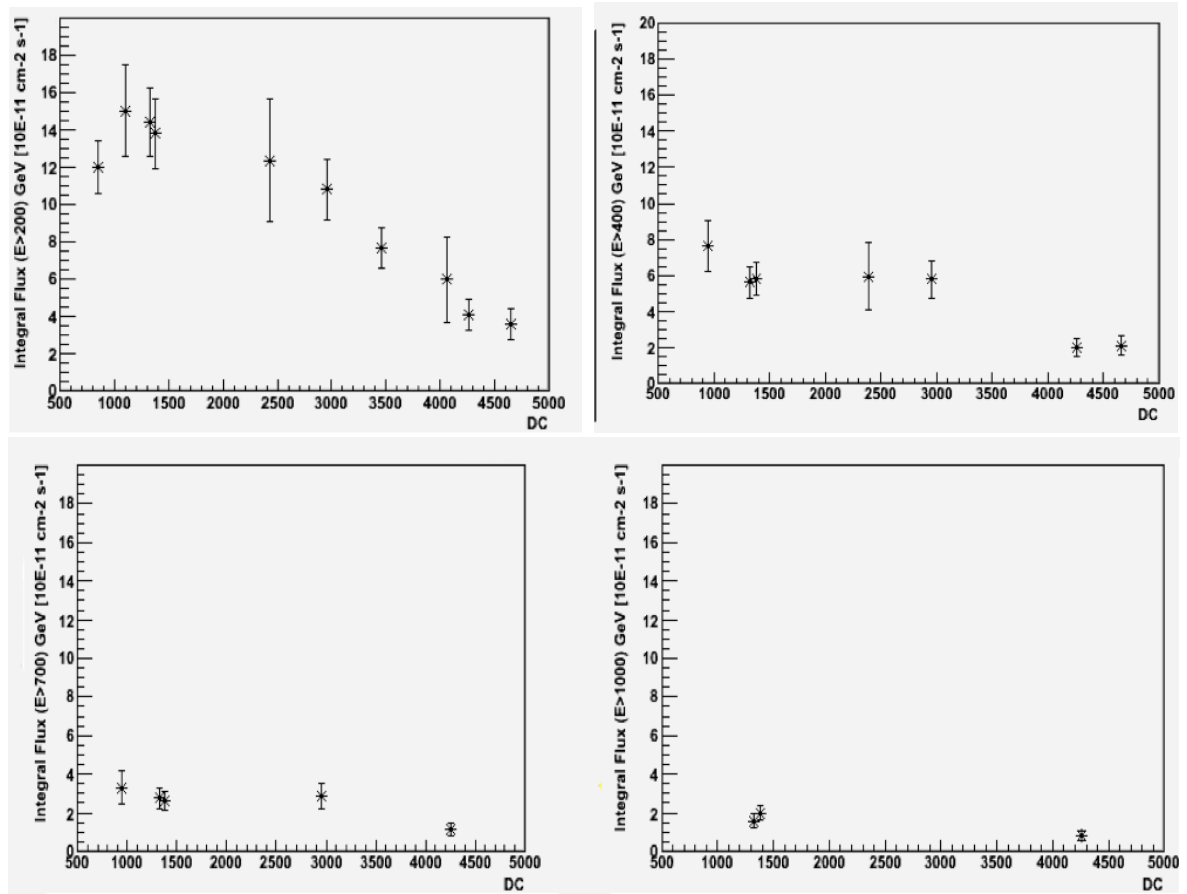


Figure 3.20: The computed integral flux decreases with increasing values of DC [mA]. Here, the flux for Crab Nebula for different energies (200, 400, 700 GeV and 1 TeV) is plotted. For a certain energy, the flux remains approximately constant until a certain value of DC, then it decreases.



# 4

## Compact Binary Systems

*M*ost of the stars in the Milky Way are not stand-alone systems, but form pairs or multi-star systems. These multi-star systems are usually identified and resolved in optical. Only some binary systems, composed by a massive star and a compact object, can be detected at X-rays and even  $\gamma$ -ray energies. In this Chapter, we introduce the X-ray and  $\gamma$ -ray binary families and review its most important characteristics.

### 4.1 Introduction to Binary Systems

---

Binary systems are those composed by two bodies orbiting each other. In this thesis, we will focus in those systems formed by a star and compact object. These systems are called *compact binaries*. In these binaries, the dense compact object orbits the companion star.

Before diving more deeply into the different types of compact binaries, it is useful to introduce some relevant definitions:

- Periastron: is the point in the orbit in which the distance between the compact object (or celestial body, in a more general definition) and the star is minimum.
- Apastron: is the point in the orbit in which the distance between the compact object (or celestial body, in a more general definition) and the star is maximum.
- Inferior conjunction (INFC): is the point in the orbit in which the compact object (celestial body) is in front of the star which is orbiting, over the line of sight of an external observer located on Earth.
- Superior conjunction (SUPC): is the point in the orbit in which the compact object (celestial body) is in behind of the star which is orbiting, over the line of sight of an external observer located on Earth.
- Compact object: celestial body of very high density and mass, remnant of stellar evolution. Depending on the mass of the initial star which evolves and dies, it can either be a black hole, BH, (when  $M \geq 10\text{--}25 M_{\odot}$ ) or a neutron star, NS, (when  $M \leq 10 M_{\odot}$ ).

- Companion star: in a binary system composed of a compact object and a star, it refers to the optical star which losses mass into the compact object. We can also refer to it as the mass-donor star.

Figure 4.1 shows a general scheme of these orbital definitions.

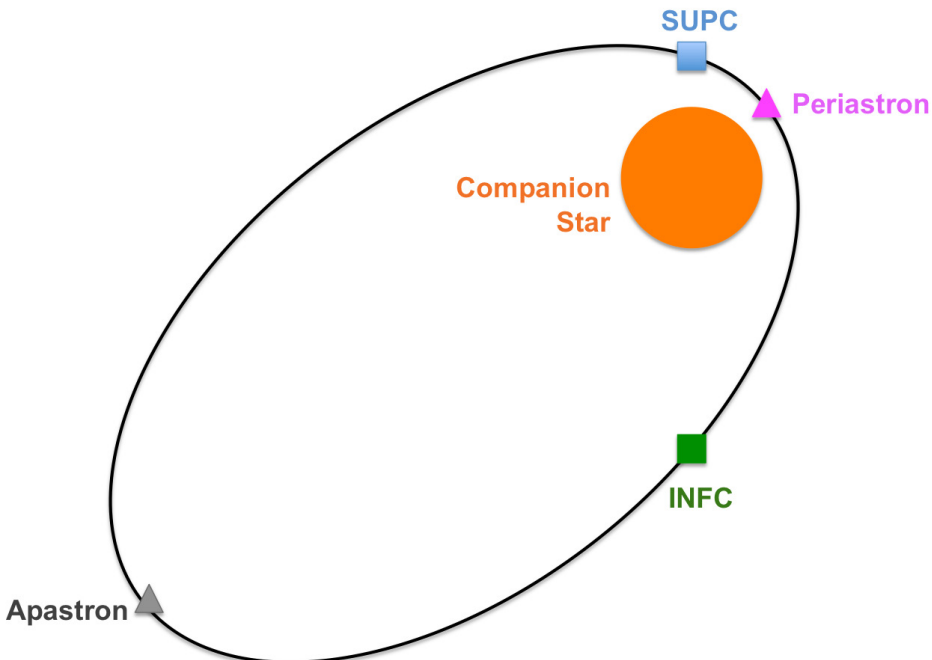


Figure 4.1: General orbital scheme of a binary system, used to show the most relevant definitions for a binary system. The orange circle is the stellar object. The orbit of the compact object is represented by a black line. The green square marks the INFC, while the blue square marks the SUPC passage. The periastron is indicated by a magenta triangle, while the apastron is labeled as a grey triangle.

## 4.2 X-Ray Binaries

X-ray binaries (XRBs) are systems composed by a star which losses mass into a compact object, which can either be a neutron star (NS) or a stellar-mass black hole. As their names indicate, these systems are X-ray sources, showing typical fluxes of  $10^{34} - 10^{38}$  erg  $cm^{-2}s^{-1}$ . The nature and properties of the compact object are mainly determined from X-ray observations. Longer wavelength observations allow detailed studies of the mass-donor star [58].

XRBs are divided into two different subclasses, depending on the mass of the donor star. Thus, they can be classified into *High-Mass X-Ray Binaries (HMXRBs)*, in the case that the mass of the companion star is  $M_\star \geq 10 M_\odot$  and *Low-Mass X-Ray Binaries (LMXRBs)*, when the donor star has a mass of  $M_\star \leq 1 M_\odot$ . Besides, this division also comes from the two different mass-transfer processes: stellar wind in the case of HMXRBs and Roche-Lobe overflow in LMXRBs. The spatial distribution of these systems in the Galaxy is represented on Figure 4.2.

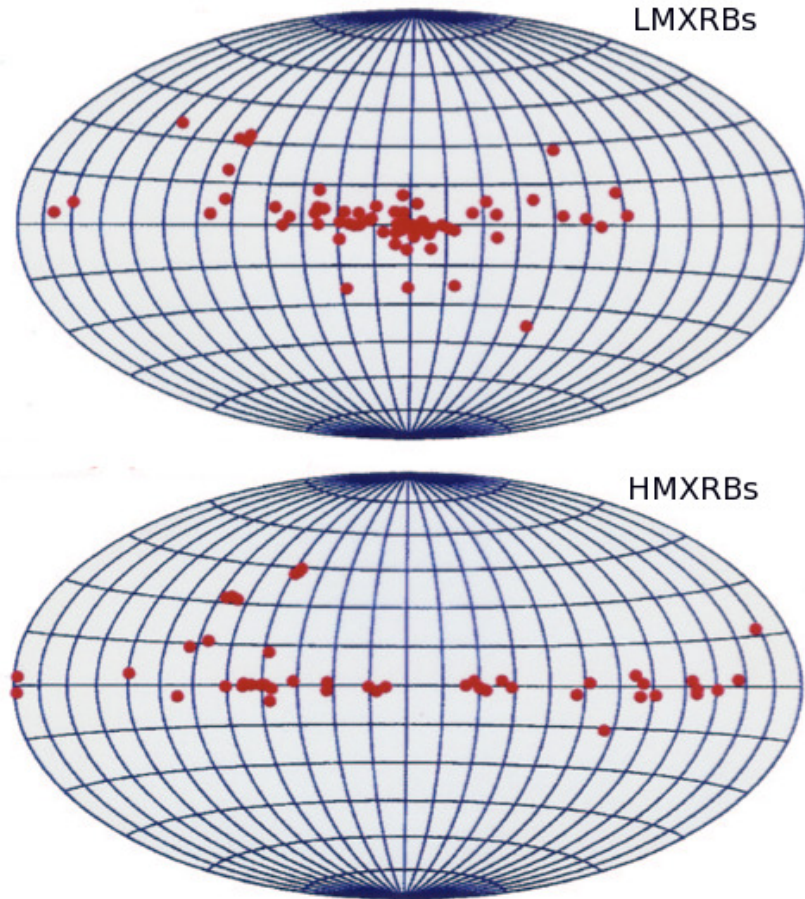


Figure 4.2: Spatial distribution of LMXRBs (top) and HMXRBs (bottom) in the Milky Way. [Credit: P. Podsiadlowski].

#### 4.2.1 High Mass X-Ray Binaries

HMXRBs are born from a supernova (SN) explosion of a massive star in a two-star system. The massive star evolves until it becomes a red giant and fills the Roche Lobe. The companion star stars to accrete material from it. The red giant losses mass until it can no longer hold the nuclear fusion. This leads the red giant to explode and provides the compact object of the X-ray binary, which can be either a NS (in the case that  $M_\star \leq 10 M_\odot$ ) or a BH ( $M_\star \geq 10\text{--}25 M_\odot$ ). The explosion can lead to the disruption of the system, but if the SN progenitor star was less massive than the companion star in the moment of the explosion, then the system will remain linked and form a HMXRB system.

HMXRBs present a relatively hard X-ray spectra ( $KT \geq 15$  keV) and are mainly concentrated in the Galactic plane and the Magellanic clouds (see Figure 4.2). About 130 HMXRBs are known [127]. This class can also be subdivided into two main subclasses, in terms of the luminosity of the donor star.

##### Supergiant binaries

They are composed by a young-age hot-star of type O or B (or even A) where the accretion process occurs from a radial outflow stellar wind. The compact object can either be a BH or a NS. Due to their circular orbits and the quite steady wind flow, the X-ray emission tends to be steady. They represent  $\sim 25\%$  of the total population of HMXRBs.

In this thesis, I study the system SS433, which was the first stellar object where precessing relativistic jets were discovered. The system is composed by an A star and a BH. It is usually classified as a supergiant binary system since that the companion star is a hot massive A-type star. The search for  $\gamma$ -ray emission is resumed on Chapter 7.

### Be/X-ray binaries

The companion star is a Be star with a circumstellar disk which presents  $H\alpha$  emission lines and continuum free-free emission (which appears as an excess in the IR flux). It represents the largest subclass of HMXRBs, about 57%. These are variable and bright sources of X-rays. The accretion in these systems may happen directly from the circumstellar disk. The X-ray outbursts can be associated to the passage of the compact object (either BH or NS) through the circumstellar disk. Periodic outburst close to periastron are classified as *Type I*. The system can also emit giant X-ray outburst at any phase, probably arising from the interaction with an expanded circumstellar disk, which are classified as *Type II*. Most of HMXRBs show X-ray pulsations, which indicates that the compact object in these systems are strongly magnetized neutron stars [117]. The first observationally proven Be/X-ray binary system hosting a black hole has recently been reported, MWC 656 [55]. Until that moment all the Be/X-ray binaries for which the compact object had been identified were hosting neutron stars. MWC 656, which has also proposed as a  $\gamma$ -ray candidate, is studied in more detail in Chapter 6.

### Other systems

The remaining  $\sim 18\%$  of the total amount of HMXRBs is composed by binaries whose companion star is different from the ones mentioned before. Inside this group, we can include, e.g, Wolf Rayet (WR) stars, which are evolved and very massive stars with very strong stellar wind. Most of their emission is peaked in the ultraviolet (UV) and soft X-rays.

#### 4.2.2 Low Mass X-Ray Binaries

LMXRBs have a soft x-ray spectra ( $KT \leq 15$  keV) and the emission in X-rays is usually due to bursts. They are short-period X-ray binaries with a faint companion star [58]. In this case, the donor is a low-mass star of late-spectral type (K or M) or a white dwarf whose material is accreted by Roche-lobe overflow into the compact object (BH or NS). They are located in the Galactic Bulge and in globular clusters (see Figure 4.2), which may be indicative of old population. 71 LMXRBs are collected in [181].

There are different theories which try to explain the birth and formation of LMXRBs ([170], [118]). The first scenario is similar to the creation of a HMXRB, but in this case the companion star is a low mass star. When the

compact object is created and coupled with the low-mass companion, the Roche Lobe starts to being filled and a common envelope is created. The other theory assume a single massive star which, after its death, forms a compact object. If the created compact object is in an environment of high star density, it may capture a second star. This is expected to happen in high density regions, as globular clusters.

The difference in the X-ray luminosity of LMXRBs and HMXRBs hosting a neutron star might be related to several factors. First, it may be connected to the fact that the magnetic field of the neutron star decays with time. Also, the difference in the masses of the donor stars in these two types of systems corresponds to a difference in ages, being the companion stars in LMXRBs older than those in HMXRBs. Furthermore, in the case of a donor star with  $M_* \leq 10 M_\odot$ , the stellar wind is not strong enough to power a strong X-ray source. On the other hand, Roche-Lobe overflow is unstable for stars more massive than a neutron star and its timescale is very short. It is not possible to make a clear case when a BH is the compact object, as the population of known HMXRBs hosting a BH is quite reduced.

### Soft X-ray transients

Transient LMXRBs are usually referred as *Soft X-ray Transients* (SXTs). They are detected during outburst in X-rays. After this outburst, they start fading in timescales of months. The typical light-curve is a fast rise followed by an exponential decay<sup>12</sup>, which has been interpreted as instabilities in the accretion disc around the compact object. The duration on the rise and the decay depends on the source to consider, however, the rise occurs in a timescale of days while the decay has a timescale of months. Within this process, the companion star, that remained hidden by the dust before the outburst, is revealed and deep studies into its nature can then be performed. During quiescence, the optical brightness decreases to  $V \sim 16\text{--}23$ , which is dominated by the companion star. Optical and spectroscopical studies can reveal the spectral type, the velocity curve and period. Approximately, 25% of SXTs are NS stars, while the rest are BH candidates.

The behavior of BH SXTs in radio and X-rays are described by an unified model [79]. The inner accretion disk region is detected in X-rays, while the synchrotron emission from the relativistic jets is studied through radio. When the outburst starts and at the beginning of the decay, the source is in hard-state. The X-ray spectrum fits a power-law with photon index  $\sim 1.5$  and jets are observed. The non-thermal emission can be due to comptonization processes in the corona next to the BH [212] or synchrotron emission from the base of the jet [141]. In this case, a steady compact radio jet is also observed. The radio luminosity correlates with X-ray luminosity during the jet-active state. This correlation is known as *disk/jet coupling* [86]. When the source reaches the maximum of the X-ray emission (reaching luminosities close to Eddington luminosity,  $L_{Edd}$ ), a significant thermal disk component is present, and powerful transient jet emission is observed. Later, the source enters a soft X-ray state with no radio jet emission. Finally, at the end of the outburst, it recovers its hard state and enters into the quiescent state.

---

<sup>12</sup>Also linear and exponential decays are possible, but not so common

The X-ray spectrum in this case can be adjusted to a power-law with photon index  $\sim 2$  and the luminosity of the system is much below  $L_{Edd}$  ([86], [172]). These changes have barely been studied in BH HMXRBs, as most of the systems detected are persistent sources. Although, this correlation has been found to describe the behavior of the Be/X-ray binary MWC 656 ([159], Chapter 6).

#### 4.2.3 X-ray Binaries as possible $\gamma$ -Ray Emitters

Many X-ray binaries are coincident with radio pulsars emitting non-thermal radiation. Between the 70s and the 90s, when a new and successful generation of X-ray satellites were providing new results, there was a generalized feeling that these sources could possibly emit  $\gamma$  rays.

In the 1970s, COSB space telescope detected flux above 100 MeV from the unidentified source 2CG 135+01. It was found to be consistent with the radio source GT 0236+610 (LS I +61°303), which was proposed as a counterpart and which resulted to be a Be binary system with an unknown compact object. This source was exhibiting strong non-thermal radio flares, which was highly unusual, bursting periodically every 26.496 days [98]. The confirmation was not possible due to the limited angular resolution. EGRET could not confirm it neither, since the limited sensitivity did not allow timing studies, although there was a hint of  $\gamma$ -ray variability.

In the 2000-s, the third generation of Imaging Air Cherenkov Telescopes (IACTs) was developed. This new generation of ground-based  $\gamma$ -ray observatories have high sensitivities and better angular and energy resolution. The combination of stereoscopic operation, high resolution pixelized camera and large reflective areas, together with an improvement in the analysis technique (which improved the background rejection, the primary incoming gamma-ray direction and lowered the energy threshold) led to the discovery of the first  $\gamma$ -ray binary, PSR B1259–63, which is composed by a massive Be star and a 48 ms pulsar. A new class of binary systems was born, the so called  *$\gamma$ -ray binaries*.

### 4.3 $\gamma$ -Ray Binaries

$\gamma$ -ray binaries are systems which emit high energy (HE: 0.1 – 100 GeV) and very high energy (VHE > 100 GeV)  $\gamma$  rays and their non-thermal emission peaks beyond 1 MeV in a spectral luminosity diagram, which means that the bulk of the non-thermal emission peaks in the  $\gamma$ -ray domain (see Figure 4.3). These systems, equally to X-ray binaries, are composed by a massive star and a compact object, either a BH or a NS [151]. The discovery of this new class of binary system provide a new window to the study of particle acceleration, accretion (and ejection) processes and magnetized relativistic outflows.

All of the discovered  $\gamma$ -ray binaries are systems which host a massive (O or B/Be) star. Not a single compact binary with a low-mass companion star has been detected in the HE nor in the VHE regime. Hint of low-energy  $\gamma$ -ray emission (above 0.18 MeV) was detected from 4U1820–30 with a balloon experiment [116]. BATSE-Compton Gamma Ray Observatory also detected flux at energies 20–230 KeV coming from SXT 4U 1543–47 [107]. Recently, the LMXRB XSS J12270-4859 has been associated with an unidenti-

fied *Fermi*-LAT source [66]. Upper limits (ULs) to the flux of some LMXRBs were set using Whipple Observatory [177]. Further observations with newer IACTs have not been performed, except for the microquasar Sco-X1, where ULs to the VHE emission were set [27]. Apart from these attempts, no  $\gamma$ -ray emission has been detected. In principle, very low  $\gamma$ -ray fluxes are expected from these sources, due to the low intensity of the UV radiation field of the companion star. It is possible that  $\gamma$  rays are produced and might be detectable during strong outburst when observing with IACTs [201].

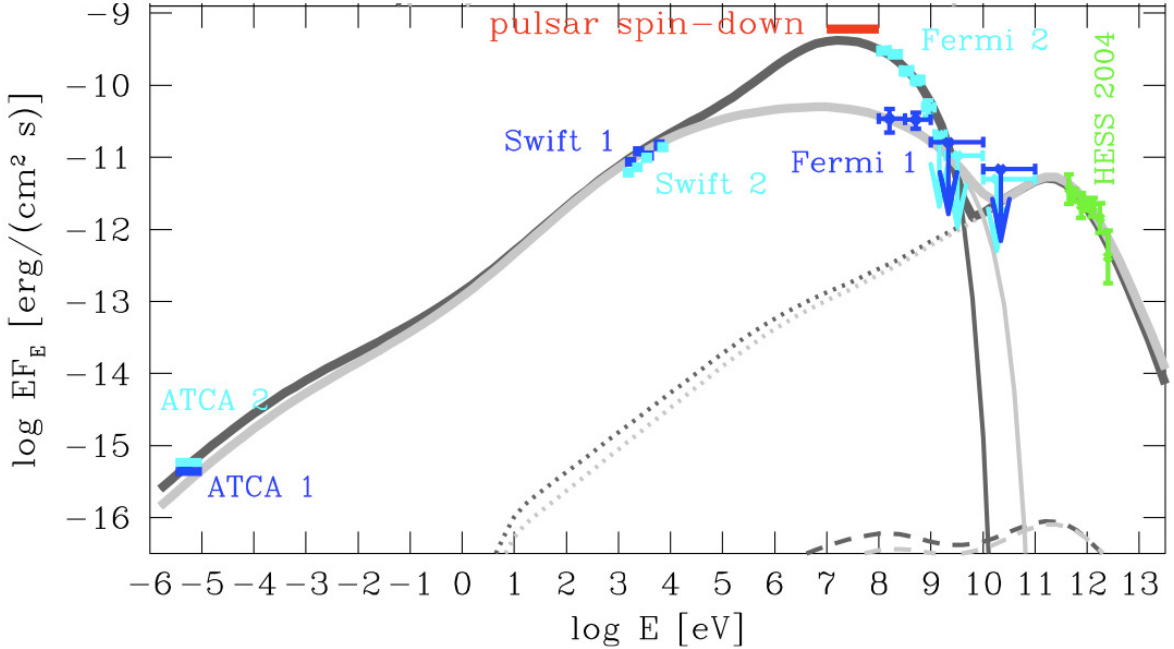


Figure 4.3: Spectral energy distribution (SED) of PSR B1259–63. The peak of the non-thermal emission is released at high energies, in the  $\gamma$ -ray domain, which is an intrinsic characteristic of a  $\gamma$ -ray binary. Taken from [2]

All known  $\gamma$ -ray binaries have in common the presence of a massive star with a compact object and show similar spectra and  $\gamma$ -ray emission variability. All of them show non-thermal radio emission and a hard X-ray spectra with moderated X-ray fluxes. On the other hand, HMXRBs rarely show radio emission, they have higher X-ray fluxes and present X-ray pulsations. These differences are clue to distinguish  $\gamma$ -ray binaries as a distinct class from HMXRBs.

Up to date, only five systems compose the  $\gamma$ -ray family. All of these sources are detected periodically along the orbit or, at least, during certain parts. The  $\gamma$ -ray binaries that have been detected in the  $\gamma$ -ray regime (shorted by discovery date) are:

- \* PSR B1259–63 was the first binary to be detected in the VHE  $\gamma$ -ray band ([13], [2]). This is the only  $\gamma$ -ray binary for which the nature of the compact object is known. It is a 48 ms pulsar, which was detected in a radio-pulsar search. The companion star is a Be star with a circumstellar disk. The VHE  $\gamma$ -ray emission has been detected in the vicinity of periastron (close to superior conjunction). The orbital period is about 3.4 years.
- \* LS 5039 is a massive O star with an unidentified compact object and

a short orbital period of 3.9 days detected in the HESS Galactic Plane Survey [14]. It emits both in the VHE and HE regime [3]. The minimum emission occurs at periastron (which is spatially very close to superior conjunction). The maximum  $\gamma$ -ray emission occurs next to inferior conjunction. It shows orbital spectral variability, although there is no report of long-term flux variations.

- \* LS I +61°303 was first detected at VHE by MAGIC [19]. HE emission has also been reported by Fermi [1]. LS I +61°303 was thought to be the first microquasar [144] to be detected at VHE. HE emission is emitted just after the periastron passage, while VHE  $\gamma$ -rays are detected during the apastron (which corresponds to phases  $\sim 0.3\text{--}0.45$  post-periastron). It also shows VHE emission just after apastron, around phases 0.6–0.7 post-periastron. The orbital period is 26.5 days. This source is deeply studied in this thesis. Detailed information and results can be found on Chapter 5.
- \* HESS J0632+057 has only been detected at VHE ([135], [29]). No HE signal has been reported [54]. This system is a Be-star binary system whose compact object nature is not known. The orbital period is 321 days. The VHE emission occurs at phases  $\sim 0.3$ , which correspond to phases close to the apastron. The VHE behavior of this source is very similar to that in LS I +61°303.
- \* 1FGL J1018.6-5856 is a binary system with a massive O star which was first detected at GeV energies by *Fermi*-LAT [81]. VHE emission has also been detected [103]. The system is composed by a massive O star and has an orbital period of 16.6 days.

A comparison of the characteristics among  $\gamma$ -ray binaries is collected on Table 4.1.

Apart from the five already mentioned  $\gamma$ -ray binaries, we shall mention two other sources which are not properly  $\gamma$ -ray binaries but which have relevant implications:

- \* Cyg X-3 is a system composed by a Wolf-Rayet star and, most probable, a black hole. It has been detected only in the HE regime [80], no emission is found in VHE gamma rays. This source can not strictly be classified as a  $\gamma$ -ray binary because most of the energy is released in the X-ray band.
- \* Cyg X-1 is a system composed of a O star and a stellar-mass black hole. It has not firmly been detected neither at HE nor VHE energies ([184], [21]). The source was observed in VHE, but only hints of detection at a  $4\sigma$  on sporadic flares have been observed at VHE. On the HE regime, *Fermi*-LAT observations have not lead to any detection, although [138] claimed detection of Cyg X-1 using *Fermi*-LAT data. Claims of detection by AGILE still remain uncertain.

### 4.3.1 Why Only Five $\gamma$ -ray Binaries?

There are about 115 known HMXRBs [128] and 71 LMXRBs [181] in the Galaxy but only five  $\gamma$ -ray binaries have been detected. The reason of this low ratio might be due to different causes:

- \* *Sensitivity of the instruments*: A first cause, might be due to the sensitivity of current IACTs, which might not be enough to detect emission

Parameter	PSR B1259-63	LS 5039	LS I +61 303	HESS J0632+057	FGL J1018.6-5856
Star Spectral Type	Be	O	Be	Be	O
Compact Object	48 ms pulsar	-	-	-	-
Star mass [ $M_\odot$ ]	31	23	12	16	31
Distance [kpc]	2.3	2.5	2.0	1.5	5.4
$P_{orb}$ [days]	1236.72	3.91	26.49	315.50	16.58
$\phi_{periast}$	0	0	0.23	0.967	-
$\phi_{sup.conj}$	0.995	0.080	0.036	0.063	-
$\phi_{inf.conj}$	0.048	0.769	0.267	0.961	-
$e$	0.87	0.35	0.54	0.83	-
$i$	19–31	13–64	10–60	47–80	-
GeV emission	~P	P	P	-	yes
TeV emission	P	INFC	A	~A	yes

Table 4.1: Characteristics and parameters for the five known  $\gamma$ -ray binaries. Values are orientative. The quoted parameters are: spectral type of the companion star, compact object nature, mass of the companion star (in solar masses), distance to the system (in kpc), orbital period (in days), phase of the periastron, phase of the superior conjunction, phase of the inferior conjunction, eccentricity, inclination angle, phase of the GeV emission and phase of the TeV emission, where P accounts to periastron, A for apastron and INFC to inferior conjunction. In the case of 1FGL J1018.6-5856, HE and VHE emission has been detected, but the phases are still not known.

from these systems. It may happen that most of the compact binaries in the Universe emit  $\gamma$  rays in the form of short intense flares, which are challenging to detect by the current generation of Cherenkov telescopes.

- \* *Geometry and environment of the system:* Another possible cause which would explain why only 5  $\gamma$ -ray binaries have been detected could be due to the geometry of the system. It may happen that the system is aligned in a manner that the  $\gamma$  rays do not point towards the observer and hence the  $\gamma$ -ray emission is missed. It is possible that, depending on the orbital geometry, i.e., the viewing angle to the observer, the inclination angle and the position of the compact object with respect to the stellar companion,  $\gamma$ -ray emission from these sources do not reach the Earth. It may also happen that these systems are embedded inside a nebula or in regions where the  $\gamma$  ray emission can be absorbed, if any is produced.
- \* *Evolution:* A theory claims that  $\gamma$ -ray binaries (with a NS as a compact object) can be the progenitors of HMXRBs [72]. In the case of a binary system hosting a neutron star, the  $\gamma$ -ray emission is powered by the spin-down of the fast rotating pulsar with a strong magnetic field. High spin-down luminosities are needed in order to have a strong pulsar wind and detectable  $\gamma$ -ray emission. After its birth, the pulsar starts rotating slower. At some point, it may happen that the pressure of the pulsar wind becomes weaker and accretion of the pulsar wind into the compact object starts. Therefore, the pulsar wind is stopped and non-thermal emission is no longer generated. Hence it may occur that the  $\gamma$ -ray component is not longer emitted. At this moment, the  $\gamma$ -ray binary has become a HMXRB. The lifetime of a  $\gamma$ -ray binary is at most that of the spin-down timescale of the pulsar, which is a short time in the time-life

of a binary system [72], which would explain why only five  $\gamma$ -ray binaries have been detected.

### 4.3.2 Scenarios

The big unresolved mystery in the  $\gamma$ -ray binary field is the nature of the compact object. Only one compact object out of five  $\gamma$ -ray binaries has been revealed. Also, a probable black hole in Cyg X-3 has been detected at HE. Two main scenarios have been proposed in order to explain the non-thermal emission component of  $\gamma$ -ray binaries [151]: a pulsar-wind scenario, where a powered-rotating neutron star orbits a massive star and a microquasar scenario, where the accretion into the compact object (BH or NS) produce  $\gamma$ -ray emission (An artistic view is shown on Figure 4.4). Both scenarios compress similar mechanisms to produce VHE  $\gamma$  rays. The detection of non-thermal pulsations (in the case of a NS) would be the definitive prove to distinguish the nature of the compact object.

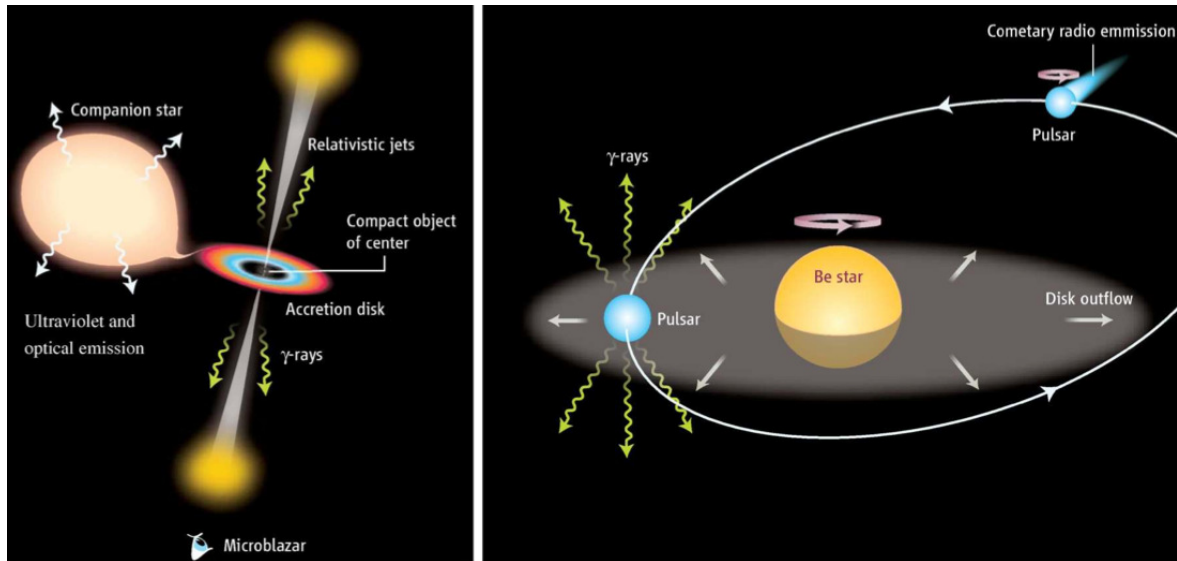


Figure 4.4: Proposed scenarios to explain the VHE  $\gamma$ -ray emission from  $\gamma$ -ray binaries. *Left:* microquasar scenario, where there is accretion of material from a massive star into the compact object, which could be either a BH or a NS. Relativistic jets are emitted. *Right:* pulsar wind scenario, where a fast-rotating neutron star orbits a Be star with a circumstellar disk. The gamma-ray photons are produced thanks to the interaction of the pulsar wind with the Be star disk or envelop. Image credit: [151]

#### Pulsar wind scenario

The pulsar wind scenario ([139], [206], [71]) involves a rotation-powered highly-magnetized ( $B \sim 10^{11}$ – $10^{13}$  G) pulsar which interacts with the stellar wind (and also with the circumstellar disk in the case of a Be star) of the massive companion star, orbiting usually in an eccentric orbit. The rapidly-rotating magnetized neutron star shall be young enough to have a large spin-down luminosity (as previously mentioned on Subsection 4.3.1) in order to create a strong pulsar wind.

In the case of a very hot massive O or B star, a high density field of ultraviolet (UV) photons is present, due to the emission of the star. The interaction of

the pulsar wind with the stellar UV photons will produce an inverse Compton effect where the UV photons will be scattered-up to  $\gamma$ -ray photons.

If the companion star is a Be star, there will be strong equatorial winds and a circumstellar disk, where mass loss from the star will be ejected into. The stellar wind can collide with the pulsar wind creating a shocked region where inverse Compton scattering of the stellar photons with the relativistic electrons present in the shock area can produce gamma-ray emission [73]. It has also been suggested that the interaction of the pulsar wind with the ions in the mass loss of the star can produce  $\gamma$ -ray emission [152]. In addition, hadronic mechanisms have been proposed [164].

### The absence of pulsations

HMXRBs hosting a NS show X-ray pulsations. In the same way, one could expect HE and VHE pulsations in  $\gamma$ -ray binaries hosting a pulsar. However, no pulsations have been detected from any of these sources. Even in the case of PSR B1259–63, where a NS is well-established as the compact object (radio pulsations are normally detected in this source), no HE/VHE pulsations can be found during the periastron passage, which is where  $\gamma$ -ray emission is detected. The reasons may be that it is intrinsically faint, that there is a high absorption due to the strong winds from the massive companion or just due to geometry issues. It is crucial to know with precision the orbital parameters, in order to coherently fold the  $\gamma$  rays on the pulse period with high accuracy. Uncertainties in these measurements translate into the coherence of the signal when doing the orbital demodulation. The current precision on the orbital parameters make the search of pulsations in  $\gamma$ -ray binaries currently unfeasible [54]. Radio pulsations are detected in PSR B1259–63 with a spectral index of -0.6. Pulsed radio emission is not expected in the other four  $\gamma$ -ray binaries, which have orbits much more compact than PSR B1259–63. Radio pulsed emission can be hidden due to free-free absorption of radio waves by the stellar wind of the massive companion. Search of X-ray pulsed emission has also been performed without any success [176].

---

### Microquasar scenario

Microquasars [48] are composed by a compact object (either BH or NS) and a massive star which losses mass into the compact companion via accretion disk. They display relativistic jets where matter is ejected out of the compact object. The ejection of this plasma occurs through synchrotron emission and can be studied at longer wavelengths as radio. This ejection is correlated with instabilities in the accretion disk, which can be studied through X-rays [153]. The non-thermal component of the jets can be detected in radio, infrared and X-rays.

Microquasars are scaled-down versions of quasars, which are galaxies with a central super-massive black hole accreting material from the whole galaxy and which also show relativistic jets. They display similar spectral characteristics. They are the perfect laboratory to understand the physics of quasars in an ambient with shorter timescales and variabilities.

They are expected to emit HE and VHE  $\gamma$  rays. No  $\gamma$ -ray binary has been

confirmed to host a black hole, although it is a proposed solution for some of them. LS I +61°303 and LS 5039 were first identified as microquasars [19], as the VHE  $\gamma$ -ray emission favored the accretion scenario. Nowadays, the nature of the compact object has not been confirmed yet. Cyg-X1 hosts a stellar-mass black hole, but only hints of emission have been detected in the HE and VHE bands. The most accepted solution for Cyg-X3 is the microquasar scenario with a black hole. Only HE emission is detected and most of its non-thermal emission does not fall in the  $\gamma$ -ray regime.

A definitive proof of the existence of a microquasar would be the confirmation of jet emission through radio observations. No confirmation has been possible due to insufficient sensitivities in current instruments or because the jets are not pointing towards us. In the case of LS I +61°303<sup>13</sup>, the microquasar scenario was at first favored by the jet-like structures observed in radio [67], although they can be also interpreted as the cometary tail of a pulsar in a pulsar wind scenario, which is the most accepted scenario for the results derived from those radio observations. The debate is still opened, as some recent observation with VLBA claim a two-peak microquasar model fitting [146].

Also, in the case of a microquasar, a cut-off in the hard X-ray spectrum should be noticed, but no evidence has been found [62].

---

<sup>13</sup>LS I +61°303 is deeper studied on Chapter 5.

# 5

## Multi-year Observations of the $\gamma$ -Ray Binary LS I +61°303

LS I +61 303 is one of the three binary systems which have been detected from radio to  $\gamma$  rays, what provides a complete view of the behavior of the system. However, the broadband emission scenario is still under debate. LS I +61°303 was thought to be the first microquasar detected in the VHE  $\gamma$ -ray regime, although observations mainly support the pulsar wind model. In this chapter, a four-year campaign performed by MAGIC is introduced. Different analysis making use of not only this new acquired data but also MAGIC historical observations are performed. Here, I search for super-orbital modulation in the VHE flux regime of this source and search for anti-/correlation with optical data taken simultaneously. Finally, I try to unveil spectral features for different conditions in the binary system.

### 5.1 Unveiling the System

---

LS I +61°303 (V615 Cas, GT 0236+610) is a  $\gamma$ -ray binary composed of a rapidly rotating Be star (of spectral type B0Ve [114]) with a circumstellar disk and a compact object of unknown nature, either a neutron star (NS) or a stellar-mass black hole (BH). The stellar luminosity is  $L_\star = 10^{38}$  erg s $^{-1}$ . The mass of the companion star is  $\sim 10 M_\odot$ , while the mass of the compact object is  $1 - 5 M_\odot$ . The separation between the star and the compact object changes from  $6.1 R_\star$  ( $R_\star$  refers to stellar radii) at the periastron to  $21 R_\star$  around apastron [211]. The system is located at a distance of  $2.0 \pm 0.2$  kpc [83]. The compact object orbits the stellar companion in an eccentric orbit ( $e = 0.54 \pm 0.03$ ) with a period of 26.4960(28) days, which was determined from radio observations [96]. The periastron passage occurs at phase  $\phi = 0.23 \pm 0.03$ , although it varies slightly depending on the orbital solution ([96], [100], [39]). The reference for the periastron passage is taken at  $T_0 = 43366.275$  MJD [96]. Figure 5.1 shows a schematics of the orbit of the binary system. Other orbital parameters, as the inclination of the orbit, remain poorly known [56]. The system is located at RA =  $02^h 40^m 31^s$  and DEC =  $+61^\circ 13' 45''$ .

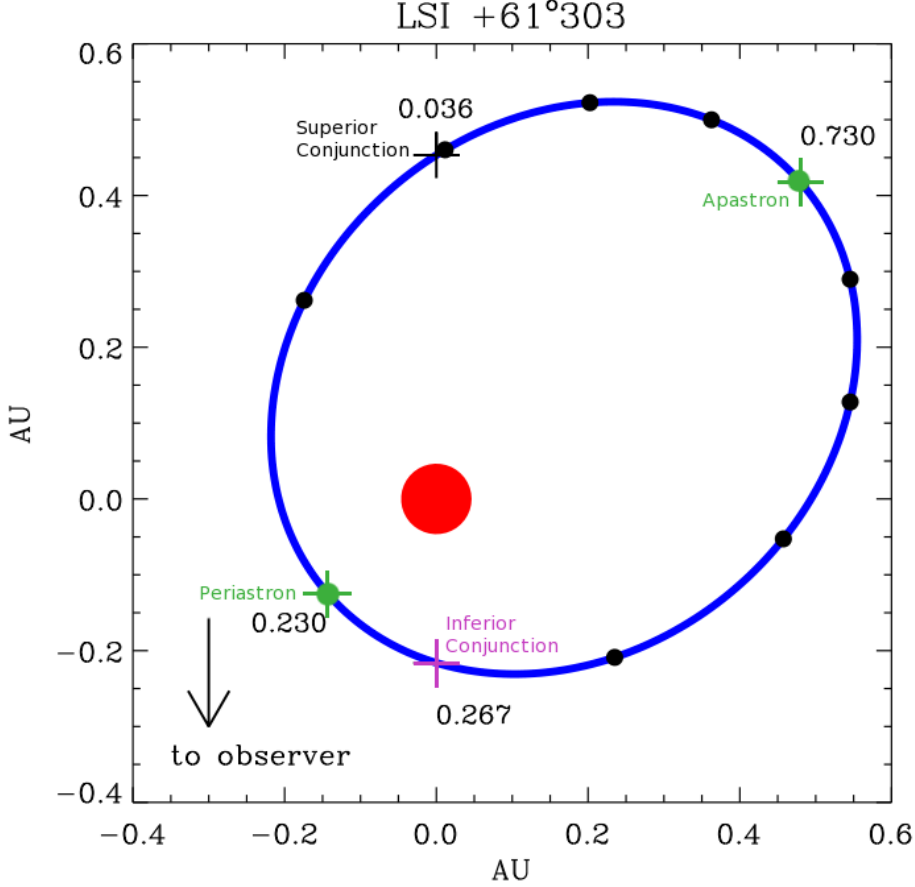


Figure 5.1: Scheme of the orbit of LS I +61°303. The periastron ( $\phi=0.23$ ) and apastron ( $\phi=0.73$ ) are marked with green crosses. The inferior conjunction ( $\phi=0.267$ ) is represented as a pink cross, while the superior conjunction ( $\phi=0.036$ ) is plotted as a black cross. The dots represent 0.1 phases. Figure taken from [71] and re-edited.

### 5.1.1 Multiwavelength Context

LS I +61°303 is one of the few binary systems which have been detected from radio to VHE  $\gamma$  rays.

#### Radio emission

LS I +61°303, also known in radio as 2CG 135+01, presents periodic radio outburst which are widely associated to the orbital period. The best estimate for the orbital period is due to observations in this wavelength, setting its value to  $26.4960 \pm 0.0028$  days. The radio outburst starts on phase 0.45 and can last until phase 0.95 [167]. The flux ratio for the maximum and minimum peaks is  $\leq 10$ .

The radio emission of LS I +61°303 has an extended structure of few milliarcseconds (mas) size, which corresponds to few astronomical units (AU). An extended jet-like radio-emitting structure was reported [144], hence LS I +61°303 was proposed to be a microquasar. Nevertheless, images obtained with VLBA during a complete orbital cycle showed a rotating tail-like elongated morphology of overall size 5 – 10 mas [67] (See Figure 5.2) which was consistent within the pulsar wind scenario [139]. Similar structures were observed

during the same phases but several orbits later, supporting the pulsar scenario [23].

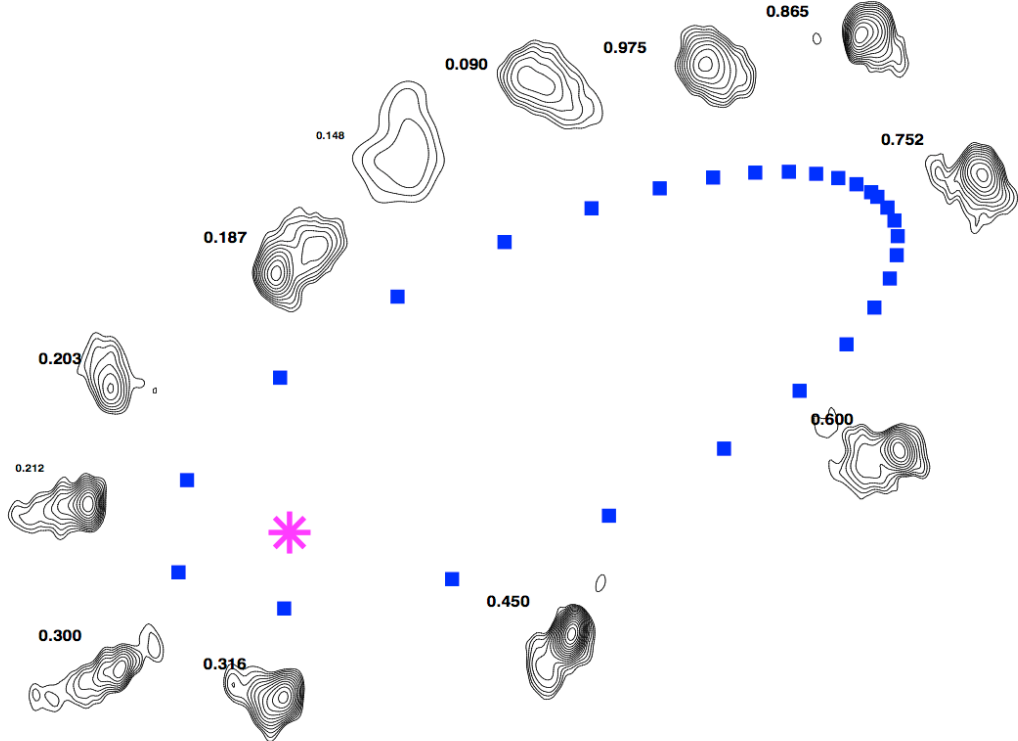


Figure 5.2: VLBA 8 GHz radio map of LS I +61°303. The cometary-like tail is clearly visible around periastron, what enforces the pulsar wind scenario. The radio contours show an extended structure of few AU. Image credit [67].

A super-orbital modulation in amplitude and phase of the radio outbursts of  $1667 \pm 8$  days has been found in LS I +61°303 [96], which was first tried to be explained with the Induced Pulsator model [126] without success. This super-orbital modulation is approximately sinusoidal and the ratio between maximum and minimum flux is  $\sim 2.5$  [96].

Radio pulses have not been detected in this system. A search of pulsations with GBT was performed, but no emission was observed and upper limits (ULs) have been set between 4.1 and  $14.5 \mu\text{mJ}$  for phases  $\sim 0.8 - 0.0$  and  $0.4 - 0.6$  [147]. A later search with GMRT centered at phase 0.54 set an UL of  $0.38 \mu\text{mJ}$  [53]. However, the absence of pulsed emission does not exclude the pulsar nature of the compact object. As discussed in Chapter 4, it can happen that the pulsar may not be beaming towards the Earth. Moreover, even if the putative pulsar was pointing to the Earth, the characteristics of the orbit and the proximity of the compact object could lead to absorption of the pulsed emission due to free-free absorption processes.

### X-ray band

In the X-ray domain, LS I +61°303 also shows orbital modulated emission within the 26.5 days, although the periodical outburst shows a wide spread in phase. The orbital outburst is visible between phases  $\phi = 0.4 - 0.8$ ,

depending on the cycle [168]. The orbital peak presents significant long-term changes which may be due to a super-orbital cycle. The X-ray emission precedes the radio emission [37]. The X-ray spectrum is well fitted by an absorbed power-law. The spectrum hardens (from  $\sim\Gamma = 1.9$  to 1.5) with the increase in brightening ([187], [23]).

Searches for super-orbital modulation have been performed, without confirmation [124], although hints have been observed [123]. Furthermore, short-timescale variability of the order of several ks (much shorter than the orbital period) was observed in this wavelength with flux fluctuations of  $\sim 25\%$  [187], which may be indicative of the existence of a variability mechanism much faster than the one producing the overall changes in the orbital motion.

Two very short-timescale ( $< 0.1$  s) highly-luminous ( $> 10^{37}$  erg s $^{-1}$ ) burst have been observed in the direction of LS I +61°303 triggered by *Swift*/BAT ([42], [52]). The lightcurve and spectra of these burst is that typical of magnetars, which are NS in which the emission is though to be powered by their strong magnetic fields.

Extended X-ray emission at a  $3\sigma$  level was reported using *Chandra* observations [169]. It was not possible to confirm this emission using a different *Chandra* dataset [175]

### HE $\gamma$ -ray Emission

LS I +61°303 is one of the four binaries which has been detected both in the HE and VHE energy regime. The outbursts in HE and VHE  $\gamma$  rays occur in different phases (periastron and apastron, respectively) and they are anti-correlated, which may indicate that the processes which generate these two components might be different.

The source was first detected in the HE regime by *Fermi*-LAT [1]. Before, EGRET performed observations at HE in this region of the sky. LS I +61°303 fell within the error box of the EGRET observation, but due to the low angular resolution the confirmation of the binary as a  $\gamma$ -ray emitter was not possible. LS I +61°303 presents periodic outbursts slightly after the periastron passage, around phases  $\phi \sim 0.3 - 0.45$ . The orbital period derived is  $26.71 \pm 0.05$  [104], consistent with the period determined through radio observations [96]. The orbital modulation in the GeV regime can be understood as changes in the absorption and generation of  $\gamma$  rays.

The spectrum is well described by a power-law with index  $\Gamma \sim 2.1$  with an exponential cut-off at  $E \sim 3.9$  GeV. The Spectral Energy Distribution (SED) shows a spectral point at 30 GeV which deviates from the fit, which may indicate the emerge of the VHE component [104]. It suggests that there are two populations of relativistic particles, one which contributes to the GeV regime and the one other emitting at TeV energies. The cut-off at 4 GeV and the possible existence of two distinct population of particles has been confirmed by [36], by performing simultaneous observations with *Fermi*-LAT and VERITAS. The SED for the *Fermi*-LAT and VERITAS observations, including also MAGIC high-state [19] and low-state [28] emission is shown on Figure 5.3. A phase-resolved spectra (with step of 0.1 phase-bin, modeling a power-law spectra with cut-off for each bin) reveals a softening of the spectra with an increasing flux [104]. The spectrum gets softer during the periastron

passage, where the GeV flux is maximum, and it becomes harder at apastron, where the flux is minimum.

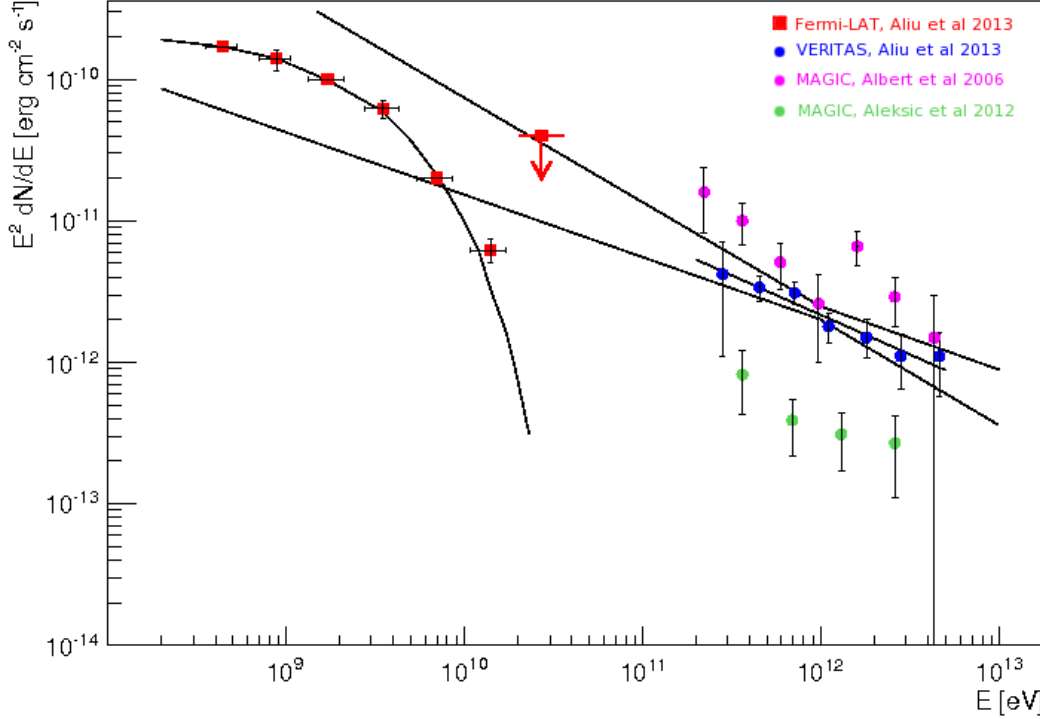


Figure 5.3: Spectral energy distribution (SED) of LS I +61°303 obtained by *Fermi*-LAT (red filled circles) and simultaneous VERITAS data (blue filled circles). The fit (power-law with exponential cut-off) to the HE points is plotted, as well as the VERITAS fit uncertainty. The MAGIC high-state (magenta filled circles) [19] and low-state (green filled circles) [28] are also plotted. The MAGIC data is not contemporaneous to *Fermi*-LAT and VERITAS points. Both the HE and VHE components (including low and high-emission states) are clearly separated. Image taken from [36] and adapted.

Long-term super-orbital variability has been observed in the HE regime (see Figure 5.4), folded within the super-orbital period found in radio,  $\sim 1667$  days [195]. This super-orbital variability is almost non visible around the periastron, where the compact object is inside (or highly affected by) the Be circumstellar disk. The flux (in terms of the super-orbital phase) in this region flattens and can be fitted by a constant value. The long-term modulation is more significant in the apastron region, where the conditions can change in, at least, three orders of magnitude (see [97] for a review).

### VHE $\gamma$ -ray Emission

LS I +61°303 was initially proposed to be the counterpart of the  $\gamma$ -ray source 2CG 135+01 detected by COS-B. Observations performed by the Whipple Cherenkov telescope set ULs for the VHE emission component at 350 GeV and 500 GeV [106]. Finally, LS I +61°303 was first detected in the VHE regime by MAGIC in 2006 [19]. VERITAS collaboration also reported detection of VHE emission [9].

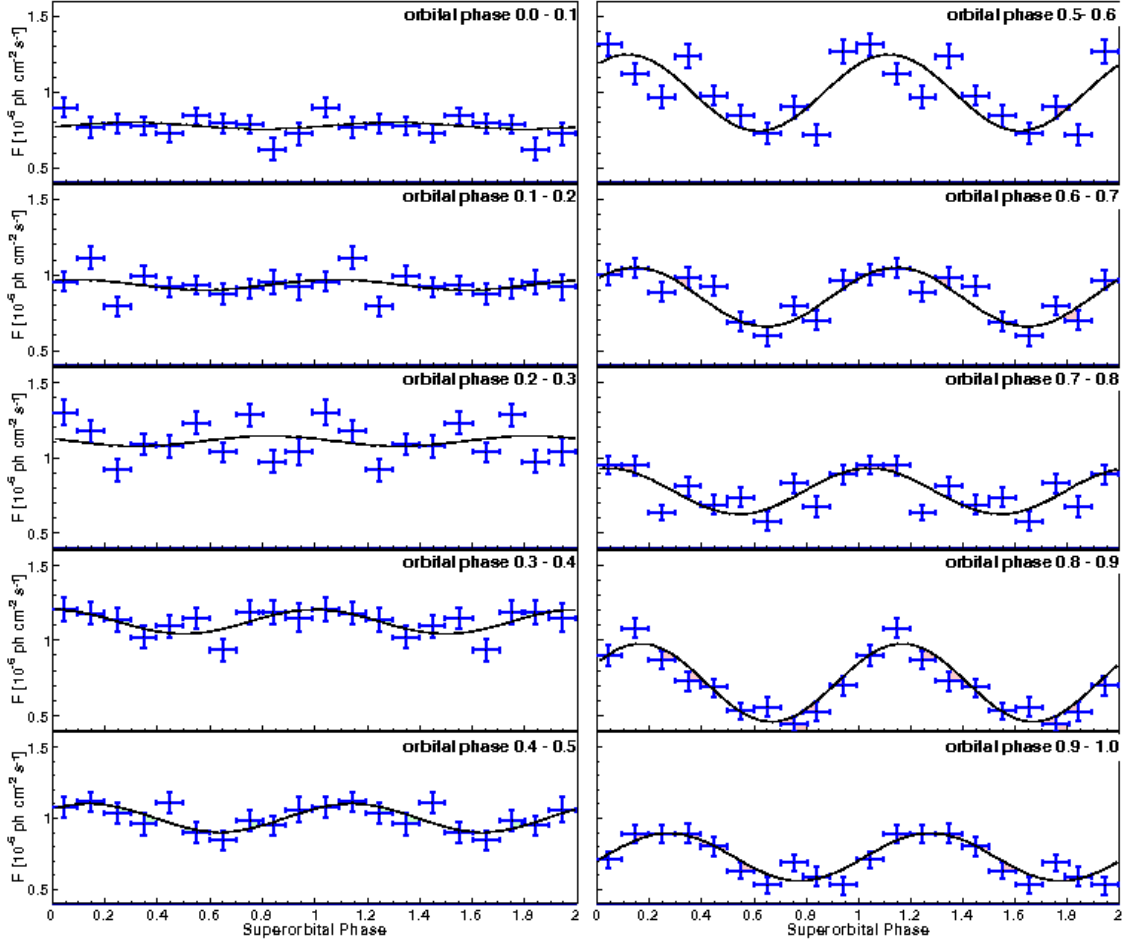


Figure 5.4: Long-term variability found by *Fermi*-LAT. *Left:* Phases close to periastron passage do not show significant changes in the flux, which is approximately flat. *Right:* Phases close to apastron show important changes in the flux. The black line is a sinusoidal fit with a period of 1667 days. Image credit : [195]

The VHE emission is point-like and its extension is constrained to be less than  $0.1^\circ$ . A TeV peak was first detected at phases  $\phi = 0.6 - 0.7$  (which correspond to the phases next to the apastron) at a level of  $\sim 16\%$  of the Crab Nebula flux, for energies above 400 GeV. The TeV emission is clearly shifted with respect to the GeV emission, which supports the theory that the processes which generate these two components might be different. The VHE emission of LS I +61°303 showed a Crab-like spectrum with spectral index  $\alpha \sim 2.6$ . The VHE emission of LS I +61°303 is modulated with the orbital period [19]. The spectrum derived from these first observations for phases 0.4 – 0.7 and energies between  $\sim 200$  GeV and  $\sim 4$ TeV is described by a power-law:

$$\frac{dN_\gamma}{dA dt dE} = (2.7 \pm 0.4 \pm 0.8) \times 10^{-12} E^{(-2.6 \pm 0.2 \pm 0.2)} \text{TeV}^{-1} \text{cm}^{-2} \text{s}^{-1} \quad (5.1)$$

were  $N_\gamma$  is the number of  $\gamma$  rays reaching the Earth per unit of area  $A$ , time  $t$ , and energy  $E$  (the latter expressed in units of TeV). Campaigns performed in the following years show a spectral slope compatible with this result.

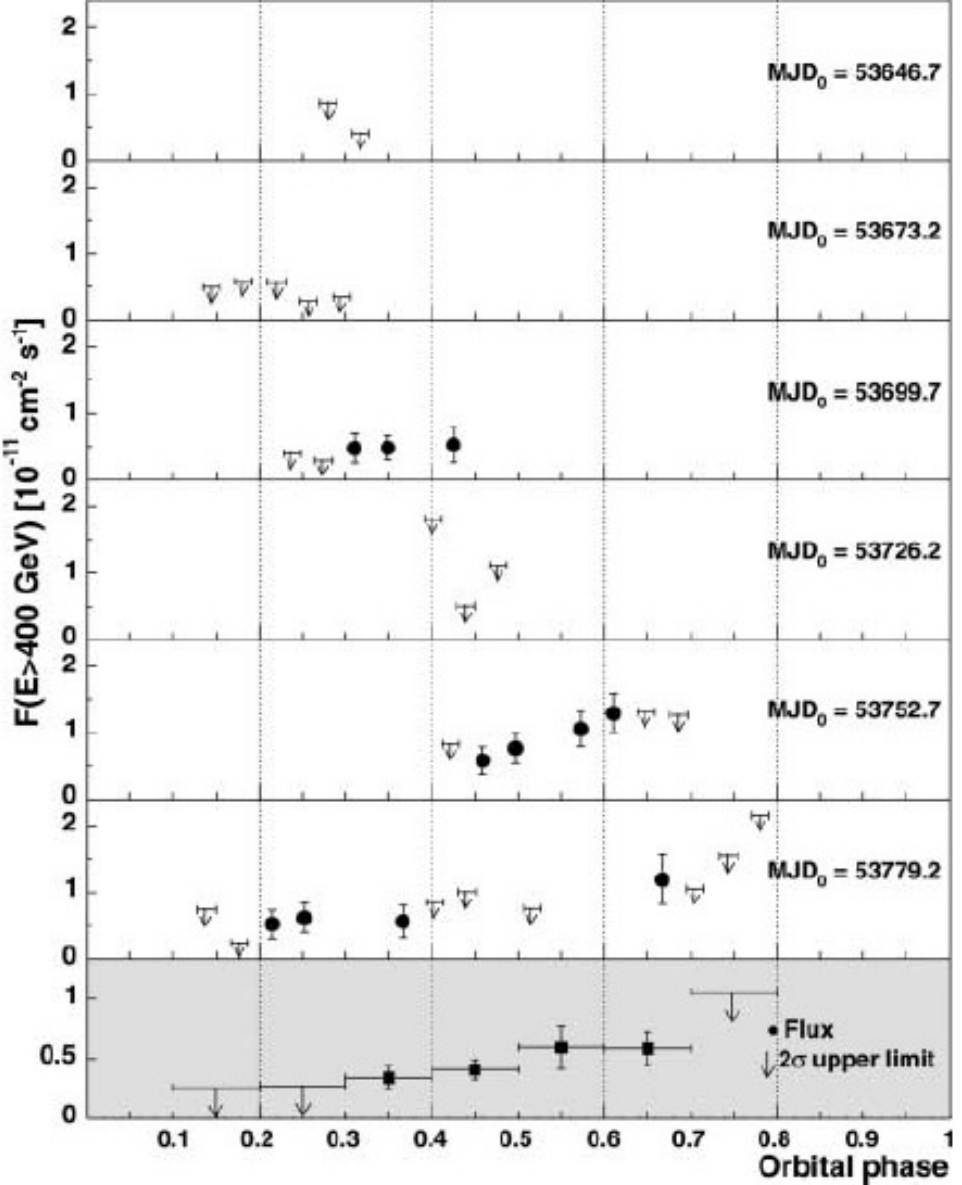


Figure 5.5: VHE  $\gamma$ -ray lightcurve of LS I +61°303 obtained during its first observational campaign as a function of the orbital phase. The campaign covered six different periods, displayed on the six top panels. The bottom panel represents the phase-averaged flux. Points with more than  $2\sigma$  significance are plotted as black dots. For the non-detection,  $2\sigma$  ULs were calculated (here represented as arrows). The maximum of the emission occurs on phases 0.6 – 0.7. Image credit : [19]

Despite a periodic outburst is almost always present in the phase range  $\phi = 0.6 - 0.7$ , a significant flux emission has also been detected among phases  $\phi = 0.8 - 1$ . The first detection of significant flux in this region was reported by MAGIC at a level of  $(5.2 \pm 1.0) \times 10^{-12} \text{ cm}^{-2} \text{ s}^{-1}$  [25].

In winter 2009-2010 campaign performed by MAGIC, the source was detected in a low-state flux emission level [28]. The maximum flux emission, which occurred at orbital phase 0.62, above 300 GeV was  $(6.1 \pm 1.4_{\text{stat}} \pm 1.8_{\text{sys}}) \times 10^{-12} \text{ cm}^{-2} \text{ s}^{-1}$ , corresponding to a 5.4 % of Crab Nebula flux, about a factor three lower than previous campaigns, which agrees with the factor found in radio for the long-term modulation. Nevertheless, the TeV peak

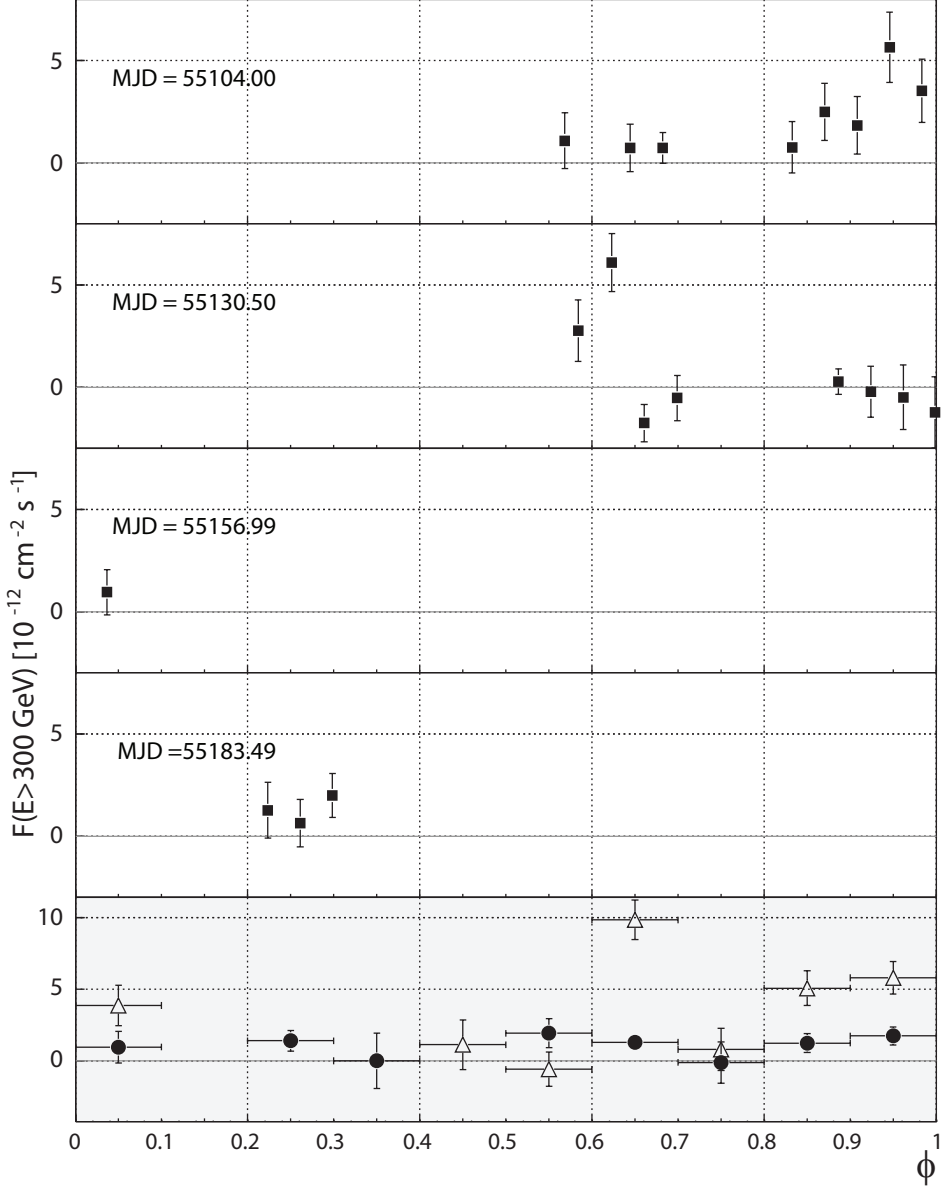


Figure 5.6: VHE flux of LS I +61°303 as function of the orbital phase, covering four orbital periods, observed during the low-emission state. The emission is clearly reduced with respect to the first campaign. The lower panel shows the phase-integrated flux (black dots) and previous published values (triangles) by [37]. The maximum of the emission occurs on phases 0.6 – 0.7, although in this case there is also significant emission at phases 0.8 – 1.0. Image credit : [28]

is still detected in the same phases  $\phi = 0.6 - 0.7$ , which is consistent with previous observations. In these observations, despite the fact that the flux was much lowered, the spectral fit parameters agree with previous values reported by MAGIC. The fact that the spectrum is compatible within the pre-established values, suggests that the same mechanisms produce the VHE emission both for the high and low-state campaigns. For 2009 – 2010 data, this processes may have reduced the VHE  $\gamma$ -ray production or they might

have been more absorbed.

No emission around periastron has been reported. Nevertheless, VERITAS once detected the system next to superior conjunction during fall 2010, between phases  $0.0 - 0.1$  ( $\phi = 0.081$ ) [8]. Assuming a pulsar-wind scenario, this emission could be explained as Inverse Compton (IC)  $\gamma$ -ray production along the observer line of sight. This process shall be most efficient at superior conjunction, where the stellar photons interact head-on with the leptons produced either directly in the pulsar wind or in the pulsar wind/stellar wind shock interaction region.

## 5.2 Accretion Model vs Pulsar Wind Scenario

---

The nature of the compact object in LS I  $+61^{\circ}303$  and the broadband emission scenario are still uncertain. Two main scenarios are proposed, the microquasar (characterized by accretion and jet emission) and pulsar-wind. Both can describe in a general scheme the broadband spectrum of LS I  $+61^{\circ}303$  although both present discrepancies with observational data:

- \* It is difficult to explain, within the microquasar scenario, the changing morphology found in radio by [67], which requires a very unstable jet. This instability could be related to density waves in the accretion disk or deflection of the jet due to the impact of the wind from the companion star. Also, accretion scenarios usually show a cut-off power-law in the hard X-ray spectra at energies below 100 KeV, which is not observed in LS I  $+61^{\circ}303$ .
- \* The colliding wind model has, in general, problems in explaining the double jet-like radio morphology studied by [146] and the non-detection of the source before the periastron passage. It is also difficult to account for the observed  $\gamma$ -ray emission when the pulsar power is on the order of  $10^{36}$  erg s $^{-1}$ . This last issue could be explained by orientation effects, but detail modeling is lacking.

In this section, it is first introduced some relevant aspects of the Be star and the compact object. Then, we will dive into the different theoretical models which try to explain the phenomenology of the  $\gamma$ -ray emission in LS I  $+61^{\circ}303$ .

### The Companion Star in LS I $+61^{\circ}303$

Before going into the details of the different models proposed to explain the behavior of this source, it is important to deeply understand the physics and characteristics of the companion star of this system. As mentioned before, LS I  $+61^{\circ}303$  hosts a Be star with an equatorial circumstellar disk. These are very hot and young stars with a strong stellar wind and a high mass loss rate.

The stellar wind has two different components. The first one is a fast, radiation-driven polar outflow, which is approximately isotropic. The second component is a slow equatorial outflow, which forms the thin decretion disk. The causes of the formation of this decretion disk are still unknown [173]. This circumstellar disk seems to be viscous and it is basically Keplerian. The radial velocity is much smaller than the rotational one. The mass

loss rate of the Be star is estimated to vary a factor 4, as derived from radio measurements [97].

The circumstellar disk radii in Be stars in binary systems are much smaller than the radii of isolated Be stars. This can be caused by tidal truncation of the disk provoked by the passage of the compact object [63]. The size of the decretion disk can be obtained by measuring the equivalent width of the H $\alpha$  line. This parameter ranges from -6 Å to -18 Å [100], which corresponds to a disk radii varying between  $4 R_\star$  and  $6 R_\star$ . A later analysis calculated that the size of the disk could vary between  $4.5 R_\star$  and  $7 R_\star$  [56]. The separation between the companion star and the compact object is estimated to change from  $6.1 R_\star$  at the periastron to  $21 R_\star$  around apastron. This indicates that the compact object can directly interact with the circumstellar disk only around the periastron and this can happens only when the disk reaches its larger size. It is worth noticing that the disk is not perfectly circular.

The variability of the size of the disk seems to be periodic. The H $\alpha$  emission line shows an orbital variability compatible with the orbital period derived from radio measurements ([208], [207]). This can be interpreted as an effect of the propagation of the density waves in the circumstellar disk, making the disk not axially symmetric [163]. The H $\alpha$  line it is also modulated within the  $\sim 4$  year super-orbital period [207]. The largest disk size corresponds to the minimum of the radio emission [205]. The orbital maximum of the EW of the H $\alpha$  line peaks after the periastron and generally coincides with the X-ray and HE  $\gamma$ -ray maxima [207].

## The Unknown Nature of the Compact Object

A clear evidence of the nature of the compact object, would be the determination of its mass from the mass function of the system. In order to perform this calculation, the mass of the Be star and the orbital inclination should be known with accuracy, which is not possible due to the large uncertainties. The parameters of the system derived ([56], [100], [39]) allow both a NS and a BH as a solution for LS I +61°303. This is mainly due to the poorly constrained values obtained for the inclination of the orbit, which is estimated to be  $10^\circ < i < 60^\circ$  [56], number which has even increased to  $70^\circ$  by more recent results [207]. The compact object would be a neutron star for orbital inclinations  $i \geq 25^\circ$  and a black hole otherwise [56]. Considering these data, it seems that the likelihood for the system to host a NS is greater than to host a BH as a compact object.

### 5.2.1 Microquasars: Accretion Scenario

The microquasar scenario was already introduced in Subsection 4.3.2. In this model, the compact object, which can either be a BH or a NS, accretes mass from a massive star. The system display relativistic jets where matter is ejected.

In 1993, VLBI radio contours of LS I +61°303 showed a structure that extended few AU [143] and that was associated to relativistic radio-jets. Later results showed a single one-sided structure, interpreted as a one-sided Doppler-boosted jet [145]. Observations performed with MERLIN in 2004 reported a double-sided precessing-jet structure very similar to that of the pre-

cessing jet in SS433 [144]. Based on these experimental results, LS I +61°303 was tough to be the first microquasar detected at VHE [19]. A recent re-analysis of the VLBA structures seen by [67] that where associated to a pulsar-wind scenario, has been performed by [146], revealing double-sided structures which support this microquasar scenario.

Different models have tried to accommodate the microquasar scenario with the  $\gamma$ -ray production. Both leptonic and hadronic scenarios can explain the main features in the  $\gamma$ -ray emission of LS I +61°303. Some of these models are presented below:

### Leptonic Models

- \* [43] proposed a leptonic scenario where the electrons are accelerated in the shock waves propagating along the jet and produced inside the inner part of the compact object. The  $\gamma$ -ray production is due to inverse Compton  $e^\pm$  pair cascades. Within this context,  $\gamma$  rays in the GeV-TeV regime are produced by IC processes, while lower energy photons (X-rays and soft X-rays) result from synchrotron emission of electrons accelerated in the jet. This model explain the GeV-TeV anti-correlation, which is consequence of two populations of electrons; the flattening of the  $\gamma$ -ray emission above few hundred GeV and the lowering of VHE flux close to periastron, which is due to the dependence between the maximum energies of the electrons accelerate from the pulsar side and the distance as  $D^{1/2}$ .
- \* In the scenario proposed by [49], the matter is accreted onto the compact object, originating a jet which is embedded in the circumstellar disk. It triggers electrons which are accelerated via shock. The accelerated electrons produce  $\gamma$  rays by synchrotron emission and IC, although the latter is significantly absorbed (for certain orbital phases) due to photon-photon annihilation in the stellar photon field (which dominates along the orbit) and circumstellar photon field (which dominates at periastron).
- \* [102] derived a model which included synchrotron, synchrotron self-Compton (SSC) and external inverse Compton emission (with seed photons from the companion star). The model proposes a time-dependent injection and acceleration of electrons. The  $\gamma$ -ray modulation is not due to changes in the accretion rate but just due to purely geometrical effects of the relative orientation of stellar companion and the compact object and its jet. The VHE component is dominated by SSC emission. The X-ray and soft  $\gamma$ -ray emission are dominated by synchrotron emission from the jet. The external IC emission is negligible. A spectral hardening during the phases of low VHE emission is expected.

### Hadronic Models

- \* [182] proposed a scenario where  $\gamma$  rays are produced by  $pp$  interactions. In this case, the accreting pulsar scenario is ruled out, since the in-falling matter should fall into the surface and produce strong and hard X-ray emission, which is not observed. In this model, the compact object is a low-mass BH. The emission comes from the interaction between the BH

and the Be circumstellar disk. At periastron, the compact object tidally deforms the Be disk and captures part of the outermost material. Also, two peaks of VHE emission are expected, one at  $\phi \sim 0.5$  and another one around periastron which is due to shrinking of the accretion disk and which is not visible due to opacity issues.

- \* [165] revisited a hadronic model proposed by [182]. In this case, the  $\gamma$  rays are generated in interactions of relativistic protons from the jet (close from the compact object) and cold protons from the equatorial wind of the companion star. The  $pp$  interactions can occur because of the mixing of the stellar wind and the material from the jet or because some protons may escape from the jet and interact with the wind. The circumstellar disk emission dominates around periastron, hence the absorption of the  $\gamma$ -ray emission in this region is significant. The main emission occurs at phase  $\sim 0.5$ .
- \* [213] presented a hadronic-dominated jet model, where the emission comes from collision of accelerated protons with the cold jet protons and stellar wind ions. The emission is due to pion decay, but also synchrotron, IC and bremsstrahlung of leptonic origin are considered. This model tries to fit all the multiwavelength data, although it can not reproduce the *Chandra* X-ray emission and the radio and TeV fluxes are higher than the prediction of the model. This model is only calculated for apastron and INFC. The orbital modulation is due to variation in the accretion rate and the stellar ions, but also to photon density along the orbit and angular dependence of the photon absorption.

### 5.2.2 Pulsar-wind Scenario

In this scenario, a fast-rotating young pulsar is orbiting a massive star. The  $\gamma$ -ray emission is accelerated in the shock produced between the relativistic pulsar wind and the slow equatorial disk of the companion star. The relativistic electrons will undergo IC interaction with the stellar photons, hence producing the VHE emission.

Several facts give support to this scenario: first, the detection of a single-side elongated radio structure pointing away from the Be star back in 2006 gave strong support to this theory. Also, the only known compact object in a  $\gamma$ -ray binary is a pulsar in PSR B1259–63. The rest of the  $\gamma$ -ray binaries share similar spectral and timing characteristics as PSR B1259–63. Finally, the recent detection of two magnetar-like events coming from the direction of LS I +61°303 suggest that LS I +61°303 hosts a highly magnetized pulsar. These events need a very high magnetic field, which can only be explained by a highly-magnetized pulsar (magnetar).

Inside this scenario there are two main flavors for the explanation of the  $\gamma$ -ray emission, the *ejector-propeller* and the pure *wind-wind* models.

#### Ejector-Propeller Models

- \* [206] proposed the first ejector-propeller model (see Figure 5.7). In this scenario, there is a transition from a propeller regime, which occurs at periastron and where there is accretion of the Be star material onto the magnetosphere of the pulsar, to a ejector regime at apastron, where the

NS behaves as a young emitting radio pulsar. The mass accretion onto the compact object is modulated by the motion of the NS through the circumstellar disk. The accretion is maximum at periastron (propeller behavior), although a low mass capture rate is also expected at apastron (ejector). The ejector phase will switch on about 0.1 – 0.4 orbital periods after periastron and a magnetized cavern of relativistic particles will be created around the NS. This cavern will appear when there are low accretion rates and will expand under the pressure of the relativistic wind of the ejector. It will switch off when entering into the circumstellar disk.

- \* [198] elaborated an ejector-propeller theory considering LS I +61°303 as the first magnetar ever detected in a binary system, implementing in this way the two magnetar-like events reported by *Swift*/BAT. In the apastron, it behaves as a ejector, acting as a rotational powered system. In here, the inter-wind shock produced by the collision of the pulsar wind and the stellar wind will accelerate particles up to TeV energies. At periastron, the magnetosphere gets disrupted and can not generate a relativistic wind anymore, hence accretion from the equatorial outflow (which dominates over the polar wind) starts. For a neutron star with the usual spin period of a magnetar, the system will bear a flip-flop behavior between these two phases (ejector and propeller) along each orbit. Small changes in the mass loss rate of the star will push the pulsar from a rotational-powered into an accreting system. The bigger the mass loss rate, the faster the system abandons the ejector regime. This can happen even at apastron for epochs of relatively large disc. This would explain not only the orbit-to-orbit TeV variations but also the long-term behavior of the source, which depends on the mass-loss rate of the star. The higher the mass-loss rate, the lower the TeV emission. It also explains the GeV-TeV anti-correlation, which can be interpreted as a result of inverse Compton scattering and pair absorption; at periastron, the cut-off for particle acceleration is sub-TeV and the cross section for pair production is maximal. The increase of mass loss rate, would favor the GeV emission, but particles would not be accelerated up to TeV energies in this case.

### Pure wind-wind models

- \* [211] modeled the emission in LS I +61°303 as the interaction of a relativistic pulsar wind with the wind from the Be companion star. In this case, the stellar wind is interpreted as a fast radiation-driven isotropic polar wind plus a slow equatorial component. The polar wind is clumpy, which causes the mixing of the pulsar wind with the stellar wind. The contact surface between both is not a smooth bow-shaped region, but it is irregularly shaped. The Coulomb losses dominate in the circumstellar disk. The IC dominates in a region larger than the orbit of the system. Synchrotron emission dominates at much larger distances. These authors claim that the circumstellar disk is tilted with respect to the orbit and that it precesses due to the tidal forces that the pulsar performs over the Be star. With this mechanism, it is possible to explain the possible long-term periodicity in LS I +61°303.
- \* [44] proposes that the  $\gamma$ -ray spectra of LS I +61°303 is due to the ex-

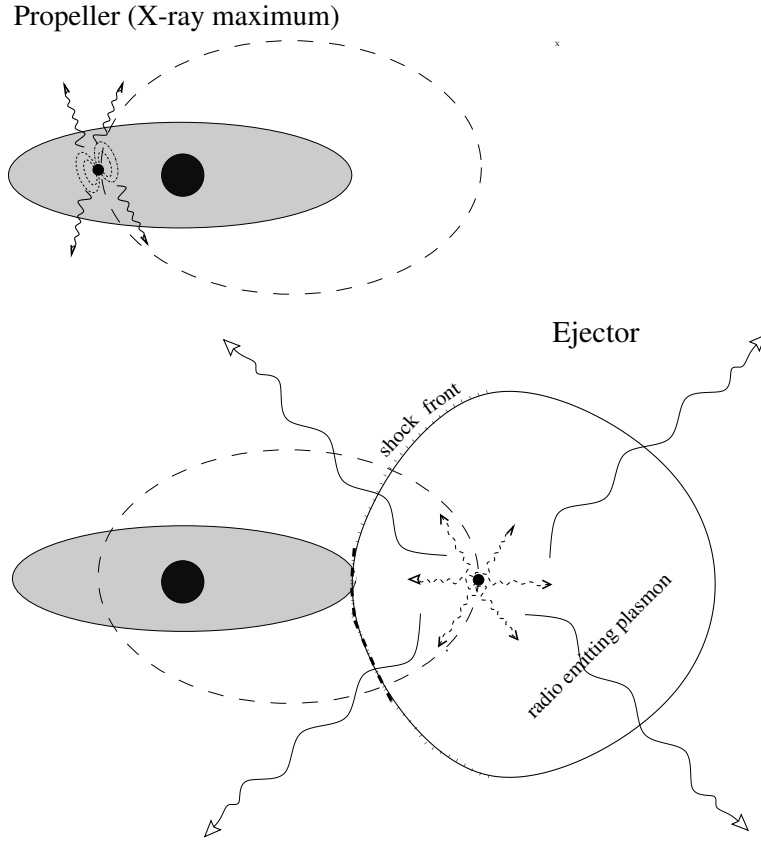


Figure 5.7: Ejector-propeller model. LS I +61°303 would behave as a propeller around periastron, accreting matter onto the magnetosphere of the NS. At apastron, it will enter into the propeller regime, where the NS will behave as a rotating radio emitting pulsar. Image credit : [206]

istence of two populations of electrons, a component at GeV energies showing an exponential cut-off at few GeV and another one at TeV energies which does not follow the extrapolation of the spectrum from the GeV energy range. These populations of electrons are accelerated in the double shock created by the collision of the pulsar and stellar wind. Both winds accelerate particles up to different energies due to the difference in their plasma properties. The shock from the pulsar wind is relativistic and contains  $e^\pm$  plasma coming from the inner pulsar magnetosphere. These electrons can be accelerated up to energies of about  $\sim 10$  TeV. The maximum energy depends on the total energy of the pulsar wind and is maximum at the apastron passage. The shock from the stellar wind is non-relativistic and the initial energies of its electron is low. These electrons can be accelerated only up to GeV energies. The maximum energy that this population can reach is  $\sim 10$  GeV and it is independent on the shock distance from the star. The TeV leptons comptonize the radiation from the massive star initiating IC  $e^\pm$  pair cascades.

## 5.3 Multi-year Observations of LS I +61°303

---

The MAGIC observational campaigns are divided into *Cycles*, which denote an approximately one-year observation time, which is not necessarily coincident with a natural year. As the data was taken and analyzed following this classification, it will also be presented here in this format. In this section, the observational campaigns of LS I +61°303 performed by the MAGIC telescopes from 2010 (*Cycle VI*) to 2014 (*Cycle IX*) are resumed. All the data was taken with the MAGIC stereoscopic system and the analysis method is the standard one described in Chapter 3, unless otherwise noted. For each Cycle, a dedicated Monte-Carlo set of  $\gamma$ -ray events was generated, considering the zenith angle range of the observations, the observation mode (wobble) and the hardware configuration of the telescopes for that epoch. The main results for the analysis of each cycle are collected in this section.

It is worth noticing that the orbital period of LS I +61°303 ( $\sim$ 26.5 days) is very similar to the Moon period (28 days), hence it is almost impossible to perform a complete coverage of all the orbital phases of LS I +61°303 within a single orbital period. MAGIC does not perform observations the nights of full moon. This implies that the orbital phases which are possible to study are approximately always the same for a given cycle, as the nights of brightest moon always fall within the same orbital interval of LS I +61°303.

The data from *Cycles VII*, *VIII* and *IX* are part of a joined campaign with optical telescopes. Simultaneous optical data was obtained first with STELLA robotic telescope (Observatorio del Teide, Tenerife, Canary Islands) and then with LIVERPOOL (Roque de los Muchachos, La Palma, Canary Islands), although our collaborators also provided archival optical spectra which is coincident with some of the observations performed by MAGIC on *Cycle VI*. This joined campaign originated with the aim of searching for anti-/correlation within TeV emission and the size of the decretion disk of the Be star, through measurements of the broadness of the H $\alpha$  line. For that purpose, simultaneous optical-TeV data was taken during orbital phases 0.75 – 1.0, where the sporadic TeV emission is sometimes detected. For an extended analysis and a review, consult Section 5.6. Furthermore, the VHE observations also took place at phases 0.5 – 0.75 to test a possible connection (correlation or anti-correlation) between the super-orbital modulation known from radio and the TeV emission.

In this section, I will first present the results on the analysis for each of the cycles studied (VI, VII, VIII and IX) separately, introducing the data used for each analysis and showing the spectra and lightcurves derived for each cycle. I will perform a search of super-orbital modulation in the flux of LS I +61°303 and look for periodicity using statistic methods using these data together with MAGIC historical data. These tests will also be repeated including VERITAS published data. Later, I will perform spectral variability studies within the four observed cycles and compare with archival data of MAGIC. Finally, I will search for correlation between the TeV emission and optical data obtained with the LIVERPOOL telescope.

### 5.3.1 Cycle VI Campaign

The Cycle VI campaign comprise uneven data samples taken from August 2010 to January 2011. The data covers a zenith angle range from 30° to 50°. The observations were performed on wobble mode with two wobble positions, the standard ones (0, +180). The total amount of data collected during this cycle was 49 hours. The complete data sample was observed under moon conditions [134, 180], hence a dedicated pre-selection was performed to reject low quality data (see Section 3.3). Then, the standard quality selection procedure was followed. The samples were optimized by using a contemporaneous Crab Nebula sample of  $\sim 9$  hours.

## Cycle VI Analysis Results

### Source detection

The cuts performed over the  $\theta^2$  distribution of the  $\gamma$ -ray candidates for *Cycle VI* were optimized over a sample of Crab Nebula data. The cuts applied on the different parameters were: *Hadronness* < 0.22, the *Size* cut for MAGIC-I  $Size_{M1} > 250$  phe and MAGIC-II  $Size_{M2} > 250$  phe and energy threshold  $E > 300$  GeV. LS I +61°303 is detected at a level of  $\sim 15\sigma$  within 27 hours of effective time, with a number of excess events of 282. According to the selection procedure stated on Section 3.3 and performing the selection of data with  $DC < 3000$  mA, the total significance remains the same for  $\sim 22$  hours of effective time, with 260 excess events. From now on, all the results will refer to the data set with  $DC < 3000$  mA.

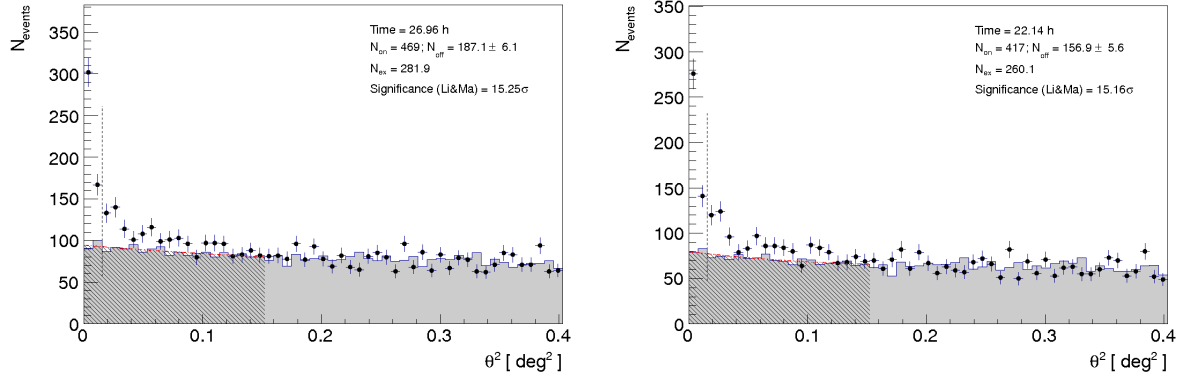


Figure 5.8:  $\theta^2$  distributions with energy threshold of 300 GeV with optimized cuts derived from a Crab Nebula sample. LS I +61°303 shows high significance, which is an indicative that the source could be back in a high-emission flux level again. The ON data is plotted as dots and the normalized OFF data as the grey-shadowed histogram. The vertical line indicates the cut used to define the signal region. *Left:* Complete data sample, with no restrictions in the DC limits. *Right:*  $\theta^2$  distribution for the data set with  $DC < 3000$  mA.

The integral flux above 300 GeV for the complete data set, covering phases  $\phi = 0.4 - 1.0$  is:

$$F(E > 300\text{GeV}) = (5.2 \pm 0.6_{stat}) \times 10^{-12} \text{cm}^{-2}\text{s}^{-1} \quad (5.2)$$

which corresponds to a 4.2 % of the Crab Nebula flux in the same energy

range. In the previous campaign [28], the source was detected at a  $6.3\sigma$  significance level with a flux of  $F(E > 300 \text{ GeV}) = (1.4 \pm 0.3_{\text{stat}} \pm 0.4_{\text{sys}}) \times 10^{-12} \text{ cm}^{-2} \text{ s}^{-1}$  (1.3 % of the Crab Nebula flux) in 48.8 hours of observation for the whole data set.

### *Lightcurve*

It has been possible to derive a nightly lightcurve above an energy of 300 GeV, see Figure 5.9. Seven orbital periods have been observed, unevenly, during this cycle. The flux, significance and time observed each night is quoted on Table 5.1. The periodic emission peak is always within phases  $\phi = 0.55 - 0.75$ , which is a range slightly bigger than the defined in previous campaigns, where the periodical outburst was always located in the range  $\phi = 0.6 - 0.7$ . Most of the signal comes from MJD  $\sim 55570 - 55572$ , which corresponds to January 2011. The peak of emission is located at phase 0.66, reaching a maximum flux of  $F(E > 300 \text{ GeV}) = (10.0 \pm 2.3) \times 10^{-12} \text{ cm}^{-2} \text{ s}^{-1}$  ( $\sim 8$  % of the Crab Nebula flux), with a statistical significance of  $6.0 \sigma$ . Nevertheless, another important peak is located at  $\phi = 0.55$ , with an integral flux of  $F(E > 300 \text{ GeV}) = (9.4 \pm 1.5) \times 10^{-12} \text{ cm}^{-2} \text{ s}^{-1}$  ( $\sim 7.6$  % of the Crab Nebula flux) and a significance of  $12.3 \sigma$ . These values show an increase in the flux with respect to the previous campaign, were LS I +61°303 was detected in a low-flux state. The increase in the flux is an indicative that LS I +61°303 is recovering its high-emission level.

MJD [Days]	$\phi$	Significance (Li&Ma) [ $\sigma$ ]	Integral Flux (E > 300 GeV) [ $10^{-12} \text{ cm}^{-2} \text{ s}^{-1}$ ]	Time <sub>eff</sub> [hours]
55415.2	0.75	1.5	$3.3 \pm 1.6$	1.14
55441.2	0.73	6.4	$5.8 \pm 1.3$	1.94
55442.1	0.76	1.8	$4.9 \pm 1.7$	1.19
55444.2	0.84	-0.7	$-1.2 \pm 0.9$	0.85
55471.1	0.86	0.6	$-0.6 \pm 1.2$	0.76
55486.1	0.42	3.4	$3.9 \pm 1.4$	1.12
55498.1	0.87	0.6	$0.4 \pm 0.7$	1.24
55499.1	0.91	-0.3	$-0.5 \pm 1.4$	0.38
55500.1	0.95	0.9	$0.2 \pm 1.4$	0.89
55512.0	0.40	1.6	$1.5 \pm 1.2$	1.92
55543.0	0.57	2.3	$3.1 \pm 1.0$	2.06
55568.9	0.55	12.3	$9.4 \pm 1.5$	1.87
55569.9	0.59	2.4	$2.3 \pm 1.1$	1.61
55571.0	0.62	7.0	$5.8 \pm 1.1$	2.62
55572.0	0.66	6.0	$10.0 \pm 2.3$	1.11
55573.0	0.70	2.9	$1.7 \pm 1.2$	1.13
55574.0	0.74	2.2	$0.4 \pm 0.3$	2.47

Table 5.1: Daily integrated flux for energies above 300 GeV for data taken on Cycle VI.

If we compare the maximum flux corresponding to this cycle to the previous campaigns of LS I +61°303, we can note that the peak of the emission is slightly lower than in the first campaigns of LS I +61°303 at approximately the same orbital phases ([19], [37], [25]), where the flux above 400 GeV

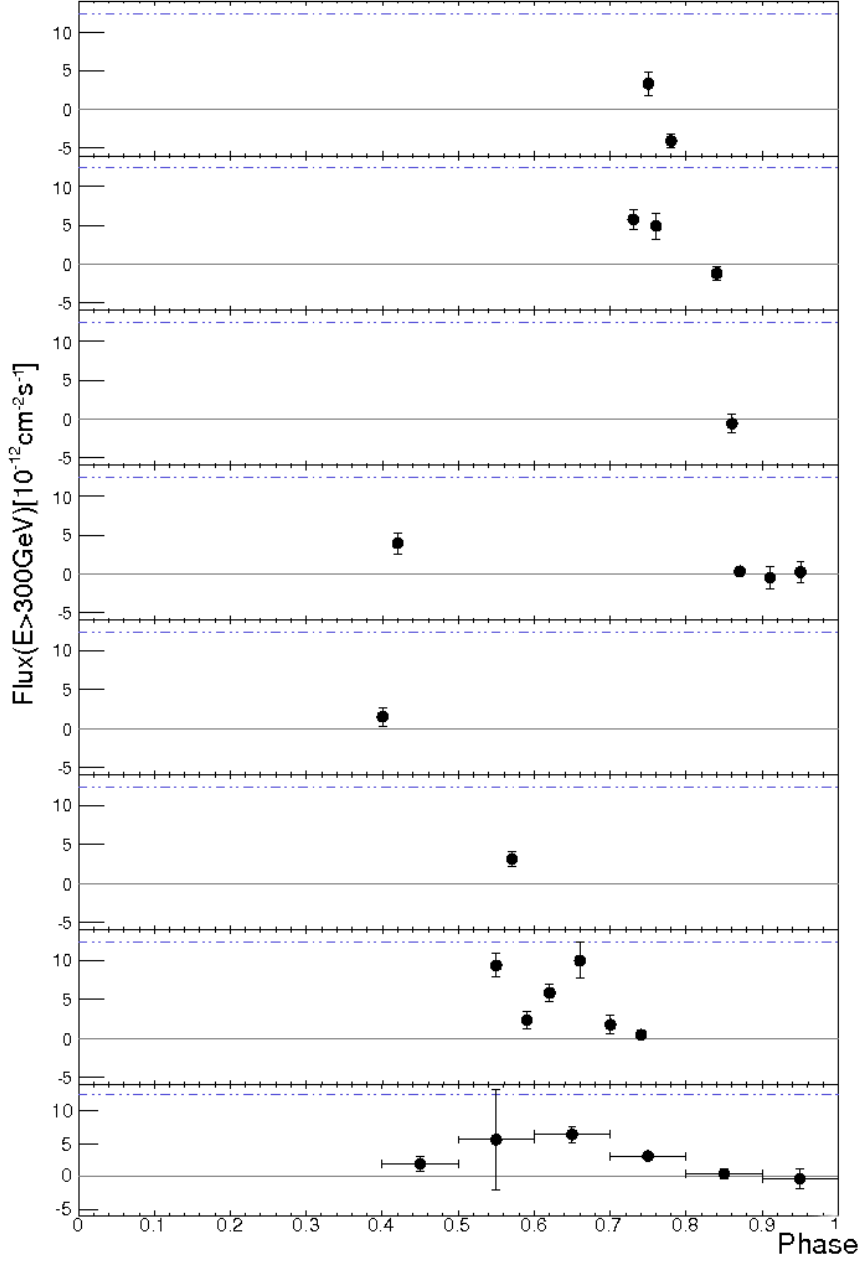


Figure 5.9: Nightly integrated flux above 300 GeV in terms of the orbital phase of the data obtained during Cycle VI observations. The main contribution to the total flux comes from the last orbital period, which corresponds to January 2011 data. The bottom panel shows the average flux over each orbital phase.

was  $\sim 12 - 17\%$  of Crab Nebula. However, on the previous campaign, LS I +61°303 was detected in a low-state of emission [28]. The outburst peak in this occasion was located at  $\phi = 0.62$  and the flux above 300 GeV was  $F(E > 300 \text{ GeV}) = (6.1 \pm 1.4_{\text{stat}} \pm 2.4_{\text{sys}}) \times 10^{-12} \text{ cm}^{-2} \text{s}^{-1}$ , corresponding to  $\sim 5.4\%$  of the Crab Nebula flux. The fact that the maximum emission on *Cycle VI* is higher than in the previous one, might be an indicative that LS I +61°303 is recovering its high-emission state again, which could be indicative of a super-orbital modulation in the  $\gamma$ -ray flux.

A closer look in the data taken on the last orbital period of *Cycle VI*, reveals the existence of a double peak in the phases where a single periodical outburst

is detected. The peaks are observed on phases  $\phi = 0.55$  and  $\phi = 0.66$ , within three days of difference. It is the first time that a double-peak structure is detected in this orbital interval.

Sporadic emission in the orbital range  $\phi = 0.8 - 1.0$  was detected on the previous cycles, although in these observations no significant flux has been detected in this phase range.

### Spectra

The VHE spectrum at energies above 300 GeV for the periodic outburst, between phases 0.55 and 0.75 can be fitted reasonably well ( $\chi^2/\text{NDF} = 3.45/3$ ) by a power-law function:

$$\frac{dN_\gamma}{dAdtdE} = (1.15 \pm 0.04_{\text{stat}} \pm 0.15_{\text{sys}}) \times 10^{-12} E^{(-2.2 \pm 0.1_{\text{stat}} \pm 0.2_{\text{sys}})} \text{TeV}^{-1} \text{cm}^{-2} \text{s}^{-1} \quad (5.3)$$

where  $N_\gamma$  is the number of  $\gamma$  rays reaching the Earth per unit of area A, time t, and energy E (the latter expressed in units of TeV). The spectral slope is slightly different from previous cycles where the spectrum showed a Crab-like index of  $\sim 2.6$ . However, it is not possible to claim a spectral variability, as the spectral index still remains compatible with previous measurements considering systematic errors.

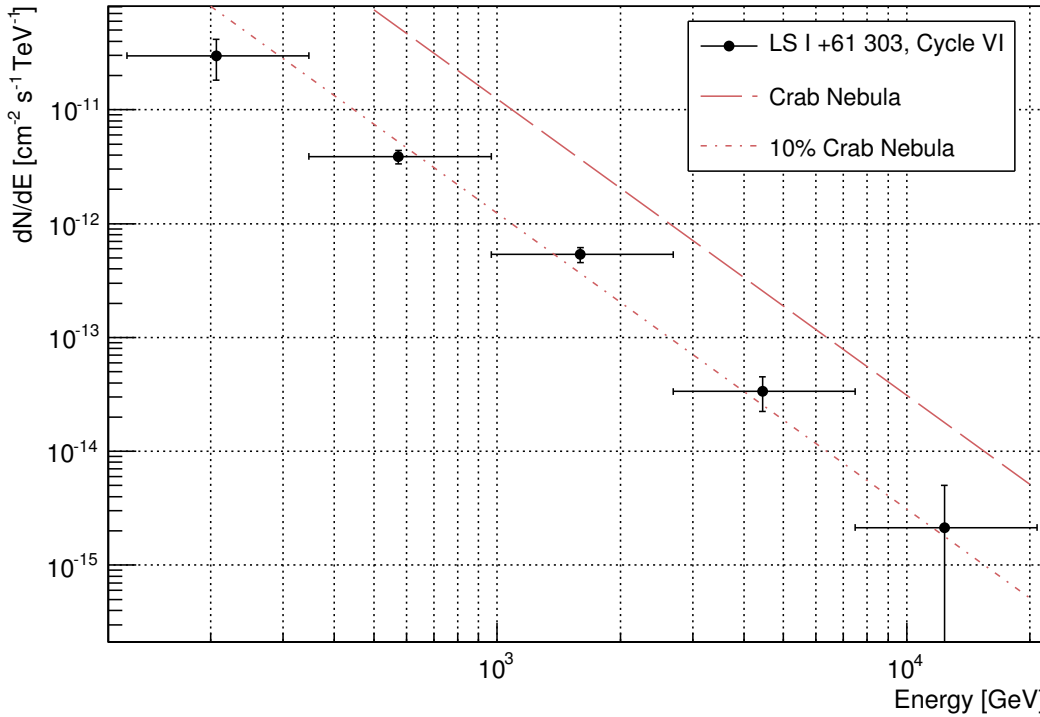


Figure 5.10: Differential energy spectrum for Cycle VI campaign, for energies above 300 GeV and averaged for orbital phases between 0.55 and 0.75. The error bars show statistical uncertainties. The dashed-red line corresponds to a 10% of the differential Crab Nebula flux, also measured by MAGIC [24].

LS I +61°303 has been found to present flux variability within a daily timescale, as seen on preceding campaigns and also visible on Figure 5.9 and Table 5.1. In this specific case, the larger flux variations happen in phases 0.55 – 0.75, where the main periodical emission peak is. However, the most important flux variability is exhibited, in general, on the sporadic second-emission peak in the orbital range 0.8 – 1.0. Nightly variations in the flux (within 24 hours) are found in both orbital phase intervals. It would be

interesting to search for variability at shorter timescales, within few hours. The *Cycle VI* observations have provided the first stereoscopic data where the system is not in the low-emission state. Hence, now that the flux is higher than the previous campaign and thanks to the improvement of sensitivity due to the installation of MAGIC-II telescope, it seems reasonable to search for variability at short timescales, within a night of observation. For that purpose, the days with highest emission have been selected, MJD 55572.0 and 55568.9, with fluxes  $F$  ( $E > 300 \text{ GeV}$ )  $> 9 \times 10^{-12} \text{ cm}^{-2} \text{s}^{-1}$ . We have selected only these two night because they are the only ones with enough statistics to obtain the unfolded spectrum.

A run-wise light-curve has been derived, hence the binning is not exactly even, but still is suitable for our purpose. The binning scale is 8 – 18 min for MJD 55568.9 and 14 – 18 min for MJD 55572.0. The lightcurves are shown on Figure 5.11. The values can be fitted to a constant flux. The probability to obtain the  $\chi^2$ , if all points are fitted with a single constant value is high in both cases, 0.98 and 0.88, which indicates that the flux variations are consistent with statistical fluctuations. From this study, we can conclude that any putative variation in the flux of LS I +61°303 within a timescale smaller than 20 minutes is below the sensitivity of the MAGIC stereoscopic system. Hence, in order to search for intra-night variability, a more sensitive array of telescopes is needed. It may be that the next generation of IACTs, as CTA, will be able to resolve the short-term lightcurve of LS I +61°303.

A spectra can also be derived for these two nights, as the flux is high enough to perform the unfolding. It is shown of Figure 5.12. The spectrum can be well described ( $\chi^2/\text{NDF} = 5.11/3$ ) by a power-law:

$$\frac{dN_\gamma}{dAdtdE} = (2.3 \pm 0.3_{\text{stat}} \pm 0.2_{\text{sys}}) \times 10^{-12} E^{(-2.1 \pm 0.2_{\text{stat}} \pm 0.2_{\text{sys}})} \text{TeV}^{-1} \text{cm}^{-2} \text{s}^{-1} \quad (5.4)$$

Once again, an apparent hint of spectral variability (hardening) is present, but the result, considering systematics, is still compatible with previous campaigns, hence no firm confirmation is possible.

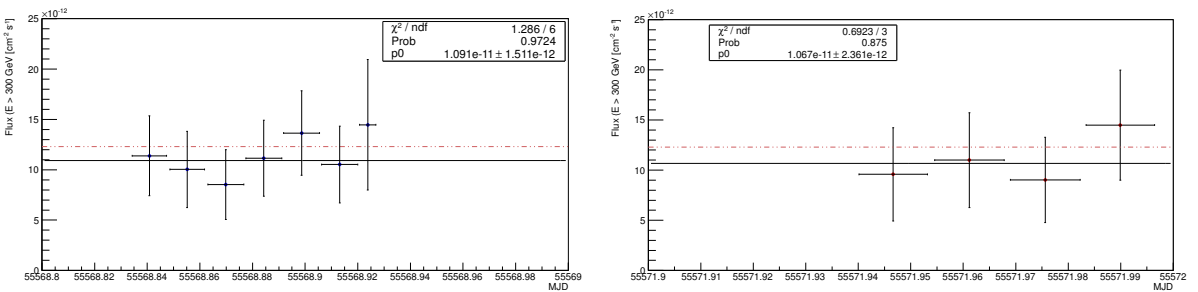


Figure 5.11: Intra-night lightcurve, above 300 GeV, for the two days with highest flux emission of Cycle VI. The black line is a fit to a constant flux value. The probability indicates that the values are highly compatible within this constant flux. The dashed red line represents 10% of the Crab Nebula flux. The vertical error bars quote the statistical errors. *Left:* MJD 55568.9. *Right:* MJD 55572.0.

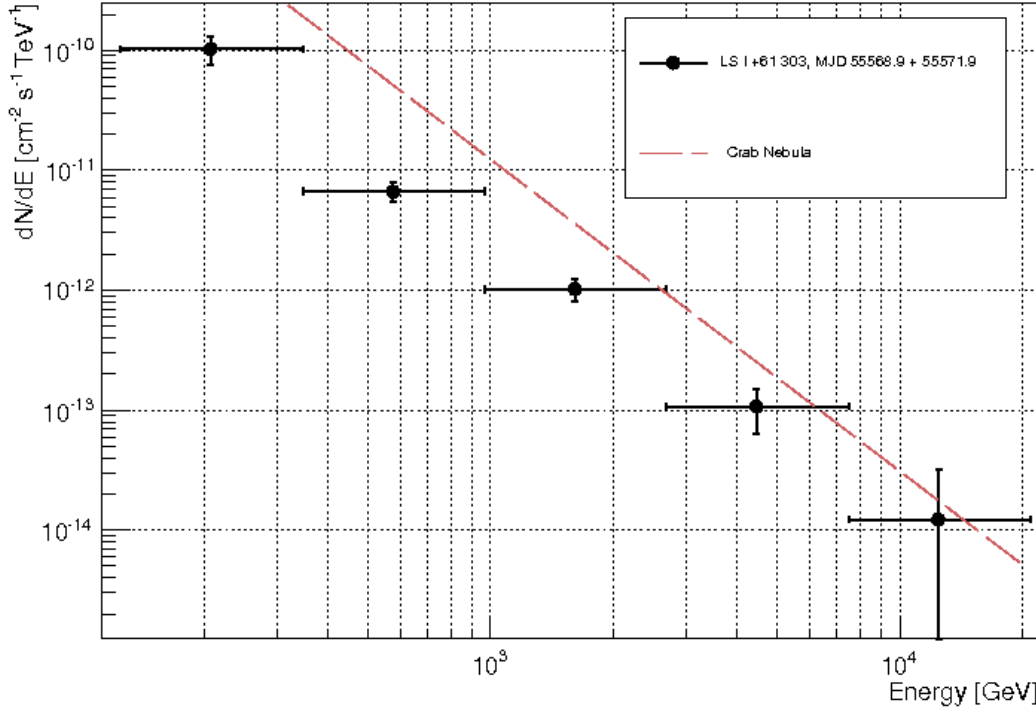


Figure 5.12: Differential energy spectrum of LS I +61°303 for the nights of 55568.9 and 55571.9, the days with the highest VHE emission.

### 5.3.2 Cycle VII Campaign

Cycle VII includes data taken in January and February 2012, for zenith angles between 30° and 50°. The plan was to observe the source for two hours each night during two different orbital periods: from MJD 55942 to 55951 and 55968 to 55978 and obtain simultaneous optical data when the system is on phases 0.75 to 1.0.

During these observations, the telescopes had already undergone a major upgrade. Among other changes, the Data AcQuisition (DAQ) system was renewed from the old DRS2 to the DRS4 chip. Furthermore, MAGIC-I telescope was not operational during some days of the data-taking time (due a break in the mast of MAGIC-I structure). Hence, there are three different configurations for the data taken during this cycle:

- MAGIC-II mono data, taken on January 2012 on days MJD 55942 and 55943, ~3 hours of observed time under dark conditions.
- Pseudo-stereo data: this data was taken on MJD 55947 – 55950, ~4 hours. There is no L3 trigger neither a trigger pattern. Many tests to understand the behavior of the new upgraded telescopes were performed during these days and there is not dedicated Monte-Carlo to analyze this data, so it has not been included in the analysis.
- Stereo data was taken on February 2012, on MJD 55969.8, 55970.8 and from 55975.8 to 55977.9, about 4 hours of data. The data was taken and dark conditions.

Therefore, I have analyzed the mono data taken on January and the stereo data

of February. This two data sets had to be analyzed separately, as they belong to different configurations of the telescopes.

### Source detection

**Mono data** Once the standard quality checks have been performed over the recorded set, 2.56 hours of good data remained. The orbital phases covered are  $\phi = 0.70 - 0.74$ . A signal with total significance of  $3.36\sigma$  has been detected over the two days of observation time with an integral flux above 300 GeV of  $(8.2 \pm 2.5) \times 10^{-12} \text{ cm}^{-2} \text{ s}^{-1}$ , corresponding to a  $\sim 6.6\%$  of the Crab Nebula flux in the same energy range. From the alpha plot distributions shown on Figure 5.13, it is visible that the bulk of the emission comes from day MJD 55944, where the source is detected at  $4\sigma$  at a level of  $(12.0 \pm 3.2) \times 10^{-12} \text{ cm}^{-2} \text{ s}^{-1}$  above 300 GeV, corresponding to a  $\sim 9.7\%$  of the Crab Nebula flux. Once again, this raise in the flux with respect the previous published data indicates that LS I +61°303 abandoned its low-emission state, which is in accordance with the long-term flux modulation predicted by some models [198].

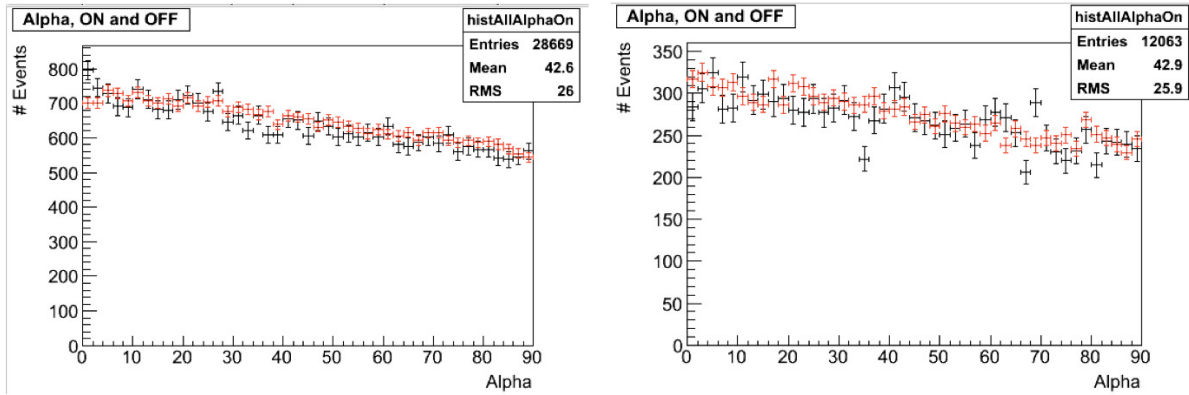


Figure 5.13: Alpha plot distribution of the excess events for the mono data of LS I +61°303 taken on January 2012. The excess is plotted in red and overlaid with the Monte-Carlo  $\gamma$  ray prediction for a point source (black). Most of the signal comes from MJD 55944. *Left:* the source is detected at almost  $4\sigma$  on MJD 55944. *Right:* Alpha plot distribution of the data taken on MJD 55945.

**Stereo data** The stereoscopic data taken on February 2012 has been analyzed using the MAGIC standard analysis and applying the standard quality checks, remaining 3.65 hours of good quality data. The total significance is  $2.4\sigma$  for the complete data set. The search for signal has been performed with the MARS tool *Odie* applying the standard *full range* cuts in the theta2 plot, defined as *Hadronness*  $< 0.16$ , *Size* cut for MAGIC-I  $\text{Size}_{M1} > 125 \text{ phe}$  and MAGIC-II  $\text{Size}_{M2} > 125 \text{ phe}$  and  $E > 250 \text{ GeV}$ . The integral flux above 300 GeV derived for this data is  $(-4.5 \pm 6.3) \times 10^{-13} \text{ cm}^{-2} \text{ s}^{-1}$ , and an upper limit at 95% C.L can be set at  $1.1 \times 10^{-12} \text{ cm}^{-2} \text{ s}^{-1}$ . It is worth remembering that the cuts applied in *Odie* (for the signal search) and *Flute* (for the flux estimation) are not the same. The observations covered the phase range  $\phi = 0.68 - 0.99$  unevenly, as adverse weather conditions did not permit a complete coverage of the orbit. It was not

possible to fulfill the two-hour observation time per night due to the bad weather.

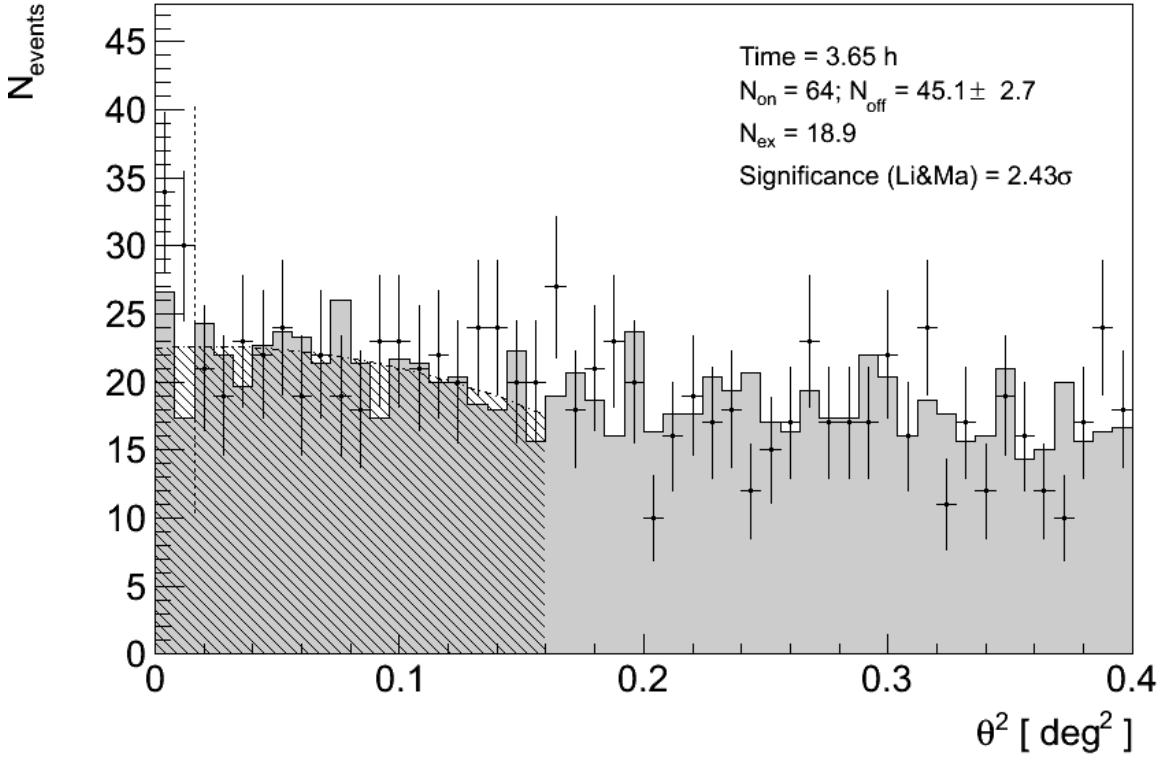


Figure 5.14:  $\theta^2$  plot for the stereo data of February 2012. No significant signal is detected.

### *Lightcurve*

A nightly lightcurve has been derived for energies above 300 GeV. The results are plotted on Figure 5.15 and the values are collected on Table 5.2. Two orbital periods have been observed with two different telescope configurations (MAGIC-II mono data and stereo). The emission peak is located at phase 0.7, with a  $4\sigma$  significance. As happened in the previous cycle, LS I +61°303 is back in high-emission state, which indicates a yearly flux modulation. No emission was detected on phases 0.8 – 1.0.

### *Spectra*

The signal of *Cycle VII* comes mainly from the night of MJD 55944, where LS I +61°303 reaches a flux of almost 10% of Crab above 300 GeV. The maximum flux is emitted at orbital phase 0.7. The spectra for the peak emission is described by a power law ( $\chi^2/\text{NDF} = 1.10/1$ ):

$$\frac{dN_\gamma}{dA dt dE} = (1.1 \pm 0.7_{\text{stat}} \pm 0.2_{\text{sys}}) \times 10^{-12} E^{(-2.7 \pm 0.5_{\text{stat}} \pm 0.2_{\text{sys}})} \text{TeV}^{-1} \text{cm}^{-2} \text{s}^{-1} \quad (5.5)$$

The value of the spectral index is in agreement with previous published values.

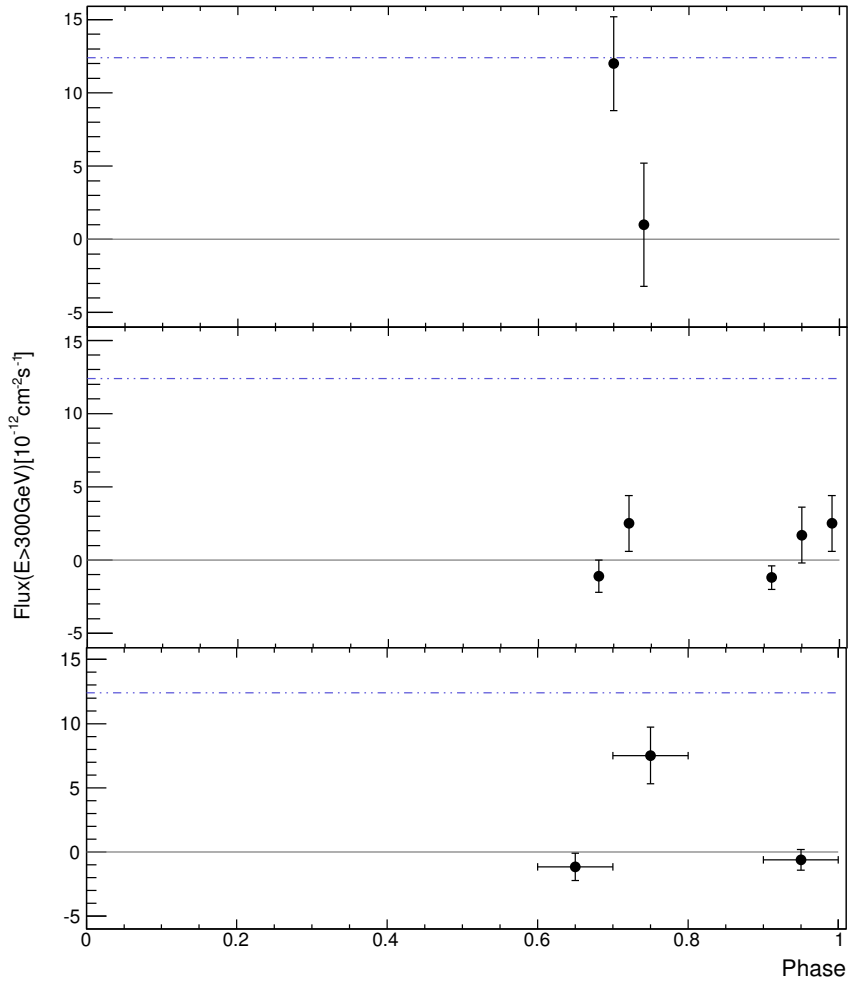


Figure 5.15: Nightly integrated flux above 300 GeV in terms of the orbital phase of the data obtained during Cycle VII observations. Two orbital periods are represented. The peak emission is centered at phase 0.7. *Bottom panel:* Average flux over each orbital phase.

MJD [Days]	$\phi$	Significance (Li&Ma) [ $\sigma$ ]	Integral Flux ( $E > 300$ GeV) [ $10^{-12} \text{ cm}^{-2} \text{s}^{-1}$ ]	Time <sub>eff</sub> [hours]
55944	0.70	4.0	$12.0 \pm 3.2$	1.70
55945	0.74	0.7	$1.0 \pm 4.2$	0.86
55969.8	0.68	-0.4	$-1.1 \pm 1.1$	0.92
55970.8	0.72	1.7	$2.5 \pm 1.9$	0.35
55975.8	0.91	1.3	$1.3 \pm 0.8$	1.66
55976.8	0.95	1.1	$1.1 \pm 1.9$	0.42
55977.8	0.99	1.3	$1.3 \pm 1.9$	0.57

Table 5.2: Daily integrated flux for energies above 300 GeV for the mono and stereo data of LS I +61°303 taken on Cycle VII.

### 5.3.3 Cycle VIII Campaign

*Cycle VIII* observations covered the complete phase range from 0.5 to 1.0 with the aim of searching for super-orbital modulation and establishing an anti-/correlation

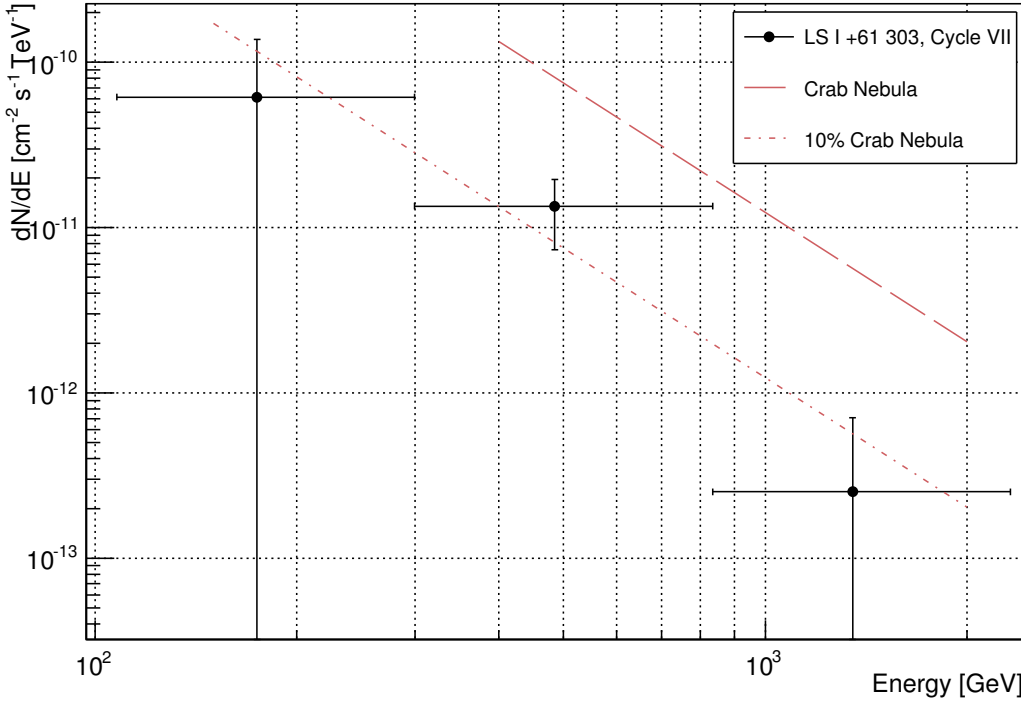


Figure 5.16: Spectra derived for the peak emission of LS I +61°303 on Cycle VII. Error bars represent statistical errors. The dashed red line represents the 10% of the Crab Nebula flux.

with optical data obtained with LIVERPOOL telescope. Considering the  $\sim$ 4 year super-orbit found on radio, and according to [198], it is expected to detect LS I +61°303 in a low-flux state of emission, similar to that found on [28].

The observations were performed between November 2012 and November 2013. From November 2012 to January 2013,  $\sim$ 19 hours of data were taken, covering only the phases  $\phi = 0.89 - 1.0$ , due to LS I +61°303 observability issues. From September to November 2013, only phases from 0.5 to 0.75 where covered, also due to the source observability and moonlight conditions. About 26 hours of data were recorded. The zenith angle of the observations ranges from  $32^\circ$  to  $45^\circ$ .

These two sets of data have been analyzed separately due to different configurations in the telescopes, hence the Monte-Carlo used in both analyses has been different. The two sets of data were recorded with the new MAGIC-I camera. However, the second set, from September to November 2013 includes some minor hardware upgrades and new LUTs applied to MAGIC-I AMC.

#### Source detection

Both data set have been analyzed using the standard analysis procedure. The cuts for the search of signal were optimized with a sample of contemporaneous Crab Nebula data, leading to  $Hadronness < 0.24$ ,  $Size$  cut for MAGIC-I  $Size_{M1} > 250$  phe and MAGIC-II  $Size_{M2} > 250$  phe.

- November 2012 – January 2013 data set: after performing the standard qual-

ity checks, 9.4 hours of good quality data remained. A signal with a  $5.3\sigma$  significance is detected. These observations covered the phases where the sporadic emission of LS I +61°303 is detected, in this case  $\phi = 0.89 - 1.0$ .

- September – November 2013 data set: 24.8 hours of good data remained after performing the quality selection. The phase coverage for this set is  $\phi = 0.5 - 0.75$ , including the orbital phases where the peak of emission is expected. The significance for this set is  $3.6\sigma$ , which is a first indicative that the flux has lowered again.

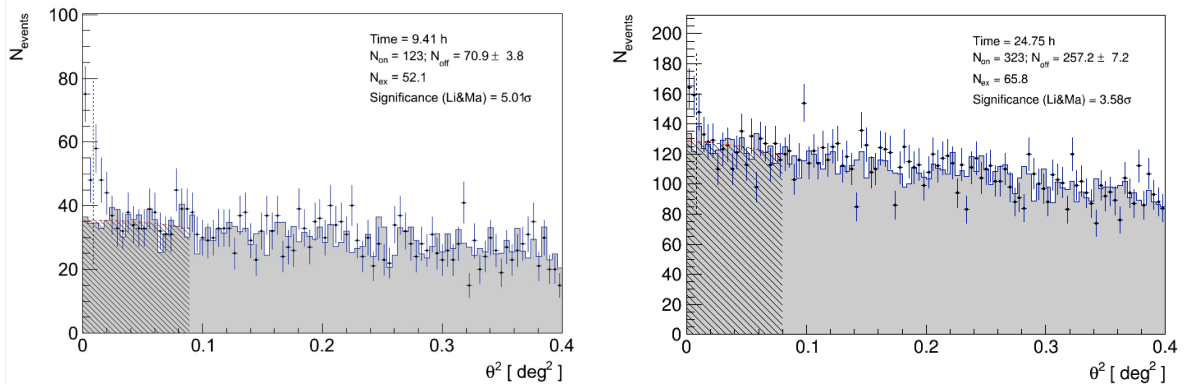


Figure 5.17:  $\theta^2$  distributions for the two data sets of LS I +61°303 observed on Cycle VIII. *Left:* phases 0.9 – 1.0. *Right:* phases 0.5-0.75.

### Lightcurve

The *Size* cut applied over the samples was 80 phe, as some moonlight observations were performed. The total integrated flux for the first data set ( $\phi = 0.9 - 1.0$ ) is  $F(E > 300 \text{ GeV}) = (3.6 \pm 0.7) \times 10^{-12} \text{ cm}^{-2} \text{ s}^{-1}$ , ( $\sim 3\%$  of the Crab Nebula flux). The peak of the emission in this phase range is located at orbital phase 0.93, with a flux of  $F(E > 300 \text{ GeV}) = (7.0 \pm 2.0) \times 10^{-12} \text{ cm}^{-2} \text{ s}^{-1}$ , ( $\sim 6\%$  of the Crab Nebula flux). For the second data set ( $\phi = 0.5 - 0.75$ ), the integral flux is  $F(E > 300 \text{ GeV}) = (9.7 \pm 4.3) \times 10^{-13} \text{ cm}^{-2} \text{ s}^{-1}$ . In this case, the peak of emission is located at orbital phase 0.73, with an integrated flux of  $F(E > 300 \text{ GeV}) = (5.3 \pm 1.8) \times 10^{-12} \text{ cm}^{-2} \text{ s}^{-1}$ , ( $\sim 4\%$  of the Crab Nebula flux), which is at the same level of the fluxes reported in [28]. From these observations, we can conclude that LS I +61°303 has recovered a low-emission state since it was first detected.

### Spectra

The emission level of LS I +61°303 is too low on this campaign to obtain significant daily spectra. However, it was sufficient to obtain differential flux spectra (See Figure 5.19) with the forward unfolding. The other unfolding methods can also be applied, but some energy bins are missing due to the low signal. We have fitted the phases for the periodic outburst, 0.5 – 0.75 to a power law:

$$\frac{dN_\gamma}{dAdtdE} = (1.5 \pm 1.1_{stat} \pm 0.2_{sys}) \times 10^{-13} E^{(-3.0 \pm 0.4_{stat} \pm 0.2_{sys})} \text{ TeV}^{-1} \text{ cm}^{-2} \text{ s}^{-1} \quad (5.6)$$

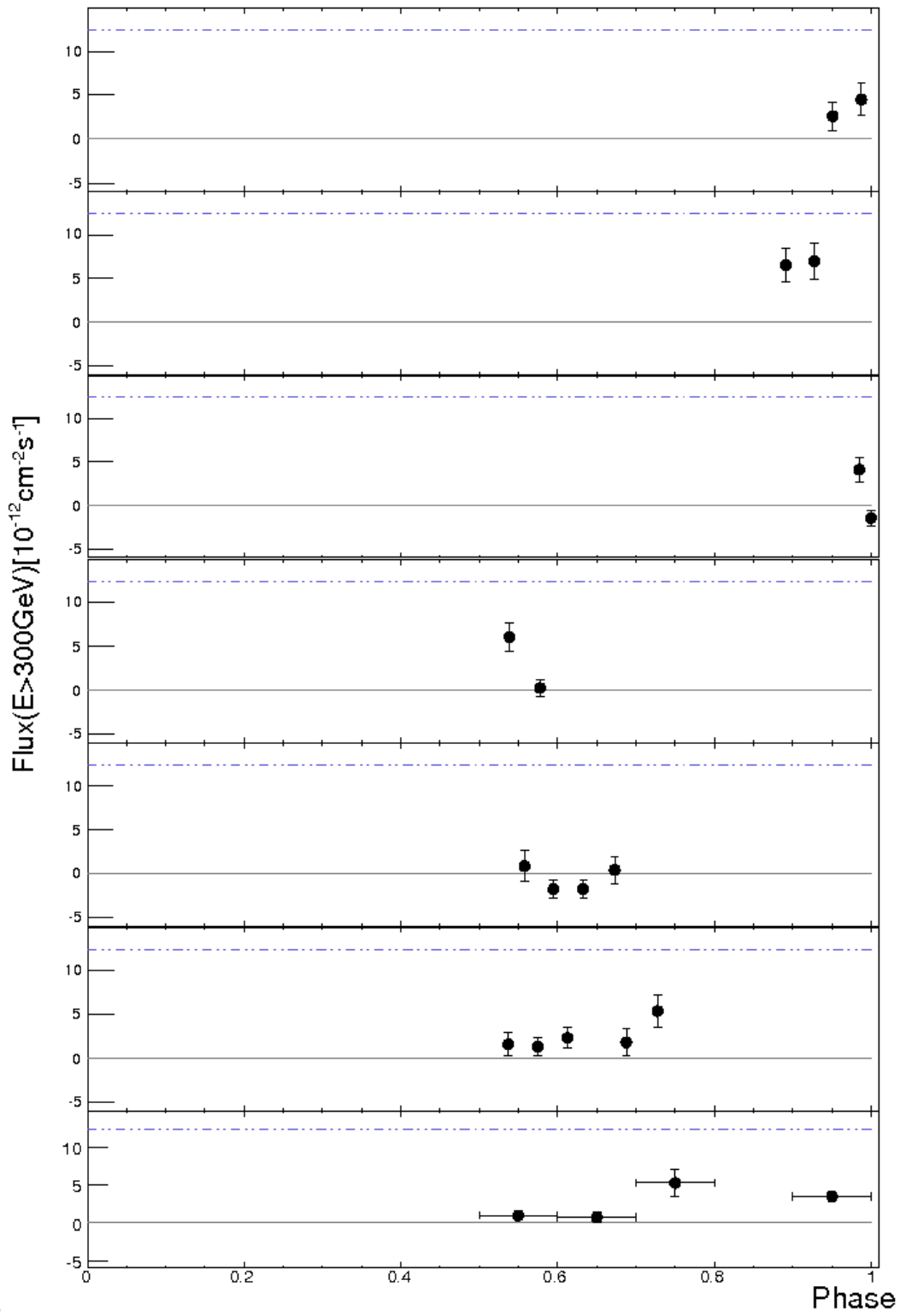


Figure 5.18: Nightly lightcurve of LS I +61°303 for *Cycle VIII* observations. *Bottom panel:* Phaseogram.

with  $\chi^2/\text{NDF} = 20.22/8$ . No evidence for spectral variability is found. The spectral slope is compatible, within errors, with those found on previous campaigns.

MJD [Days]	$\phi$	Significance (Li&Ma) [ $\sigma$ ]	Integral Flux ( $E > 300$ GeV) [ $10^{-12} \text{cm}^{-2}\text{s}^{-1}$ ]	Time <sub>eff</sub> [hours]
56242.0	0.95	0.7	$2.6 \pm 1.6$	0.99
56243.0	0.99	1.7	$4.5 \pm 1.8$	1.24
56266.9	0.89	2.3	$6.6 \pm 1.9$	1.09
56267.9	0.93	5.0	$7.0 \pm 2.0$	1.02
56295.9	0.99	3.0	$4.1 \pm 1.4$	1.71
56296.8	1.01	-0.6	$-1.4 \pm 0.9$	2.33
56549.1	0.54	3.1	$6.1 \pm 1.6$	2.69
56550.1	0.58	0.6	$0.3 \pm 1.0$	2.98
56576.1	0.56	0.2	$0.8 \pm 1.8$	1.09
56577.0	0.60	-2.7	$-1.8 \pm 1.1$	2.82
56578.0	0.63	-2.7	$-1.8 \pm 1.0$	2.69
56579.1	0.67	0.2	$0.4 \pm 1.5$	1.30
56602.0	0.54	0.7	$1.6 \pm 1.3$	2.10
56603.0	0.58	2.6	$1.3 \pm 1.0$	2.93
56604.0	0.61	1.0	$2.3 \pm 1.2$	2.72
56606.0	0.69	1.6	$1.8 \pm 1.6$	0.98
56607.1	0.73	3.6	$5.3 \pm 1.9$	1.17

Table 5.3: Daily integrated flux for energies above 300 GeV for the observations of LS I +61°303 performed on Cycle VIII.

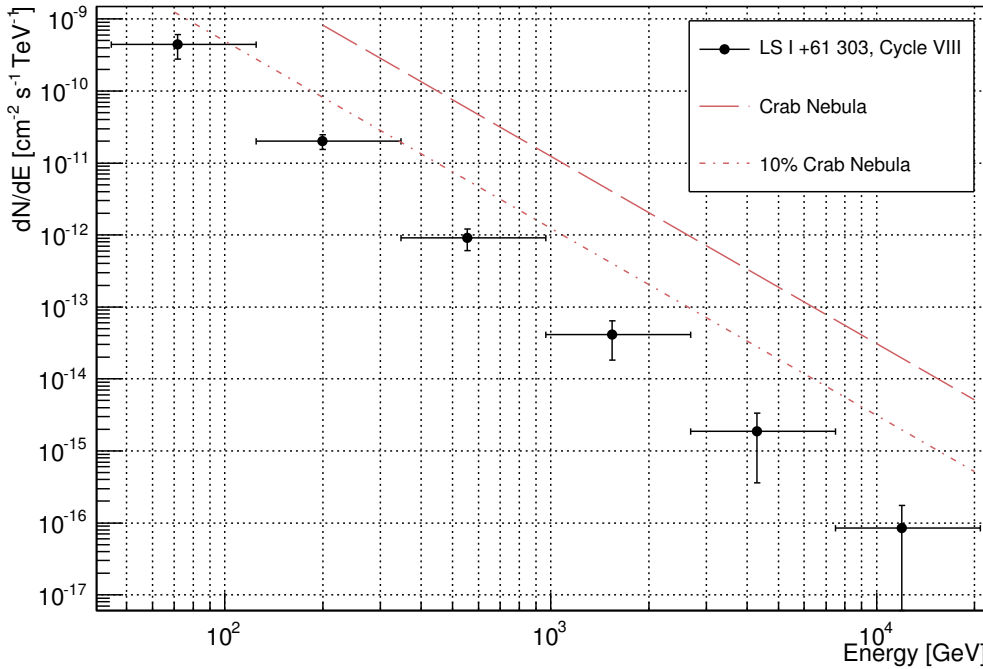


Figure 5.19: Differential energy spectra for Cycle VIII data for the phases 0.5 – 0.75, where the periodical VHE outburst is expected. The spectral index is compatible with previous campaigns.

### 5.3.4 Cycle IX Campaign

Finally, LS I +61°303 was observed for 15.7 hours for a zenith angle range 32°–45° on Cycle IX, from 31st December 2013 to 07th January 2014, during one orbital

period. The data set spans from orbital phase 0.61 to 0.88. The intention was to observe the full trend starting on phase 0.5, although adverse weather conditions did not permit it.

### Source Detection

The hardware status did not change from the last data set of *Cycle VIII* to *Cycle IX*, hence the same cuts were applied. After performing the standard selection cuts, 15.7 hours of good quality data remained for the analysis. The total significance is  $1.4\sigma$  (see Figure 5.20).

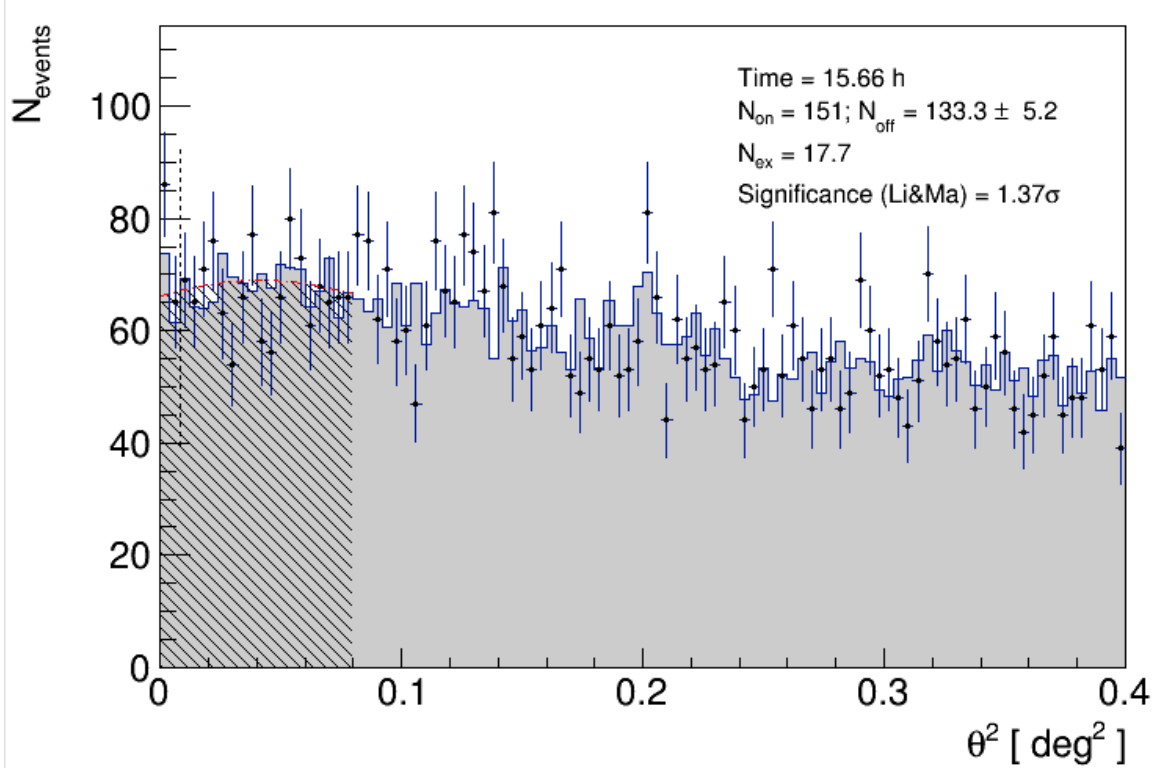


Figure 5.20:  $\theta^2$  distribution for the *Cycle IX* data.

### Lightcurve

As in the precedent case, a *Size* cut of 80 phe was applied, as some moonlight observations were performed. The integral flux above 300 GeV for the complete data set is  $F$  ( $E > 300 \text{ GeV}$ ) =  $(5.8 \pm 5.8) \times 10^{-13} \text{ cm}^{-2} \text{s}^{-1}$  ( $\sim 5\%$  the Crab Nebula flux in the same energy range), hence an upper limit can be set at  $2.4 \times 10^{-12} \text{ cm}^{-2} \text{s}^{-1}$ . The integral flux is 2.4 times lower than the one reported on [28]. A daily lightcurve has been derived, see Figure 5.21 and Table 5.4. The emission reaches a maximum flux of  $(5.0 \pm 1.4) \times 10^{-12} \text{ cm}^{-2} \text{s}^{-1}$  around orbital phase 0.87, with a significance of  $4.6\sigma$ .

The non-detection of LS I +61°303 during *Cycle IX* is an indicative of the recovery of the low-state reported by MAGIC [28].

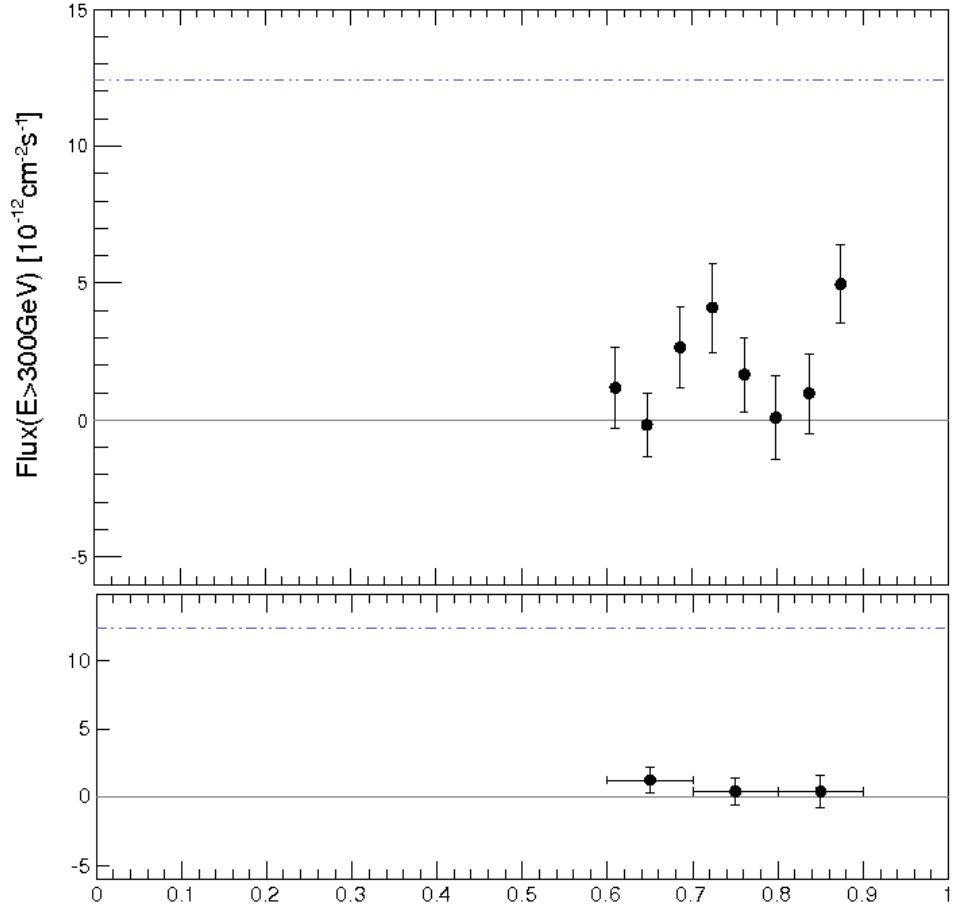


Figure 5.21: *Top:* Lightcurve of LS I +61°303 on cycle IX. *Bottom:* Phaseogram for *Cycle IX*. The integral fluxes were computed above 300GeV.

MJD [Days]	$\phi$	Significance (Li&Ma) $[\sigma]$	Integral Flux ( $E > 300$ GeV) $[10^{-12} \text{cm}^{-2} \text{s}^{-1}]$	Time <sub>eff</sub> [hours]
56656.9	0.61	0.9	$1.2 \pm 1.5$	1.68
56657.9	0.65	-0.1	$-0.2 \pm 1.1$	2.93
56658.9	0.69	2.0	$2.7 \pm 1.5$	2.37
56659.9	0.72	3.0	$4.1 \pm 1.6$	1.75
56660.9	0.76	1.3	$1.7 \pm 1.4$	2.20
56661.9	0.80	0.1	$0.1 \pm 1.5$	1.14
56662.9	0.84	0.7	$1.0 \pm 1.5$	1.95
56663.9	0.87	4.6	$5.0 \pm 1.4$	1.63

Table 5.4: Nightly lightcurve of LS I +61°303 on *Cycle IX*. The data covers one orbital cycle.

### Spectra

The total signal is not sufficient to obtain a VHE spectrum. Differential upper limits have been computed, assuming a Crab-like spectrum with spectral slope 2.6. The spectrum is plotted on Figure 5.22.

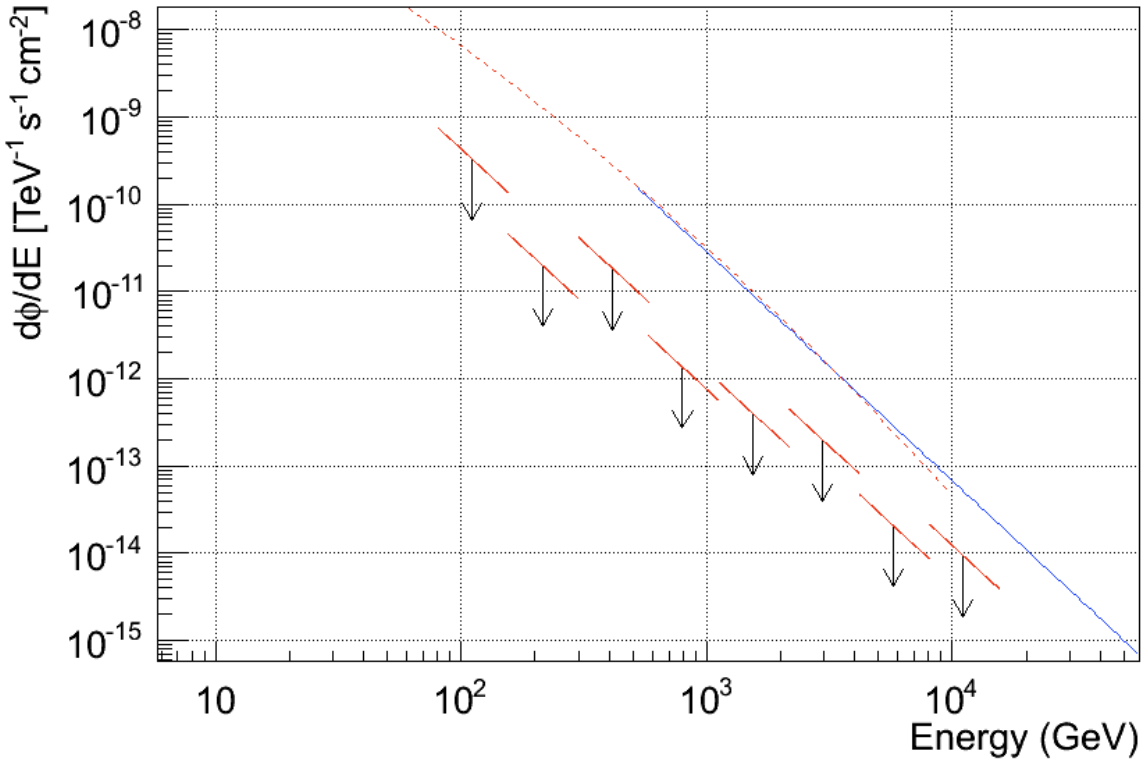


Figure 5.22: Differential upper limits, at 95% C.L., calculated for *Cycle IX* data of LS I +61°303. The red dashed line is the Crab spectrum defined in [24] and the blue line is the Crab spectrum observed by HEGRA.

## 5.4 Super-orbital variability

There is an evidence, from published results of LS I +61°303 and also from the results of the 4-year data analyzed on Section 5.3, that the average flux emission of LS I +61°303 suffers a yearly variability. The flux can reach a maximum emission of 10 – 17 % the Crab Nebula flux on periods of high emission as reported on [19], [25] and [37] and also based on the results of *Cycle VI* in Subsection 5.3.1 and *Cycle VII* Subsection 5.3.2 reported on this thesis. In epochs of low-state, the maximum flux of the source is reduced to a ∼4 – 5% the Crab Nebula flux, as described in [28] and measured on Subsections 5.3.3 and Subsection 5.3.4.

A cyclical behavior was proposed by [198], whose model predicted that the system would be back in high state around May 2010 and then it would lower or disappear about October 2012. This model maintains the radio super-orbital modulation of the flux. Hence, the source should be detected on high state on super-orbital phase  $\phi_{super-orbit} \sim 0.2$  and disappear around  $\phi_{super-orbit} \sim 0.7 - 0.8$ . A very significantly lower flux shall be detected at super-orbital phase  $\sim 1 \pm 0.2$ . From the studies from *Cycle VI* to *Cycle IX*, it can be concluded that LS I +61°303 was back to high state in January 2011, at  $\phi_{super-orbit} \sim 0.32$  and was still high until January 2012, at  $\phi_{super-orbit} \sim 0.55$ . The flux was reduced on September–November 2013, at super-orbital phase  $\phi_{super-orbit} \sim 0.92$ . On January 2014, at  $\phi_{super-orbit} \sim 0.97$ , the source was still in the low-emission state.

Still, it is needed to understand if the yearly variability of LS I +61°303 maintains the cyclical behavior inferred by radio data, where the outbursts, peak flux den-

sities and spectral index show a super-orbital modulation of  $1667 \pm 8$  days [96]. This super-orbital phase behavior has recently been found at HE  $\gamma$  rays [195].

For that purpose, we have folded within a super-orbit of 1667 days all the data of LS I +61°303 recorded by MAGIC since it was first detected on 2005 until the last data taken on 2014. The archival data used in the analysis was taken from MAGIC publications: [19], [23], [37], [25] and [28]. The data from 2010 to 2014 is the one presented in this thesis. The data will be fitted to a sinusoidal signal:

$$y = p_0 + p_1 \times \sin((x + p_2) \times 2\pi) \quad (5.7)$$

where  $p_0$  represents a pedestal flux value,  $p_1$  is the amplitude of the signal and  $p_2$  the phase shift. The fit to a sinusoidal is performed over one orbital cycle. The same procedure is followed when a constant fit is performed. When plotting the super-orbital function, a super-orbital cycle, repeated twice, is represented to see more clearly the possible periodicity. The choice of a sinusoidal signal is not based in any *a priori* physical theory but due to the relatively low number of data points and also due to the fact that any periodical function can be described as a serie of sines. Hence, it is worth noticing that the signal could be periodic but have a different shape.

Statistical and systematic uncertainties in the integral flux have been considered in this study. In the case of the systematics, a 12% uncertainty is applicable for the stereo performance [32]. No official systematics in the integral flux has been calculated for the single telescope configuration. However, on [24], where the performance on the MAGIC-I telescope is studied, the nightly integral flux for the Crab Nebula is study along approximately three months and those values are compatible to a constant flux considering a 20% statistical uncertainty. This value can set an upper limit to the value of the systematics of the mono system. Also, the inclusion of another telescope (MAGIC-II) does not necessarily imply a remarkable improvement of the systematics, although it may change a bit. Hence, it has been decided to consider 15% uncertainty for the mono configuration.

In principle, a search for super-orbital modulation of the flux in the phases where the periodic VHE outburst is present will be performed, at orbital phases  $\phi = 0.5 - 0.75$ , near apastron, because these phases have presented the maximum periodic peaks of emission for several cycles. Also, the periodicity in radio and HE is detected in the phases where the periodic outburst is emitted, hence a similar behavior may occur at VHE in the correspondent phase interval. As it has been commented before, the source has been detected twice in high and low-emission states at VHE  $\gamma$  rays, its signature visible only at the apastron orbital phases.

The aim of this search is to detect the VHE periodical outburst and test if it follows the  $\sim 4.5$  year modulation found in radio. For that purpose, the peak of the flux emission for each orbital period is sought, between orbital phases 0.5 – 0.75. For being certain that the highest peak in a certain orbital period is selected, the maximum emission is selected when at least three consecutive fluxes have been detected. With this procedure, it is assured to have detected the peak of the periodic outburst for a certain orbital period. Adopting this definition, it is expected to detect yearly variability in the peak, as it is already visible in MAGIC observations, and probe its long-term periodicity.

The integral flux as a function of the super-orbital phase is shown on Figure 5.23.

The probability of the fit is 0.13, which is compatible within the radio modulation while the probability of the flux of being a statistical fluctuation of a constant flux is  $8.9 \times 10^{-15}$ . Therefore, it exists a yearly variability in the VHE emission of the source and a compatibility with the radio long-term period. Furthermore, the change in the amplitude is also similar to that found in radio, where the ratio between maximum and minimum flux was stated to be  $\leq 10$ . Hence, to confirm the super-orbital signature with the radio period, it is then necessary to detect the peak of emission in the region outburst.

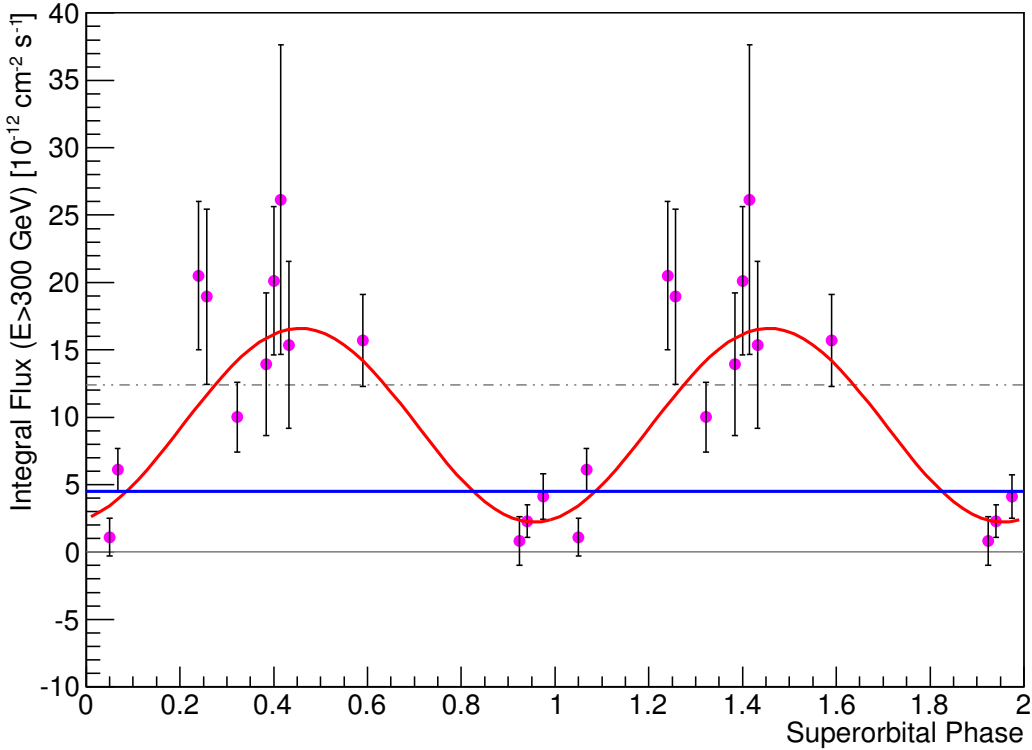


Figure 5.23: Peak of the integral flux emitted for each orbital period, for orbital phases 0.5 – 0.75, when at least three consecutive days have been observed and their flux computed, in terms of the super-orbital phase (magenta dots), as defined by radio [96]. The fit to a sinusoidal (red solid line) and to a constant (blue solid line) are also represented. The grey dashed line represents the 10% Crab Nebula flux. The gray solid line marks the zero level, just as a reference. Statistical and systematic errors are considered.

To increase the sampling in the search for the super-orbital signature, another set of data containing the maximum flux emitted in the phase interval  $\phi = 0.5 - 0.75$ , independently on the significance of the signal is defined. The maximum emission is defined just as the highest flux in the considered phase for each orbital period, without any constraints on the number of days observed and analyzed. The result of the folded data is shown on Figure 5.24. The data points have been fitted to the sinusoidal function stated before. The probability of the fit is  $4.0 \times 10^{-5}$ , which is not significant to claim for a super-orbital period and it is several orders of magnitude below the probability found on the former case. The probability of the flux being a statistical fluctuation of a constant flux is  $1.4 \times 10^{-12}$ . This result confirms that the selection of the peak of emission as a proxy to determine if there is a long-term signature is the appropriate approach. By selecting the

peak of emission, when at least three consecutive fluxes have been measured, it is assured that the outburst peak has been detected. However, the selection of the maximum emission only indicates that a maximum flux has been detected, which might be the peak of the flux in that period or not. Since it does not take into account the fluxes measured just previously or after, it is not possible to determine if the maximum flux measured corresponded to the outburst peak.

The data used for the computation of the super-orbital modulation by selecting the peak of emission is collected on Table 5.5. The uncertainties in the TeV fluxes are statistical and systematic, added quadratically.

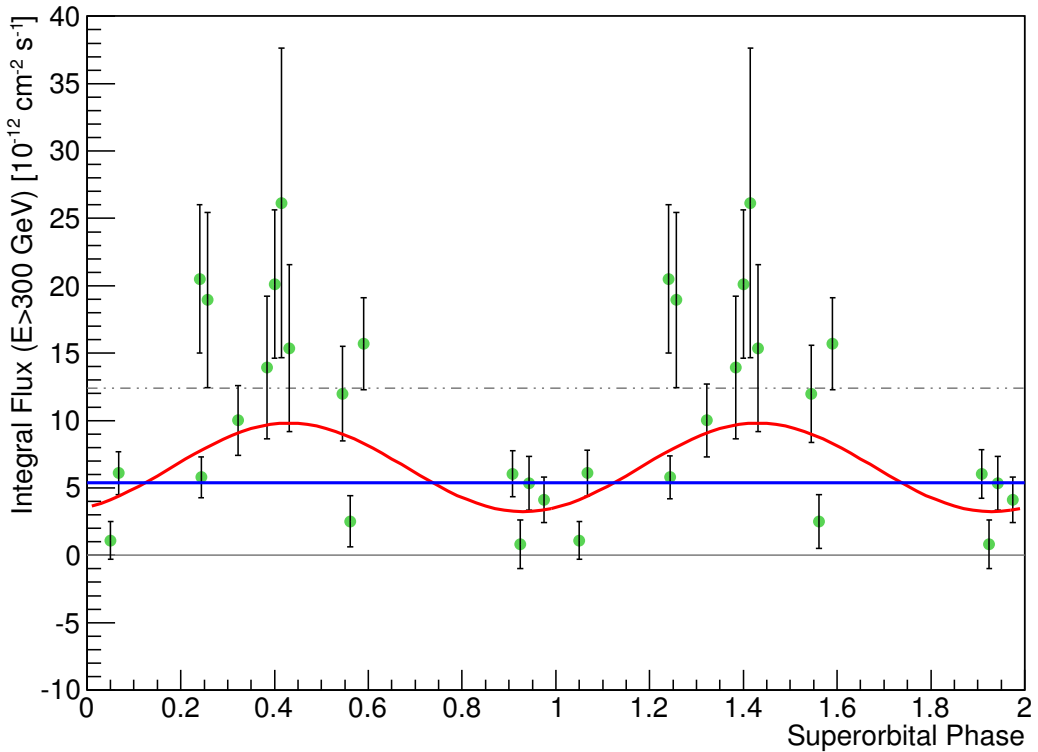


Figure 5.24: Maximum flux emitted for each orbital period, for orbital phases 0.5 – 0.75, in terms of the super-orbital phase (green dots), as defined by radio [96]. The fit to a sinusoidal (red solid line) and to a constant (blue solid line) are also represented. The grey dashed line represents the 10% Crab Nebula flux. The gray solid line marks the zero level, just as a reference.

Hence, the existence of a long-term variability folded into the  $\sim 1667$  days radio super-orbital period and following a sinusoidal distribution is compatible at a 13% with the TeV fluxes of LS I +61°303 measured by MAGIC. It is possible to confirm from our observations that there is a yearly variation in the VHE flux of LS I +61°303 in the peak intensity for the phases near apastron ( $\phi = 0.5 - 0.75$ ), being the maximum peak of emission, in average,  $\sim 3 - 5$  times higher than the minimum flux. The probabilities of the flux of being a statistical fluctuation with respect a constant value is highly unlikely, with a value of  $8.9 \times 10^{-15}$ .

VERITAS has also performed numerous observations of LS I +61°303 along years [9, 7, 8, 36]. In order to increase the data sample to search for super-orbital modulation of the signal, published data of VERITAS has been included in the

MJD [Days]	$\phi_{super-orbit}$	Integral Flux ( $E > 300$ GeV) $[10^{-12} cm^{-2}s^{-1}]$
53768.9	0.24	$20.5 \pm 5.5$
53796.9	0.26	$19.0 \pm 6.5$
54008.0	0.38	$13.9 \pm 5.3$
54035.1	0.40	$20.1 \pm 5.5$
54060.0	0.41	$26.1 \pm 11.5$
54088.0	0.43	$15.4 \pm 6.2$
54352.2	0.59	$15.7 \pm 3.4$
55119.0	0.05	$1.1 \pm 1.4$
55147.0	0.07	$6.1 \pm 1.6$
55572.0	0.32	$10.0 \pm 2.6$
56576.1	0.92	$0.8 \pm 1.8$
56604.0	0.94	$2.3 \pm 1.2$
56659.9	0.97	$4.1 \pm 1.7$

Table 5.5: Values of the peak (*top*) and maximum (*bottom*) emission for the data taken on orbital phases 0.5 – 0.75, where the periodic VHE outburst is located.

analysis [9, 7, 36]. The peak of emission for phases 0.5 – 0.75 data has been selected. 20 % systematic uncertainties have been considered [136], which have been added quadratically to statistical uncertainties. The resulting plot is shown on Figure 5.25. By including the VERITAS points, the probability has increased with respect using only MAGIC data. The TeV flux is 25 % compatible with the radio super-orbital period. The probability of the flux of being a fluctuation is  $5.9 \times 10^{-9}$ .

Sporadic VHE  $\gamma$ -ray emission has also been detected at phases 0.75 – 1.0. This emission, in principle, does not seem to present yearly periodical variability of the flux level (for a review, see [28], Section 5.4). However, it is appropriate to check if it fits within the radio super-orbital modulation of the flux, just to cover all possibilities. In this case, all the data lying in the desired orbital interval is considered. Since no periodical outburst is detected in this region, it makes no sense in searching for the peak of the TeV flux, since the emission is not periodical. The considered data is collected on Table 5.6. The super-orbital trend is shown on Figure 5.26. The spread in the flux is larger than in the other phases, since the variability in the flux is larger in this orbital range. The probability of the sinusoidal fit is  $2.1 \times 10^{-7}$ , hence it is not compatible with the radio super-orbital period. The probability of the emission of being a statistical fluctuation is  $4.3 \times 10^{-9}$ . The low probabilities confirm that the sporadic behavior of the TeV flux in the orbital interval 0.75 – 1.0 does not show yearly periodicity modulated within the radio period.

Finally, the VHE emission variability can be represented in terms of the temporal evolution with respect the MJD, to study the tendency of the flux along the years. In this case, the fit to a sinusoidal is:

$$y = a_0 + a_1 \times \sin \left( \left( \frac{x - MJD_0}{a_2} + a_3 \right) \times 2\pi \right) \quad (5.8)$$

where  $a_0$  represents a pedestal flux value,  $a_1$  is the amplitude of the signal,  $a_2$

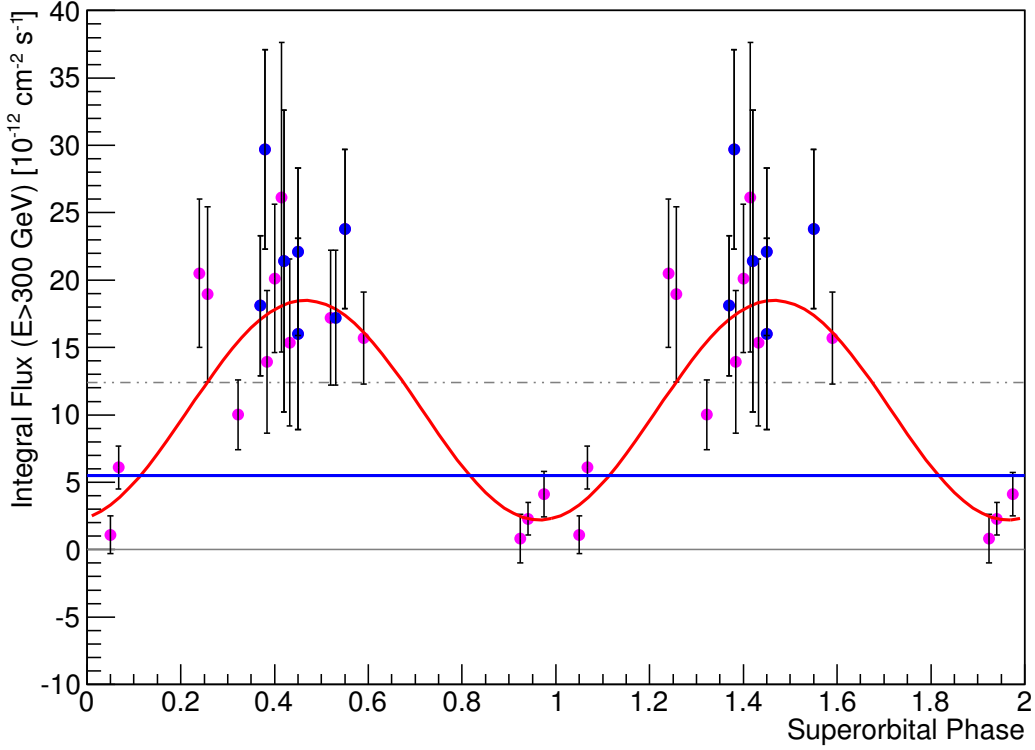


Figure 5.25: Peak flux emitted for each orbital period, for orbital phases  $0.5 - 0.75$ , in terms of the super-orbital phase as defined by radio [96]. MAGIC (magenta dots) and VERITAS (blue dots) points have been used in this analysis. The fit to a sinusoidal (red solid line) and to a constant (blue solid line) are also represented. The grey dashed line represents the 10% Crab Nebula flux. The gray solid line marks the zero level, just as a reference.

is the period of the signal and  $a_3$  the phase shift.  $MJD_0 = 43366.275$  is the reference MJD.

On Figure 5.27, it is plotted the trend of the emission for the peak of the flux on orbital phases  $0.5 - 0.75$ . A sinusoidal function of period  $1747 \pm 127$  days provides the best fit with a probability value of 0.19, while the fit to a constant flux ( $y = a_0 x$ ) is  $1.3 \times 10^{-8}$ . The flux being a statistical fluctuation is discarded. The parameters of the fit are collected on Table 5.7. This result supports the theory that the VHE component of LS I +61°303 is variable in a yearly timescale with a similar behavior than the radio and HE bands.

The temporal evolution has also been studied including VERITAS data to the MAGIC data set. Figure 5.28 shows the resulting fit to the samples. The best fitting period is  $1782 \pm 106$ , value that is compatible with the radio super-orbital period. The probability of the fit is 0.39, high enough to claim for compatibility.

It can be concluded, from the analysis presented in this Section, that there is a yearly variability in the VHE flux emitted by LS I +61°303, which is more clearly visible in the region near apastron, at phases  $\phi = 0.5 - 0.75$ , which is where the periodic outburst is detected. The source has been detected twice in a high-flux emission state and twice in a low state, which is compatible with the behavior at other wavebands and with theoretical predictions. The TeV emission is 13% compatible with the  $\sim 1667$ -day periodicity found in other wavelengths.

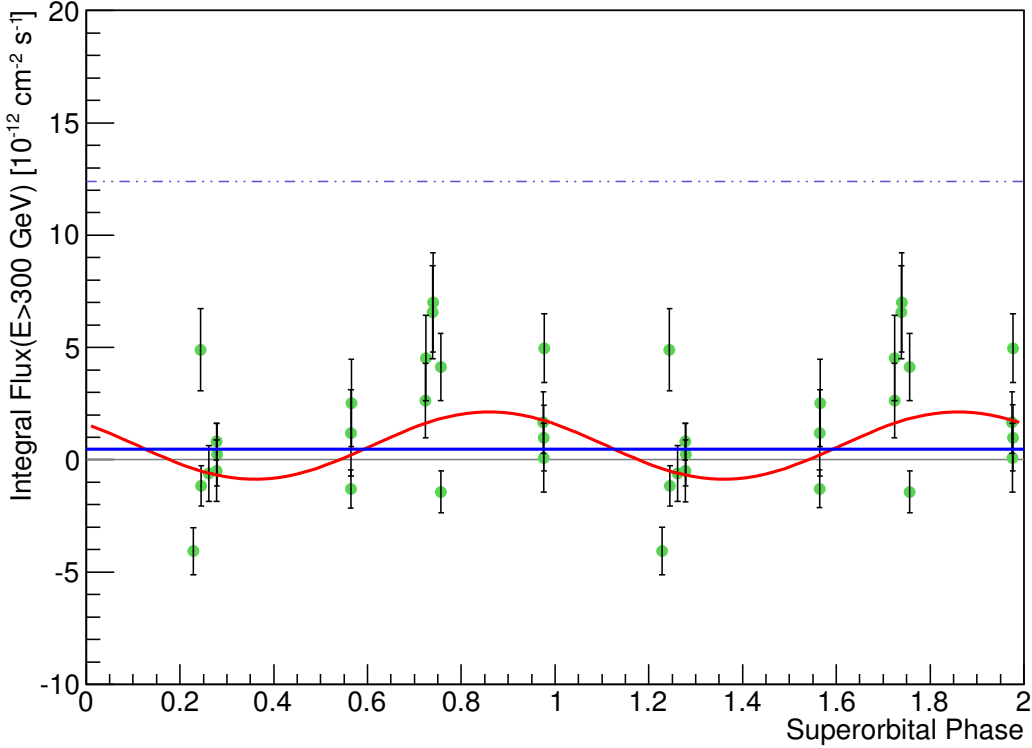


Figure 5.26: VHE emission of LS I +61°303 for orbital phases 0.75 – 1.0, in terms of the super-orbital phase (green dots), as defined by radio [96]. The fit to a sinusoidal (red solid line) and to a constant (blue solid line) are also represented. The grey dashed line represents the 10% Crab Nebula flux. The gray solid line marks the zero level, just as a reference.

The possibility that the flux variability can be due to statistical fluctuations from a constant value is discarded, as the probability is very low, always below  $1.3 \times 10^{-8}$ . The temporal evolution of the TeV emission is described at a 19% probability by a sinusoidal function with period  $1747 \pm 127$  days, compatible with the radio super-orbital period. If VERITAS data is included into the analysis to enlarge the sampling, the probabilities of compatibility are enlarged. The peak of emission for MAGIC+VERITAS data sets is compatible at 25% with the radio super-orbital modulation. In the case of the temporal evolution of the VHE emission, the MAGIC+VERITAS data is fitted by a sinusoidal function of period  $1782 \pm 106$ , compatible at 39% with the known super-orbital period at other wavelengths. Therefore, it is possible to conclude that the long-term TeV emission of LS I +61°303 is compatible with the  $\sim 1667$  days of periodicity found in radio and HE. Figure 5.29 shows the super-orbital variability in radio, optical (measured thought the equivalent width (EW) of the H $\alpha$  line) and the peak emission measured in TeV by MAGIC and VERITAS. Super-orbital modulation has been found in radio [96] and optical [207]. The optical data taken by LIVERPOOL telescope (see Section 5.6 for further details) also shows variability, although it is not so strong as in the case of [208] and [207]. This difference might be due just to the reduced sample used in the latter or it might be due to a change in the circumstellar disk. This thesis has proven that the TeV emission is also compatible within this super-orbital variability.

MJD [Days]	$\phi_{super-orbit}$	Integral Flux ( $E > 300$ GeV) $[10^{-12} cm^{-2}s^{-1}]$
55442.1	0.24	$4.9 \pm 1.8$
55444.2	0.25	$-1.2 \pm 0.9$
55471.1	0.26	$-0.6 \pm 1.2$
55498.1	0.28	$0.8 \pm 0.8$
55499.1	0.28	$-0.5 \pm 1.4$
55500.1	0.28	$0.2 \pm 1.4$
55975.8	0.56	$-1.3 \pm 0.8$
55976.8	0.56	$1.2 \pm 1.9$
55977.9	0.57	$2.5 \pm 1.9$
56242.0	0.72	$2.6 \pm 1.7$
56243.0	0.72	$4.5 \pm 1.9$
56266.9	0.74	$6.6 \pm 2.1$
56267.9	0.74	$7.0 \pm 2.2$
56295.9	0.76	$4.1 \pm 1.5$
56296.8	0.76	$-1.4 \pm 0.9$
56660.9	0.98	$1.7 \pm 1.4$
56661.9	0.98	$0.1 \pm 1.5$
56662.9	0.98	$1.0 \pm 1.5$
56663.9	0.98	$5.0 \pm 1.5$

Table 5.6: Values of the TeV emission of LS I +61°303 for the data taken on orbital phases 0.75 – 1.0. The first column shows the MJD, the second represents the super-orbital phase and the third and the fourth indicate the integral flux for each day with its uncertainty (statistical + systematics).

Function	$\chi^2/NDF$	$a_0$	$a_1$	$a_2$	$a_3$	Prob
Sinusoidal	9.97/7	$9.0 \pm 1.0$	$7.5 \pm 1.3$	$1747.0 \pm 126.7$	$9.1 \pm 0.5$	0.2
Constant	61.26/12	$4.5 \pm 0.6$				$1.3 \times 10^{-8}$

Table 5.7: Parameters of the sinusoidal and constant fits for the temporal evolution of the data at orbital phases 0.5 – 0.75, for MAGIC data. The first column indicates the fitting function, the second shows the  $\chi^2$  flavor, and  $a_0$ ,  $a_1$ ,  $a_2$  and  $a_3$  are the parameters for the different fits; the last column shows the probability of the goodness of the fit.

### 5.4.1 Periodicity Analysis

LS I +61°303 is known to be not only variable but also periodic in optical, radio, X-rays, HE and VHE  $\gamma$  rays. Super-orbital modulation of the flux has been stated in radio [96] and HE  $\gamma$  rays [195]. Yearly variations on the peak emission and average flux of LS I +61°303 have been detected in the VHE regime. A search for the super-orbital 1667 days period found in radio was performed on Section 5.4, with a probability of compatibility of 13%. Timing analysis methods can be used with the aim of finding periodic modulation in the flux of LS I +61°303.

In the case of uneven data samples, as it is the case of the observations performed by MAGIC of LS I +61°303 the primary method employed to search for periodic modulation is the *Lomb-Scargle Periodogram* ([129], [186]), which basically calcu-

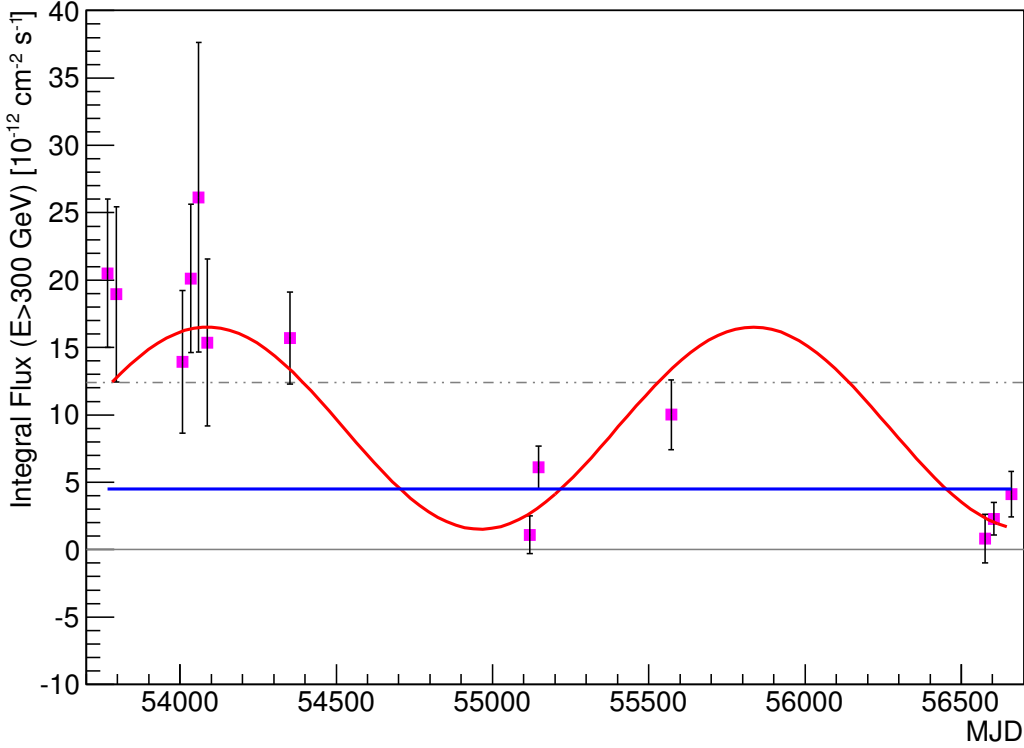


Figure 5.27: Temporal evolution of the peak of the VHE emission for each orbital period, for orbital phases 0.5 – 0.75, in terms of the MJD. The gray dashed line represents the Crab Nebula flux. The gray line marks the zero level. The fit to a sinusoidal is plotted in red. The fit to a constant is represented in blue.

lates the weighted periodogram of the lightcurve and performs a spectral analysis. The arrival time of the  $\gamma$  ray will be folded at a given frequency to produce a phase distribution of the complete data sample.

### Lomb-Scargle Periodogram

Consider  $N$  data points unequally spaced at time  $t_i$ ,  $x_i = h(t_i)$ ,  $i = 1, \dots, N$ . The spectral power as a function of the angular frequency  $\omega$ , named as *Lomb-Scargle Periodogram*, is defined by:

$$P(\omega) = \frac{1}{2\sigma^2} \left\{ \frac{\left[ \sum_i (x_i - \bar{x}) \cos(\omega(t_i - \tau)) \right]^2}{\sum_i \cos^2(\omega(t_i - \tau))} + \frac{\left[ \sum_i (x_i - \bar{x}) \sin(\omega(t_i - \tau)) \right]^2}{\sum_i \sin^2(\omega(t_i - \tau))} \right\} \quad (5.9)$$

where  $\sigma^2$  is the variance of the data points,  $\bar{x}$  is the mean. The constant factor  $\tau$ , which is a phase factor which makes the power  $P(\omega)$  independent of time shifts, is defined as:

$$\tau = \frac{1}{2\omega} \arctan \left( \frac{\sum_i \sin(2\omega t_i)}{\sum_i \cos(2\omega t_i)} \right) \quad (5.10)$$

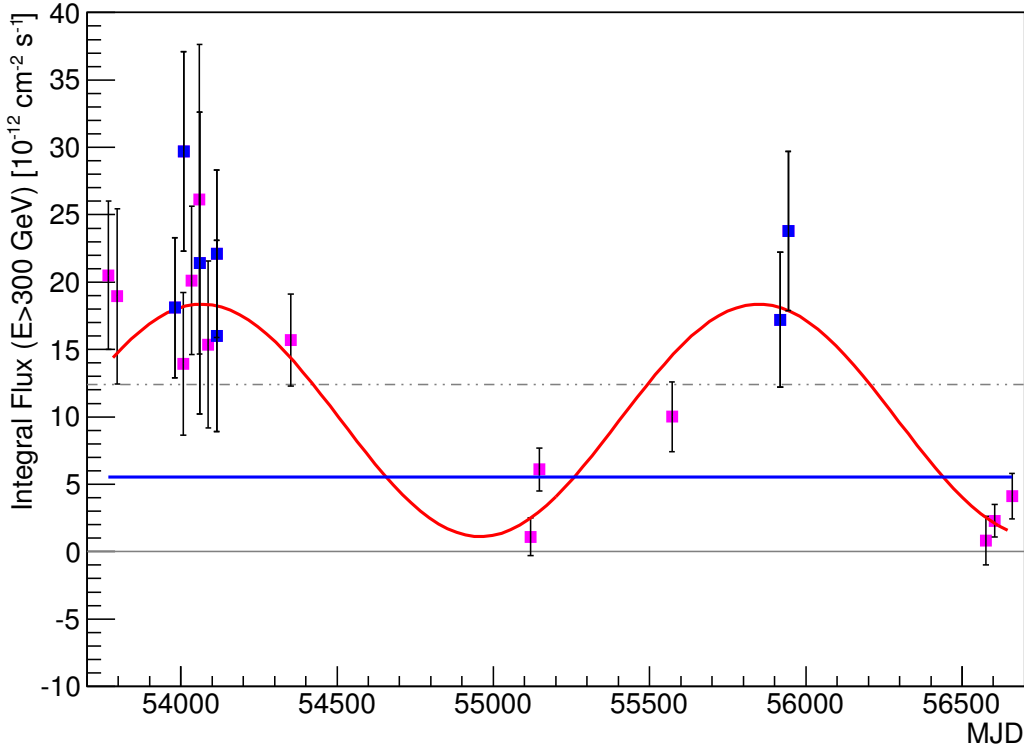


Figure 5.28: Temporal evolution of the peak of the VHE emission for each orbital period, in terms of the MJD. MAGIC and VERITAS data within orbital phases 0.5 – 0.75 have been considered. The gray dashed line represents the Crab Nebula flux. The gray line marks the zero level. The fit to a sinusoidal is plotted in red. The fit to a constant is represented in blue.

To test how significant is a peak in the power spectrum, its probability can be calculated. The null hypothesis is that the data values are random independent Gaussian values. The false-alarm probability of the null hypothesis is defined as:

$$P(> z) = 1 - (1 - \exp^{-z})^M \quad (5.11)$$

where  $M$  is the number of independent frequencies. It represents the probability that at least one of the computed powers  $z$  is above a certain threshold. A small value for the false alarm indicates a highly significant periodic signal.

The Lomb-Scargle test will be used in this Section to test the existence of a super-orbital signature in the VHE  $\gamma$  ray emission of LS I +61°303 detected by MAGIC and its compatibility with statistical fluctuations. However, it is worth noticing that less than two super-orbital periods have been covered at VHE, hence it is not expected that the periodicity is clearly revealed. The input physical variables  $x_i$  are the integral fluxes above 300 GeV measured for a certain time interval.

The data will be divided into the same categories as previously defined in Section 5.4. First, the data taken on the orbital interval  $\phi = 0.5 – 0.75$ , where the periodic outburst is, will be examined. Then, data on orbital phases  $\phi = 0.75 – 1.0$  will also be studied to search for periodicity.

First, just for the sake of clarity and to really confirm that it does not provide any

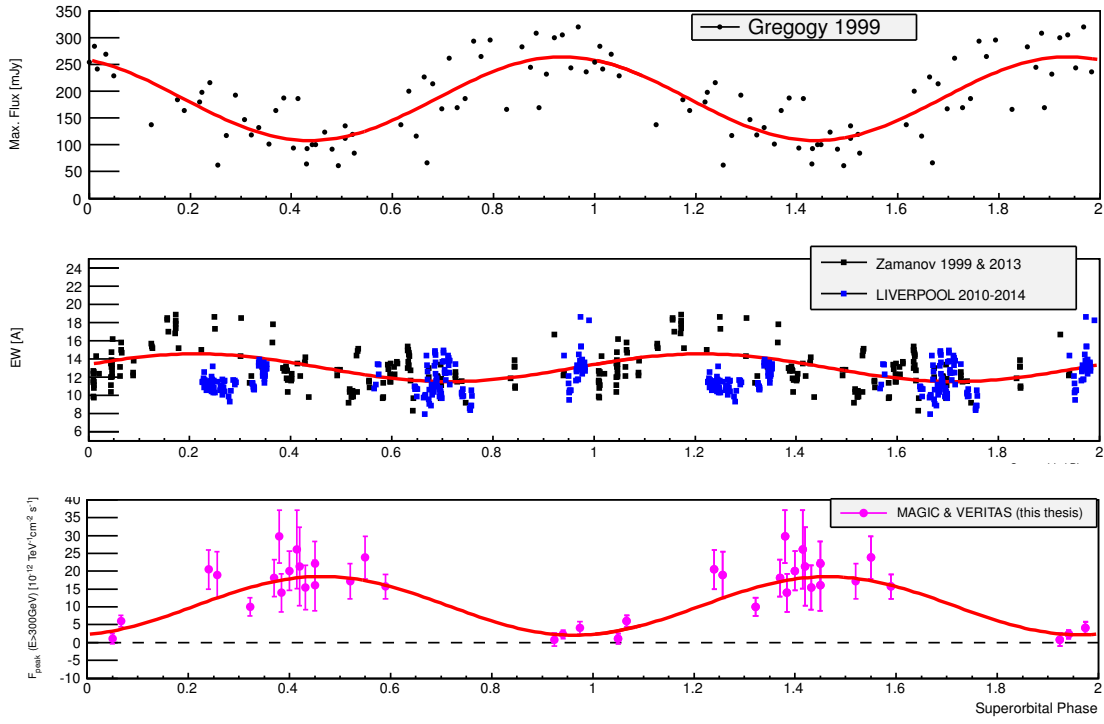


Figure 5.29: Super-orbital variability of LS I +61°303 in different wavelengths, folded within the radio super-orbital period at fit to a sinusoidal. *Top*: radio data [95]. *Center*: EW of the H $\alpha$  line from [208] and [207] (black dots). LIVERPOOL data taken simultaneously with the data presented in this thesis (see Section 5.6) are represented as blue dots. It is worth noticing that Zamanov and LIVERPOOL data-sets are not contemporaneous. The sinusoidal fit is performed over the Zamanov data. *Bottom*: TeV super-orbital emission measured by MAGIC and VERITAS obtained in this thesis. The radio and TeV are anti-correlated, being in anti-phase.

new information about the system, the complete data set between orbital phases 0.5 and 0.75 has been analyzed. The resulting plot is shown on Figure 5.30, which covers data from MJD 53765 to 56660 and permits the study of the orbital and super-orbital signature. The orbital peak is clearly revealed, in this case slightly offset from the measurement in radio at  $\nu = 0.0377 \text{ days}^{-1}$  to  $\nu = 0.0379 \text{ days}^{-1}$ , which corresponds to 26.35 days. The probability is  $1.8 \times 10^{-3}$ . Figure 5.31 shows a zoom into this region. If we investigate the smallest frequencies, a peak is visible for the value of the super-orbital phase, at  $\nu = 0.000599 \text{ days}^{-1} \sim 1667 \text{ days}$ , although the peak is compatible with a statistical fluctuation. A zoom is shown on Figure 5.32.

A search for the super-orbital signature has been performed on the samples with the highest peak of emission for each orbital cycle, for phases 0.5 – 0.75, when at least three consecutive days were observed and analyzed, using the same sample described in Section 5.4. Figure 5.33 shows the power spectrum for the cited data set. The highest power has a probability of 0.40 to be compatible with a statistical fluctuation, which corresponds to a period of  $\sim 243.67$  days. The peak at the radio modulation  $\nu \sim 0.000599 \text{ days}^{-1}$  is more clearly revealed in this case, being the second highest, with a probability of 0.52. This hint of super-orbital periodicity might be confirmed with a larger data set including the peaks of the emission for each orbital period, when more super-orbital cycles are covered.

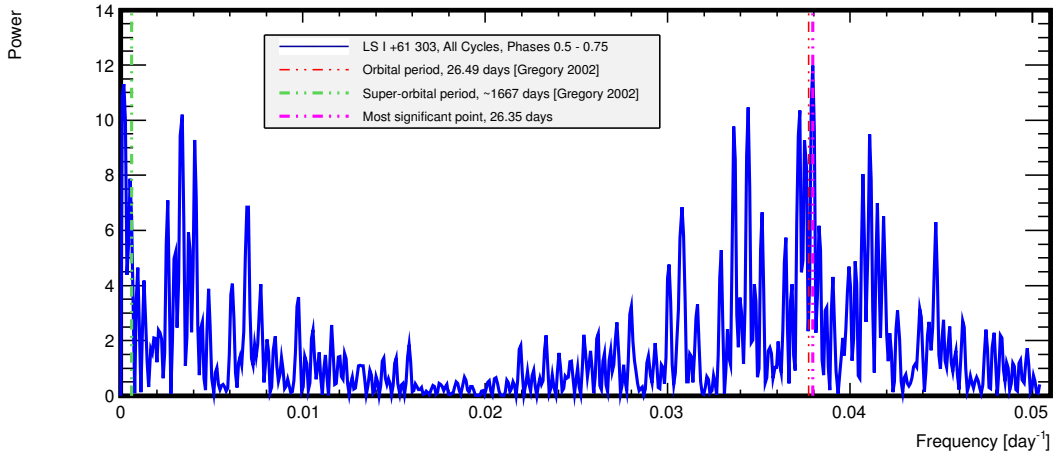


Figure 5.30: Lomb-Scargle periodogram for the orbital interval 0.5 – 0.75, for the complete data set of LS I +61°303. The orbital period is clearly revealed.

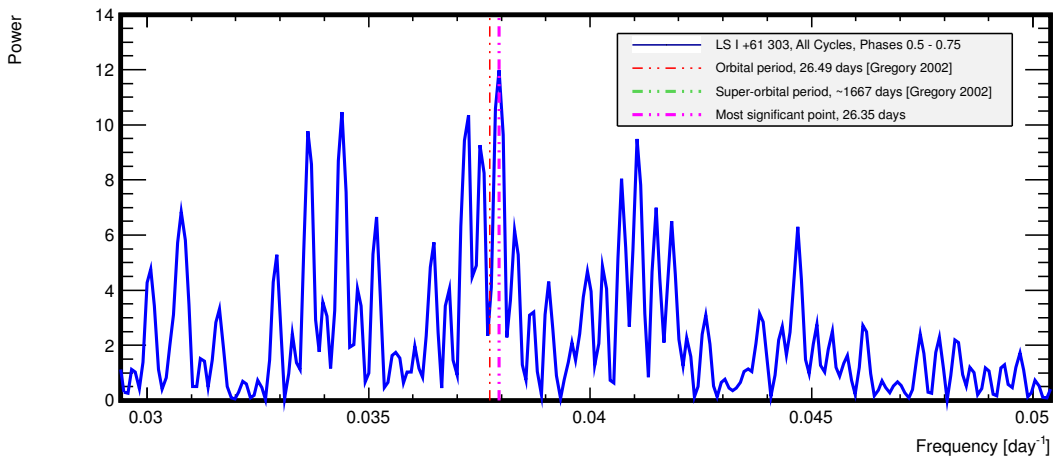


Figure 5.31: Zoom on Figure 5.30 on the orbital peak frequencies. The orbital modulation is clearly visible at 26.5 days.

The data set of VERITAS used in the previous Section has been included to the MAGIC data in the periodicity analysis, the enlarge the sampling. The resulting periodogram is shown on Figure 5.34. The most significant peak is centered at  $\nu \sim 0.000611 \text{ days}^{-1}$ , which corresponds to  $\sim 1636$  days, compatible with the radio super-orbital periodicity. The probability of the null hypothesis is 0.28. Although the probability is still high, it represents a strong hint of periodicity of the TeV signal, compatible with the radio super-orbital period. By including the VERITAS sample, the super-orbital peak is more clearly revealed.

In the case of data within the orbital interval 0.75 – 1.0, the Lomb-Scargle test has been performed on the data sample collected on the previous Section. Figure 5.35 shows the corresponding periodogram. The highest power shows a probability of 0.91, which indicates that this periodicity signature is not significant at all. In this case, there is no peak centered in the frequency of the radio super-orbital periodicity.

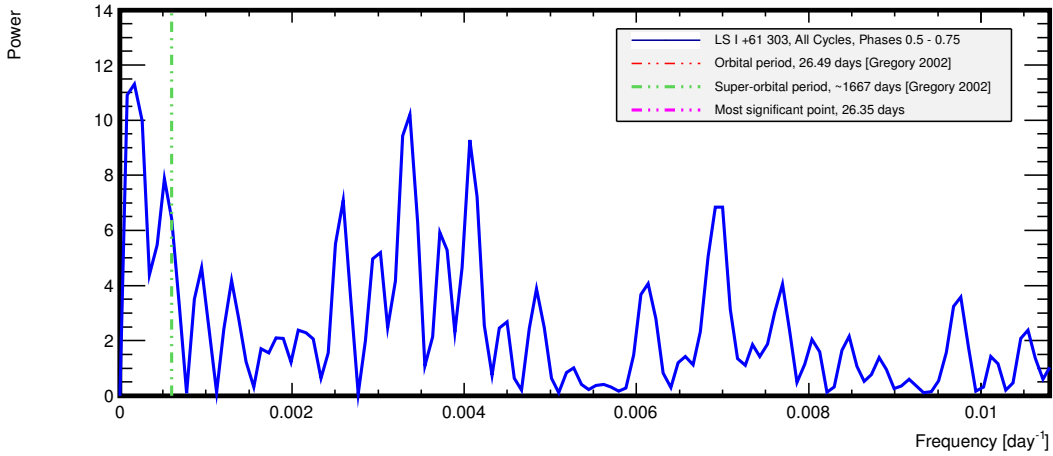


Figure 5.32: Zoom of Figure 5.30. The peak which corresponds to the long-term modulation found in radio (dashed green line) is not significant enough. No other long-term periodicity is found to be significant.

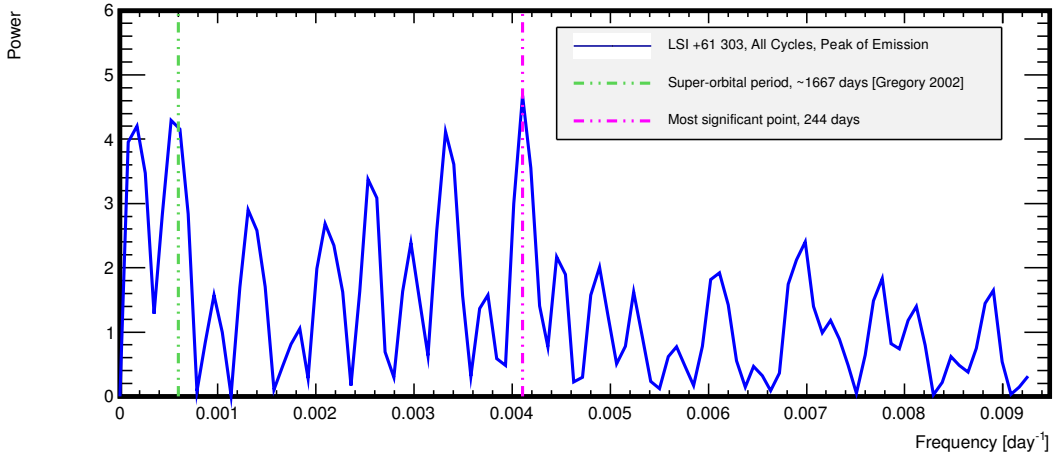


Figure 5.33: Lomb-Scargle test for the peak emission of the TeV flux LS I +61°303. The long-term radio modulation peak is clearly distinguishable, but not significant enough.

Concluding, a search for a periodical signature with MAGIC data was performed over the samples lying in the orbital ranges  $0.5 - 0.75$  and  $0.75 - 1.0$ , where a periodic outburst and sporadic emission is detected, respectively. However, although no very significant periodicity is revealed, one of the most significant peaks is coincident with the radio super-orbital period at the frequency  $\nu = 0.000599 \text{ days}^{-1}$  in the three periodograms obtained for the selected phase range (complete data set, the maximum emission and the peak emission) by performing a visual inspection. Nevertheless, the power is always compatible with statistical fluctuations. In the case of the samples taken in the orbital interval  $\phi = 0.75 - 1.0$ , neither super-orbital periodicity is found. From these studies, it seems that the Lomb-Scargle test is not suitable to search for periodicity on reduced data samples. When VERITAS data is included to enlarge the sampling, a peak at frequency  $\nu \sim 0.000611 \text{ days}^{-1}$  (1636 days), compatible with the radio super-orbital pe-

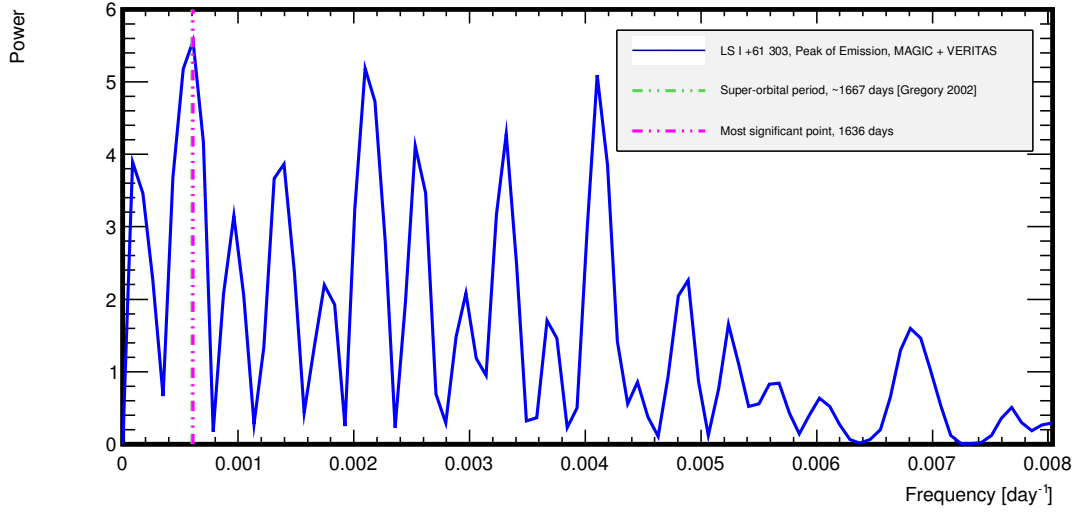


Figure 5.34: Lomb-Scargle test for the peak emission of the TeV flux LS I +61°303 for MAGIC and VERITAS data sets. The highest peak is compatible with the radio super-orbital period.

riodicity, appears as the most significant peak. However, its probability, 0.28, is still high to claim for periodicity, although it represents a strong hint. More observations in the 0.5 – 0.75 range are still needed to account for the possible appearance of the super-orbital periodicity signature. Hence, observations in this phase range with the aim of detecting a clear peak of emission are encouraged to be performed in a future in order to unveil a possible long-term signature.

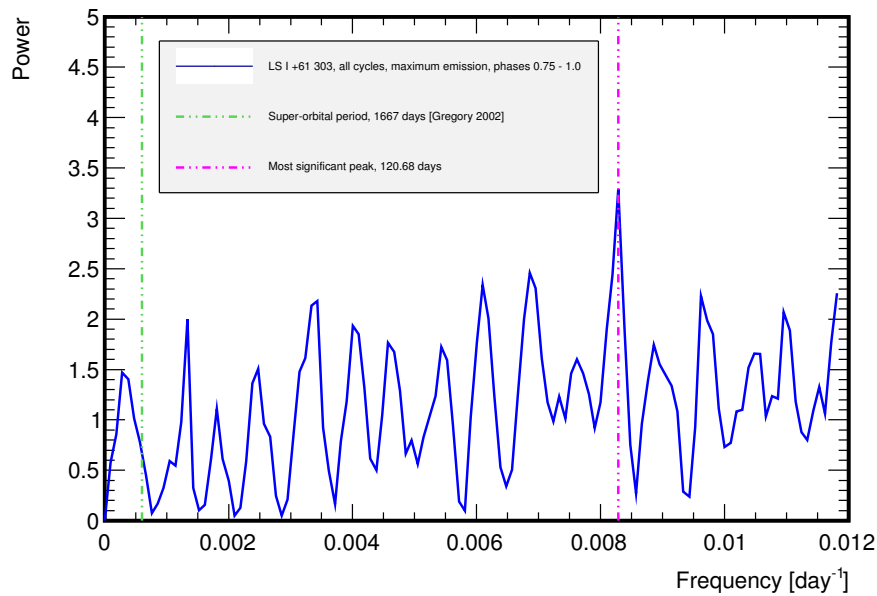


Figure 5.35: Lomb-Scargle Periodogram of the maximum emission of LS I +61°303 for orbital interval 0.75 - 0.10 for the complete data set

## 5.5 Spectral Variability Studies

On Section 5.3, it was derived the VHE spectrum of LS I +61°303 from *Cycle VI* to *Cycle IX*, for the epoch of the TeV outburst. Except for *Cycle IX*, where the flux was not enough to obtain a SED and only ULs were set, the spectrum could always be fitted by a power-law. The values of the spectral indexes for the different epochs are collected on Table 5.8. Although all values are compatible within systematic errors, on *Cycle VI* a hint of variability is present. Therefore, on this Section, spectral variability studies will be performed in order to check for hardening/softening of the state of the source.

Campaign	Orbital Interval	Super-orbital Phase	Spectral Index
Cycle I [19]	0.4 – 0.7	~0.22	$-2.6 \pm 0.2 \pm 0.2$
Cycle II [37]	0.4 – 0.7	~0.59	$-2.6 \pm 0.2 \pm 0.2$
Cycle IV [25]	0.6 – 0.7	~0.41	$-2.6 \pm 0.2 \pm 0.2$
Cycle V [28]	0.6 – 0.8	~0.08	$-2.5 \pm 0.5 \pm 0.2$
Cycle VI 5.3.1	0.6 – 0.8	~0.28	$-2.2 \pm 0.1 \pm 0.2$
Cycle VII 5.3.2	0.7	~0.55	$-2.7 \pm 0.5 \pm 0.2$
Cycle VIII 5.3.3	0.5 – 0.8	~0.92	$-2.5 \pm 0.5 \pm 0.2$

Table 5.8: Spectral indexes for the different observational campaigns of LS I +61°303. The first column indicates the campaign name, the second, the orbital range where the SED was computed, the third the average super-orbital phase of the campaign and fourth the spectral index with statistical and systematic uncertainties.

On Figure 5.36, it is shown the dependence of the spectral index,  $\alpha$ , which respect to the super-orbital phase defined in radio of 1667 days. No strong dependence of the spectra with respect to the yearly flux emission is found. The data can be fitted ( $\chi^2/\text{NDF} = 8.19/6$ ) to a constant value of  $2.41 \pm 0.05$ , with a probability of 0.23. A priori, the temporal evolution of the spectral index is constant, or at least, if there is any variability, it is below the sensitivity of the telescopes.

As discussed in Section 5.4, the TeV flux of LS I +61°303 suffers a yearly variability, with strong hints of periodicity compatible with the radio and HE super-orbital period. Hence, it is worth searching for possible spectral variability for epochs of *high* TeV emission (above 5% of the Crab Nebula flux) and *low* flux (2 – 5 % of the Crab Nebula flux). No lower fluxes have been considered in order to have enough significance to perform the unfolding and extract the spectrum. Figure 5.37 shows the super-orbital dependence of the spectral index, from *Cycle VI* to *Cycle IX* (which is the data which has being analyzed in this thesis), considering this division within *high* and *low* flux. As mentioned in 5.1.1, the HE emission of LS I +61°303 suffers hardening/softening of the spectra with decreasing/increasing flux [104]. It might be possible that also the TeV component of LS I +61°303 shows a spectral hardening/softening in function of the orbital phase. However, it may also occur that the VHE emission does not suffer spectral variability since the origin of the HE and VHE emission seems to be different [104, 36]. The spectral index also shows super-orbital modulation in the radio band [96]. Hence, as performed in the precedent section, a division into the *periodic* and *sporadic* outburst has also been performed.

Figure 5.37 shows the dependence of the spectral index with the super-orbital

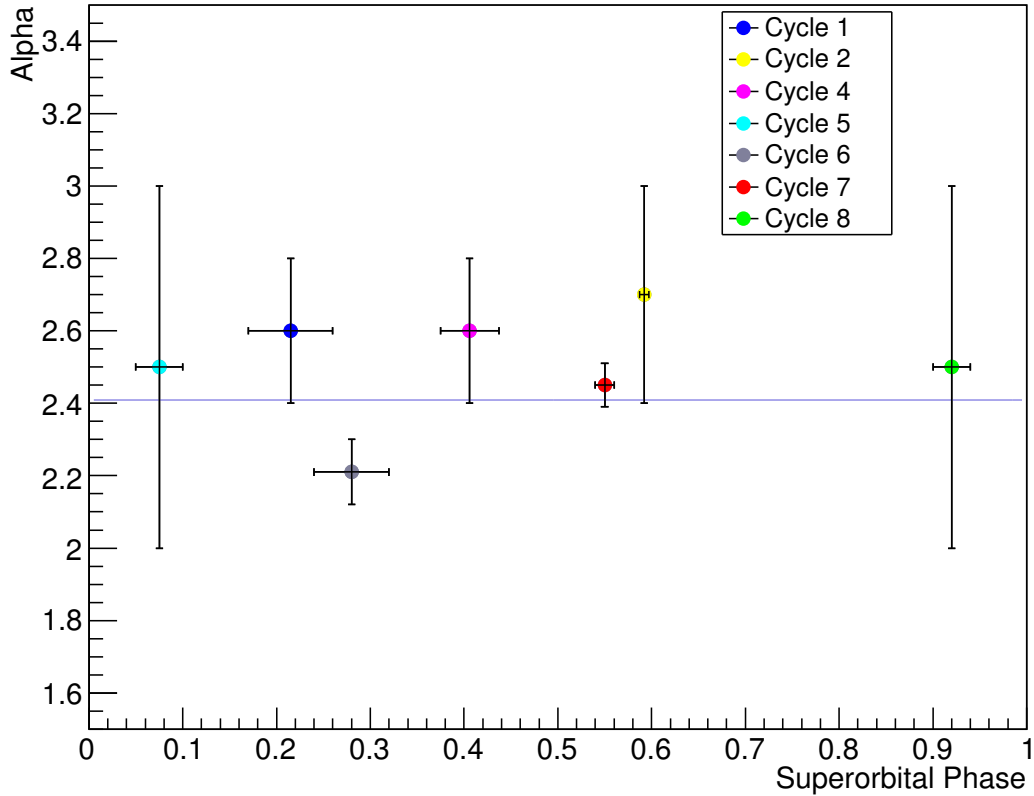


Figure 5.36: Super-orbital dependence of the spectral index for the campaigns of LS I +61°303, considering a 1667 days period. The blue line corresponds to the average value. No strong variability is found.

phase considering the divisions commented above. The big uncertainties in the sample corresponding to 2 – 5 % of Crab and  $\phi = 0.8 – 1.0$  is due to the low signal enclosed in these data. The spectral index does not show variability for the measured periods, fitting ( $\chi^2/NDF = 0.90/2$ ) to an average value of  $2.41 \pm 0.10$ , with a high probability, of 0.83. If there exists any variation in the spectral index, it is below the sensitivity of the MAGIC telescopes.

In order to search for variability within shorter timescales, the hardness ratio method can be used. The hardness ratio is defined as the ratio in terms of integral flux between two energy bands. In this case, it has been defined as  $HR = \text{Flux} (E > 1 \text{ TeV}) / \text{Flux} (1 \text{ TeV} > E > 300 \text{ GeV})$ . The HR has been represented in terms of the orbital phase (Figure 5.38) to study the hardening/softening of the source within the orbital position; it has also been plotted in terms of the MJD to study the temporal evolution (see Figure 5.39) and finally it has also been represented against a lower integral flux  $F$  ( $E > 300 \text{ GeV}$ ) (see Figure 5.40). Only data from *Cycle VI* to *Cycle IX* above  $1.5\sigma$  of significance (for the integral flux above 300 GeV) has been considered, in order to minimize systematic effects on the calculation of the correlation coefficient. The fit probability of the HR to a constant value is 33% considering statistical errors. However, the data on Figure 5.40 can be fitted ( $\chi^2/NDF = 12.93 / 22$ ) to a first order polynomial with a probability 0.94, which might indicate variability. Nevertheless, as the fit to a

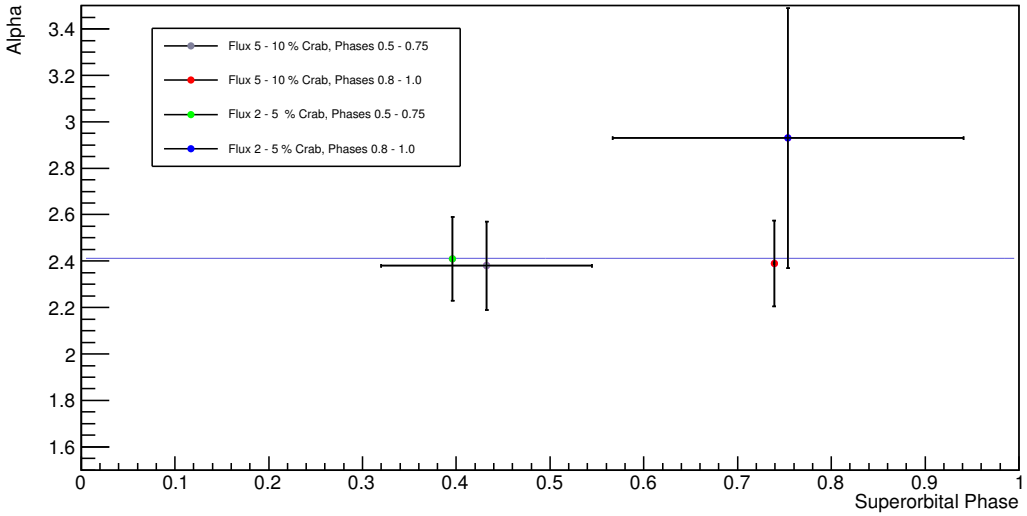


Figure 5.37: Super-orbital dependence of the spectral index for the *Cycle VI* to *Cycle IX* campaigns of LS I +61°303, considering a 1667 days period. The blue line corresponds to the average value. No spectral variability is found.

constant value is also compatible, no firm claim can be stated.

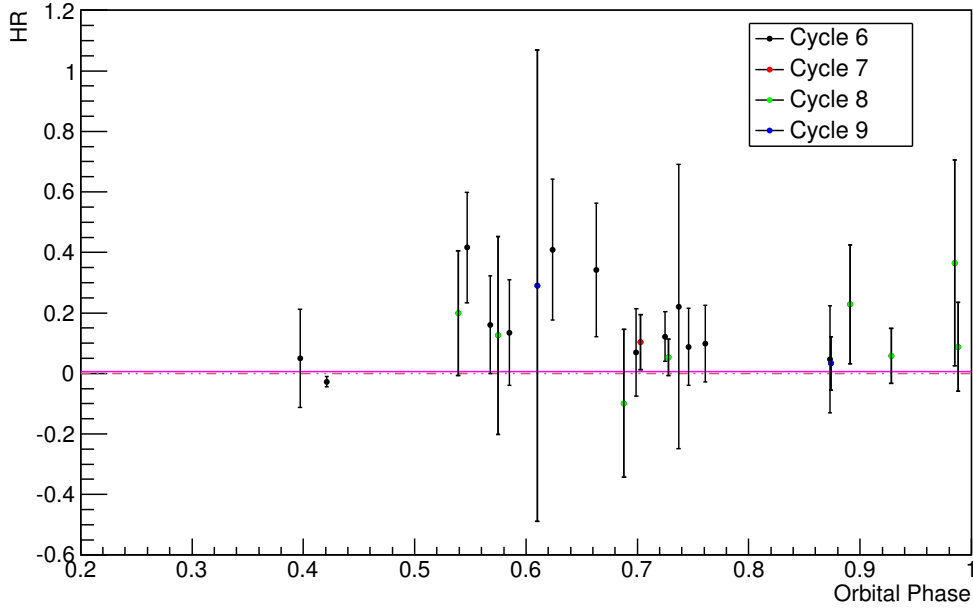


Figure 5.38: Orbital variability of the HR. The fit to a constant value is represented as a magenta line. No hardening/softening of the spectra is visible

The analysis performed on this Section permit to confirm that LS I +61°303 shows hints of spectral variability, although the confirmation it is not possible because it is constant inside MAGIC precision. These hints are visible on some observational cycles or when studying the HR in terms of the integral flux above 300GeV for individual nights, but they are inside MAGIC capabilities. In principle, the spectral hardness does not seem to be dependent neither on the yearly

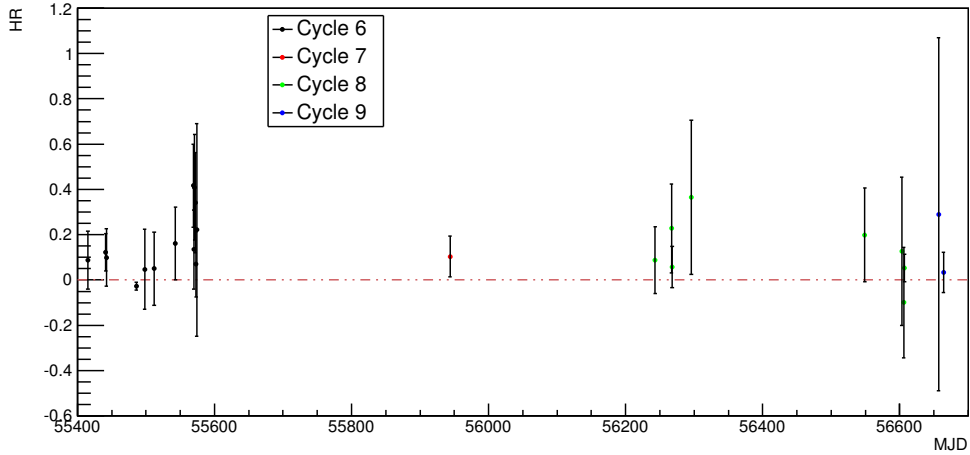


Figure 5.39: Temporal dependence of the HR. The HR is constant within errors.

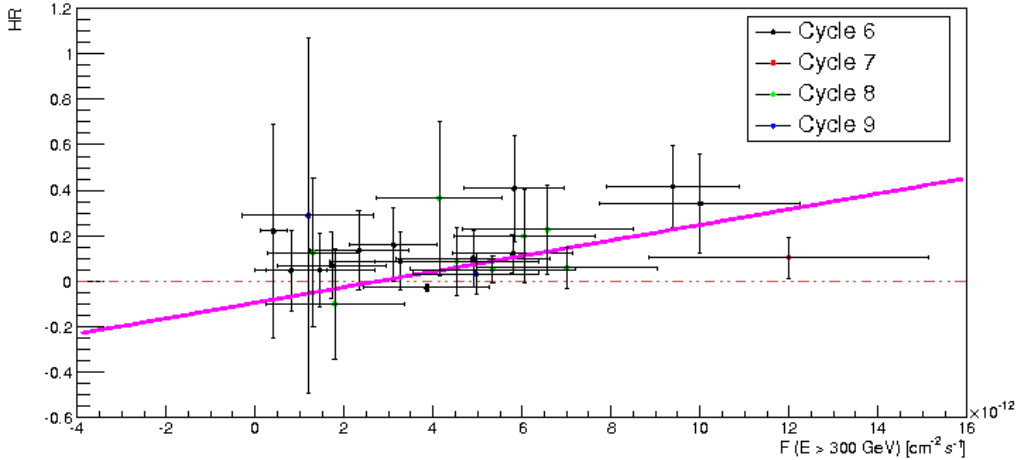


Figure 5.40: HR versus the integral flux above 300 GeV. The data can be fitted both to a first order polynomial and a constant value.

flux level of the TeV emission neither on the orbital phase range considered.

## 5.6 Optical H $\alpha$ -TeV Correlation

In the flip-flop magnetar model described by [198], it is suggested that LS I +61°303 changes from a propeller model at periastron to an ejector regime at apastron. This switch from one mechanism from the other is thought to be triggered by variations in the mass-loss rate of the Be star. For periods of a large disk, which implies a large mass-loss rate, the propeller regime can be set even in the apastron region. This mechanism would explain the yearly variability found in the TeV flux of LS I +61°303 next to the apastron. If this is the case, the optical emission shall be anti-correlated with the TeV flux.

An extensive campaign to search for (anti-)correlation between the optical and TeV emission was held on *Cycles VII, VIII and IX* between MAGIC and LIVER-POOL telescopes, although the optical analyzers have also provided archival data

taken on Cycle VI in order to broaden the data samples. On *Cycle VII*, there was a first attempt of performing observations with STELLA, a robotic telescope situated in the Canary Island of Tenerife. However, the quality of the data seemed not to be good enough for the purposes of the proposal (determining the size of the Be stellar disk through measurements of the H $\alpha$  and HeII lines), hence it was decided not to use this telescope anymore and just observe with LIVERPOOL.

LIVERPOOL is a robotic telescope placed in the Canary Island of La Palma. It provides  $\sim$ 5500 resolution spectra both in the blue and red spectral ranges. The H $\alpha$  line is a proxy of the circumstellar disk of the star and it allows the measurement of the mass-loss rate of the star. It is contained in the red arm. The parameters to extract information from are the equivalent width (EW [Å]) which is a measurement of the area of the line; the full width half maximum (FWHM [km/s]), which indicates the velocity dispersion in the disk and the centroid velocity (vel [km/s]), which is the radial velocity of the H $\alpha$  line. These measurements will be used to search for correlations with MAGIC. In addition, the HeII  $\lambda$  4542Å and  $\lambda$  4686Å are measured through the blue arm. These lines are good tracers for the polar stellar wind, as the stellar wind distorts the photospheric lines, as the HeII. The profiles of these lines shall be adjusted with combined models of atmosphere+wind. Therefore, the HeII lines are direct trackers of the mass-loss rate of the Be star. However, in this thesis, only the H $\alpha$  parameters will be used in the search of correlation with TeV emission, since the optical analysis for the HeII lines has not yet been finished. In a future, compatibility with these results will also be searched.

The goal of the campaign was to perform simultaneous observations of LS I +61°303 mainly focusing on the phases of sporadic emission  $\phi = 0.75 - 1.0$ . This orbital interval does not show periodical outbursts. The largest flux variations in a daily and orbit-to-orbit basis have been found in this range. However, LIVERPOOL has also performed observations at orbital phases 0.6 – 0.75 and at some other phases for them to enlarge the data sample and be able to improve the current orbital solutions of LS I +61°303. Figure 5.41 collects all the observations performed on optical and TeV between *Cycle VI* and *Cycle IX* for all orbital phases and shows all the temporal evolution of the parameters with time. As a first visual inspection, it does not seem to be any particular behavior.

The correlation between the TeV flux and the H $\alpha$  parameters will be performed taking into account the statistical uncertainties in the data. The (linear) correlation between a pair of quantities  $(x_i, y_i)$ ,  $i = 1, \dots, N$ , can be measured through the weighted *Pearson Correlation Coefficient* defined as:

$$r = \frac{\sum_i w_i(x_i - \bar{x})(y_i - \bar{y})}{\sqrt{\sum_i w_i(x_i - \bar{x})^2} \sqrt{\sum_i w_i(y_i - \bar{y})^2}} \quad (5.12)$$

where  $\bar{x}$  and  $\bar{y}$  are the mean of x and y, respectively. The weight,  $w_i$ , is defined as:

$$w_i = \frac{\sigma_{xi}\sigma_{yi}}{\sum_i \sigma_{xi}\sigma_{yi}} \quad (5.13)$$

being  $\sigma$  the variance. However, to decide if a correlation is statistically significant, the probability has been calculated. The standard null hypothesis assumed is that

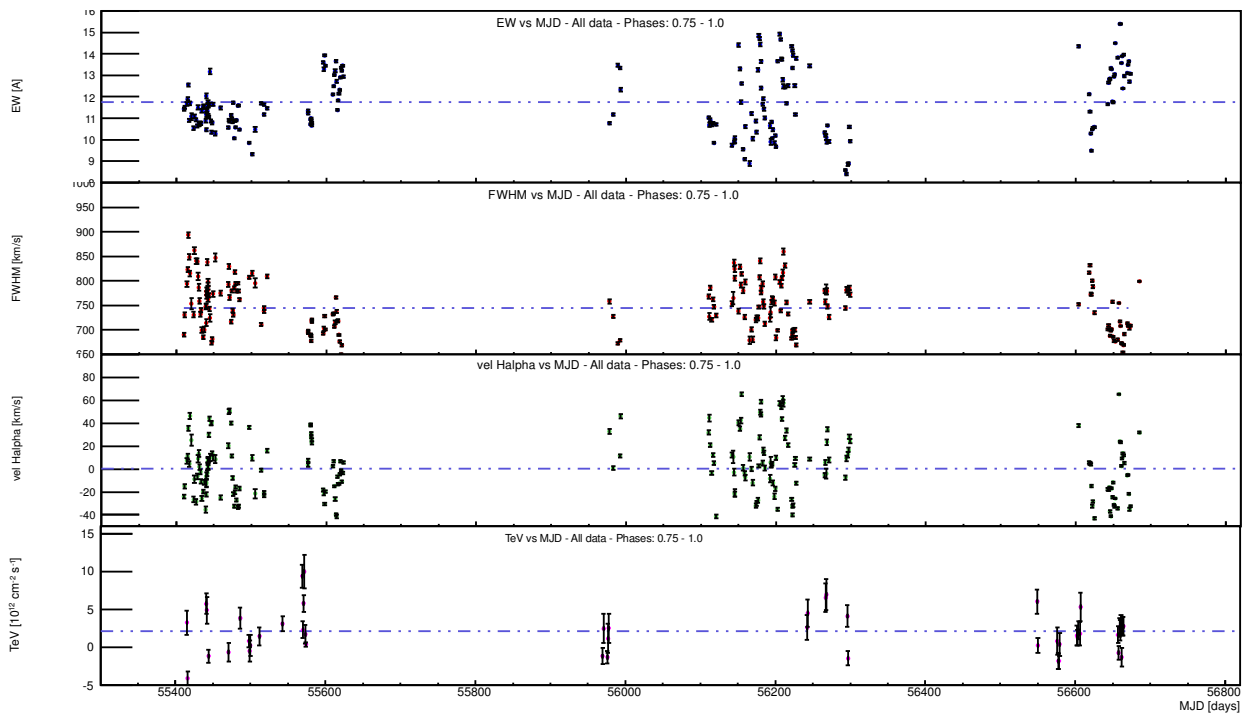


Figure 5.41: Evolution with time of the optical parameters EW, FWHM, vel and TeV flux (from top to bottom) measured from Cycle VI to Cycle IX.

the correlation coefficient from two random set of variables will lead to a  $|r|$  larger than measured, hence low values of the probability indicate high correlation.

Three *degrees* of simultaneity will be consider: first, the optical observations which where taken exactly during the period when MAGIC was performing its observations, which will be denoted at *strict* observations; second, a slot of three hours of difference between both observations, named *3 hours* observations and finally data which was obtained during the same observational night but not exactly simultaneously in time, denoted as *nightly*. Table 5.9 and Table 5.10 collect the simultaneous TeV and extracted optical parameters for data which was observed within the same observational night. For some nights, i.e. MAGIC MJD 55442.06, there is more than one optical spectra for the same observational slot of MAGIC. These spectra were taken because, at the moment of the observations, the telescope operators were not sure that the spectra was properly taken, but a later analysis showed that all of them are valid and hence are included into the correlation. The MAGIC observations where scheduled for 2 hours of observation each night for the nights where LS I +61°303 is at orbital phases 0.75 – 1.0. The temporal evolution in terms of the MJD for this data is plotted on Figure 5.42. The LIVERPOOL observations where scheduled to happen at the same time as MAGIC, but as it is a robotic telescope, it sometimes did not occur and the observations were slightly delayed. It also may have happened that due to bad weather, some nights there are no observations of one of the two telescopes, either LIVERPOOL or MAGIC. It is worth remembering that the phases considered for the study do not suffer yearly variations in the flux neither.

The different parameters of  $H\alpha$  are plotted against MAGIC TeV flux in Figure 5.43. The values of the correlation for each degree of simultaneity (nightly, 3 hours and strict) and the probability of the null hypothesis to be certain are

$\phi$	MAGIC MJD start	MAGIC MJD end	TeV flux $[10^{-12} \text{cm}^{-2}\text{s}^{-1}]$
0.75	55415.16	55415.22	$3.27 \pm 1.58$
0.76	55442.06	55442.12	$4.90 \pm 1.74$
0.76	55442.06	55442.12	$4.90 \pm 1.74$
0.76	55442.06	55442.12	$4.90 \pm 1.74$
0.76	55442.06	55442.12	$4.90 \pm 1.74$
0.84	55444.15	55444.19	$-1.16 \pm 0.89$
0.84	55444.15	55444.19	$-1.16 \pm 0.89$
0.86	55471.05	55471.11	$-0.61 \pm 1.24$
0.87	55498.01	55498.07	$0.81 \pm 0.81$
0.99	55977.87	55977.90	$2.53 \pm 1.92$
0.89	56266.94	56267.00	$6.57 \pm 1.92$
0.93	56267.92	56267.96	$7.01 \pm 2.05$
0.93	56267.92	56267.96	$7.01 \pm 2.05$
0.99	56295.91	56296.01	$4.14 \pm 1.41$
0.01	56296.83	56296.93	$-1.43 \pm 0.92$
0.76	56660.93	56661.02	$2.98 \pm 1.27$
0.80	56661.93	56661.99	$-1.31 \pm 1.24$
0.84	56662.94	56663.03	$2.80 \pm 1.24$
0.87	56663.94	56664.01	$2.78 \pm 1.24$

Table 5.9: TeV data used in the search for anti-/correlation with optical data. The first column indicates the orbital phase, the second and third column indicate the starting and ending time for the MAGIC observation and the fourth column shows the TeV flux measured by MAGIC.

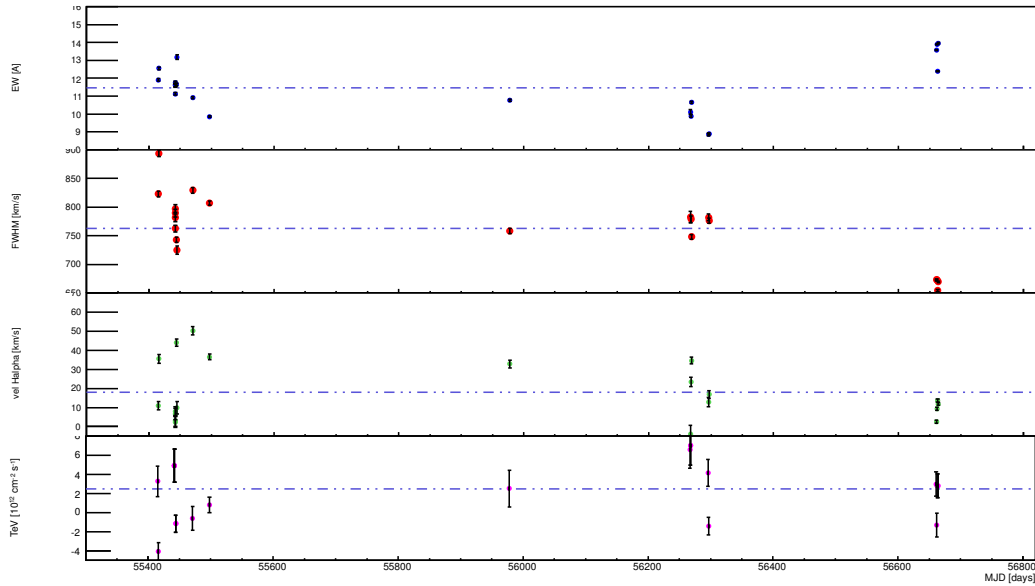


Figure 5.42: Evolution with time of the optical parameters EW, FWHM, vel and TeV flux (from top to bottom) measured from Cycle VI to Cycle IX, for phase interval 0.75 – 1.0.

collected on Table 5.11. No significant correlation is found from the statistical test performed over the sample at  $\phi = 0.75 - 1.0$ . The parameters which show the highest correlation are the TeV and the velocity of the centroid of the  $H\alpha$

$\phi$	Optical MJD [days]	EW [Å]	FWHM [km/s]	vel [km/s]
0.75	55415.15	11.90 $\pm$ 0.07	822.95 $\pm$ 5.11	10.90 $\pm$ 2.21
0.78	55416.12	12.55 $\pm$ 0.07	893.45 $\pm$ 5.48	35.47 $\pm$ 2.36
0.76	55442.22	11.13 $\pm$ 0.08	762.50 $\pm$ 5.67	8.03 $\pm$ 2.51
0.76	55442.23	11.75 $\pm$ 0.09	789.49 $\pm$ 6.56	2.37 $\pm$ 2.87
0.76	55442.23	11.63 $\pm$ 0.10	797.18 $\pm$ 6.73	3.01 $\pm$ 2.91
0.76	55442.23	11.60 $\pm$ 0.10	781.34 $\pm$ 7.09	6.60 $\pm$ 3.09
0.84	55444.03	11.66 $\pm$ 0.07	743.23 $\pm$ 4.58	43.99 $\pm$ 1.98
0.84	55445.00	13.18 $\pm$ 0.13	724.90 $\pm$ 7.37	9.94 $\pm$ 3.19
0.86	55470.07	10.92 $\pm$ 0.06	829.29 $\pm$ 5.04	50.15 $\pm$ 2.15
0.87	55497.10	9.86 $\pm$ 0.04	807.20 $\pm$ 3.50	36.46 $\pm$ 1.50
0.99	55977.85	10.77 $\pm$ 0.07	758.06 $\pm$ 4.74	32.85 $\pm$ 2.05
0.89	56267.00	10.12 $\pm$ 0.13	782.64 $\pm$ 10.28	-3.91 $\pm$ 4.46
0.93	56267.92	9.88 $\pm$ 0.07	778.83 $\pm$ 5.91	23.40 $\pm$ 2.55
0.93	56268.86	10.67 $\pm$ 0.06	747.94 $\pm$ 4.14	34.65 $\pm$ 1.80
0.99	56295.85	8.86 $\pm$ 0.07	781.98 $\pm$ 5.70	12.76 $\pm$ 2.46
0.01	56296.87	8.90 $\pm$ 0.06	776.45 $\pm$ 4.82	16.83 $\pm$ 2.10
0.76	56660.91	13.57 $\pm$ 0.04	673.01 $\pm$ 1.62	2.59 $\pm$ 0.72
0.80	56661.92	13.89 $\pm$ 0.04	672.25 $\pm$ 1.82	9.27 $\pm$ 0.81
0.84	56662.86	12.39 $\pm$ 0.04	654.30 $\pm$ 1.73	13.65 $\pm$ 0.76
0.87	56663.85	13.96 $\pm$ 0.04	669.41 $\pm$ 1.67	11.90 $\pm$ 0.73

Table 5.10: Optical parameters of the data used to search for correlation with the TeV flux. The first column indicated the orbital phase, the second the time of the observation, the third column shows the value of the EW, the fourth the FWHM and the fifth the measurements on the velocity of the centroid.

line which, in the case of the strict observations, shows a correlation of  $r = 0.79$  and a probability of 0.3.

Simultaneity	Parameters	$r$	Prob
Nightly	TeV - EW	-0.19	0.78
Nightly	TeV - FWHM	-0.15	0.70
Nightly	TeV - vel	-0.41	0.96
3 hours	TeV - EW	-0.28	0.77
3 hours	TeV - FWHM	-0.22	0.70
3 hours	TeV - vel	-0.41	0.87
Strict	TeV - EW	-0.27	0.58
Strict	TeV - FWHM	0.47	0.45
Strict	TeV - vel	0.79	0.30

Table 5.11: Correlations between the TeV flux obtained by MAGIC and the H $\alpha$  parameters (EW, FWHM and vel) measured by LIVERPOOL, for the extended orbital interval 0.75 – 1.0. First column indicates the level of simultaneity of the observations, second the parameters to search correlation for, third the Pearson correlation coefficient and fourth the probability.

First, I have searched for correlation between the TeV emission and the EW of

the  $H\alpha$  line (top panel). In principle, it is expected that, the broader the EW, the larger the mass-loss rate of the Be star and hence the less TeV emission shall be detected. The EW shall be anti-correlated with the TeV flux. However, no correlation is found neither in a nightly nor in a 3h nor in a strict simultaneous observation basis. The probability of the correlation to also be reproducible by two random samples is always larger than 0.58.

In the case of the FWHM, it is expected that the TeV flux is correlated with it, because EW and FWHM are supposed to be anti-correlated values. Nevertheless, as shown on the medium panel of Figure 5.43, no correlation is detected. The probability of the correlation to also be reproducible by two random samples is always larger than 0.45.

Finally, the velocity of the centroid of the  $H\alpha$  line is generated in the outer areas of the Be circumstellar disk. It shall be a proxy of the orbit of the star, but its profile is complex and probably contaminated by the tidal forces of the NS. When searching for a correlation with the TeV flux (bottom panel of Figure 5.43), no correlation is found. This parameter, for the strict observation, shows the highest correlation coefficient  $r = 0.79$  with the lowest probability, 0.30. However, it is far from being significant enough to claim for correlation.

As LIVERPOOL also performed observations on other orbital phases than the accorded once and provided us some archival data coincident with MAGIC *Cycle VI* observations, these plots have also been generated for all the orbital phases where there is simultaneous optical and TeV data ( $\phi = 0.65 - 1.0$ ), following the same distinctions described before. This adds four points for the nightly observations and one point for the 3 hours and strict observations. The result is plotted on Figure 5.44 and the values of the correlation and its probability is collected on Table 5.12.

Simultaneity	Parameters	$r$	Prob
Nightly	TeV - EW	-0.26	0.87
Nightly	TeV - FWHM	-0.08	0.64
Nightly	TeV - vel	-0.50	0.99
3 hours	TeV - EW	-0.28	0.79
3 hours	TeV - FWHM	-0.09	0.58
3 hours	TeV - vel	-0.49	0.94
Strict	TeV - EW	-0.19	0.62
Strict	TeV - FWHM	0.68	0.12
Strict	TeV - vel	0.09	0.46

Table 5.12: Correlations between the TeV flux obtained by MAGIC and the  $H\alpha$  parameters (EW, FWHM and vel) measured by LIVERPOOL, for the extended orbital interval 0.65 – 1.0. First column indicates the level of simultaneity of the observations, second the parameters to search correlation for, third the Pearson correlation coefficient and fourth the probability.

It is possible to conclude, from the optical - TeV data taken simultaneously, that not correlation between the TeV emission and the  $H\alpha$ . It might be that there is correlation, but it can be blurred due to the fast variability of the optical parameters in short timescales. Strict observations of TeV and FWHM show a hint of correlation as predicted by the pulsar-wind model proposed by [198]. More

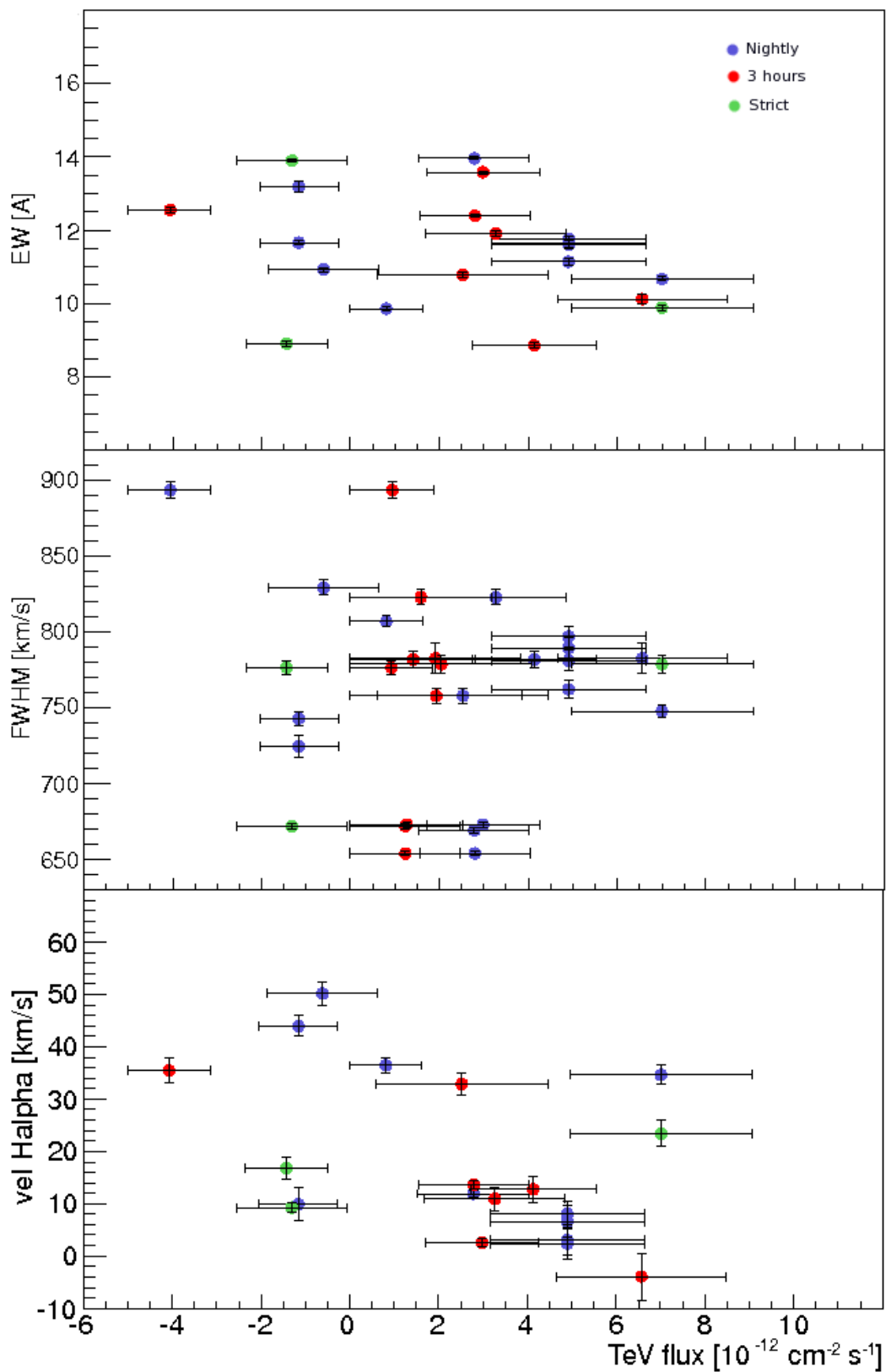


Figure 5.43: Parameters of the  $H\alpha$  line plotted versus the MAGIC TeV flux, for data taken under the orbital interval  $\phi = 0.75 - 1.0$ . *From top to bottom:* EW, FWHM and vel. Each data point represents a 10 minute observation in the optical and a nightly flux in TeV.

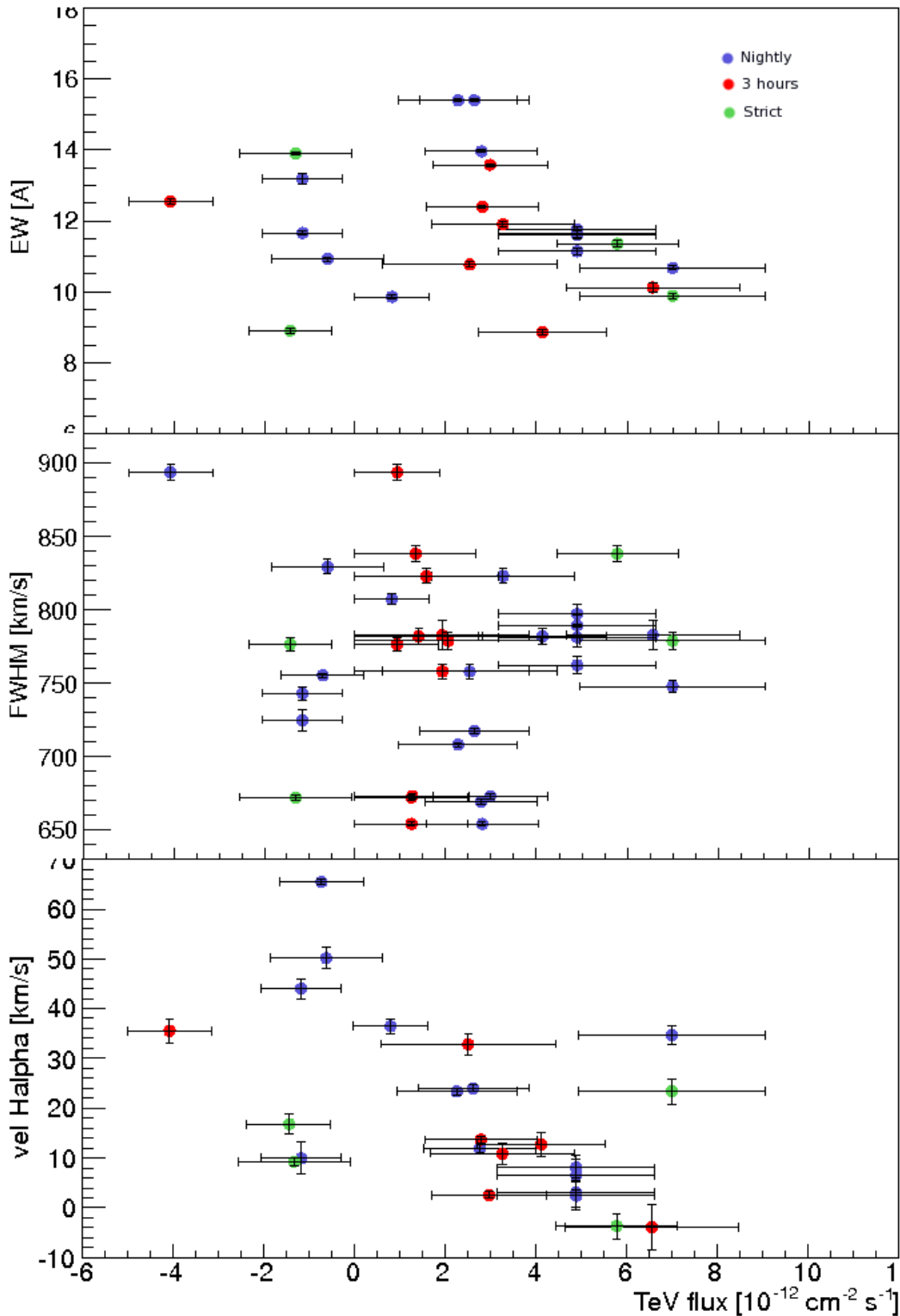


Figure 5.44: Parameters of the  $H\alpha$  line plotted versus the MAGIC TeV flux, for data taken under the orbital interval  $\phi = 0.65 - 1.0$ . *From top to bottom:* EW, FWHM and vel. Each data point represents a 10 minute observation in the optical and a nightly flux in TeV.

data with higher quality might be needed to average the fast variability.

## 5.7 Discussion

The spectra of LS I +61°303 can generally be described by a power-law with a Crab-like photon index. The spectrum derived for the complete set of observations from *Cycle VI* to *Cycle IX*, considering all orbital phases, can be adjusted to:

$$\frac{dN_\gamma}{dAdtdE} = (4.4 \pm 0.1_{stat} \pm 0.2_{sys}) \times 10^{-13} E^{(-2.4 \pm 0.2_{stat} \pm 0.2_{sys})} TeV^{-1} cm^{-2} s^{-1} \quad (5.14)$$

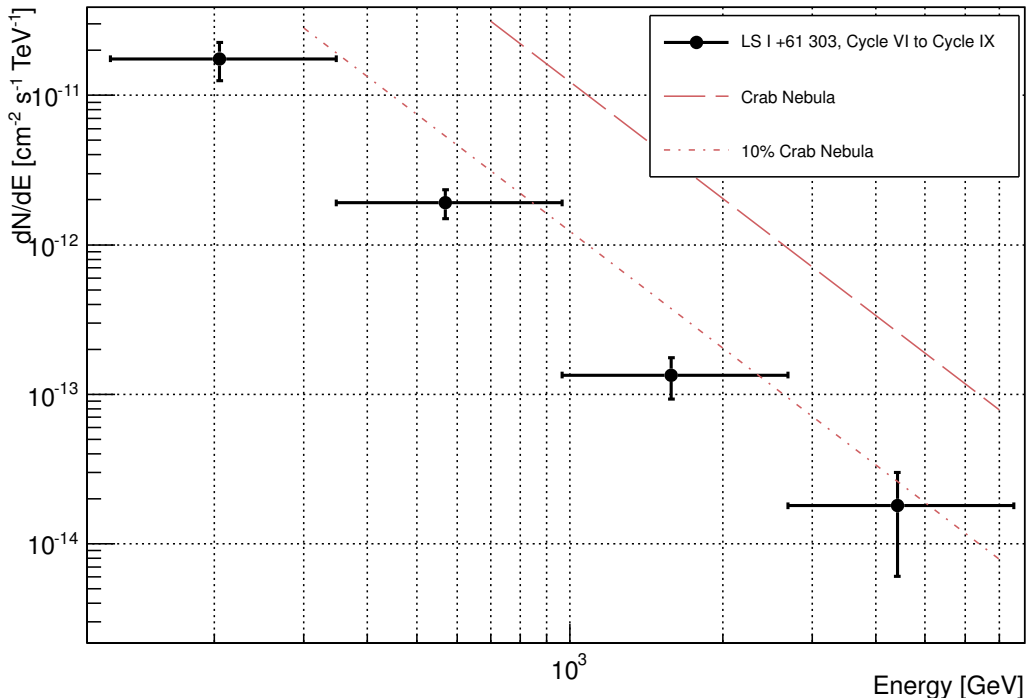


Figure 5.45: Derived spectrum of LS I +61°303 obtained with the complete data sample from Cycle VI to Cycle IX. The dashed red line represents the 10% of the Crab Nebula flux.

which is consistent with previous results. The spectrum is shown on Figure 5.45. However, this spectrum does not provide any new information and it is compatible with previous published results. Hence, the data was first splitted into the different observational Cycles, in order to study each of them separately in order to search for changes in the spectra and/or the lightcurve.

- On *Cycle VI*, after a period of low-flux emission, the source was recovering the high emission state. The total significance was  $15\sigma$  for a total observation time of  $\sim 23$ h. Two peaks of emission were found at orbital phases 0.55 and 0.66, at 8% of the Crab Nebula flux. It is the first time that a double-peak is detected in the same orbital period. The spectral slope of the VHE spectrum shows a hardening from previous published results,  $\Gamma = 2.2 \pm 0.1_{stat}$ . Nevertheless, this hint of spectral variability can not be confirmed because the fit it is still compatible with a Crab-like index due to systematic uncertainties.
- The source recovered the high-flux emission state on *Cycle VII*, on January 2012, with a peak emission on phase 0.7 with a flux of 10% the Crab Neb-

ula flux. The spectral index for this campaign is compatible with previous publications.

- On *Cycle VIII*, the source was back to the low TeV emission state, with a peak emission of 5% the Crab Nebula flux, which is at the same level stated in [28] for the orbital period 0.5 – 0.75. On this cycle, TeV fluxes of 6% the Crab Nebula flux are also detected on phases 0.75 – 1.0.
- The source remains in low state on *Cycle IX*. On this cycle, the flux is too low to extract an unfolded spectrum. Not a single night has a signal with more than  $2\sigma$  significance.

Nevertheless, to really understand the behavior of the source, it is necessary to deeper study the long-term periodicity and spectral variability. Also, to test theoretical pulsar-wind nebula models as the one proposed by [198], correlations between the  $H\alpha$  line parameters and the TeV flux has been calculated.

On Section 5.4 a search for super-orbital modulation within the 1667-day radio period was performed. Hints of long-term modulation of the TeV flux have been found on these studies. Radio and HE long-term modulation has been detected for the region of the periodical outburst at those wavelengths. Hence, the data was splitted on two different data sets in terms of the orbital interval, 0.5 – 0.75 for the periodic outburst phases and 0.75 – 1.0, to cover all the regions where VHE emission has been detected. The peak emission for each orbital cycle was adjusted to a sinusoidal function with the same period that the radio one. The TeV flux has been found to present yearly variability in the overall and peak emission, which is a 13% compatible with the  $\sim$ 4.5 years of radio long-term period for the data 0.5 – 0.75. No periodic long-term variability was found for the orbital phases 0.75 – 1.0. When studying the temporal evolution of the TeV flux in terms of the MJD, the data can be fitted to a sinusoidal function of period  $1747 \pm 127$  days with a probability of 19%. Enlarging the sample with MAGIC+VERITAS data, the peak emission is compatible with the radio super-orbital periodicity on a 20%, and the temporal evolution is described by a sinusoidal function with period  $1782 \pm 106$  days with a 39% probability.

Statistical tests were performed over the complete data set (archival and recent) of LS I +61°303 by the use of the Lomb-Scargle Periodogram in order to search for periodicity. Both MAGIC and MAGIC+VERITAS samples have been analyzed with this test. Hints of a possible periodicity are observed in the different tests performed, since a peak at the frequency corresponding to the 1667 days radio period is always visible, for the peak emission in phases 0.5 – 0.75. However, the significance is not large enough to claim for periodicity.

Tests for spectral hardening/softening of the source spectra were performed over different cycles. The temporal and super-orbital dependence (assuming the radio long-term period) were accomplished, but the results were always compatible within a constant value, inside the MAGIC capabilities. The hardness ratio was calculated in order to search for spectral variability on single nights. Again, temporal, orbital and energy dependences were studied. No evidence of hardening/softening has been found on the two first cases. If there exists a variation, it is below the instrument sensitivity.

Finally, searches for anti-/correlation of the TeV emission and the mass-loss rate of the Be star have been performed. For that purpose, the Pearson correlation coefficients and the probabilities of the correlation for the EW, FWHM and velocity

of the  $H\alpha$  line and the TeV flux were calculated. The studies were accomplished on the orbital phases where the sporadic TeV emission has been detected, as this phase has presented the maximum fluxes variations and it does not seem to present long-term modulation. No clear correlation has been found. However, the fast change in the optical measurements might blur the putative correlation. Studies of the HeII lines, proxies of the polar wind, might help to unveil the (un-)existence of correlation between the two mentioned wavelengths.

Observations on the phase range 0.5 – 0.75 are encouraged on super-orbital phases (assuming the 1667 days period)  $\sim 0.2$  and  $\sim 0.8$ , when the flux goes from low (high) to high (low) levels, to reveal the possible long-term modulation of LS I +61°303 and its sinusoidal behavior and confirm the hints found in this thesis. The best would be to observe the complete trend from  $\phi = 0.5$  to  $\phi = 0.75$  to detect the peak of the emission for each orbital period. In order to search for spectral variability, both in short ( $\sim$  several minutes) and long ( $\sim$ years), observation with more sensitive instruments as CTA are encouraged. Observations on the orbital interval 0.75 – 1.0 are encouraged to search for optical-TeV correlations. However the fast change in the optical parameters of  $H\alpha$  may blur the relation between these wavelengths.



# 6

## Observations of the $\gamma$ -Ray Binary Candidate MWC 656

*This chapter contains the observations performed by the MAGIC telescopes of the Be/X-ray binary MWC 656 in search for VHE  $\gamma$ -ray emission. No gamma ray emission has been detected and upper limits have been set for the VHE emission of this source.*

### 6.1 Historical Introduction

---

On July 2010, *AGILE* detected  $\gamma$ -ray emission from the unidentified point-like source AGL J2241+4454 at a level of more than  $5\sigma$  (maximum likelihood analysis) and with a flux of  $1.5 \times 10^{-6}$  ph cm $^{-2}$  s $^{-1}$  above 100 MeV [133]. The source location was, in galactic coordinates,  $(l, b) = (100^\circ.0, -12.2^\circ) \pm 0.6^\circ$ (95%stat.)  $\pm 0.1^\circ$ (syst.). The observation was performed observing a large portion of the sky in spinning mode<sup>14</sup>. The integration time started on 25th of July of 2010 at 01:00 UT(HJD<sup>15</sup> = 2455402.5434) and finished on 26th 2010 July at 23:30 UT (HJD = 2455404.4810).

Within the error circle of the observation performed by *AGILE* (with an error radius of approximately 0.6 deg) lies the Be star MWC 656 also known as HD 215227, which is located at  $(l, b) = (100^\circ.1755, -12^\circ.3985)$ . This source has been proposed as the optical counterpart of this new  $\gamma$ -ray source, based on its probable binary nature [204]. MWC 656 is placed at a relatively high altitude from the Galactic plane, points that it may be a runaway star formed by a supernova explosion in a binary system [91]. The explosion causes that the star moves away at velocities comparable to its orbital speed. If the supernova progenitor was the less massive of the two stars, then the system will remain linked, and will form a binary system composed of a star and a compact object. The suggested orbital period, derived from photometric modulation, was  $60.37 \pm 0.04$  days. The system is located at  $2.6 \pm 1.0$  kpc, which is derived by fitting the spectral energy distribution in the UV and B-band [204].

<sup>14</sup>On spinning mode, the instrument axis is sweeping the accessible sky with an angular speed of 1 degree/sec

<sup>15</sup>HJD corresponds to Heliocentric Julian Day. The HJD is the JD corrected by the position of the Earth which respect the Sun.

Optical spectroscopy studies of this star confirmed its binary nature [57]. The H $\beta$  shows a double-peak profile characteristics of Be stars with a circumstellar disk fed by an stable mass loss. The main H $\alpha$  parameters present long-term modulation according to the period proposed by [204]. The maximum for the optical modulation occurs  $\sim$ 0.25 orbits after periastron, which matches with the peak of the equivalent width (EW) of the H $\alpha$  line. This is consistent with the concept that the size of the circumstellar disk is truncated due to tidal forces by the compact object.

The Be star presents a circumstellar disk and the optical emission is modulated, which is indicative of instabilities in the disk. Recent studies revealed that the mass of the companion star is  $10 - 16 M_{\odot}$  and that the compact object is a stellar-mass black hole of  $3.8 - 6.9 M_{\odot}$  [55]. This black hole has been observed in quiescent state in X-rays and is fed by and inefficient accretion flow, which leads to a very low luminosity of  $L_X < 1.0 \times 10^{32} \text{ erg s}^{-1}$  in the  $0.1 - 2.4 \text{ keV}$  band ( less than  $1.6 \times 10^{-7} L_{Edd}$ ). This is the first observational evidence of a binary system hosting a Be star and a black hole [55]. This study also provided new updated ephemeris. Some relevant information about the system and orbital parameters (taken from [204], [57] and [55]) are displayed on Table 6.1.

Parameter	Value
Star Spectral Type	B3IVne+sh
Compact Object	Black Hole
Star mass [ $M_{\odot}$ ]	$10 - 16$
BH mass [ $M_{\odot}$ ]	$3.8 - 6.9$
$M_{BH}/M_{\star}$	$0.41 \pm 0.07$
$P_{orb}[\text{days}]$	$60.37 \pm 0.04$
$T_0$ [HJD - 2,450,000]	$3243.70 \pm 4.30$
$\phi_{periastron}$	$0.01 \pm 0.10$
$e$	$0.10 \pm 0.04$
$i$	$67 - 80$
$a_{\star} \sin i$ [ $R_{\odot}$ ]	$38.0 \pm 6.3$
$a_{BH} \sin i$ [ $R_{\odot}$ ]	$92.8 \pm 3.8$

Table 6.1: Information about the  $\gamma$ -ray binary candidate MWC 656 (from [204], [57] and [55]).  $M$  is the mass,  $P_{orb}$  the orbital period,  $T_0$  the epoch of the periastron,  $\phi_{periastron}$  the phase of the periastron,  $e$  the eccentricity,  $i$  the inclination angle of the system,  $a$  the semi-major axis and  $\star$  and BH subscripts are referred to the star and the black hole, respectively.

MWC 656 was detected in X-rays with *XMM-Newton* when the source was at orbital phase 0.07 and it was established as a high-mass X-ray binary (HMXRB) [159]. It was studied within the context of the radio/X-ray correlation found for low-mass X-ray binaries (LMXRBs) [86] finding that it displays an X-ray flux that it may be compatible with the correlation and comparable to the faintest black hole (BH) LMXRBs. Hard X-ray emission has been searched with INTEGRAL [87] with an offset angle of 14 deg. No significant emission was detected in the 18–60 KeV energy band for a total exposure time of 2.1 Ms. In addition, the MAXI mission, which continuously monitors the X-ray sky in the 2–20 KeV band, has not detected emission coming from the AGL J2241+4454 position [Morooka et al.].

The source was observed in radio with the European VLBI Network (EVN) and

was not detected either. Flux density upper limits at  $3\sigma$  C.L. were set at the 30– $66\ \mu\text{Jy}$  level [155], supporting the compatibility with the radio/X-ray correlation. No more information about radio observations of MWC 656 was found in the bibliography.

MWC 656 has been detected at HE gamma rays only once, by the time it was discovered by *AGILE* back in 2010. *Fermi*-LAT performed observations on AGL J2241+4454 the same night of the discovery, but could not confirm the detection. They set an upper limit of  $1.0 \times 10^{-7}\ \text{ph cm}^{-2}\ \text{s}^{-1}$  (at 95% C.L) above 100 MeV assuming a photon index of -2, for the same day of the *AGILE* detection [5]. For a softer spectra of index -3, the upper limit is  $3.0 \times 10^{-7}\ \text{ph cm}^{-2}\ \text{s}^{-1}$  for the same energy. An independent analysis performed by [157] on the same data-set of *Fermi* LAT and also collecting 3.5 years of data where AGL J2241+4454 source is located, still led to no evidence of HE  $\gamma$ -ray emission. Two upper limits at 90% C.L were set at energies above 100 MeV with values of  $7.2 \times 10^{-8}\ \text{ph cm}^{-2}\ \text{s}^{-1}$  for the same night of the discovery and  $9.4 \times 10^{-10}\ \text{ph cm}^{-2}\ \text{s}^{-1}$  for the 3.5-year data [157]. The authors do not give any clue about the assumed spectra used for the calculations.

In this work, I present the first reported search for VHE  $\gamma$ -ray emission from MWC 656.

## 6.2 MAGIC Observations

---

The fact that the unidentified point-like  $\gamma$ -ray source AGL J2241+4454 was spatially coincident with a massive star which resulted to be a Be binary system, made of MWC 656 a good  $\gamma$ -ray binary candidate. Performing a simple flux extrapolation from the *AGILE* detection up to VHE gamma rays, the expected differential flux at 300 GeV would be about  $\sim 4 \times 10^{-11}\ \text{TeV}^{-1}\ \text{cm}^{-2}\ \text{s}^{-1}$ , which should be detectable with the MAGIC telescopes within few hours. The assumed spectrum is a power-law with an spectral index of -2.5. These facts made of MWC 656 a good target for MAGIC.

The observations of MWC 656 were performed in three different epochs: in November-December 2011 , May-June 2012 and in June 2013.

### 2011 Observations

The observations were performed on 28th of November, and 22nd and 24th–26th of December . About 2 hours of MAGIC-II mono-mode data (MAGIC-I telescope was not operational due to technical reasons) were taken. Besides, these data was taken just right after the first upgrade of the telescopes. No dedicated Montecarlo was produced for these specific settings and, moreover, the quality of these data was rather poor. We have discarded these observations from the data analysis. The first night corresponded to phase 0.88, which is covered in the observations performed on 2012. The December observations covered the phase range 0.29–0.34, which we have missed and has not been covered in subsequent observations.

## 2012 Observations

The observations were performed from 23rd to 31st of May and 14th to 19th of June. MAGIC-I telescope was not operational (due to technical issues), so the observations were done in mono mode (MAGIC-II stand-alone). The sensitivity of MAGIC-II stand-alone system is not regularly monitored. Moreover, there is no contemporaneous Crab Nebula observations, so we take as a reference the integral sensitivity for MAGIC-I mono observations above 250 GeV, which is about 2.2% of the Crab Nebula flux in 50 hours [22]. MWC 656 was observed for a total of 23.4 hours under dark conditions and covering a zenith angle range between 22° and 51°. After a selection of good-quality data, following the standard analysis procedure, a total of 21.3 hours of effective time remained.

The MWC 656 data taken in May covered the orbital phase range 0.83–0.95 (see Figure 6.1). The observations performed in June covered orbital phases 0.21–0.28. They were performed on these phases just because of observability restrictions due to the moon phase. Still, they cover the post-periastron passage and the phases where other  $\gamma$ -ray binaries as HESS J0632+057 or LS I +61°303 exhibit VHE  $\gamma$ -ray emission, usually around phases 0.2 – 0.45 post-periastron [30].

## 2013 Observations

The observations of MWC 656 in 2013 were performed between 3rd and 5th of June, covering a range of orbital phases between 0.05–0.09 (see Figure 6.1), just right after periastron. Observations were made in stereoscopic mode with the upgraded MAGIC system, which permits to achieve a sensitivity of 0.71%  $\pm$  0.02% of the Crab Nebula flux in 50 h of observation for energies above 250 GeV [188]. The source was observed for a total of 3.3 hours during this period in dark conditions covering a zenith angle range between 28° and 45°. The quality of this data set was good and almost all data survived the quality selection cuts.

A multiwavelength campaign was performed for this period. The observation on June 4 was taken almost simultaneously with a *XMM-Newton* observation. On 2nd, 3rd, 5th and 8th of June, MWC 656 was observed with the optical robotic telescope STELLA, at Observatorio del Teide (Tenerife). The spectra covered the wavelength range 3870 – 8800 Å.

## 6.3 Data Analysis

---

The dataset of the year 2012 was analyzed using the standard MAGIC mono-analysis chain. A general explanation of the analysis is collected on Chapter 3. The training of the RF was done for source-dependent analysis. The lack of OFF data taken under the same conditions (this implies a weak source observed in mono mode data observed under the same zenith angle range) needed to perform the RF  $\gamma$ /hadron separation caused that the same dataset of MWC 656 was used. This solution is not optimal, but in the case of having a weak source the effect is negligible and, for strong sources, it will not make the signal disappear. The RF  $\gamma$ /hadron separation is performed with a random subsample from the input sample, which is largely dominated by hadron showers, compared to the big amount of pure gammas of the Montecarlo. The analysis is scarcely less sensitive.

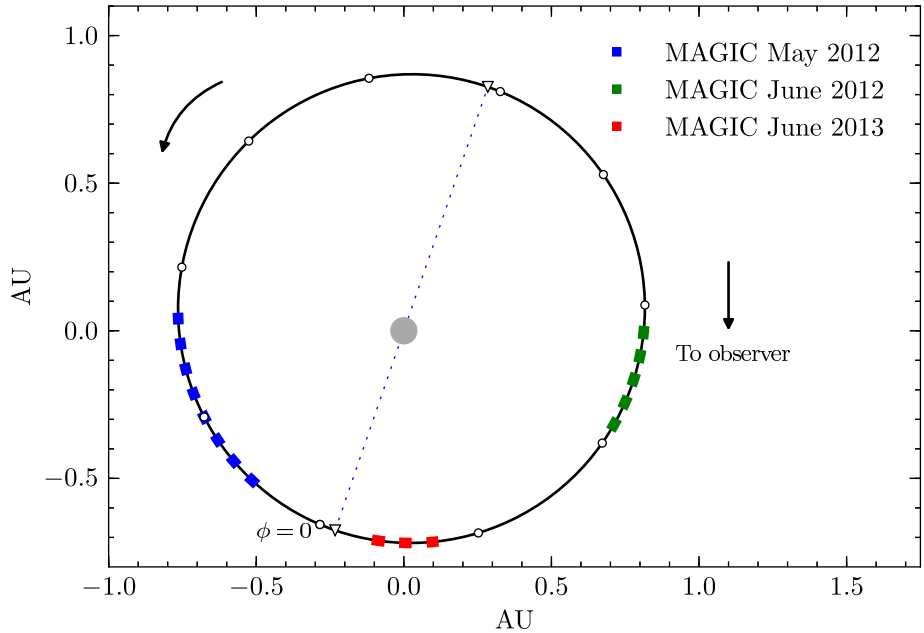


Figure 6.1: Orientative scheme of the orbit of MWC 656. Triangles mark the position of the periastron and the apastron. The MAGIC observations are over-plotted on top of the orbit. The periastron is situated at phase  $0.01 \pm 0.10$ .

For this analysis, a cut in *Size* of 200 phe in the Hillas parameters has been applied in the flux calculation in *Fluxlc*. Using a high cut in the *Size* permits the use of more OFF regions and so increase the statistics for the background determination.

The analysis of the 2013 data was performed applying the standard MAGIC stereo-analysis chain. The OFF data, which covered the same zenith angle range and was observed simultaneously under the same conditions, used in this case were three different DarkPatches (which are random regions of the sky where no  $\gamma$ -ray sources are expected and are observed to be used as a background reference). For the flux and lightcurve calculations, *Flute* has been used.

In order to combine both datasets we have used the same binning for both *Fluxlc* and *Flute*, adjusting them to where we had more statistics. The lower energy cut has been chosen to the lower bin where we had enough background statistics.

## 6.4 Results

I have search for signal coming from the Be/X-ray binary MWC 656 but no significant  $\gamma$ -ray emission has been detected from MWC 656 for none of our two observational campaigns. No excess is found in the whole data set and the significance is about  $0.5\sigma$  and  $1.2\sigma$  [125] for the 2012 and 2013 samples of MWC 656 respectively.

Based on the non-detection, I have computed 95% C.L. integral flux upper limits above 300 GeV. The integral flux upper limit for the whole observational campaign of MWC 656 for energies above 300 GeV is  $2.0^{-12} \text{ ph cm}^{-2} \text{ s}^{-1}$ . I have assumed a photon index of -2.5 and a simple power law.

I have also computed differential flux upper limits from 250 GeV to 7.7 TeV,

$E_{center}$ [GeV]	Differential Flux UL [cm $^{-2}$ s $^{-1}$ ]
245	$1.4 \times 10^{-11}$
390	$1.2 \times 10^{-11}$
615	$4.6 \times 10^{-12}$
980	$1.2 \times 10^{-12}$
1550	$3.0 \times 10^{-13}$
2450	$1.7 \times 10^{-13}$
3900	$5.3 \times 10^{-14}$
7760	$2.9 \times 10^{-14}$

Table 6.2: Differential flux ULs (95% c.l.) for the whole data set, assuming a power law spectra with index -2.5.

defining five bins per decade of energy. Results are shown on Table 6.2 and Figure 6.2. Again, the calculations were performed assuming a simple power-law with a -2.5 photon index at a 95% C.L.

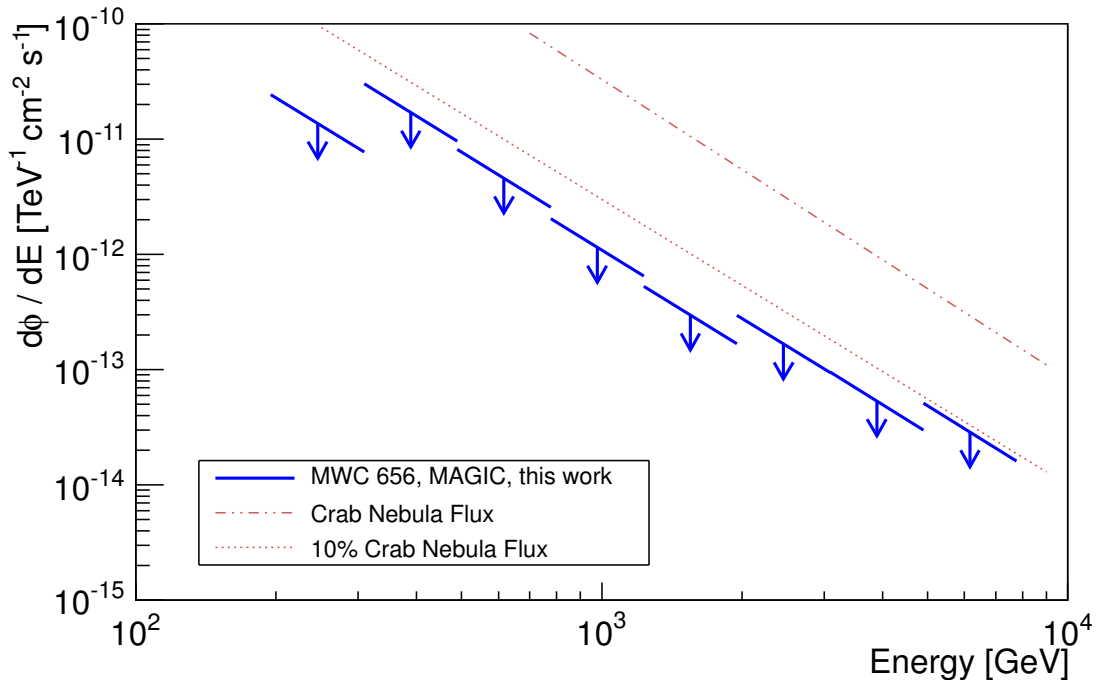


Figure 6.2: Differential ULs obtained for the complete data-set of MWC 656 (95% C.L.). The upper limits have been calculated assuming a simple power-law with spectral index -2.5. The red dashed lines mark the integral flux of Crab Nebula and 10% of Crab Nebula flux.

No signal was neither detected in a day-to-day analysis. The results of the daily analysis are collected on Table 6.3 and Figure 6.3.

It was possible to divide the samples in different phase bins, defining a binning of width 0.1 phases. In this case, four different phase-bins can be differentiated: in the 2012 campaign, the observations covered the phases 0.8–0.9, 0.9–1.0 and 0.2–0.3, which corresponds to the phases before the periastron (remember that

MJD [days]	$\phi$	Integral Flux UL (E >300 GeV) [ $10^{-12} \text{ph cm}^{-2} \text{s}^{-1}$ ]	Significance (Li&Ma) [ $\sigma$ ]	teff [hours]
56070	0.83	17.2	1.5	0.9
56071	0.85	8.7	0.4	1.1
56072	0.87	7.1	-0.1	0.9
56073	0.88	7.0	-0.2	1.0
56074	0.89	7.6	0.0	1.0
56075	0.90	7.8	0.1	1.1
56076	0.91	15.2	1.5	1.1
56077	0.93	2.0	-2.6	1.3
56078	0.95	8.0	0.4	1.4
56092	0.20	9.6	0.8	1.4
56093	0.21	8.4	0.8	2.0
56094	0.23	8.4	0.8	2.0
56095	0.25	2.9	-1.1	2.0
56096	0.26	8.4	0.8	2.1
56097	0.28	8.4	0.7	2.0
56446	0.06	2.6	0.6	1.2
56447	0.07	5.3	0.0	1.3
56448	0.08	5.1	0.7	0.8

Table 6.3: Daily values for the MWC 656 observations performed by MAGIC on 2012 and 2013. No  $\gamma$ -ray emission is detected and integral ULs were calculated assuming an spectral index of -2.5.

periastron is defined at phase  $0.01 \pm 0.10$ ) and also covers the phases where other  $\gamma$ -ray binaries have been detected. The 2013 campaign covered the phase range 0.0-0.1, right during the periastron passage. No signal was detected. Integral upper limits defined with the same binning in phase have also been computed (see Figure 6.3). Details of the values of the upper limits for the phase-to-phase analysis can be found on Table 6.4.

Phase bin	Integral Flux UL (E >300 GeV) [ $\text{ph cm}^{-2} \text{s}^{-1}$ ]	Significance [ $\sigma$ ]
0.0-0.1	$2.0^{-12}$	1.0
0.2-0.3	$8.7^{-12}$	2.1
0.8-0.9	$6.5^{-12}$	1.0
0.9-1.0	$2.5^{-12}$	-1.1

Table 6.4: Integral flux ULs for  $E > 300$  GeV calculated at 95% c.l. for MWC 656 for each orbital range-phase. In this case, the same power law spectrum with index -2.5 has been assumed.

*AGILE* detected the source on phases 0.76–0.78, a phase range which could not been observed by MAGIC because of observability restrictions due to the moon phase. The closest observation is the one that took place on phase 0.83 (on MJD 56069.5), approximately 2–3 days later. The integral upper limit set for that night for energies above 300 GeV is  $< 1.7 \times 10^{-11} \text{ cm}^{-2} \text{s}^{-1}$ , which corresponds to a 14% of the Crab Nebula flux.

I have also computed all these upper limits assuming two other photon indexes, -2.0 and -3.0, as there are no indications of what the spectrum of MWC 656 at VHE is. The value of the upper limits obtained for the three different spectral indexes are compatible at 5% level.

The MAGIC observation carried out in 2013 June 4 was scheduled contemporaneously with an *XMM-Newton* observation from which it was revealed that MWC 656 is indeed a HMXRB [159]. The source was in the quiescent state during the observation. The integral flux UL for this night is  $F(E > 300 \text{ GeV}) < 4.9 \times 10^{-12} \text{ cm}^{-2} \text{ s}^{-1}$  (1.3% of Crab Nebula).

There is no information about the X-ray state of the binary system during the 2012 observation with *XMM-Newton*. Other spatial missions as MAXI have not reported emission from MWC 656 during the 2012-2013 campaign, which may be indicative of a quiescent state.

Finally, the STELLA spectra taken simultaneously with the June 2013 campaign, shows the double-peaked HeII  $\lambda 4686$  emission line, with an equivalent width comparable to that in [55]. Also H $\alpha$ , H $\beta$  and weak FeII lines with comparable strengths as reported in [57] are detected. With these observations, it is possible to conclude that MWC 656 shows similar activity as in past observations.

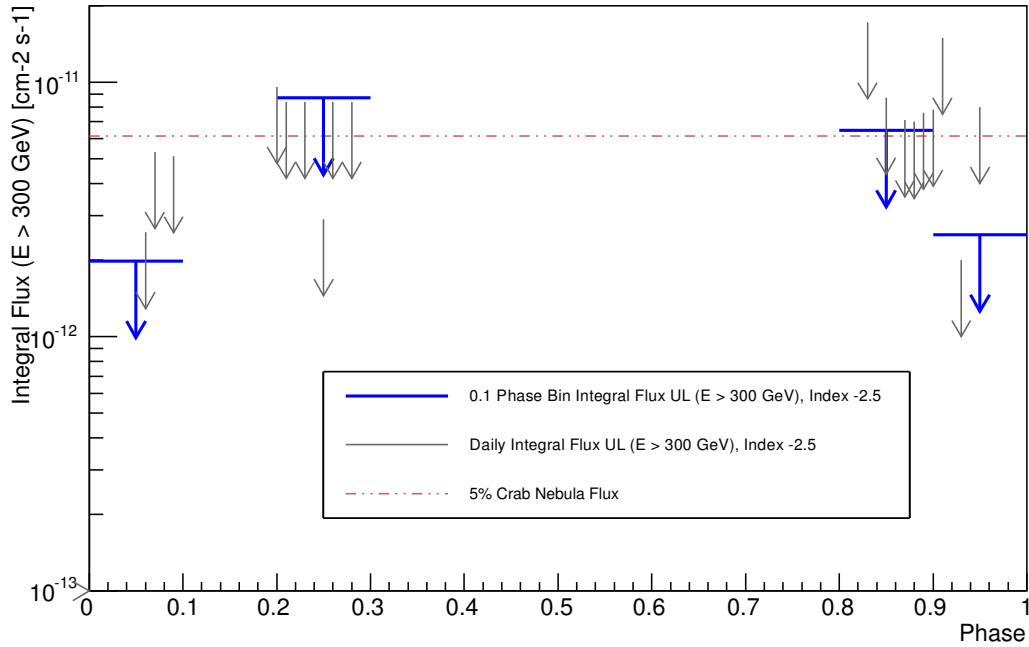


Figure 6.3: Orbital phase-resolved (blue) upper limits (95% C.L) for MWC 656 assuming an orbital period of 60.37 days. Daily upper limits (grey) are also plotted. Upper limits have been calculated assuming a -2.5 spectral index.

## 6.5 Discussion

MWC 656 has not been detected by MAGIC in any of the periods in which the system has been observed. We have set upper limits on the flux for different data subsamples assuming a spectral index of -2.5. Upper limits with softer and

harder spectrum were also calculated. They are compatible within 5% with the previous one.

*AGILE* detected the source between phases 0.76 and 0.79, which is around 0.2 phases before periastron<sup>16</sup>. Considering the new ephemeris from [55], the periastron passage occurs at phase  $0.01 \pm 0.10$  close to inferior conjunction. The emission detected by *AGILE* fits within the Be/BH scenario proposed by [55], where the BH is in a quiescence state and eventually produce  $\gamma$ -ray flares. What it is still difficult to explain is how this  $\gamma$ -ray flares can be produced considering the low X-ray luminosity of the system and considering that other XRBs have not been detected by *Fermi*/LAT when they display an outburst (e.g. GRS 1915+105). The *AGILE* flare could be the result of different mechanisms: accretion/ejection processes, magnetic reconnection or strong shocks in the jet, etc. These phenomena can also happen in BH LMXBs with outbursts, although no GeV emission has ever been detected from LMXBs. However, similar transient GeV phenomena seems to take place in the BH HMXB Cygnus X-1, as it has been reported by *AGILE*, although *Fermi*-LAT does not detect it. A notable difference between LMXBs and HMXBs is the powerful wind of the massive companion which can play an important role in sudden accretion events, shocks in the jet and reconnection events as well as the huge amount of optical/UV photons that could lead to GeV emission through inverse Compton scattering. On the other hand, it might happen that the *AGILE* detection is not related to MWC 656 and it is just a transient event of an unknown nature in the direction of the binary system. However, the lack of contemporaneous data at other wavelengths during the *AGILE* flare make these ideas just speculations.

Extrapolating the flux from the *AGILE* detection (assuming a power-law spectrum and -2.5 as spectral index), MAGIC would have expected a differential flux of about  $\sim 4 \times 10^{-11} \text{ TeV}^{-1} \text{ cm}^{-2} \text{ s}^{-1}$  at 300 GeV, which is above the upper limit set by MAGIC. Still, the *AGILE* and MAGIC measurements are not simultaneous and the state of the source could have been different, hence flaring episodes can not be excluded. It can also happen that the spectral index is softer or that there is a cut-off.

XRBs in the quiescent state show a hard X-ray spectrum and very faint or undetectable radio emission. The X-ray spectrum of MWC 656 can be fitted with a black body plus a power-law, with  $\sim 80\%$  of the total flux coming from the non-thermal component. The non-thermal X-ray luminosity of MWC 656 is  $L_{\text{nt}}(0.3-5.5 \text{ keV}) = (1.6^{+1.0}_{-0.9}) \times 10^{31} \text{ erg s}^{-1} \equiv (3.1 \pm 2.3) \times 10^{-8} L_{\text{Edd}}$  [159] for the estimated BH mass range  $3.8 - 6.9 M_{\odot}$  [55]. This non-thermal emission can be interpreted as the contribution coming close to the black hole. The low X-ray luminosity indicates that the production of VHE particles at detectable levels is very challenging. Making an extrapolation of the X-ray luminosity to the VHE regime, assuming a power-law with a spectral index of -2.5, the expected differential energy flux at 300 GeV is  $\sim 2 \times 10^{-23} \text{ TeV}^{-1} \text{ cm}^{-2} \text{ s}^{-1}$ , which is several orders of magnitude lower than current and planned IACTs sensitivities.

The only other known HMXRB in our Galaxy containing a BH is Cygnus X-1, which hosts a O-type star. This system was observed by the MAGIC Telescope in mono observation mode in 2006 [21]. A hint of signal was found in these observations at  $4.1\sigma$  (post-trials), being the first hint of VHE  $\gamma$ -ray emission arising from a BH HMXRB. This  $\gamma$ -ray excess coming from Cygnus X-1 was

<sup>16</sup>Phase 0 has been set to the maximum of optical brightness, on HJD 2453243.3 (MJD 53242.8)

detected during a hard X-ray flare registered by the *INTEGRAL*, *Swift* and *RXTE* satellites, when the system was at orbital phase 0.91 (being phase 0 the moment when the BH is behind the companion star). It was suggested that the hard and soft X-ray photons were produced in different regions of the system, and that hard X-rays and gamma rays could be produced in regions linked by the collimated jet, such as the base of the jet and the interaction region between the jet and the stellar wind, respectively [21]. However, MWC 656 is not as active as Cygnus X-1 in X-rays, displaying a flux  $\sim 5$  orders of magnitude lower than Cygnus X-1. During the simultaneous X-ray and VHE observations, MWC 656 was in the quiescent state, at which the accretion disk is truncated at several gravitational radii from the BH. The MAGIC observations took place at orbital phases at which the compact object is almost in front of the companion star and the expected absorption due to the companion's photon field should be low. Even assuming a flaring state and a ratio between X-rays and VHE gamma rays of  $F_X/F_{\text{TeV}} \sim 8.5$ , the expected emission would be too low to be detectable by the current generation of Cherenkov telescopes. However, these are speculations and it may happen that MWC 656 really shows stronger VHE flares.

The only possible manner to detect the putative  $\gamma$ -ray emission of MWC 656 would be to observe it on flaring state during several hours. For that purpose, MAGIC would need another telescope to send an alarm warning that the source is in high state. Right now, the only possible option would have been that *AGILE* reported the flaring state, but since the gyroscope is broken, no pointing-mode observations are performed and, hence, it is not possible to send these alarms.

The spectral energy distribution (SED) of MWC 656 is presented in Figure 6.4. Contemporaneous *XMM-Newton* and MAGIC data of 2013 taken when the source was in quiescent state are plotted. The *AGILE* detection and the *Fermi*/LAT upper limit are also represented. These values correspond to the same night of observation and are in contradiction. However, the observation mode of these two satellites are different: while *Fermi*-LAT observes the sky in survey mode, *AGILE* performs pointing observations. In case that the  $\gamma$ -ray emission detected by *AGILE* comes really from MWC 656, the source must have been in a completely different emission state from the quiescence stated during MAGIC and *XMM-Newton* observations.

In conclusion, we have observed the first Be/BH binary system with the MAGIC Telescopes and we have not detected it. There is no information about the X-ray state of the binary system during the 2012 MAGIC observations. During the 2013 observations, the source was in the quiescent state as stated from the simultaneous X-ray observations. Optical data taken simultaneously with the 2013 campaign shows that the source is in a similar state as in [57]. Compared to Cygnus X-1, MWC 656 displays a much weaker X-ray emission and thus the expected VHE emission, if any, will be challenging to detect by the current and planned IACTs. The possible manner to detect the putative TeV emission would be by observing the source during flaring states for several (at least  $\sim 30$ ) hours.

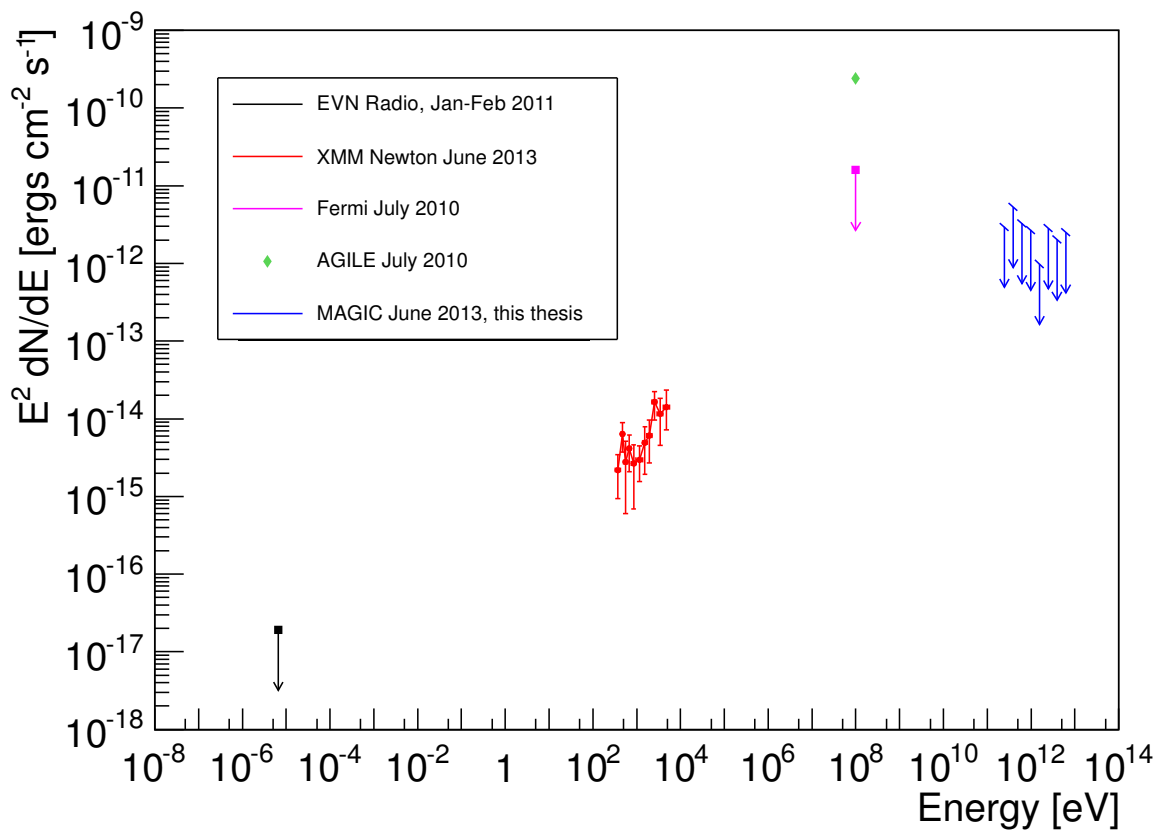


Figure 6.4: SED of MWC 656 including MAGIC 2013 ULs together with simultaneous XMM-Newton data from [159]. The EVN radio ULs from [155], the AGILE detection from [133] and the *Fermi*/LAT UL [5]. The *AGILE* and *Fermi*-LAT ULs are simultaneous.



# 7

## Search for $\gamma$ -ray Emission from the Microquasar SS-433

**SS** 433 is the first microquasar where precessional relativistic jets were detected. In this chapter, MAGIC observations of the source performed on two different campaigns are presented. No TeV emission has been detected from SS 433. Upper limits to the VHE flux have been computed.

### 7.1 The Microquasar SS 433

---

SS 433 (= V1343 Aql) is a massive eclipsing binary system in a close circular orbit located at RA =  $19^h 11^m 49.56^s$  and DEC =  $+04^\circ 58' 57.6''$ . The companion star is a massive A3-8 supergiant of mass  $\sim 30M_\odot$ , which was first identified by its H $\alpha$  emission lines [190]. The donor star fills its Roche Lobe and its material is continuously accreted onto the compact object. Hence, the system is classified as a microquasar. The measurements of the mass of the compact object varies from  $1.25M_\odot$  to  $15M_\odot$  ([77], [121], [94]), what permits both the black hole (BH) and neutron star (NS) solution. Historically, the mass of the compact object has been calculated to be  $\sim 9M_\odot$ , suggesting it to be a black hole. However, [94] re-determined the parameters of the system using photometric measurements, providing new and more accurate ephemeris, and re-calculated the mass of the compact object, concluding it is a  $1.25 - 1.87M_\odot$  neutron star (NS). Nevertheless, the luminosity of the system has also reliably been measured by other authors ([60], [78]), with a value of  $L_{bol} \sim 10^{40} \text{ ergs}^{-1}$  (with peak emission in the ultraviolet), which is a value too high to be due to a neutron star [148]. The system is located at a distance of  $5.5 \pm 0.2$  kpc and the orbital period is  $\sim 13.08$  days ([76], [61]).

SS 433 is the only supercritical accretor, with a constant mass transfer of  $\dot{M} \sim 10^{-4} M_\odot \text{year}^{-1}$ , known in the Milky Way and it was the first microquasar where relativistic jets were discovered [6]. The jets show a relativistic velocity of  $0.26c$  and a precessional period of  $P_{pre} = 162.3$  days with a half-opening angle of  $\theta \sim 21^\circ$ . The inclination angle of the jets with respect to the line of sight of the observer is  $78.83^\circ$  [74]. The jets are collimated, with an opening angle of  $\sim 1.2^\circ$ .

Furthermore, the jets present a jittering movement with a period  $P_{jit} = 6.28$  days [161] and an amplitude of  $\sim 2.8^\circ$ . The kinetic power carried by the jets is  $L_{kin} \sim 10^{39} \text{ erg s}^{-1}$  [70]. The peak of the radiative output occurs at UV and optical wavelengths. The X-ray emission is 1000 times lower than  $L_{kin}$ , probably due to screening. The main energy emission comes from the super-Eddington regime accretion disk, which also precesses with the  $P_{pre}$  and is inclined  $i \sim 20^\circ$ . The *moving* H and HeI lines are created in the jets. These lines are Doppler shifted and they move along the spectrum in accordance to the orientation of the jet [140].

The system lies in the center of the W50 nebula (= SNR G39.7–2.0), a  $(2 \times 1)^\circ$  non-thermal radio shell complex. Both the jet and the nebula are detected in optical [74], radio [70] and X-rays ([142], [202]). The elongated east-west morphology of W50, coincident with the double-jet axis of SS 433, indicates interaction between the jet and the nebula [70]. The radio and X-ray lobes at the west and east ends of the nebula are a signature of the precessional movement of the jets. The jets are found to be hadronic. The baryonic content propagates to large distances without visible deceleration. At large distances, hot gas at  $T \sim 10^7 K$  is found, which is indicative of a continuous source of heating [149]. The extended X-ray emission is likely non-thermal and its spectrum is softer than that of the central source. Figure 7.1 shows the radio and X-ray emission of SS 433 and W50, where the association of both systems is clearly visible. No HE emission has been reported neither from *AGILE* nor from *Fermi*-LAT.

The W50 region and the binary SS 433 have been objects of extensive devoted studies performed by HEGRA [12] and CANGAROO-II [110], although no  $\gamma$ -ray emission was detected. Upper limits (ULs) were established both for the inner system, SS 433 and the east (namely e1, e2 and e3, located at C and D regions in Figure 7.1) and west (namely w1, w2, w3, p1 and p2, located between regions A and B in Figure 7.1) interaction regions. HEGRA set an UL for SS 433 of flux  $8.9 \times 10^{-12} ph cm^{-2}s^{-1}$  for energies above 800 GeV, with a total integration time of  $\sim 96h$ .

Ephemeris have been settled for SS 433 by different authors. At first place, the ephemeris calculated by [92] and [76] were considered, providing very different phases for the precessional jets. Recently, [94] provided new and most accurate values. Hence, the ephemeris used for the calculation of the orbital and the precessional phases have been taken from [94]:

$$MinI = JD\ 2450023.746 + 13^d.08223 \quad (7.1)$$

$$T_{max} = JD\ 2449998.0 + 162^d.278 \quad (7.2)$$

being Min I the orbital phase  $\phi = 0$  for the mid-eclipse of the accretion disk by the donor star. The precessional phase  $\Psi = 0$ , denoted by  $T_{max}$  is given by the second equation, and denotes the maximum separation of the lines in the spectrum. The edge-on occurs at precessional phases  $\Psi = 0.33$  and  $\Psi = 0.66$ . The main parameters of the binary system are collected on Table 7.1.

Summarizing, SS 433 is a unique microquasar because of:

- The accretion onto the compact object is supercritical, with a mass transfer of  $\dot{M} \sim 10^{-4} M_\odot/\text{year}$ .

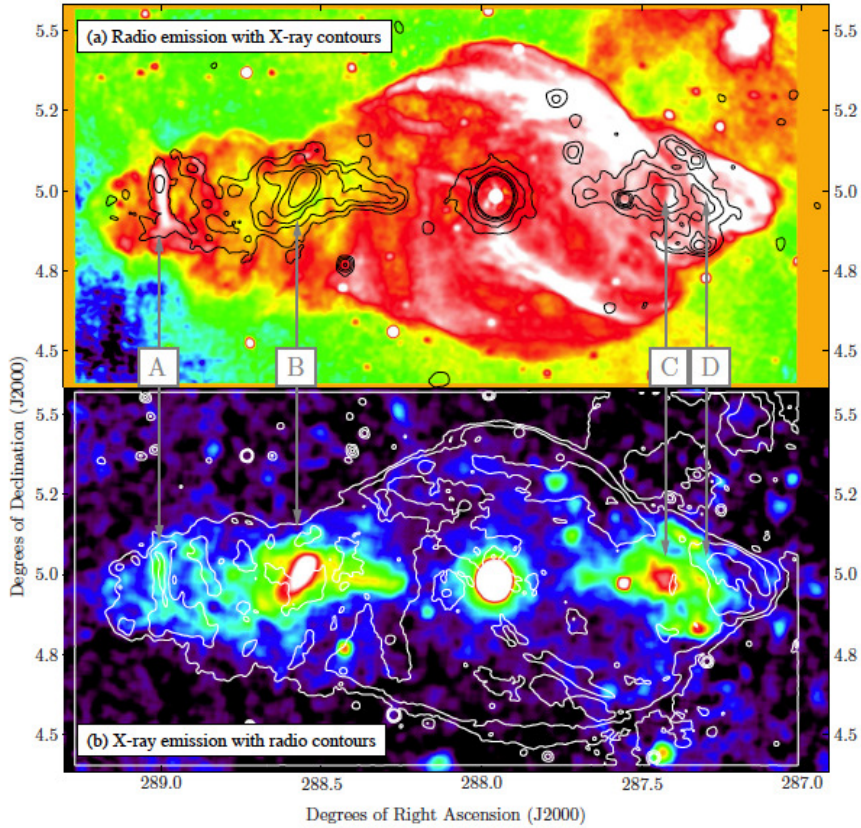


Figure 7.1: *Top:* VLA radio image with ROSAT X-ray contours overlaid. *Bottom:* ROSAT X-ray image with VLA radio contours. There is a clear correspondence between both wavelengths. A: marks a bright filament visible in both wavelengths, B and C indicate the radio lobes, where X-ray emission is maxima and radio is minima. D points the termination of the eastern lobe, followed by the brightening of the radio source

- The system shows two strongly-collimated persistent relativistic jets ( $0.26c$ ) and their characteristics have remained constant with time.
- The jets and the accretion disk present a precessional period of 162.3 days. This precession, as well has the disk inclination angle, has remained constant over the years.
- The orbital period, 13.1 days, has remained unaltered over decades, despite the supercritical exchange of mass between donor star and compact object.

### 7.1.1 $\gamma$ -ray Emission and Absorption Processes

$\gamma$  rays are expected to be emitted by microquasars (for a review of models, see Section 5.2.1), and SS 433 is a suitable binary system to test theoretical predictions on HE and VHE production in microquasar jets. The  $\gamma$  rays are supposed to be created in the inner jet region, in the base of the jet and also in the interaction regions between the jet and W50. Three shocks are formed due to the impact of the jets with the nebula: a forward (bow) shock which propagates into the interstellar medium and encloses the shell, a reverse shock, with the same direction but inwards and which causes the inflation of the cocoon and finally a re-confinement shock which is formed where the pressure of the jet is equal to the pressure of the cocoon [46].

Parameter	Value
Star Spectral Type	A3-A8
Compact Object	(Most likely) Black Hole
$R [R_\star]$	79
Star mass [ $M_\odot$ ]	$\sim 30$
BH mass [ $M_\odot$ ]	1.2 – 15 (most likely 9)
$P_{orb} [\text{days}]$	$13.08223 \pm 0.00007$
$T_0 [\text{JD}]$	$2450023.746 \pm 0.30$
$P_{pre} [\text{days}]$	162.278
$T_{0-pre} [\text{JD}]$	2449998.0
$\phi_{\text{eclipse}}$	0
$\Psi_{\text{edge-on}}$	0.33 & 0.66
$i_{\text{jet}} [\circ]$	78.83
$i_{\text{disk}} [\circ]$	20

Table 7.1: Information about the  $\gamma$ -ray binary candidate SS 433 (from [94]). R is the orbital radius,  $M$  is the mass,  $P_{orb}$  the orbital period,  $T_0$  the epoch of the mid-eclipse,  $P_{pre}$  the precessional period,  $T_{0-pre}$  the reference epoch for the precessional movement,  $\Psi_{\text{edge-on}}$  are the faces where the jets lie in the plane of the sky (disk edge-on),  $i_{\text{jet}}$  and  $i_{\text{disk}}$  are the inclination angles of the jets and the disk respectively.

In the case of the central source, SS 433, and considering a hadronic scenario, interactions of relativistic protons in the jet can produce gamma-rays through  $\pi^0$  decay [164]. The target ions could be provided both by the companion and disk winds, or by the pool of thermal protons outflowing within the jet itself. In a leptonic framework,  $\gamma$  rays could be produced through inverse Compton (IC), by scattering of the ambient stellar photons [61] and from the accretion disk (92, 84). In addition, self-synchrotron Compton (SSC) and Bremsstrahlung from the interaction of electrons with the jet ions is expected. Concerning the interaction regions, the most efficient mechanism for  $\gamma$ -ray production in the shell is Bremsstrahlung, while IC dominates in the cocoon and the reconfiment shocks [47].

However, strong absorption processes may occur in the system, making the detection of VHE emission in SS 433 highly difficult. Absorption of the  $\gamma$ -ray flux is expected to occur along  $\sim 80\%$  of the orbit. First, the donor star and the compact object are embedded in a thick equatorial envelope, which provides a big amount of mid-IR and UV photons, causing strong attenuation of the putative  $\gamma$ -ray emission. Furthermore, the photon field of the companion star may be a strong source of  $\gamma$ -ray absorption through pair creation [178]. Moreover, partial eclipses occur every orbit when the donor star crosses in front of the compact object, along the line of sight of the observer. This is the point of strongest absorption. Finally, the optical depth presents variability with the precessional phase [179]: when the approaching jet points away from the Earth, the equatorial envelop changes its orientation and blocks the inner jet.

Hence, and according to [179], the best opportunity to detect  $\gamma$ -ray emission from SS 433 is at the precessional phases where the absorption due to the envelope will be minimal, at  $\Psi_{pre} = 0.91 - 0.09$ . On this phase interval, the  $\gamma$  rays created in the base of the jet will escape and will travel through the equatorial disk. In agreement with the ephemeris, the eclipse happens at orbital phase  $\phi = 0$ , which

is the point along the orbit of strongest absorption.

## 7.2 MAGIC Observations of SS 433

---

MAGIC performed observations of the binary system SS 433 on two different epochs, August 2008 and May-June 2010. The observations were scheduled during the precessional phases of expected minimum  $\gamma$ -ray absorption,  $\Psi_{pre} = 0.91 - 0.09$ . The day of the eclipse, at orbital phase  $\phi = 0$ , is the point of minimum transparency to the putative TeV flux, hence this day shall neither be considered. The observations were planned according to the most accurate ephemeris existing by the moment, which were those suggested by [92]. However, in the analysis performed in this thesis, the most recent ephemeris will be used, those defined by [94]. The field of view covers not only the central system, SS 433 but also the *e1* and *e2* interaction regions between the jet and the nebula, which are 2' far from the central system, SS 433. These two interaction regions are not expected to be spatially resolvable by MAGIC (in the sense that it will be not possible to differentiate source *e1* from *e2*), but as they fall within the field of view of MAGIC and ULs have been set there by HEGRA, they will also be analyzed. The western interaction regions also fall within the field of view of MAGIC, about 3' away from the central system. The western region is more extended than the eastern regions, since it includes five different interaction regions [110], hence the analysis in this area is more complex. Since no hot spot is observed in a skymap (see Figure 7.5), no further studies in this area were considered.

### August 2008

SS 433 was observed with MAGIC-I telescope in wobble mode for 11.5 hours at a zenith angle range  $23^\circ - 31^\circ$ , between 21<sup>st</sup> and 29<sup>th</sup> of May of 2008. However, during the first five days there were adverse weather conditions, hence the data taken on these days was discarded. After quality cuts, 7.4 hours of data remained. The *Size* cut applied was  $> 200\text{phe}$ , because it is the value below where the sensitivity starts to worsen. The standard analysis cuts were applied. For this data set, there is no contemporaneous Crab Nebula data, neither a OFF data taken under the same conditions, hence SS 433 itself has been used as training sample for the  $\gamma$ -hadron separation, which induce negligible effects for not strong sources. According to the ephemeris [94], the complete data set fulfills the observability requirements.

### May - June 2010

Stereoscopic observations were performed on 20<sup>th</sup> – 23<sup>rd</sup> of May and 08<sup>th</sup> - 10<sup>th</sup> of June of 2010 for a total time of 10 hours, and a zenith angle coverage  $23.7^\circ - 29.8^\circ$ . After performing the standard selection procedure, 8.6 hours of good quality data remained. Contemporaneous Crab Nebula data was taken in this occasion. The OFF data used were observations pointing to Cygnus-Loop, at the same zenithal interval as the SS 433 observations. The applied cut in this case was *Size*  $> 100\text{phe}$ . In this case, 20<sup>th</sup> and 21<sup>th</sup> of May are at  $\Psi_{pre} \sim 0.9$ , which is outside the desired phase range and absorption of  $\gamma$  rays is expected [179], hence this data

has been rejected. Considering the ephemeris and the precessional orbital period, 5.9h of data survived the requirements.

### 7.3 Results

No significant signal has been detected in the SS433/W50 nebula complex, neither from the central source, the eclipsing binary SS 433, nor from the eastern interaction regions e1 & e2. The total significance for the central source is  $0.7\sigma$  for the 2008 mono data and  $0.5\sigma$  for the 2010 stereo data. The Alpha and Theta2 plots are shown on Figure 7.2. The nightly fluxes and significance obtained for the observations of the binary SS 433 is collected on Table 7.2.

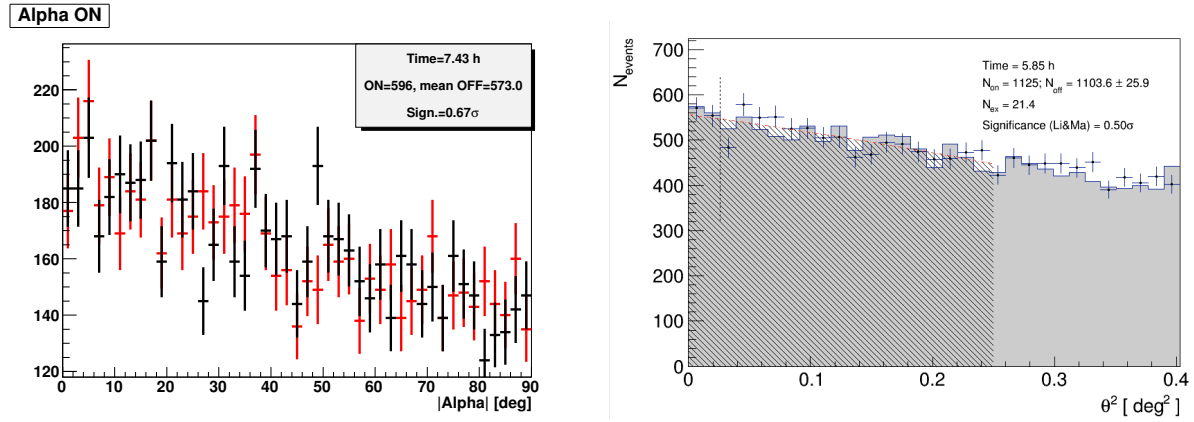


Figure 7.2: *Alpha* and  $\theta^2$  distributions for the two samples of SS 433. Standard cuts were applied. No significance signal has been detected. *Left:* *Alpha* distribution for the 2008 mono data. *Right:*  $\theta^2$  distribution for the 2010 stereo data set.

MJD [Days]	$\phi$	$\Psi_{pre}$	Significance (Li&Ma) [ $\sigma$ ]	Integral Flux ( $E > 300$ GeV) $[10^{-12} \text{cm}^{-2} \text{s}^{-1}]$	$t_{eff}$ [hours]
54704	0.41	0.00	-1.0	$-1.5 \pm 4.2$	1.8
54705	0.49	0.01	-0.1	$-0.4 \pm 4.1$	1.8
54706	0.57	0.02	1.0	$3.7 \pm 3.7$	2.2
54707	0.66	0.02	1.32	$5.9 \pm 4.6$	1.6
55338	0.88	0.91	-0.1	$-0.1 \pm 1.5$	1.4
55339	0.97	0.92	-1.1	$-2.5 \pm 1.7$	0.8
55355	0.29	0.01	0.3	$0.6 \pm 2.6$	0.6
55356	0.37	0.02	-0.9	$-1.7 \pm 1.4$	1.3
55357	0.45	0.03	-0.5	$0.0 \pm 1.2$	1.9

Table 7.2: Nightly lightcurve of SS 433 for 2008 mono and 2010 stereoscopic data. The first column indicates the date in MJD, the second the orbital phase, the third, the precessional phase, the fourth the significance, the fifth, the integral flux and the sixth the effective observation time.

Integral flux upper limits for the combined (mono + stereo) observations were calculated for SS 433 at 300 GeV, which is the energy for which the effective collection area is stable, and also at 800 GeV, in order to compare with previous

published data from HEGRA [12]. Furthermore, ULs for the integral flux of the eastern interaction regions have been calculated at 300 GeV and at 800 GeV in order to compare with the results from HEGRA. The search of signal and the spectrum were calculated around the position of  $e2$ . The values are shown on Table 7.3. The assumed spectrum was a power-law with spectral index -2.6.

Region	IACT	$t_{eff}[h]$	$E_{th} [\text{GeV}]$	Integral flux UL [ $\text{cm}^{-2}\text{s}^{-1}$ ]	$\Psi_{pre}$
SS 433	HEGRA [12]	96.3	800	$8.9 \times 10^{-13}$	0.0 - 1.0
SS 433	MAGIC (this thesis)	13.3	800	$4.1 \times 10^{-12}$	0.91 - 0.09
SS 433	MAGIC (this thesis)	13.3	300	$3.3 \times 10^{-12}$	0.91 - 0.09
$e2$	HEGRA [12]	73.1	800	$9.2 \times 10^{-13}$	0.0 - 1.0
$e1 \& e2$	MAGIC (this thesis)	13.3	800	$3.4 \times 10^{-12}$	0.91 - 0.09
$e1 \& e2$	MAGIC (this thesis)	13.3	300	$1.5 \times 10^{-12}$	0.91 - 0.09

Table 7.3: Integral flux ULs derived for SS 433 and eastern interaction regions and comparison with published results. The first column denotes the region of study; the second the IACT which performed the observation; the third column is the effective time of the observations, the fourth column shows the energy threshold for the UL calculation and the fifth column shows the integral flux UL. The last column indicates the precessional phase interval of the observations.

Differential ULs have been calculated from 215 to 3000 GeV for the central source, which are the lower and higher bins of energy with enough events to perform the flux estimation. The resulting plot is shown on Figure 7.3 and its values are collected on Table 7.4. In the case of the eastern interaction regions, no signal has neither been detected and differential ULs have been calculated from 155 to 1110 GeV, which are the bins with enough statistics to perform the estimation of the flux. The resulting values are display on Figure 7.4 and Table 7.5.

A skymap of the SS433/W50 region, obtained with 2010 stereoscopic data, is shown on Figure 7.5. No excess is visible neither at the emplacement of SS 433 neither at the interaction regions  $e1 \& e2$ . X-ray (ROSAT Broadband) and radio (GB6 4.85GHz) contours are over-plotted.

## 7.4 Discussion

No VHE emission has been detected coming from the SS433/W50 system, neither from the central source, SS 433, nor from the eastern interaction regions,  $e1 \& e2$  or western regions. However, the reported ULs can help into constraining different physical parameters related to the mechanisms associated to  $\gamma$ -ray production in this system.

The VHE emission can be produced both in the inner jet region of SS 433 and also in the zones of interaction between the jets and the surrounding nebula. Nevertheless, the inner jet regions ( $z < 10^{-13}\text{cm}$ ) are affected by a strong absorption of the  $\gamma$ -ray flux due to the thick envelope [179], hence only further distances are considered for the acceleration processes. The donor star and the surrounding envelope provide the photon and matter fields necessary for efficient particle acceleration processes. Both hadronic and leptonic processes are expected.

The  $\gamma$ -ray production is associated to the particle acceleration efficiency processes

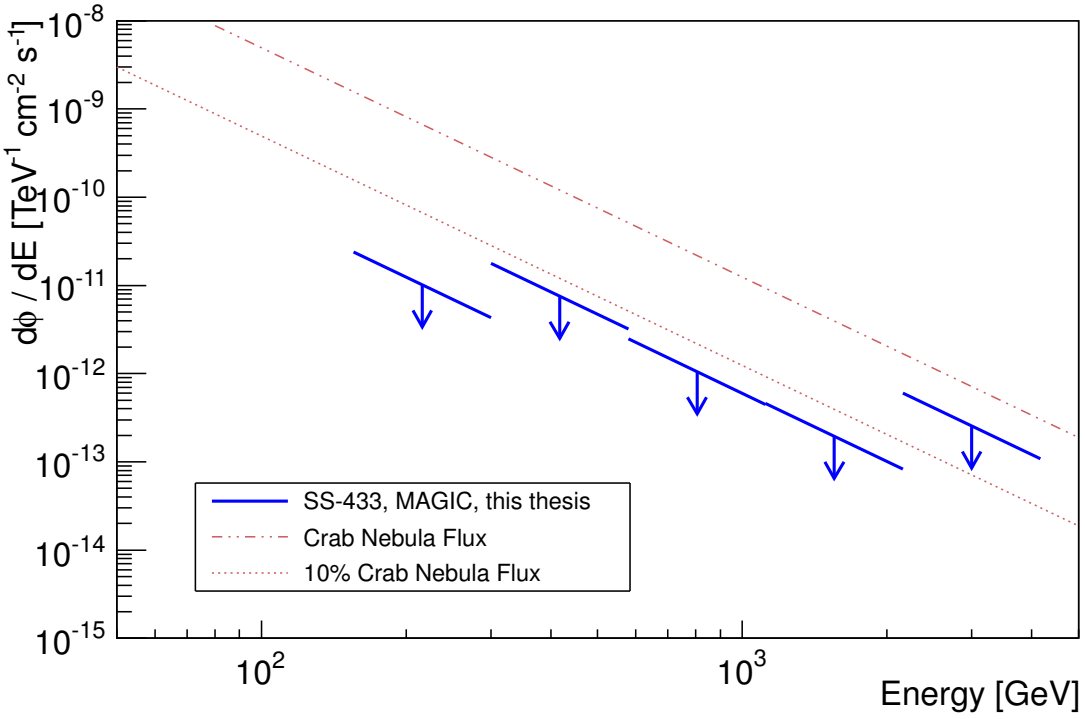


Figure 7.3: Differential flux ULs computed for the total data set of SS 433. The assumed spectrum was a power-law with spectral index -2.6. The red dashed lines mark the Crab Nebula flux at 100% and 10% level.

$E_{center}$ [GeV]	Differential Flux UL [cm $^{-2}$ s $^{-1}$ ]
215	$1.0 \times 10^{-11}$
415	$7.5 \times 10^{-12}$
805	$1.1 \times 10^{-12}$
1550	$2.0 \times 10^{-13}$
3000	$1.6 \times 10^{-13}$

Table 7.4: Differential flux ULs (95% C.L.) for the whole data set, assuming a power law spectra with index -2.6. The first two columns quote the lower and upper edges for each energy bin. The third column collects the values of the differential flux ULs.

$E_{center}$ [GeV]	Differential Flux UL [cm $^{-2}$ s $^{-1}$ ]
215	$3.3 \times 10^{-12}$
415	$5.7 \times 10^{-12}$
805	$1.8 \times 10^{-12}$
1550	$1.5 \times 10^{-13}$

Table 7.5: Differential flux ULs (95% C.L.) for the easter regions, assuming a power law spectra with index -2.6. The first two columns quote the lower and upper edges for each energy bin. The third column collects the values of the differential flux ULs.

in the system. In the case of SS 433, the power transferred to the non-thermal par-

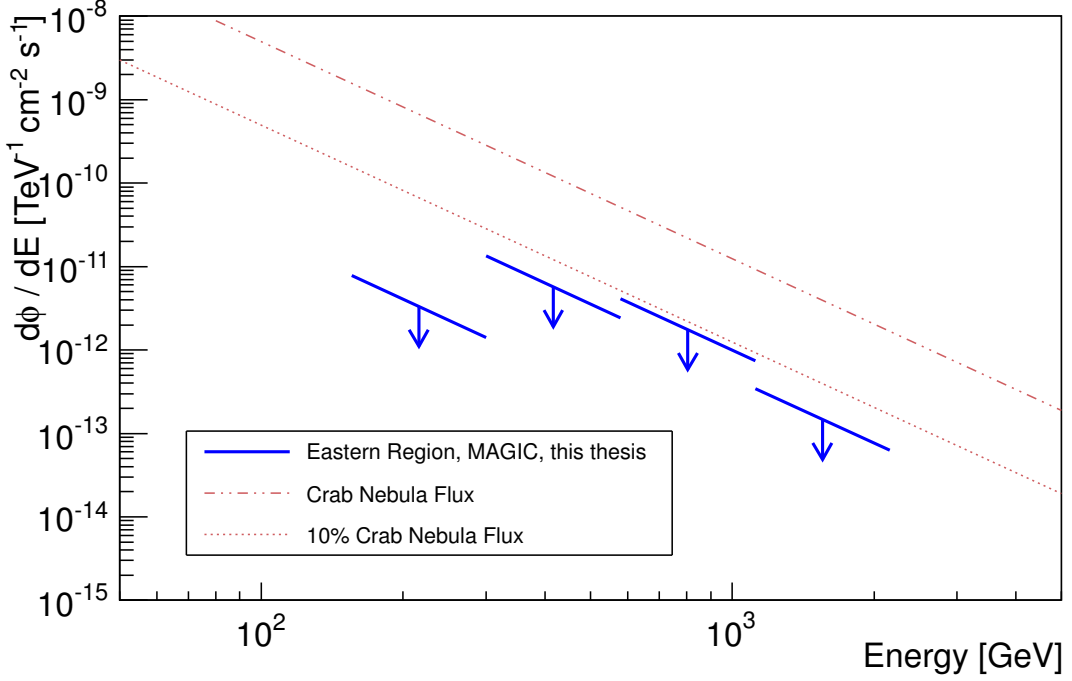


Figure 7.4: Differential flux ULs computed for the total data set of the eastern interaction regions. The assumed spectrum was a power-law with spectral index -2.6. The red dashed lines mark the Crab Nebula flux at 100% and 10% level.

ticle populations depends on the acceleration efficiency,  $q_{acc}$ , which can be defined as the ratio between the relativistic non-thermal power and the jet bulk kinetic power  $q_{acc} = L_{rel} / L_{kin}^{jet}$ , where  $L_{kin}^{jet} \sim 10^{39} erg s^{-1}$  [70]. The parameter  $q_{acc}$  is related to the acceleration of electrons and protons.

In the hadronic model proposed by [179], the  $\gamma$ -ray production is due to  $pp$  interaction between relativistic and cold protons in the jet. It differs from other hadronic models where the hadronic emission arises from interactions between relativistic jet protons and protons of the stellar wind [183]. In this model,  $q_{acc} \sim 10^{-4}$ , which in this case corresponds to the theoretical value for the acceleration of the relativistic protons. The predicted flux above 800 GeV, for precessional phases of low absorption ( $\Psi = 0.91 - 0.01$ ) is  $2.0 \times 10^{-12} ph cm^{-2}s^{-1}$ , which is compatible with the integral UL derived in this thesis,  $4.1 \times 10^{-12} ph cm^{-2}s^{-1}$ . The maximum limit for the acceleration of the relativistic protons  $q_{rel}^{max}$ , considering the UL set by HEGRA at 800GeV and the equations listed in [179], is  $q_{acc}^{max} \leq 2.9 \times 10^{-4}$ . In the case of the UL calculated in this thesis at the same energy, the maximum value for the acceleration obtained is  $q_{acc}^{max} = 2.1 \times 10^{-4}$ . Although the UL set by HEGRA ( $8.9 \times 10^{-13} cm^{-2}s^{-1}$ ) is lower than the one calculated in this thesis ( $4.1 \times 10^{-12} cm^{-2}s^{-1}$ ), it is averaged over a complete precessional cycle, including phases of high absorption of the putative  $\gamma$ -ray emission, hence the flux could have been severely reduced. On the other hand, the UL derived in this thesis applies only to the precessional phases of expected low absorption,  $\Psi = 0.91 - 0.09$ , hence it is more restrictive. The expected TeV flux in terms of the precessional phase derived from this model, together with the ULs calculated on this thesis and the HEGRA UL are shown on Figure 7.6.

According to the integral UL, the maximum non-thermal power is  $L_{rel} \sim 2.1 \times$

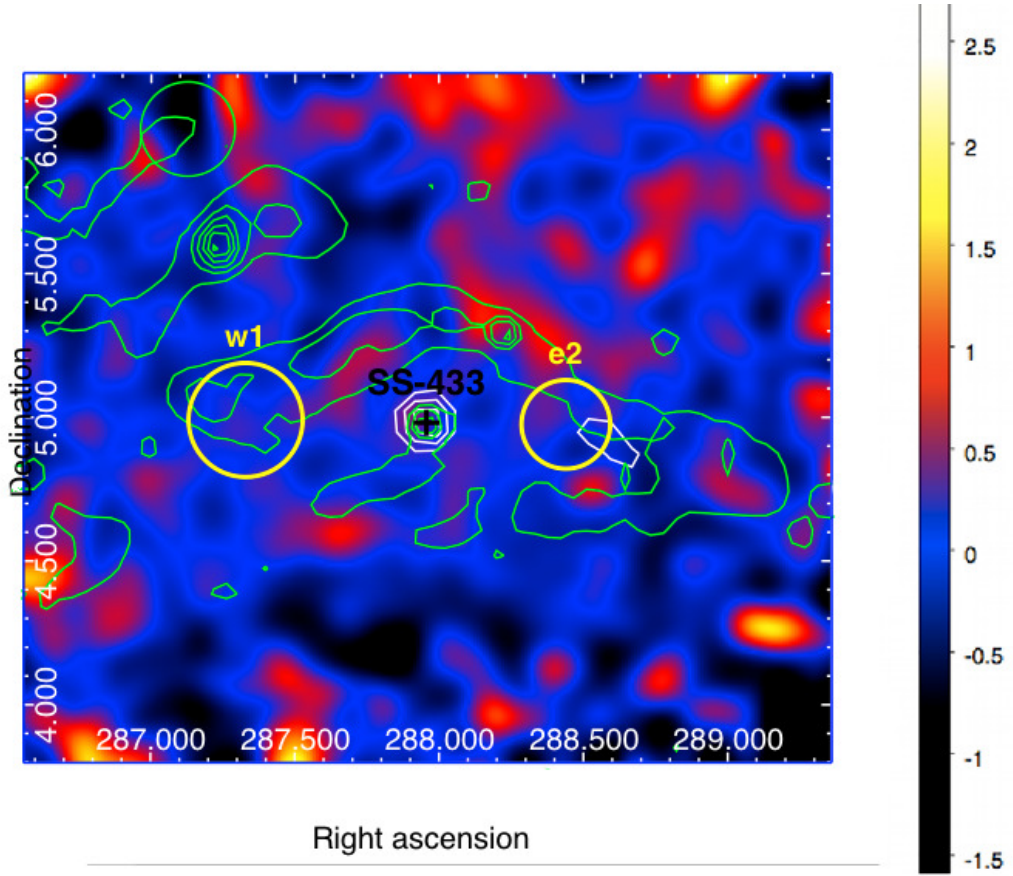


Figure 7.5: Skymap of the SS433/W50 region. No significant excess is revealed neither at the position of the binary system (black cross), nor at the eastern  $e2$  / western  $w1$ , interaction regions (yellow). GB6 4.85GHz radio contours (green) and ROSAT broadband X-ray contours (white) are over-plotted. The grid marks the RA and DEC coordinates, in degrees.

$10^{35} \text{ erg s}^{-1}$ . Hence, just a small fraction of the total energy injected by the jets is destined to accelerate particles up to relativistic energies.

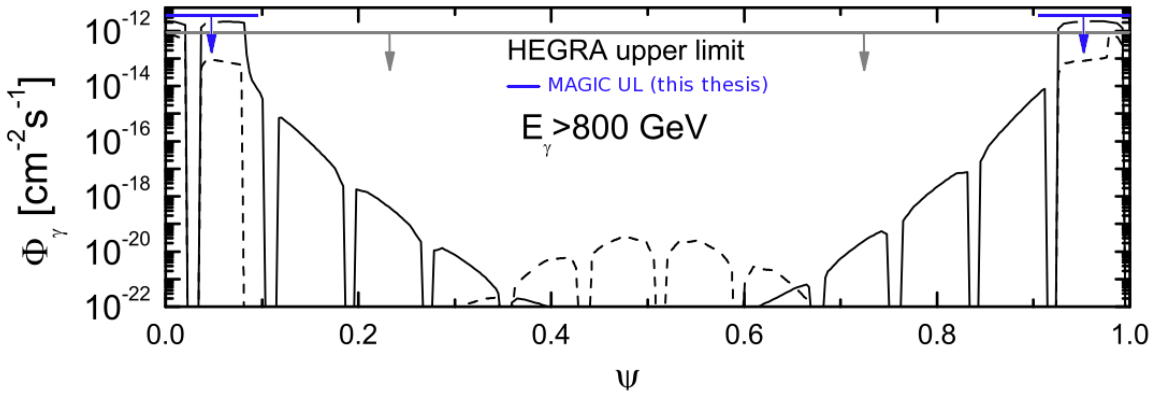


Figure 7.6: Predicted  $\gamma$ -ray emission from SS 433 in terms of the precessional phase for energies above 800GeV, according to [179]. The HEGRA UL is plotted as grey line, covering all precessional phases. The MAGIC combined ULs calculated for the phases of low absorption are also shown on blue. The solid black line represents the approaching jet, while the dashed black line represents the preceding jet.

Leptonic scenarios are not generally used to model the expected  $\gamma$ -ray emission arising from SS 433, due to the fact that the relativistic jets are hadronic. [46] proposed a leptonic scenario to model the putative VHE emission component of SS 433, considering that the emission would come from IC scattering of electrons in the acceleration regions inside the jet for distances where the optical depth is  $\tau < 1$ . However, this model was specific for the results obtained and can not be easily extrapolated. A more generalized leptonic scenario to predict  $\gamma$ -ray emission from SS 433 is still lacking.

A general lepto-hadronic scenario was proposed by [201] to explain the non-thermal radiation component in jets. Different models are computed and some of them predict VHE emission from microquasars. This scenario was applied to a LMXRB, namely XTE J1118+480, and it can even reproduce its SED and predicts that the source can be able to emit TeV emission. This scenario may also be applied to SS 433 which is a microquasar and a super-critical accretor, hence TeV emission can be expected. It may occur that SS 433 emit  $\gamma$  rays in flaring episodes, as theorized in the case of LMXRBs.

Predictions for  $\gamma$ -ray emission in the interaction regions have only been addressed by [46], who modeled the emission from the shell, the cocoon and the re-confinement jets. In their model, relativistic bremsstrahlung is important only in the shell. The integrated  $\gamma$ -ray flux for  $E > 150\text{GeV}$  is  $1.6 \times 10^{-13} \text{ph cm}^{-2}\text{s}^{-1}$ . Computing the UL at the same energies, the value obtained is approximately two orders of magnitude larger,  $1.2 \times 10^{-11} \text{ph cm}^{-2}\text{s}^{-1}$ , which is compatible with the model. The latter UL is calculated considering only stereoscopic data, because 150GeV is too low for mono configuration at the zenith angle range of the considered observations.

The non-detection of TeV emission can be mainly caused by the fact that the observational time ( $\sim 13$  hours) dedicated to the source may not have been large enough to achieve a detection. The MAGIC-I integral sensitivity above 800GeV for 50 hours is  $(4.1 \times 10^{-12} \text{cm}^{-2}\text{s}^{-1})$ , while the stereoscopic system has an integral sensitivity of  $(2.4 \times 10^{-12} \text{cm}^{-2}\text{s}^{-1})$  at the same energies for the same observation time. Hence, it seems that more integration time is needed to be able to detect emission from SS 433, in the case that  $\gamma$  rays are produced. The model proposed by [179] estimated an integrated flux of  $2.0 \times 10^{-12} \text{cm}^{-2}\text{s}^{-1}$  above 800GeV. For energies above 100GeV, the predicted flux is  $9.0 \times 10^{-11} \text{cm}^{-2}\text{s}^{-1}$ , which is above one order of magnitude of the MAGIC-I telescopes sensitivity in 50 hours. Hence, following the model predictions, SS 433 shall be detectable within  $\sim 30$  hours of observation, or at least a hint of signal should be visible. It may also happen that SS 433 is not a steady source of  $\gamma$  rays and that its putative VHE emission appears as flaring episodes, similar to the models proposed for LMXRBs. This would imply that the detection of TeV emission is challenging for current IACTs. Since the source has not been detected at HE, it is not straightforward to estimate what the flux at VHE shall be, and an extrapolation from X-rays is not the proper method to estimate it.

It may also happen that the hadronic model proposed by [179] predicts larger fluxes than expected, but as the data still does not reach the model predictions, this is just speculation. This statement was addressed by [199], based on an error in an equation related to the Lorentz factors stated in [183] and commenting that this error was propagated to [179]. The claim suggested that the  $\gamma$ -ray flux is dramatically affected by the viewing angle, specially for those larger than

$\theta \sim 10^\circ$ , as it is the case of SS 433 with  $\theta \sim 20^\circ$ . It notes that the proton spectra is supposed to be overestimated, leading to an over-prediction of the  $\gamma$ -ray emission and making the detection of the putative  $\gamma$  rays challenging for the current generation of IACTs. Nevertheless, it seems that this effect is only important for systems such as blazars or GRBs, where the Lorentz factor is usually  $\Gamma = 10$  and can even reach values of  $\Gamma = 50$  during strong flares. In the case of microquasars, the Lorentz factor is much lower, of the order of  $\Gamma \sim 2$ , hence the effect is supposed to be negligible [199]. The effect should affect the calculated flux in a 5 – 10 %.

In the HE regime, no emission has been reported neither from *AGILE* nor from *Fermi*-LAT. SS 433 is not visible in the *Fermi*-LAT Second Source Catalog [162]. The model proposed by [179] predicted a flux of  $\sim 2.0 \times 10^{-6} \text{ cm}^{-2} \text{ s}^{-1}$  for energies above 100MeV. The *Fermi*-LAT integral sensitivity is  $\sim 6.0 \times 10^{-9} \text{ cm}^{-2} \text{ s}^{-1}$  for energies  $100\text{MeV} < E < 300\text{GeV}$  (for 1-year exposure and assuming a photon index of -2). Then, the estimated flux is more than two orders of magnitude above the instrument sensitivity. Hence, it should have been detected in [162] if HE  $\gamma$  rays are emitted. It may happen that the model does not really reproduce the putative emission.

To conclude, SS 433 is a unique microquasar which presents steady hadronic relativistic jets and a supercritical accretion regime. The source was observed by the MAGIC telescopes, however no VHE emission has been detected neither from SS 433 nor from the eastern or western interaction regions. Differential and integral ULs to the flux have been computed, for the phases of expected low absorption of the putative  $\gamma$ -ray flux. Physical parameters such as the maximum acceleration efficiency in the jet and the non-thermal power of the relativistic particles have been constrained, assuming a hadronic scenario, although the theoretical values are still possible and have not been discarded with our observations. Deeper observations with IACTs are required to search for VHE emission arising from this source.

# 8

## Conclusions & Perspectives

The last decades of the XX century and the opening decades of the XXI century have been the golden years of  $\gamma$ -ray astronomy. Satellites were sent to space to detect high-energy  $\gamma$  rays up to energies of  $\sim 50$  GeV. On the ground, the Imaging Air Cherenkov Technique was developed to indirectly detect  $\gamma$  rays from below 25 GeV up to several TeV. This novel technique studies the Cherenkov light emitted by air showers produced by primary incoming  $\gamma$  rays. The advent of a new generation of Cherenkov telescopes in the 2000's, like HESS, MAGIC and VERITAS, improved the sensitivity, the energy and the angular resolution with respect to previous observatories. Even the energy threshold was lowered, with MAGIC being able to cover the uncharted range between 25 – 100 GeV. This progress was due to larger collection areas, highly sensitive and pixelized cameras along with fast triggering and readout data acquisition systems.

The technological improvements led to the discovery of a new kind of source: the  $\gamma$ -ray binary. These systems are composed by a massive star (of spectral type O / Be) and a compact object, either a neutron star or a black hole. Only five of these systems are known up to date. The first  $\gamma$ -ray binary to be detected was PSR B1259–63, which is composed of a O star and a 48 ms pulsar. The first  $\gamma$ -ray binary detected by MAGIC was LS I +61°303, which was first thought to be a microquasar. All of the five  $\gamma$ -ray binaries host a massive star and do not show neither pulsations (except PSR B1259–63) nor jets. Hence the nature of the compact object is unknown for four of them. However, theories largely support the pulsar-wind/stellar-wind scenario to account for the VHE  $\gamma$ -ray emission of these systems, and hence assuming the compact object is a neutron star. The study of these binaries is crucial to understand the behavior of this exclusive family of objects and to define common characteristics . This thesis is focused in the long-studied  $\gamma$ -ray binary, LS I +61°303, and in the search for TeV emission from two other  $\gamma$ -ray candidates, MWC 656 and SS 433.

LS I +61°303 has largely been studied from radio up to TeV  $\gamma$  rays. The system, composed of a Be star and an unknown compact object, has an orbital period of  $\sim 26.5$  days. The binary system was first detected in the  $\gamma$ -ray domain by MAGIC. It shows periodical VHE outbursts in the apastron region,  $\phi \sim 0.5 - 0.75$  and

sporadic emission afterwards,  $\phi \sim 0.75 - 1.0$ . The source was once detected at superior conjunction by VERITAS. The binary shows a super-orbital modulation of the radio flux of  $\sim 1667$  days. This super-orbital variability has been confirmed in the HE regime by *Fermi*-LAT.

It is clear from the observations performed by MAGIC since its discovery in 2006 and the observations performed by VERITAS, that LS I +61°303 presents yearly variations in the average flux in the apastron region: the source has been detected twice in high-emission state at 10 – 15 % the Crab Nebula flux and has been detected twice at a low-emission state at a level of  $\sim 5$  % the Crab Nebula flux. In this thesis, a search for super-orbital modulation of the TeV flux within the radio period has been performed. For that purpose, a selection of the outburst peak in phases  $\phi \sim 0.5 - 0.75$  for the complete data set of the source was chosen and fitted to a sinusoidal function with a resulting probability of 25%. The VHE emission is compatible with the radio super-orbital modulation, leading to a period of  $1782 \pm 106$  days. The TeV flux being a statistical fluctuation from a constant value is discarded, with a probability less than  $6.0 \times 10^{-9}$ . Hence, it can be concluded that the TeV emission of LS I +61°303 shows yearly flux variations and it is compatible with the radio period.

The search for a periodical signal was also performed by the use of the Lomb-Scargle Periodogram. The orbital peak is clearly revealed. Hints of a possible periodicity are observed in the different tests performed, since a peak at the frequency corresponding to the 1667 days radio period is always visible. Nevertheless, the significance is not enough to claim for periodicity. However, small data sets (due to the selection conditions and due to the super-orbital period of about  $\sim 4.5$  years) were used, limiting the power of the method. Also, less than two super-orbital periods have been covered with the current TeV observations, hence the claim of the detection of periodicity is yet not possible. Observations focused on the orbital period  $\phi = 0.5 - 0.75$  to detect the peak of emission, are encouraged in order to increase the statistics and confirm or exclude the hint of super-orbital modulation. At least two additional super-orbital cycles (about 9 years) will be necessary to reveal the putative periodicity.

The HE emission component of LS I +61°303 shows hardening / softening of the spectra as a function of the orbital phase. Searches for this signature in the VHE regime have also been performed in this thesis. The search has been performed over different cycles, with a temporal and super-orbital dependence, but the results are always compatible with a constant value of the spectral index. If there exists any variability, it is inside MAGIC capabilities, where the systematic uncertainties in the spectral index have a value of  $\sim 20\%$ . The search for this spectral variability has to wait for more sensitive instruments like CTA or wait until the LIDAR technique is further developed in order to reduce systematic errors from  $\sim 15\%$  to  $\sim 5\%$ .

Finally, in the case of LS I +61°303, searches for anti-/correlation of the TeV emission and the mass-loss rate of the Be star have been performed to test the ejector-propeller model. The weighted Pearson correlation coefficient and the probabilities of the correlation for the different parameters of the  $H\alpha$  line and the TeV flux were calculated. No clear correlation is found. Nevertheless, the fast change in the optical parameters of  $H\alpha$  may blur the relation between these wavelengths, if any. Observations during the orbital interval 0.75 – 1.0 are encouraged to search for optical-TeV correlations. Studies of the polar wind through the HeII

lines are proposed to complement these studies and prove the un-/existence of correlation.

The compatibility with the radio period and the hint of periodicity within the radio and HE super-orbital modulation support the pulsar-wind scenario. The predictions stated in the propeller-ejector model with respect of the TeV variability have been confirmed within these observations. However, the relation between the mass-loss rate of the star and the flux TeV emission can not be confirmed with the current generation of telescopes since the timescale of the observations in optical and TeV is different (order of minutes in optical and order of hours in TeV) and the variability in the measured parameters in optical is faster. Hence, the ejector-propeller model proposed by [198] can not be confirmed with these observations. It can neither be excluded since the fast variability of the  $H\alpha$  parameters might blur the possible correlation between the larger size of the Be star disk and the diminishing of the VHE emission component of LS I +61°303.

Two  $\gamma$ -ray binary candidates have been studied in this thesis, MWC 656 and SS 433. However, no TeV emission has been detected from any of these systems and upper limits to the flux have been calculated, setting new limits on the physics of these two binaries.

MWC 656 is the first observationally proven binary system hosting a Be star and a black hole. Significant signal above 100 MeV was reported by AGILE, but no HE emission has been reported by *Fermi*-LAT. MAGIC observed the source on two different campaigns at different orbital phases, but no signal was detected. Contemporaneous observations in X-rays with *XMM-Newton* showed that the system was in quiescence. The emission of the source in X-ray is similar to that found in LMXRBs, where VHE emission episodes may occur only during very short flares, which is very challenging to detect for the current generation of IACTs. To detect the putative  $\gamma$ -ray emission from this system it shall be detected on flaring state for  $\sim$ 30 hours. Although it is challenging for the current generations of IACTs, it is possible to perform this kind of observations if a trigger signal from another telescopes is received. Observations of this system (and related systems) are encouraged with CTA, since the sensitivity will be better and might be able to detect this kind of short-flaring sources, if  $\gamma$  rays are emitted.

SS 433 is a microquasar composed of a massive A-type star with a (most likely) black hole, that displays hadronic jets and a supercritical accretion regime. The system is embedded inside the W50 complex, where the jets interact with the surrounding material. VHE emission is expected from this system, arising both from the inner jet region and the interaction regions with the nebula. MAGIC performed observations but no TeV flux was detected, either at the position of the central system or at the eastern interaction region. The observations were performed during the phases of expected low absorption of the putative  $\gamma$ -ray emission. The upper limits derived are compatible with the hadronic model proposed for this source and sets an upper value for the acceleration efficiency of the particles in the system. Since the total observation time dedicated to this source was low, more observations with MAGIC are encouraged in order to collect more statistics and either detect emission and confirm the predictions or to constraint the existing models. These observations are part of a MAGIC – HESS collaboration. It is expected to combine the results of both observatories to improve the obtained upper limits on the flux and constraint the model.

From the studies performed on this thesis, it is clear that  $\gamma$ -ray binaries are extraordinarily complex systems. Only few members of this exclusive class have been detected and it is not easy to add more binaries to the reduced list. Still, several questions remain. Why are  $\gamma$ -ray binaries so special? What are the compact objects that lie in these systems? Do low-mass binary systems emit  $\gamma$  rays? These are open questions that CTA, the future of Cherenkov astronomy, should be able to answer.

# Bibliography

- [1] Abdo, A. A., Ackermann, M., Ajello, and et al (2009a). Fermi LAT Observations of LS I +61 303: First Detection of an Orbital Modulation in GeV Gamma Rays. *ApJ Letters*, 701:L123–L128.
- [2] Abdo, A. A., Ackermann, M., Ajello, and et al (2011). Discovery of High-energy Gamma-ray Emission from the Binary System PSR B1259-63/LS 2883 around Periastron with Fermi. *ApJ Letters*, 736:L11.
- [3] Abdo, A. A., Ackermann, M., Ajello, M., and et al (2009b). Fermi/LAT observations of LS 5039. *ApJ Letters*, 706:L56–L61.
- [4] Abdo, A. A., Ackermann, M., Ajello, M., and et al (2010a). Gamma-Ray Emission from the Shell of Supernova Remnant W44 Revealed by the Fermi LAT. *Science*, 327:1103–.
- [5] Abdo, A. A., Ackermann, M., Ajello, M., and et al (2010b). Non-detection of AGL J2241+4454. *Fermi Sky Blog*.
- [6] Abell, G. O. and Margon, B. (1979). A kinematic model for SS433. *Nature*, 279:701–703.
- [7] Acciari, V. A., Aliu, E., Arlen, T., and et al (2009). Multiwavelength Observations of LS I +61deg 303 with Veritas, Swift, and RXTE. *ApJ*, 700:1034–1041.
- [8] Acciari, V. A., Aliu, E., Arlen, T., and et al (2011). VERITAS Observations of the TeV Binary LS I +61deg 303 During 2008-2010. *ApJ*, 738:3.
- [9] Acciari, V. A., Beilicke, M., Blaylock, G., and et al (2008). VERITAS Observations of the  $\gamma$ -Ray Binary LS I +61 303. *ApJ*, 679:1427–1432.
- [10] Ackermann, M., Ajello, M., Allafort, A., and et al (2013). Detection of the Characteristic Pion-Decay Signature in Supernova Remnants. *Science*, 339:807–811.
- [11] Actis, M., Agnetta, G., Aharonian, F., and et al (2011). Design concepts for the Cherenkov Telescope Array CTA: an advanced facility for ground-based high-energy gamma-ray astronomy. *Experimental Astronomy*, 32:193–316.
- [12] Aharonian, F., Akhperjanian, A., Beilicke, M., and et al (2005a). TeV gamma-ray observations of SS-433 and a survey of the surrounding field with the HEGRA IACT-System. *A&A*, 439:635–643.
- [13] Aharonian, F., Akhperjanian, A. G., Aye, K.-M., Bazer-Bachi, A. R., and et al (2005b). Discovery of the binary pulsar PSR B1259-63 in very-high-energy gamma rays around periastron with HESS. *A&A*, 442:1–10.

- [14] Aharonian, F., Akhperjanian, A. G., Aye, K.-M., Bazer-Bachi, A. R., and et al (2005c). Discovery of Very High Energy Gamma Rays Associated with an X-ray Binary. *Science*, 309:746–749.
- [15] Aharonian, F., Akhperjanian, A. G., Bazer-Bachi, A. R., and et al. (2006). Observations of the Crab nebula with HESS. *A&A*, 457:899–915.
- [16] Aharonian, F., Buckley, J., Kifune, T., and Sinnis, G. (2008). High energy astrophysics with ground-based gamma ray detectors. *Reports on Progress in Physics*, 71(9):096901.
- [17] Aharonian, F. A. (2013). *Gamma-Ray Emission of Supernova Remnants and the Origin of Galactic Cosmic Rays*, page 789.
- [18] Aharonian, F. A., Krawczynski, H., Puehlhofer, G., Rowell, G. P., and HEGRA Collaboration (2000). Search for TeV Gamma Rays from Supernova Remnants Cas A and Tycho with the HEGRA Stereoscopic System of Atmospheric Cherenkov Telescopes. In *AAS/High Energy Astrophysics Division #5*, volume 32 of *Bulletin of the American Astronomical Society*, page 1239.
- [19] Albert, J., Aliu, E., Anderhub, H., and et al (2006). Variable Very-High-Energy Gamma-Ray Emission from the Microquasar LS I +61 303. *Science*, 312:1771–1773.
- [20] Albert, J., Aliu, E., Anderhub, H., and et al (2007a). Unfolding of differential energy spectra in the MAGIC experiment. *Nuclear Instruments and Methods in Physics Research A*, 583:494–506.
- [21] Albert, J., Aliu, E., Anderhub, H., and et al (2007b). Very High Energy Gamma-Ray Radiation from the Stellar Mass Black Hole Binary Cygnus X-1. *ApJ Letters*, 665:L51–L54.
- [22] Albert, J., Aliu, E., Anderhub, H., and et al (2008a). FADC signal reconstruction for the MAGIC telescope. *Nuclear Instruments and Methods in Physics Research A*, 594:407–419.
- [23] Albert, J., Aliu, E., Anderhub, H., and et al (2008b). Multiwavelength (Radio, X-Ray, and  $\gamma$ -Ray) Observations of the  $\gamma$ -Ray Binary LS I +61 303. *ApJ*, 684:1351–1358.
- [24] Albert, J., Aliu, E., Anderhub, H., and et al (2008c). VHE  $\gamma$ -Ray Observation of the Crab Nebula and its Pulsar with the MAGIC Telescope. *ApJ*, 674:1037–1055.
- [25] Albert, J., Aliu, E., Anderhub, H., and et al (2009). Periodic Very High Energy  $\gamma$ -Ray Emission from LS I +61deg303 Observed with the MAGIC Telescope. *ApJ*, 693:303–310.
- [26] Aleksić, J., Alvarez, E. A., Antonelli, and et al (2012a). Phase-resolved energy spectra of the Crab pulsar in the range of 50-400 GeV measured with the MAGIC telescopes. *A&A*, 540:A69.
- [27] Aleksić, J., Alvarez, E. A., Antonelli, L. A., and et al (2011). A Search for Very High Energy Gamma-Ray Emission from Scorpius X-1 with the Magic Telescopes. *ApJ Letters*, 735:L5.

- [28] Aleksić, J., Alvarez, E. A., Antonelli, L. A., and et al (2012b). Detection of the  $\gamma$ -Ray Binary LS I +61deg303 in a Low-flux State at Very High Energy  $\gamma$ -Rays with the MAGIC Telescopes in 2009. *ApJ*, 746:80.
- [29] Aleksić, J., Alvarez, E. A., Antonelli, L. A., and et al (2012c). Detection of VHE  $\gamma$ -Rays from HESS J0632+057 during the 2011 February X-Ray Outburst with the MAGIC Telescopes. *ApJ Letters*, 754:L10.
- [30] Aleksić, J., Alvarez, E. A., Antonelli, L. A., and et al (2012d). Detection of VHE  $\gamma$ -Rays from HESS J0632+057 during the 2011 February X-Ray Outburst with the MAGIC Telescopes. *ApJ Letters*, 754:L10.
- [31] Aleksić, J., Alvarez, E. A., Antonelli, L. A., and et al (2012e). Morphological and spectral properties of the W51 region measured with the MAGIC telescopes. *A&A*, 541:A13.
- [32] Aleksić, J., Alvarez, E. A., Antonelli, L. A., and et al (2012f). Performance of the MAGIC stereo system obtained with Crab Nebula data. *Astroparticle Physics*, 35:435–448.
- [33] Alexandreas, D., Bartoli, B., Bastieri, D., and et al (1995). Status report on CLUE. *Nuclear Instruments and Methods in Physics Research A*, 360:385–389.
- [34] Aliu, E., Anderhub, H., Antonelli, and MAGIC Collaboration (2008). Observation of Pulsed  $\gamma$ -Rays Above 25 GeV from the Crab Pulsar with MAGIC. *Science*, 322:1221–.
- [35] Aliu, E., Anderhub, H., Antonelli, L. A., and et al (2009). Improving the performance of the single-dish Cherenkov telescope MAGIC through the use of signal timing. *Astroparticle Physics*, 30:293–305.
- [36] Aliu, E., Archambault, S., Behera, B., and et al (2013). Multiwavelength Observations of the TeV Binary LS I +61deg 303 with VERITAS, Fermi-LAT, and Swift/XRT during a TeV Outburst. *ApJ*, 779:88.
- [37] Anderhub, H., Antonelli, L. A., Antoranz, P., and et al (2009). Correlated X-Ray and Very High Energy Emission in the Gamma-Ray Binary LS I +61 303. *ApJ Letters*, 706:L27–L32.
- [38] Ansmann, A., Wandinger, U., Riebesell, M., Weitkamp, C., and Michaelis, W. (1992). Independent measurement of extinction and backscatter profiles in cirrus clouds by using a combined raman elastic-backscatter lidar. *Appl. Opt.*
- [39] Aragona, C., McSwain, M. V., Grundstrom, E. D., and et al (2009). The Orbits of the  $\gamma$ -Ray Binaries LS I +61 303 and LS 5039. *ApJ*, 698:514–518.
- [40] Atwood, W. B., Abdo, A. A., Ackermann, M., Althouse, W., Anderson, B., Axelsson, M., Baldini, L., Ballet, J., Band, D. L., Barbiellini, G., and et al. (2009). The Large Area Telescope on the Fermi Gamma-Ray Space Telescope Mission. *ApJ*, 697:1071–1102.
- [41] Auger, P., Ehrenfest, P., Maze, R., Daudin, J., and Fréon, R. A. (1939). Extensive Cosmic-Ray Showers. *Reviews of Modern Physics*, 11:288–291.

- [42] Barthelmy, S. D., Baumgartner, W., Cummings, J., and et al (2008). Swift-BAT/-XRT refined analysis on trigger 324362 (LS I +61 303). *GRB Coordinates Network*, 8215:1.
- [43] Bednarek, W. (2006). Inverse Compton  $e^{+/-}$  pair cascade model for the  $\gamma$ -ray production in massive binary LSI +61deg 303. *MNRAS*, 371:1737–1743.
- [44] Bednarek, W. (2011). A model for the two component  $\gamma$ -ray spectra observed from the  $\gamma$ -ray binaries. *MNRAS*, 418:L49–L53.
- [45] Bock, R. K., Chilingarian, A., Gaug, M., Hakl, F., Hengstebeck, T., Jiřina, M., Klaschka, J., Kotrč, E., Savický, P., Towers, S., Vaiciulis, A., and Wittek, W. (2004). Methods for multidimensional event classification: a case study using images from a Cherenkov gamma-ray telescope. *Nuclear Instruments and Methods in Physics Research A*, 516:511–528.
- [46] Bordas, P., Bosch-Ramon, V., and Paredes, J. M. (2010). Gamma-rays from SS 433 and its interaction with the W50 nebula.
- [47] Bordas, P., Bosch-Ramon, V., Paredes, J. M., and Perucho, M. (2009). Non-thermal emission from microquasar/ISM interaction. *A&A*, 497:325–334.
- [48] Bosch-Ramon, V. and Khangulyan, D. (2009). Understanding the Very-High Emission from Microquasars. *International Journal of Modern Physics D*, 18:347–387.
- [49] Bosch-Ramon, V., Romero, G. E., and Paredes, J. M. (2006). A broadband leptonic model for gamma-ray emitting microquasars. *A&A*, 447:263–276.
- [50] Bretz, T., Dorner, D., Wagner, R. M., and Sawallisch, P. (2009). The drive system of the major atmospheric gamma-ray imaging Cherenkov telescope. *Astroparticle Physics*, 31:92–101.
- [51] Britzger, D., Carmona, E., and Majumdar, P. (2009). Studies of the Influence of Moonlight on Observations with the MAGIC Telescope. *ArXiv e-prints*.
- [52] Burrows, D. N., Chester, M. M., D'Elia, V., and et al (2012). Swift detection of a burst from LS I +61 303. *GRB Coordinates Network*, 12914:1.
- [53] Cañellas, A., Joshi, B. C., Paredes, J. M., and et al (2012). Search for radio pulsations in LS I +61 303. *A&A*, 543:A122.
- [54] Calandro, G. A., Hill, A. B., Torres, D. F., Hadasch, D., Ray, P., Abdo, A., Hessels, J. W. T., Ridolfi, A., Possenti, A., Burgay, M., Rea, N., Tam, P. H. T., Dubois, R., Dubus, G., Glanzman, T., and Jogler, T. (2013). The missing GeV  $\gamma$ -ray binary: searching for HESS J0632+057 with Fermi-LAT. *MNRAS*, 436:740–749.
- [55] Casares, J., Negueruela, I., Ribó, M., Ribas, I., Paredes, J. M., Herrero, A., and Simón-Díaz, S. (2014). A Be-type star with a black-hole companion. *Nature*, 505:378–381.
- [56] Casares, J., Ribas, I., Paredes, J. M., Martí, J., and Allende Prieto, C. (2005). Orbital parameters of the microquasar LS I +61 303. *MNRAS*, 360:1105–1109.

- [57] Casares, J., Ribó, M., Ribas, I., Paredes, J. M., Vilardell, F., and Negueruela, I. (2012). On the binary nature of the  $\gamma$ -ray sources AGL J2241+4454 (= MWC 656) and HESS J0632+057 (= MWC 148). *MNRAS*, 421:1103–1112.
- [58] Charles, P. A. and Coe, M. J. (2013). Optical, Ultraviolet and Infrared Observations of X-ray Binaries.
- [59] Cherenkov, P. A. (1934). Visible emission of clean liquids by action of gamma radiation. *Doklady Akademii Nauk SSSR*, 2:451–.
- [60] Cherepashchuk, A. (2002). Observational Manifestations of Precession of Accretion Disk in the SS 433 Binary System. *Space Sci. Rev.*, 102:23–35.
- [61] Cherepashchuk, A. M., Sunyaev, R. A., Fabrika, S. N., and et al (2005). INTEGRAL observations of SS433: Results of a coordinated campaign. *A&A*, 437:561–573.
- [62] Chernyakova, M., Neronov, A., and Walter, R. (2006). INTEGRAL and XMM-Newton observations of LSI +61deg 303. *MNRAS*, 372:1585–1592.
- [63] Coe, M. J. and Edge, W. R. T. (2004). AX J0049.4-7323: a close look at a neutron star interacting with a circumstellar disc. *MNRAS*, 350:756–760.
- [64] Da Deppo, V., Doro, M., Blanch, O., Font, L., López-Oramas, A., Gaug, M., and Martínez, M. (2012). Preliminary optical design of a polychromator for a Raman LIDAR for atmospheric calibration of the Cherenkov Telescope Array. *Spie Optical System Design*, 1:4.
- [65] Daum, A., Hermann, G., Heß, M., and et al (1997). First results on the performance of the HEGRA IACT array. *Astroparticle Physics*, 8:1–11.
- [66] de Martino, D., Falanga, M., Bonnet-Bidaud, J.-M., and et al (2010). The intriguing nature of the high-energy gamma ray source XSS J12270-4859. *A&A*, 515:A25.
- [67] Dhawan, V., Mioduszewski, A., and Rupen, M. (2006). LS I +61 303 is a Be-Pulsar binary, not a Microquasar. In *VI Microquasar Workshop: Microquasars and Beyond*.
- [68] Doro, M., Gaug, M., Blanch, O., Eizmendi, M., Font, L., Garrido, D., López-Oramas, A., and Martinez, M. (2013a). Atmospheric Calibration for CTA. CTA internal report COM-CCF/130311, available at [https://portal.cta-observatory.org/recordscentre/Records/COM/COM-CCF/lidar\\_loi2.pdf](https://portal.cta-observatory.org/recordscentre/Records/COM/COM-CCF/lidar_loi2.pdf).
- [69] Doro, M., Gaug, M., Blanch, O., Font, L., Garrido, D., Lopez-Oramas, A., and CTA Consortium, M. M. f. t. (2013b). Towards a full Atmospheric Calibration system for the Cherenkov Telescope Array. *ArXiv e-prints*.
- [70] Dubner, G. M., Holdaway, M., Goss, W. M., and Mirabel, I. F. (1998). A High-Resolution Radio Study of the W50-SS 433 System and the Surrounding Medium. *AJ*, 116:1842–1855.
- [71] Dubus, G. (2006). Gamma-ray binaries: pulsars in disguise? *A&A*, 456:801–817.

- [72] Dubus, G. (2013). Gamma-ray binaries and related systems. *A&A Rev.*, 21:64.
- [73] Dubus, G., Cerutti, B., and Henri, G. (2010). The relativistic jet of Cygnus X-3 in gamma-rays. *MNRAS*, 404:L55–L59.
- [74] Eikenberry, S. S., Cameron, P. B., Fierce, B. W., Kull, D. M., Dror, D. H., Houck, J. R., and Margon, B. (2001). Twenty Years of Timing SS 433. *ApJ*, 561:1027–1033.
- [75] Eizmendi, M. (2011). IFAE-UAB Raman LIDAR Link Budget and Components.
- [76] Fabrika, S. (2004). The jets and supercritical accretion disk in SS433. *Astrophysics and Space Physics Reviews*, 12:1–152.
- [77] Fabrika, S. N. and Bychkova, L. V. (1990). The mass function of SS 433. *A&A*, 240:L5–L7.
- [78] Fabrika, S. N. and Sholukhova, O. (2008). SS433 as ultraluminous UV source. Comparison with ULXs. In *Microquasars and Beyond*.
- [79] Fender, R. (2010). ‘Disc-Jet’ Coupling in Black Hole X-Ray Binaries and Active Galactic Nuclei. In Belloni, T., editor, *Lecture Notes in Physics, Berlin Springer Verlag*, volume 794 of *Lecture Notes in Physics, Berlin Springer Verlag*, page 115.
- [80] Fermi LAT Collaboration, Abdo, A. A., Ackermann, M., Ajello, M., and et al (2009). Modulated High-Energy Gamma-Ray Emission from the Microquasar Cygnus X-3. *Science*, 326:1512–.
- [81] Fermi LAT Collaboration, Ackermann, M., Ajello, M., and et al. (2012). Periodic Emission from the Gamma-Ray Binary 1FGL J1018.6-5856. *Science*, 335:189–.
- [82] Fomin, V. P., Stepanian, A. A., Lamb, R. C., and et al (1994). New methods of atmospheric Cherenkov imaging for gamma-ray astronomy. I. The false source method. *Astroparticle Physics*, 2:137–150.
- [83] Frail, D. A. and Hjellming, R. M. (1991). Distance and total column density to the periodic radio star LSI + 61 deg 303. *AJ*, 101:2126–2130.
- [84] Fuchs, Y., Koch Miramond, L., and Ábrahám, P. (2006). SS 433: a phenomenon imitating a Wolf-Rayet star. *A&A*, 445:1041–1052.
- [85] Gaisser, T. K. (1991). Book-Review - Cosmic-Rays and Particle Physics. *Journal of the British Astronomical Association*, 101:128.
- [86] Gallo, E., Miller, B. P., and Fender, R. (2012). Assessing luminosity correlations via cluster analysis: evidence for dual tracks in the radio/X-ray domain of black hole X-ray binaries. *MNRAS*, 423:590–599.
- [87] Gallo, E., Miller, B. P., and Fender, R. (2013). INTEGRAL and RXTE View of Gamma-ray Binaries. *Proceedings of Science*.

- [88] Galper, A. M., Adriani, O., Aptekar, R. L., and et al (2013). Design and performance of the GAMMA-400 gamma-ray telescope for dark matter searches. In Ormes, J. F., editor, *American Institute of Physics Conference Series*, volume 1516 of *American Institute of Physics Conference Series*, pages 288–292.
- [89] García, J. R., Dazzi, F., Häfner, D., Herranz, D., López, M., Mariotti, M., Mirzoyan, R., Nakajima, D., Schweizer, T., and Teshima, M. (2014). Status of the new Sum-Trigger system for the MAGIC telescopes. *ArXiv e-prints*.
- [90] Gaug, M., Bartko, H., Cortina, J., and Rico, J. (2005). Calibration of the MAGIC Telescope. *International Cosmic Ray Conference*, 5:375.
- [91] Gies, D. R. and Bolton, C. T. (1986). The binary frequency and origin of the OB runaway stars. *ApJS*, 61:419–454.
- [92] Gies, D. R., McSwain, M. V., Riddle, R. L., Wang, Z., Wiita, P. J., and Wingert, D. W. (2002). The Spectral Components of SS 433. *ApJ*, 566:1069–1083.
- [93] Goebel, F., Bartko, H., Carmona, E., and et al. (2008). Upgrade of the MAGIC Telescope with a Multiplexed Fiber-Optic 2GSamples/s FADC Data Acquisition System system. *International Cosmic Ray Conference*, 3:1481–1484.
- [94] Goranskij, V. (2011). Photometric Mass Estimate for the Compact Component of SS 433: And Yet It Is a Neutron Star. *Peremennye Zvezdy*, 31:5.
- [95] Gregory, P. C. (1999). Bayesian Periodic Signal Detection. I. Analysis of 20 Years of Radio Flux Measurements of the X-Ray Binary LS I +61deg303. *ApJ*, 520:361–375.
- [96] Gregory, P. C. (2002). Bayesian Analysis of Radio Observations of the Be X-Ray Binary LS I +61deg303. *ApJ*, 575:427–434.
- [97] Gregory, P. C. and Neish, C. (2002). Density and Velocity Structure of the Be Star Equatorial Disk in the Binary LS I +61°303, a Probable Microquasar. *ApJ*, 580:1133–1148.
- [98] Gregory, P. C. and Taylor, A. R. (1978). New highly variable radio source, possible counterpart of gamma-ray source CG135+1. *Nature*, 272:704–706.
- [99] Greisen, K. (1966). End to the cosmic-ray spectrum? *Phys. Rev. Lett.*, 16:748–750.
- [100] Grundstrom, E. D., Caballero-Nieves, S. M., Gies, D. R., and et al (2007). Joint H $\alpha$  and X-Ray Observations of Massive X-Ray Binaries. II. The Be X-Ray Binary and Microquasar LS I +61 303. *ApJ*, 656:437–443.
- [101] Gumiero, G. (2014). Analysis of the Two Gamma-Ray Flares of the BL-Lac RGB 0521+212 observed by MAGIC.
- [102] Gupta, S. and Böttcher, M. (2006). A Time-dependent Leptonic Model for Microquasar Jets: Application to LS I +61 303. *ApJ Letters*, 650:L123–L126.
- [103] H. E. S. S. Collaboration, Abramowski, A., Acero, F., Aharonian, F., and et al (2012). Discovery of VHE emission towards the Carina arm region with the H.E.S.S. telescope array: HESS J1018-589. *A&A*, 541:A5.

- [104] Hadasch, D., Torres, D. F., Tanaka, T., and et al (2012). Long-term Monitoring of the High-energy  $\gamma$ -Ray Emission from LS I +61deg303 and LS 5039. *ApJ*, 749:54.
- [105] Haefner, D. (2011). New improved Sum-Trigger system for the MAGIC telescopes. *International Cosmic Ray Conference*, 9:251.
- [106] Hall, T. A., Bond, I. H., Bradbury, S. M., and et al (2003). Search for TeV Emissions from Pulsars in Binary Systems. *ApJ*, 583:853–860.
- [107] Harmon, B. A., Wilson, R. B., Finger, M. H., Paciesas, W. S., Rubin, B. C., and Fishman, G. J. (1992). U 1543-47. , 5510:2.
- [108] Haungs, A. (2011). From the Knee to the Ankle:. From Galactic to Extra-galactic Origin of Cosmic Rays? In Giani, S., Leroy, C., and Rancoita, P. G., editors, *Cosmic Rays for Particle and Astroparticle Physics*, pages 181–189.
- [109] Haungs, A., Apel, W. D., Arteaga-Velazquez, J. C., and et al (2013). KASCADE-Grande observation of features in the cosmic ray spectrum between knee and ankle. *Journal of Physics Conference Series*, 409(1):012005.
- [110] Hayashi, S., Kajino, F., Naito, T., and et al (2009). Search for VHE gamma rays from SS433/W50 with the CANGAROO-II telescope. *Astroparticle Physics*, 32:112–119.
- [111] HEGRA Collaboration (1995). Status of the HEGRA Experiment at La Palma. *International Cosmic Ray Conference*, 1:474.
- [112] Hillas, A. M. (1985). Cerenkov light images of EAS produced by primary gamma. *International Cosmic Ray Conference*, 3:445–448.
- [113] Horan, D. t. (2007). VERITAS: Status, Performance and Latest Results. In *American Astronomical Society Meeting Abstracts*, volume 39 of *Bulletin of the American Astronomical Society*, page 784.
- [114] Hutchings, J. B. and Crampton, D. (1981). Spectroscopy of the unique degenerate binary star LSI + 61 deg 303. *PASP*, 93:486–489.
- [115] Inaba, H. (1976). Laser Monitoring of the Atmosphere. *Springer-Verlag*.
- [116] Jayanthi, U. B., Jablonski, F. J., and Steiner, J. E. (1989). Gamma-rays above 184 keV from 4U1820-30 associated with 685 second period. *Astrophysical Letters and Communications*, 27:347–350.
- [117] Joss, P. C. and Rappaport, S. A. (1984). Neutron Stars in Interacting Binary Systems. *ARA&A*, 22:537–592.
- [118] Kagohera, V. and Webbink, R. F. (1998). Formation of Low-Mass X-Ray Binaries. II. Common Envelope Evolution of Primordial Binaries with Extreme Mass Ratios. *ApJS*.
- [119] Kilde, J., Atkins, R. W., Badran, H. M., Blaylock, G., and et al (2007). The Whipple Observatory 10 m gamma-ray telescope, 1997 2006. *Astroparticle Physics*, 28:182–195.
- [120] Klages, H. O., Apel, W. D., Bekk, K., and et al (1997). The KASCADE Experiment. *Nuclear Physics B Proceedings Supplements*, 52:92–102.

- [121] Kubota, K., Ueda, Y., Fabrika, S., and et al (2010). Subaru And Gemini Observations Of SS 433: New Constraint On The Mass Of The Compact Object. *ApJ*, 709:1374–1386.
- [122] Kumar, D. (2012). *Concept Design, Analysis, and Integration of the New U.P.C. Multispectral Lidar System*. PhD thesis, Universitat Politecnica de Barcelona.
- [123] Li, J., Torres, D. F., and Zhang, S. (2014). Spectral analysis in orbital/superorbital phase space and hints of superorbital variability in the hard X-rays of LS I +61 303. *ArXiv e-prints*.
- [124] Li, J., Torres, D. F., Zhang, S., and et al (2011). Long-term X-Ray Monitoring of LS I +61deg303: Analysis of Spectral Variability and Flares. *ApJ*, 733:89.
- [125] Li, T.-P. and Ma, Y.-Q. (1983). Analysis methods for results in gamma-ray astronomy. *ApJ*, 272:317–324.
- [126] Lipunov, V. M. and Nazin, S. N. (1994). A model of the source LS I +61 deg 303. *A&A*, 289:822–826.
- [127] Liu, Q. Z., van Paradijs, J., and van den Heuvel, E. P. J. (2005). High-mass X-ray binaries in the Magellanic Clouds. *A&A*, 442:1135–1138.
- [128] Liu, Q. Z., van Paradijs, J., and van den Heuvel, E. P. J. (2006). Catalogue of high-mass X-ray binaries in the Galaxy (4th edition). *A&A*, 455:1165–1168.
- [129] Lomb, N. R. (1976). Least-squares frequency analysis of unequally spaced data. *Ap&SS*, 39:447–462.
- [130] López-Oramas, A. (2010). Development and description of a Raman LIDAR.
- [131] López-Oramas, A., Abril, O., Blanch Bigas, O., et al, and CTA Consortium (2013). The IFAE/UAB and LUPM Raman LIDARs for Cherenkov Telescope Array Observatory. *ArXiv e-prints*.
- [132] López-Oramas, A., Barceló, M., Blanch, O., et al, and CTA Consortium (2011). Development of Raman Lidars made with former CLUE telescopes for CTA. *International Cosmic Ray Conference*, 9:22.
- [133] Lucarelli, F., Verrecchia, F., Striani, E., and et al (2010). AGILE detection of the new unidentified gamma-ray source AGL J2241+4454. *The Astronomer's Telegram*, 2761:1.
- [134] MAGIC Collaboration and Albert, J. (2007). Very high energy gamma-ray observations during moonlight and twilight with the MAGIC telescope. *ArXiv Astrophysics e-prints*.
- [135] Maier, G. (2011). VHE Observations of the Binary Candidate HESS J0632+057 with H.E.S.S. and VERITAS. *International Cosmic Ray Conference*, 7:78.
- [136] Maier, G. (2014). VERITAS Performance.

- [137] Majumdar, P., Moralejo, A., Bigongiari, C., Blanch, O., and Sobczynska, D. (2005). Monte Carlo simulation for the MAGIC telescope. *International Cosmic Ray Conference*, 5:203.
- [138] Malyshev, D., Zdziarski, A. A., and Chernyakova, M. (2013). High-energy gamma-ray emission from Cyg X-1 measured by Fermi and its theoretical implications. *MNRAS*, 434:2380–2389.
- [139] Maraschi, L. and Treves, A. (1981). A model for LSI +61 ° 303. *MNRAS*, 194:1P–5P.
- [140] Margon, B. and Anderson, S. F. (1989). Ten years of SS 433 kinematics. *ApJ*, 347:448–454.
- [141] Markoff, S., Nowak, M. A., and Wilms, J. (2005). Going with the Flow: Can the Base of Jets Subsume the Role of Compact Accretion Disk Coronae? *ApJ*, 635:1203–1216.
- [142] Marshall, F. E., Swank, J. H., Boldt, E. A., and et al (1979). X-ray observations of H1908+050 / =SS 433/. *ApJ Letters*, 230:L145–L148.
- [143] Massi, M., Paredes, J. M., Estalella, R., and Felli, M. (1993). High resolution radio map of the X-ray binary LSI+61 ° 303. *A&A*, 269:249–254.
- [144] Massi, M., Ribó, M., Paredes, J. M., and et al (2004). Hints for a fast precessing relativistic radio jet in LS I +61303. *A&A*, 414:L1–L4.
- [145] Massi, M., Ribó, M., Paredes, J. M., Peracaula, M., and Estalella, R. (2001). One-sided jet at milliarcsecond scales in LS I +61deg303. *A&A*, 376:217–223.
- [146] Massi, M., Ros, E., and Zimmermann, L. (2012). VLBA images of the precessing jet of LS I +61deg303. *A&A*, 540:A142.
- [147] McSwain, M. V., Ray, P. S., Ransom, S. M., and et al (2011). A Radio Pulsar Search of the  $\gamma$ -ray Binaries LS I +61 303 and LS 5039. *ApJ*, 738:105.
- [148] Medvedev, P. S., Fabrika, S. N., Vasiliev, V. V., and et al (2013). Superbroad component in emission lines of SS 433. *Astronomy Letters*, 39:826–843.
- [149] Migliari, S., Fender, R., and Méndez, M. (2002). Iron Emission Lines from Extended X-ray Jets in SS 433: Reheating of Atomic Nuclei. *Science*, 297:1673–1676.
- [150] Millikan, R. A. (1926). Cosmic Rays. *Scientific American*, 134:149–150.
- [151] Mirabel, I. F. (2006). Very energetic gamma-rays from microquasars and binary pulsars. *Science*, 312:1759.
- [152] Mirabel, I. F. (2012). Gamma-Ray Binaries Revealed. *Science*, 335:175–.
- [153] Mirabel, I. F. and Rodríguez, L. F. (1999). Sources of Relativistic Jets in the Galaxy. *ARA&A*, 37:409–443.
- [154] Mirzoyan, R. (1997). On the Calibration Accuracy of Light Sensors in Atmospheric Cherenkov Fluorescence and Neutrino Experiments. *International Cosmic Ray Conference*, 7:265.

- [155] Moldón, J. (2012). *Structure and nature of gamma-ray binaries by means of VLBI observations*. PhD thesis, Universitat de Barcelona.
- [156] Moralejo, A., Gaug, M., Carmona, E., and for the MAGIC collaboration (2009). MARS, the MAGIC Analysis and Reconstruction Software. *ArXiv e-prints*.
- [157] Mori, M., Kawachi, A., Nagataki, S., and Naito, T. (2013). Fermi-LAT study of two gamma-ray binaries, HESS J0632+057 and AGL J2241+4454. *ApJ*, 14:22.
- [Morooka et al.] Morooka, Ogawa, Negoro, and MAXI Team. . <http://maxi.riken.jp>.
- [159] Munar-Adrover, P., Paredes, J. M., Ribó, M., Iwasawa, K., Zabalza, V., and Casares, J. (2014). Discovery of X-Ray Emission from the First Be/Black Hole System. *ApJ Letters*, 786:L11.
- [160] Mussa, R. and et al. (2009). Atmospheric Monitoring for the Pierre Auger Observatory. *Nuclear Physics B*.
- [161] Newsom, G. H. and Collins, II, G. W. (1981). Short-period variations in the moving line spectrum of SS 433. *AJ*, 86:1250–1258.
- [162] Nolan, P. L., Abdo, A. A., Ackermann, M., Ajello, M., Allafort, A., Antolini, E., Atwood, W. B., Axelsson, M., Baldini, L., Ballet, J., and et al. (2012). Fermi Large Area Telescope Second Source Catalog. *ApJS*, 199:31.
- [163] Okazaki, A. T. (1997). On the confinement of one-armed oscillations in discs of Be stars. *A&A*, 318:548–560.
- [164] Orellana, M. and Romero, G. E. (2005). Gamma-Ray Emission from Be/X-ray Binaries. *Ap&SS*, 297:167–178.
- [165] Orellana, M., Romero, G. E., and Christiansen, H. R. (2005). A hadronic model for the high-energy gamma-ray emission of LS I +61 303. *Boletin de la Asociacion Argentina de Astronomia La Plata Argentina*, 48:334–340.
- [166] Paoletti, R. and et al (2008). The global trigger system of the MAGIC telescope array. *Nuclear Science Symposium Conference Record*.
- [167] Paredes, J. M., Estalella, R., and Rius, A. (1990). Observation at 3.6 CM wavelength of the radio light curve of LSI + 61 deg 303. *A&A*, 232:377–380.
- [168] Paredes, J. M., Martí, J., Peracaula, M., and Ribo, M. (1997). Evidence of X-ray periodicity in LSI+61 303. *A&A*, 320:L25–L28.
- [169] Paredes, J. M., Ribó, M., Bosch-Ramon, V., and et al (2007). Chandra Observations of the Gamma-Ray Binary LS I +61 303: Extended X-Ray Structure? *ApJ Letters*, 664:L39–L42.
- [170] Patterson, J. (1984). The evolution of cataclysmic and low-mass X-ray binaries. *ApJS*, 54:443–493.
- [171] Pegna, R., Barceló, M., Bitossi, M., and et al (2007). A GHz sampling DAQ system for the MAGIC-II telescope. *Nuclear Instruments and Methods in Physics Research A*, 572:382–384.

- [172] Plotkin, R. M., Gallo, E., and Jonker, P. G. (2013). The X-Ray Spectral Evolution of Galactic Black Hole X-Ray Binaries toward Quiescence. *ApJ*, 773:59.
- [173] Porter, J. M. and Rivinius, T. (2003). Classical Be Stars. *PASP*, 115:1153–1170.
- [174] Punch, M., Akerlof, C. W., Cawley, M. F., and et al (1992). Detection of TeV photons from the active galaxy Markarian 421. *Nature*, 358:477.
- [175] Rea, N. and Torres, D. F. (2011). The TeV Binary HESS J0632+057 in the Low and High X-Ray State. *ApJ Letters*, 737:L12.
- [176] Rea, N., Torres, D. F., van der Klis, M., Jonker, P. G., Méndez, M., and Sierpowska-Bartosik, A. (2010). Deep Chandra observations of TeV binaries - I. LSI+61deg303. *MNRAS*, 405:2206–2214.
- [177] Reynolds, P. T., Akerlof, C. W., Cawley, M. F., and et al (1993). Survey of candidate gamma-ray sources at TeV energies using a high-resolution Cerenkov imaging system - 1988-1991. *ApJ*, 404:206–218.
- [178] Reynoso, M. M., Christiansen, H. R., and Romero, G. E. (2008a). Gamma-ray absorption in the microquasar SS433. *Astroparticle Physics*, 28:565–572.
- [179] Reynoso, M. M., Romero, G. E., and Christiansen, H. R. (2008b). Production of gamma rays and neutrinos in the dark jets of the microquasar SS433. *MNRAS*, 387:1745–1754.
- [180] Rico, J., de Oña-Wilhelmi, E., Cortina, J., and et al. (2008). Observations of Very High Energy Gamma-Rays during Moonlight and Twilight with the MAGIC Telescope. *International Cosmic Ray Conference*, 3:1365–1368.
- [181] Ritter, H. and Kolb, U. (2003). Catalogue of cataclysmic binaries, low-mass X-ray binaries and related objects (Seventh edition). *A&A*, 404:301–303.
- [182] Romero, G. E., Christiansen, H. R., and Orellana, M. (2005). Hadronic High-Energy Gamma-Ray Emission from the Microquasar LS I +61 303. *ApJ*, 632:1093–1098.
- [183] Romero, G. E., Torres, D. F., Kaufman Bernadó, M. M., and Mirabel, I. F. (2003). Hadronic gamma-ray emission from windy microquasars. *A&A*, 410:L1–L4.
- [184] Sabatini, S., Tavani, M., Striani, E., and et al (2010). Episodic Transient Gamma-ray Emission from the Microquasar Cygnus X-1. *ApJ Letters*, 712:L10–L15.
- [185] Sánchez, C. (2011). Caracterització del LIDAR de CTA.
- [186] Scargle, J. D. (1982). Studies in astronomical time series analysis. II - Statistical aspects of spectral analysis of unevenly spaced data. *ApJ*, 263:835–853.
- [187] Sidoli, L., Pellizzoni, A., Vercellone, S., Moroni, M., Mereghetti, S., and Tavani, M. (2006). XMM-Newton observation of a spectral state transition in the peculiar radio/X-ray/ $\gamma$ -ray source LS I +61 303. *A&A*, 459:901–907.

- [188] Sitarek, J., Carmona, E., Colin, P., et al, and for the MAGIC Collaboration (2013a). Physics performance of the upgraded MAGIC telescopes obtained with Crab Nebula data. *ArXiv e-prints*.
- [189] Sitarek, J., Gaug, M., Mazin, D., and et al (2013b). Analysis techniques and performance of the Domino Ring Sampler version 4 based readout for the MAGIC telescopes. *Nuclear Instruments and Methods in Physics Research A*, 723:109–120.
- [190] Stephenson, C. B. and Sanduleak, N. (1977). New H-alpha emission stars in the Milky Way. *ApJS*, 33:459–469.
- [191] Tavani, M., Barbiellini, G., Argan, A., and et al (2009). The AGILE Mission. *A&A*, 502:995–1013.
- [192] Tescaro, D. (2010). *TeV  $\gamma$ -ray observations of nearby Active Galactic Nuclei with the MAGIC telescope: exploring the high energy region of the multiwavelength picture*. PhD thesis, Universitat Autònoma de Barcelona.
- [193] Tescaro, D., López-Oramas, A., Moralejo, A., and et al (2013). The MAGIC telescopes DAQ software and the on-the-fly online analysis client. *ArXiv e-prints*.
- [194] Tescaro, D. t. (2013). The Upgraded MAGIC Cherenkov Telescopes. In *RICH 2013*.
- [195] The Fermi-LAT Collaboration (2013). Associating long-term gamma-ray variability with the superorbital period of LS I 61 303. *ArXiv e-prints*.
- [196] The Pierre Auger Collaboration, Abreu, P., Aglietta, M., and et al (2011). The Pierre Auger Observatory I: The Cosmic Ray Energy Spectrum and Related Measurements. *ArXiv e-prints*.
- [197] Thompson, D. J., Bertsch, D. L., Fichtel, C. E., and et al (1993). Calibration of the Energetic Gamma-Ray Experiment Telescope (EGRET) for the Compton Gamma-Ray Observatory. *ApJS*, 86:629–656.
- [198] Torres, D. F., Rea, N., Esposito, P., Li, J., Chen, Y., and Zhang, S. (2012). A Magnetar-like Event from LS I +61deg303 and Its Nature as a Gamma-Ray Binary. *ApJ*, 744:106.
- [199] Torres, D. F. and Reimer, A. (2011). Hadronic beam models for quasars and microquasars. *A&A*, 528:L2.
- [200] Vasileiadis, G. and H.E.S.S. Collaboration (2005). The H.E.S.S experimental project. *Nuclear Instruments and Methods in Physics Research A*, 553:268–273.
- [201] Vila, G. S., Romero, G. E., and Casco, N. A. (2012). An inhomogeneous lepto-hadronic model for the radiation of relativistic jets. Application to XTE J1118+480. *A&A*, 538:A97.
- [202] Watson, M. G., Stewart, G. C., King, A. R., and Brinkmann, W. (1986). Doppler-shifted X-ray line emission from SS433. *MNRAS*, 222:261–271.

- [203] Weekes, T. C., Cawley, M. F., Fegan, D. J., and et al (1989). Observation of TeV gamma rays from the Crab nebula using the atmospheric Cerenkov imaging technique. *ApJ*, 342:379–395.
- [204] Williams, S. J., Gies, D. R., Matson, R. A., and et al (2010). The Be Star HD 215227: A Candidate Gamma-ray Binary. *ApJ Letters*, 723:L93–L97.
- [205] Zamanov, R. and Martí, J. (2000). First correlation between compact object and circumstellar disk in the Be/X-ray binaries. *A&A*, 358:L55–L58.
- [206] Zamanov, R., Martí, J., and Marziani, P. (2001). Be/X-ray Binary LSI+61303 in Terms of Ejector-Propeller Model. In *The Second National Conference on Astrophysics of Compact Objects*, page 50.
- [207] Zamanov, R., Stoyanov, K., Martí, J., and et al (2013). H $\alpha$  observations of the  $\gamma$ -ray-emitting Be/X-ray binary LSI+61°303: orbital modulation, disk truncation, and long-term variability. *A&A*, 559:A87.
- [208] Zamanov, R. K., Martí, J., Paredes, J. M., Fabregat, J., Ribó, M., and Tarasov, A. E. (1999). Evidence of H $\alpha$  periodicities in LS I+61deg303. *A&A*, 351:543–550.
- [209] Zanin, R. (2011). *Observation of the Crab pulsar wind nebula and microquasar candidates with MAGIC*. PhD thesis, Universitat Autònoma de Barcelona.
- [210] Zatsepin, G. T. and Kuzmin, V. A. (1966). End to the cosmic-ray spectrum? *Soviet Journal of Experimental and Theoretical Physics Letters*, 4:78–80.
- [211] Zdziarski, A. A., Neronov, A., and Chernyakova, M. (2010). A compact pulsar wind nebula model of the  $\gamma$ -ray-loud binary LS I +61303. *MNRAS*, 403:1873–1886.
- [212] Zdziarski, A. A., Poutanen, J., Mikolajewska, J., Gierlinski, M., Ebisawa, K., and Johnson, W. N. (1998). Broad-band X-ray/gamma-ray spectra and binary parameters of GX 339-4 and their astrophysical implications. *MNRAS*, 301:435–450.
- [213] Zhang, J.-F., Zhu, Y., and Zhang, L. (2011). The multiwavelength emission from the gamma-ray binary LS I +61 303. *Research in Astronomy and Astrophysics*, 11:445–456.
- [214] Zimmer, P. C. and McGraw, J. T. (2010). I. *Bulletin of the American Astronomical Society, AAS Meeting 215*.

# List of Figures

1.1	Cosmic ray spectrum . . . . .	8
1.2	<i>Fermi</i> -LAT detector . . . . .	12
1.3	EAS . . . . .	14
1.4	Shower Images in the Camera Plane . . . . .	16
1.5	IACT Technique . . . . .	16
1.6	Hillas Parameters . . . . .	18
1.7	Theta parameter . . . . .	18
2.1	Raman Spectroscopy Principle . . . . .	22
2.2	CLUE unit for Raman LIDAR . . . . .	24
2.3	Overlapping function for coaxial and biaxial LIDARs. . . . .	24
2.4	Harmonics configuration for the pulsed laser . . . . .	27
2.5	Coaxial configuration . . . . .	28
2.6	Multiwavelength Detector . . . . .	30
2.7	Gaussian profile of the PSF . . . . .	31
2.8	Gaussian profile of the PSF . . . . .	32
2.9	Spot size of the third harmonic . . . . .	34
2.10	Spot size of the second harmonic . . . . .	34
2.11	Transmitivity of the LLG . . . . .	36
2.12	Temperature dependence of the LLG . . . . .	36
2.13	Dependence of the transmitivity with the entrance angle . . . . .	37
2.14	Dependence of the output angle with the entrance angle . . . . .	38
2.15	Dependence of transmitivity with the shape . . . . .	39
2.16	Monochromatic Wavelength Detector . . . . .	39
2.17	PMT single photoelectron . . . . .	40
2.18	Transmission of the 355 nm DM . . . . .	42
2.19	Transmission of the 387 nm DM . . . . .	42
2.20	Transmission of the 532 nm DM . . . . .	43
3.1	MAGIC-I and MAGIC-II telescopes . . . . .	46
3.2	Evolution of the integral sensitivity. . . . .	47
3.3	MAGIC cameras . . . . .	48

3.4	MAGIC-I and MAGI-II telescopes . . . . .	49
3.5	Structure of MAGIC-I . . . . .	50
3.6	DAQ readout . . . . .	53
3.7	DAQ general scheme . . . . .	54
3.8	Online Analysis thread . . . . .	54
3.9	Wobble observation mode . . . . .	57
3.10	Image cleaning . . . . .	59
3.11	Disp method for mono and stereo configurations . . . . .	60
3.12	Skymap . . . . .	63
3.13	Effective area distribution . . . . .	64
3.14	Differential Energy Spectrum . . . . .	64
3.15	Unfolding . . . . .	65
3.16	Relation between DC and DT for Crab Nebula Sample . . . . .	66
3.17	Relation between Rate and DT for Crab Nebula Sample . . . . .	67
3.18	Pre-selection results of Crab Nebula Sample . . . . .	68
3.19	Rate vs Zenith angle for Cycle VI Campaign of Crab Nebula . . . . .	68
3.20	Flux dependence with DC . . . . .	69
4.1	Orbital Scheme of a Binary System . . . . .	72
4.2	X-ray Binaries Spatial Distribution . . . . .	73
4.3	PSR B1259–63 SED . . . . .	77
4.4	Proposed scenarios for $\gamma$ -ray binaries . . . . .	80
5.1	LS I +61°303 Orbital Scheme . . . . .	84
5.2	VLBA Radio Contours of LS I +61°303 . . . . .	85
5.3	HE and VHE SED of LS I +61°303 . . . . .	87
5.4	<i>Fermi</i> -LAT Super-orbital Modulation of LS I +61°303 . . . . .	88
5.5	VHE $\gamma$ -ray Lightcurve of LS I +61°303 on high state . . . . .	89
5.6	VHE $\gamma$ -ray Lightcurve of LS I +61°303 for the low flux state . . . . .	90
5.7	Ejector-Propeller model proposed for LS I +61°303 . . . . .	96
5.8	Cycle VI Signal Significance . . . . .	98
5.9	Cycle VI Lightcurve of LS I +61°303 . . . . .	100
5.10	Cycle VI Spectrum of LS I +61°303 . . . . .	102
5.11	Cycle VI, intra-night variability . . . . .	103
5.12	Spectrum of peak emission on cycle VI of LS I +61°303 . . . . .	104
5.13	Alpha plots for Cycle VII data . . . . .	105
5.14	Significance of February 2012 data . . . . .	106
5.15	Cycle VII Lightcurve of LS I +61°303 . . . . .	107
5.16	Cycle VII Spectra of LS I +61°303 . . . . .	108

---

5.17 Significance plots of Cycle VIII of LS I +61°303 . . . . .	109
5.18 Cycle VIII Lightcurve of LS I +61°303 . . . . .	110
5.19 Cycle VIII Spectra . . . . .	111
5.20 Cycle IX Significance . . . . .	112
5.21 Lightcurve of LS I +61°303 during Cycle IX . . . . .	113
5.22 Differential ULs derived for Cycle IX . . . . .	114
5.23 Super-orbital fit for the peak of emission of LS I +61°303 on phases 0.5 – 0.75 . . . . .	116
5.24 Super-orbital fit for the maximum emission of LS I +61°303 on phases 0.5 – 0.75 . . . . .	117
5.25 MAGIC and VERITAS super-orbital fit for the peak emission of LS I +61°303 on phases 0.5 – 0.75 . . . . .	119
5.26 Super-orbital fit for the emission of LS I +61°303 on phases 0.75 – 1.0 . . . . .	120
5.27 Super-orbital fit to a sinusoidal for the peak emission in terms of the MJD . . . . .	122
5.28 Super-orbital fit to a sinusoidal for the peak emission in terms of the MJD for MAGIC and VERITAS . . . . .	123
5.29 Multiwavelength super-orbital variability of LS I +61°303 . . . . .	124
5.30 Lomb-Scargle Periodogram of LS I +61°303 for orbital interval 0.5 - 0.75 . . . . .	125
5.31 [Lomb-Scargle Periodogram of LS I +61°303 for orbital interval 0.5 - 0.75, zoom 1 . . . . .	125
5.32 [Lomb-Scargle Periodogram of LS I +61°303 for orbital interval 0.5 - 0.75, zoom 2 . . . . .	126
5.33 Lomb-Scargle Periodogram for the peak emission of LS I +61°303, phases 0.5 -0.75 . . . . .	126
5.34 Lomb-Scargle Periodogram for the peak emission of LS I +61°303, phases 0.5 -0.75, MAGIC and VERITAS . . . . .	127
5.35 Lomb-Scargle Periodogram of the maximum emission of LS I +61°303 for orbital interval 0.75 - 1.0 . . . . .	127
5.36 Super-orbital dependence of the spectral index of LS I +61°303 . . . . .	129
5.37 Super-orbital dependence of the spectral index of LS I +61°303, <i>high</i> and <i>low</i> fluxes . . . . .	130
5.38 HR versus orbital phase . . . . .	130
5.39 HR versus MJD . . . . .	131
5.40 HR versus F ( E >300 GeV) . . . . .	131
5.41 Optical Parameters and TeV fluxes measured from Cycle VI to Cycle IX . . . . .	133
5.42 Optical Parameters and TeV fluxes measured from Cycle VI to Cycle IX . . . . .	134
5.43 Optical Parameters vs TeV flux, phases 0.75 - 1.0 . . . . .	137

5.44 Optical Parameters vs TeV flux, all simultaneous data . . . . .	138
5.45 Spectra of LS I +61°303, from Cycle VI to Cycle IX . . . . .	139
6.1 MWC 656 Orbital Scheme . . . . .	147
6.2 MAGIC differential ULs of MWC 656 . . . . .	148
6.3 Orbital phase-resolved and daily ULs for MWC 656 . . . . .	150
6.4 SED of MWC 656 . . . . .	153
7.1 Radio and X-ray Contours of SS 433W50 . . . . .	157
7.2 SS433 Significance . . . . .	160
7.3 Differential flux ULs calculated for SS 433 . . . . .	162
7.4 Differential flux ULs of the eastern region . . . . .	163
7.5 Skymap of the region SS433/W50 . . . . .	164
7.6 Flux predictions by hadronic model for SS433 . . . . .	164

## List of Tables

2.1	Pulsed laser characteristics . . . . .	26
4.1	Characteristics and parameters of known $\gamma$ -ray binaries . . . . .	79
5.1	Daily Lightcurve of LS I +61°303 on Cycle VI . . . . .	99
5.2	Daily Lightcurve of LS I +61°303 on Cycle VII . . . . .	107
5.3	Daily Lightcurve of LS I +61°303 on Cycle VIII . . . . .	111
5.4	Daily Lightcurve of LS I +61°303 on Cycle IX . . . . .	113
5.5	Maximum and peak of emission for each orbital cycle, orbital phases 0.5 – 0.75 . . . . .	118
5.6	Super-orbital variability for orbital phases 0.75 – 1.0 . . . . .	121
5.7	Parameters of the fit for data at orbital phases 0.5 – 0.75 . . . . .	121
5.8	Spectral indexes for LS I +61°303 campaigns . . . . .	128
5.9	TeV data used for correlation with optical parameters . . . . .	134
5.10	Optical parameters of the data used to search for correlation with the TeV flux . . . . .	135
5.11	Correlation between TeV flux and $H\alpha$ parameters, phases 0.75 - 1.0	135
5.12	Correlation between TeV flux and $H\alpha$ parameters, phases 0.65 - 1.0	136
6.1	Parameters of MWC 656 . . . . .	144
6.2	MAGIC differential flux ULs of MWC 656 . . . . .	148
6.3	Daily values for the MWC 656 observations . . . . .	149
6.4	Phase-to-phase and daily integral ULs of MWC656 . . . . .	149
7.1	Parameters of SS 433 . . . . .	158
7.2	Nightly Lightcurve of SS 433 . . . . .	160
7.3	Integral flux ULs for SS 433 . . . . .	161
7.4	MAGIC differential flux ULs of SS 433 . . . . .	162
7.5	MAGIC differential flux ULs of the eastern regions . . . . .	162



# A

## Acronyms

**AGN** Active Galactic Nuclei

**a.s.l** Above Sea Level

**AU** Astronomical Units

**BH** Black Hole

**C.L.** Confidence Level

**CR** Cosmic Ray

**C.U.** Crab Units

**DAQ** Data AcQuisition

**EAS** Extensive Air Showers

**GRB** Gamma Ray Burst

**FR** Full Range

**FoV** Field of View

**HE** High Energy

**HMXRB** High Mass X-Ray Binary

**HJD** Heliocentric Julian Day

**INFC** INFerior Conjunction

**JD** Julian Day

**LE** Low Energy

**LIDAR** LIght Detection And Ranging

**LLG** Liquid Light Guide

**LMXRB** Low Mass X-Ray Binary

**MAGIC** Majot Atmospheric Gamma-ray Imaging Cherenkov

**MC** Monte-Carlo

**MJD** Modified Julian Day

**NDF** Number of Degrees of Freedom

**NSB** Night Sky Background

**NS** Neutron Star

**phe** Photo-Electron

**PMT** PhotoMultiplier Tube

**PSF** Point Spread Function

**PWN** Pulsar Wind Nebulae

**SED** Spectral Energy Distribution

**SNR** SuperNova Remnant

**SUPC** SUPerior Conjunction

**UL** Upper Limit

**VHE** Very High Energy